The Effects of Chemical and Physical Pressure on Heavy Atom Radicals

by

Kristina Lekin

A thesis
presented to the University of Waterloo
in fulfillment of the
thesis requirement for the degree of
Doctor of Philosophy
in
Chemistry

Waterloo, Ontario, Canada, 2013

Author's Declaration

I hereby declare that I am the sole author of this thesis. This is a true copy of the thesis, including any required final revisions, as accepted by my examiners.

I understand that my thesis may be made electronically available to the public.

Abstract

Neutral radicals have been pursued as building blocks for conductive and magnetic materials for several decades. Carbon-based materials are typically plagued by dimerization and quenching of spins, but the incorporation of heteroatoms has led to many systems that remain open-shell. Radicals based on the thiazyl subunit, which are the subject of this thesis, have evolved through many generations. While the early frameworks possessed a very high onsite Coulomb repulsion energy, *U*, which caused the spins to be localized so that the radicals were trapped in Mott insulating ground states, the development of resonance stabilized bisdithiazolyl radicals, and their selenazyl counterparts, has led to decreased values of *U*, in addition to inducing major improvements in the bandwidth, *W*. Variation in the ligand environment and selenium content can significantly change solid state packing and hence physical properties. This so-called effect of *chemical pressure* has been explored and structure-property correlations have been well established.

In addition to studies involving the variation of chemical pressure, in this thesis the effect of *physical pressure* on these resonance stabilized heavy atom radicals is presented. In the radical building blocks of the present systems there are four possible combinations of sulfur and selenium atoms, sets of which constitute a family. The families may crystallize as an isostructural set in the solid state, but this is rare. Earlier work established that radicals in one isostructural family crystallize as undimerized π-radicals in the $P\bar{4}2_1m$ space group, the selenium variants of which all order magnetically. In this thesis, subtle molecular modification of this family is first explored. Exploration of the substituent effects with selenium fixed in the central position of the heterocycle has provided radicals that order as bulk ferromagnets in the range T_c = 9–12 K. The highest T_c ferromagnets in this group are those based on the all-selenium framework. The magnetic response of these radicals was studied under pressure, and it was discovered that with the initial application of pressure, T_c rises from 17–18 K to 21–24 K, before retreating upon further pressurization. In the 7–9 GPa range, the magnetic insulators begin to metallize, as evidenced by the loss in activation barrier to conductivity and a saturation of the resistance to a finite value at low temperature. The crystal structures in the entire pressure range have been determined and the changes in transport properties have been attributed to decreased slippage of the π-stacks with increasing pressure.

Although most of the resonance stabilized bisdithiazolyl radicals and their selenium variants are undimerized in the solid state, a few derivatives exist that dimerize through unique 4-center 6-electron S···E–E···S σ-bonds. When E = Se, hypervalent σ-dimerization is especially prevalent. Under ambient conditions, these materials pack in crossbraced π-stacks and exhibit semiconducting behavior. Upon mild pressurization ($P \leq 5$ GPa), however, conductivity increases 5–6 orders of magnitude and the

activation energy decreases remarkably. Solid state structures have now been elucidated for these dimers under pressure. For two of the variants, including one (rare) E = S σ-dimer, increasing pressure results in simple contraction of the structure. This leads to enhanced orbital overlap and gradual coalescence of the valence and conduction bands, eventually leading to metallization at $P > 13$ GPa. This behavior is in sharp contrast to a previously reported σ-dimer, which undergoes a transition to a π-dimer at 5 GPa, the structure of which leads to abrupt closure of the HOMO-LUMO gap and, hence, the sudden onset of a weakly metallic state.

As a departure from the behavior of any of the other known hypervalent σ-dimers, one bisdithiazolyl variant undergoes an abrupt $S = 0 \rightarrow S = ½$ transition. This change can be initiated thermally, optically and with mild pressure. The thermal process, which is observed in the magnetic susceptibility measurements, is hysteretic, with $T\uparrow = 380$ K and $T\downarrow = 375$ K, giving rise to a small region of bistability. Irradiation results in the photomagnetization of the metastable $S = ½$ state that persists to an unprecedented relaxation temperature of 242 K. Under the influence of pressure, the same dimer-to-radical transition occurs (at room temperature) near 0.7 GPa. In all cases, the crystal structure of the metastable excited state has been determined by single crystal or powder X-ray diffraction. The novel behavior of the σ-dimer is in addition to the existence of a second polymorph of this material, which is paramagnetic and belongs to the $P\bar{4}2_1m$ space group under ambient conditions.

Further exploration of the effects of chemical pressure on bisdithiazolyl radicals has led to new systems with extremely long alkyl chains. This was explored for the purpose of separating the plates to generate lower dimensional frameworks. The crystal structure of one derivative belongs to the familiar tetragonal space group $P\bar{4}2_1m$. However, upon increasing chain length of the alkyl substituent, an isomorphous set is generated, with all three compounds crystallizing in the $P2_1/c$ space group. The structures consist of pairs of radical π-stacks pinned together by strong intermolecular F···S' bridges to create spin ladder arrays. The slipped π-stack alignment of radicals produces close non-covalent S···S' interactions which serve as the "rungs" of a spin ladder, and the long chain alkyl substituents serve as buffers that separate the ladders from each other laterally. The "legs" of the spin ladder are generated by magnetic exchange along the π-stacks. Magnetic susceptibility measurements reveal the presence of very strong antiferromagnetic coupling in all three compounds, which have been successfully modeled as strong-leg spin ladders.

Acknowledgements

I would like to take this opportunity to thank all of the people in my life who have directly influenced how far I have come. First and foremost, I would like to thank my supervisor, Prof. Rich Oakley, for his enthusiasm when I succeeded, and patience when I stumbled. I could not be more grateful for our conversations about everything from chemistry to life, which have guided me in more ways than he is aware. Thank you.

I owe a great deal of what I know about chemistry and crystallography to my fellow lab mates, including Dr. Alicea Leitch, Dr. Craig Robertson, Dr. Aaron Mailman, Dr. Jaclyn Brusso, Dr. Rob Reid, Karinna Yu, Ryan Roberts and Joanne Wong. A special 'thank you' goes to Stephen Winter for always making time to teach me physics. I will cherish all of the days spent in the Oakley Lab and reflect on them with fondness as a result of the lifelong relationships built with this group.

Thank you to my Ph. D. supervisory committee, Prof. Holger Kleinke, Prof. Sonny Lee, and Prof. Michael Denk for being a part of this journey with me. Your advice throughout this process has been greatly appreciated. I would also like to thank my external examiner, Prof. Jeremy Rawson, for providing constructive feedback and thoughtful questions during the defence.

I must also show my deepest appreciation for our collaborators around the world, without whom the experiments presented in this thesis, particularly those under physical pressure, would not be possible. Thank you to Dr. Paul Dube (Brockhouse), Prof. Rick Secco (Western Ontario), Prof. John Tse (Saskatoon), Dr. Serge Desgreniers (Ottawa), Dr. Masaki Mito (Kitakyushu, Japan), Yasuo Ohishi (Beijing, China), and Dr. Michael Shatruk (Florida State).

Lastly, I would like to thank my friends and family for standing by me during the hard times and celebrating this achievement with me. I want to thank my husband, Vladimir, for moving across the world so that I could become a doctor. I couldn't have done this without you. A big thank you goes to my brother, Stefan Cvrkalj, for always being my cheerleader and often reminding me what's truly important in life. Finally, and most importantly, a very heartfelt 'thank you' goes to my mother and father, Bojana and Djuro. Without their unwavering guidance and support, I would not be here writing these words. They always provided me with the love and tools I needed to succeed, while giving me the freedom to follow my heart. This is for you.

To my Mom and Dad.

Za moju Mamu i Tatu.

Table of Contents

List of Tables

List of Captioned Figures

List of Uncaptioned Figures

Figures are numbered sequentially in each chapter. The numerical prefix in the figure label corresponds to the chapter in which the figure may be found. For example, a figure in Chapter 1 will be assigned the prefix **1-**. The same figure may appear in multiple chapters, having the appropriate prefix each time.

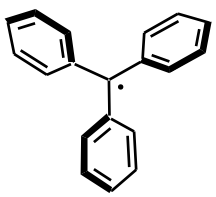

1-1

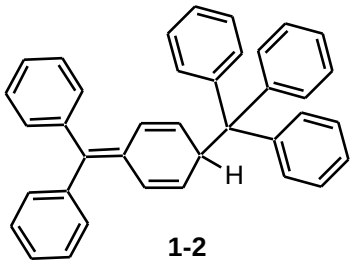

1-2

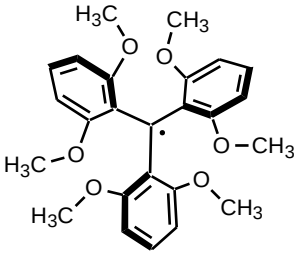

1-3

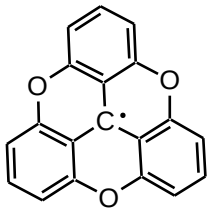

1-4

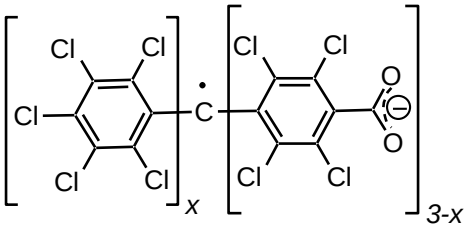

1-5

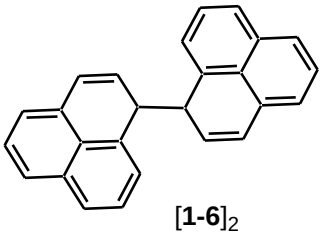

[**1-6**]$_2$

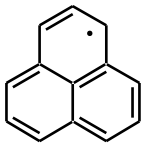

1-6

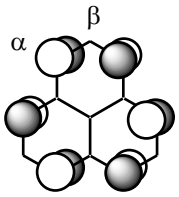

1-7

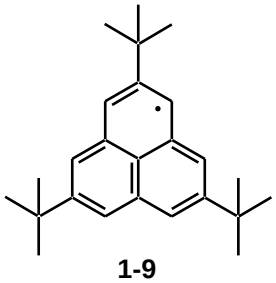

1-9

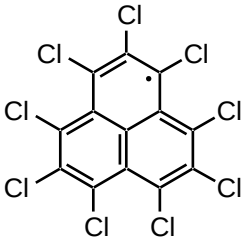

1-10

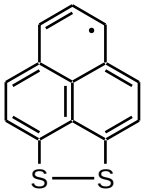

1-11

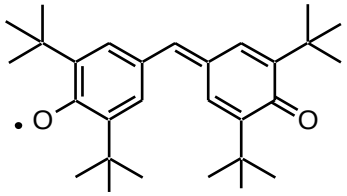

1-12

1-13

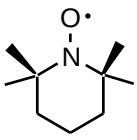

1-14

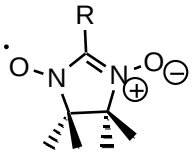

1-15

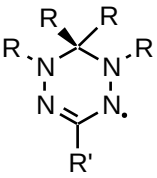

1-16

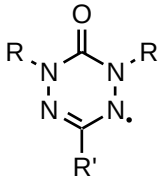

1-17

1-18

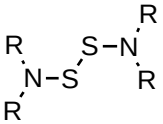

[**1-18**]$_2$

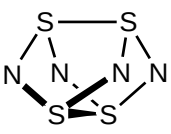

1-19

1-20

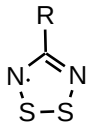

1-21

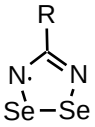

1-22

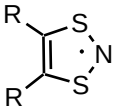

1-23

1-24

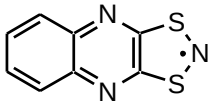

1-25

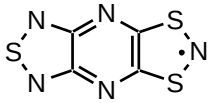

1-26

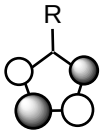

1-21a

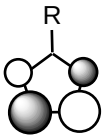

1-22a

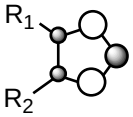

1-23a

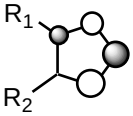

1-24a

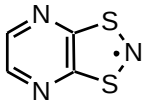

1-28

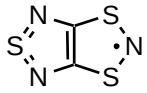

1-29

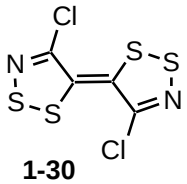

1-30

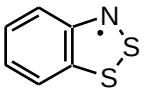

1-31

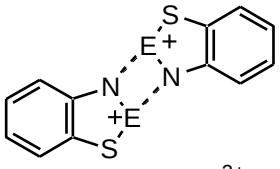

[**1-32**]$_2^{2+}$

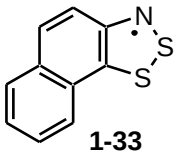

1-33

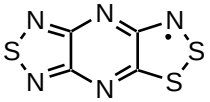

1-34

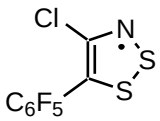

1-35

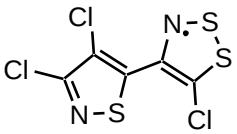

1-36

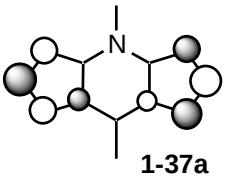

1-37a

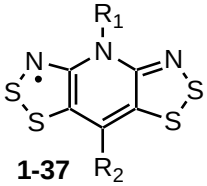

1-37

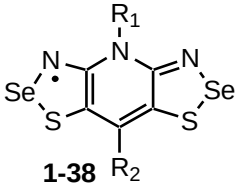

1-38

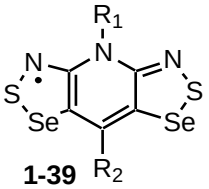

1-39

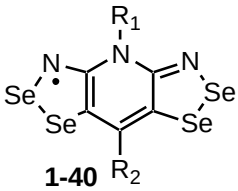

1-40

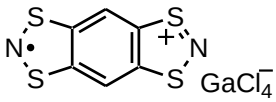

1-41

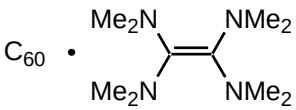

1-42

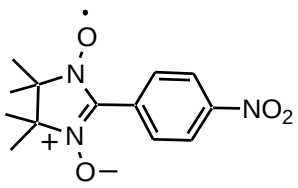

1-43

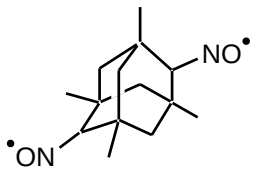

1-44

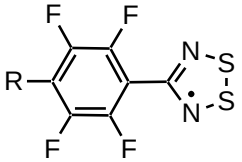

1-45

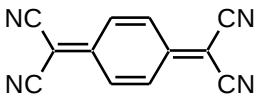

1-47

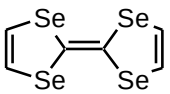

1-48

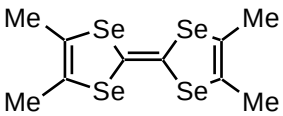

1-49

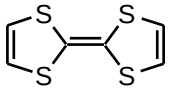

1-46

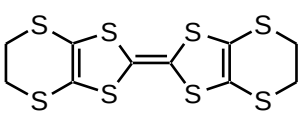

1-50

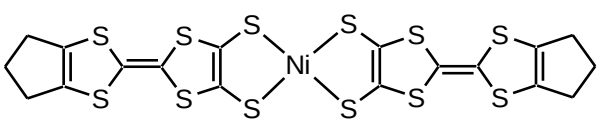

1-51

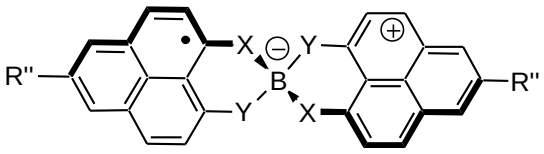

1-52

a X = O, Y = O, R'' = Me, H
b X = NR, Y = O, R'' = H
c X = NR, Y = NR', R'' = H

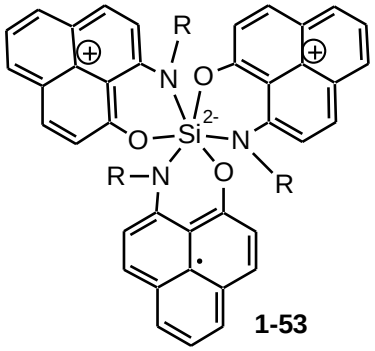

1-53

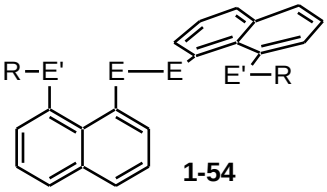

1-54

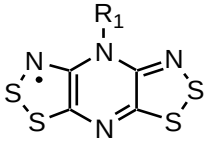

1-56

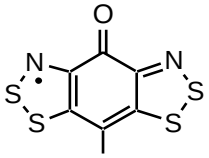

1-57

	E_1	E_2
2-1	S	S
2-2	S	Se
2-3	Se	S
2-4	Se	Se

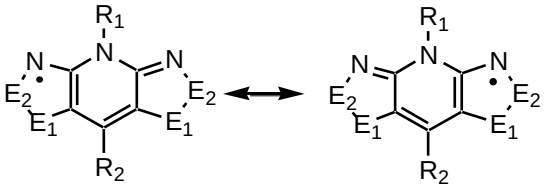

R_1	Et	Et	Et	Et
R_2	**F**	**Cl**	**Br**	**I**
2-1	2-1a	2-1b	2-1c	2-1d
2-2	2-2a	2-2b	2-2c	2-2d
2-3		2-3b	2-3c	
2-4		2-4b	2-4c	

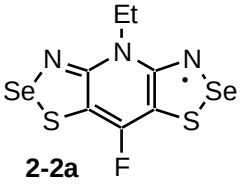

2-2a

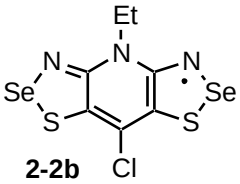

2-2b

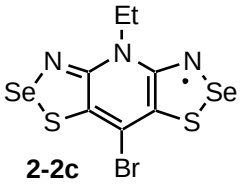

2-2c

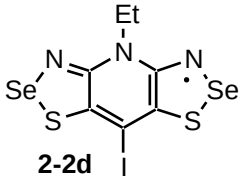

2-2d

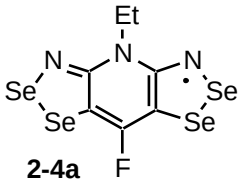

2-4a

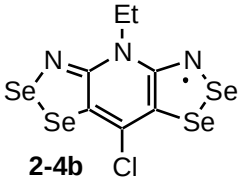

2-4b

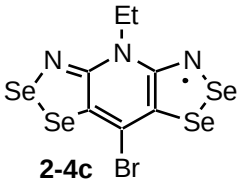

2-4c

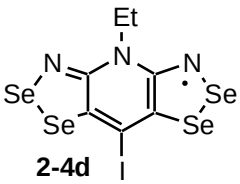

2-4d

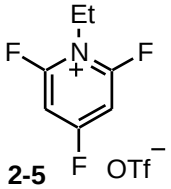

2-5

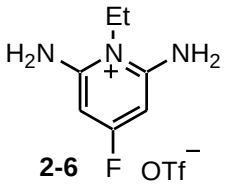

2-6

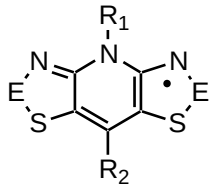

3-1 (E = S)
3-2 (E = Se)

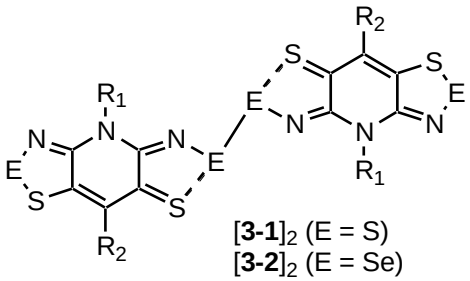

[**3-1**]$_2$ (E = S)
[**3-2**]$_2$ (E = Se)

	E	R_1	R_2
α-**3-1a**	S	Me	F
β-[**3-1a**]$_2$	S	Me	F
[**3-2a**]$_2$	Se	Me	F
[**3-2b**]$_2$	Se	Me	H

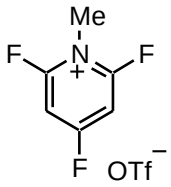

3-3

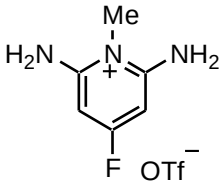

3-4

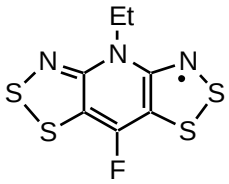

4-1a

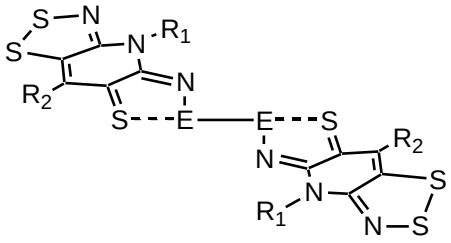

β-[**4-1**]$_2$: E = S, R_1 = Et, R_2 = F

	E	R_1	R_2
β-[**4-1**]$_2$	S	Et	F
[**4-2**]$_2$	S	Me	F
[**4-3**]$_2$	Se	Me	F
[**4-4**]$_2$	Se	Me	H

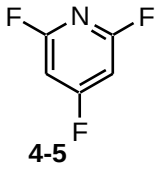

4-5

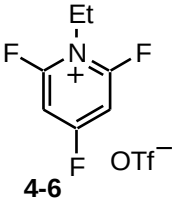

4-6

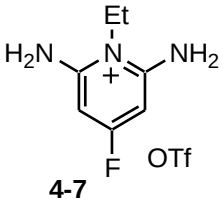

4-7

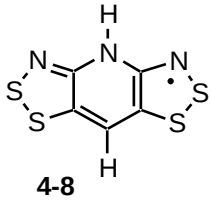

4-8

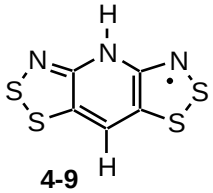

4-9

	E_1	E_2
5-1	S	S
5-2	S	Se
5-3	Se	S
5-4	Se	Se

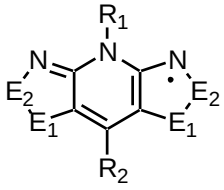

	5-1a	5-1b	5-1c	5-1d
R_1	Pr	Bu	Pn	Hx

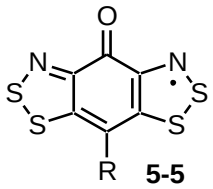

5-5

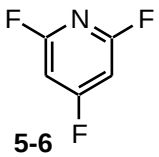

5-6

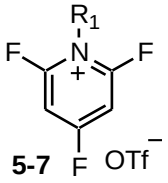

5-7

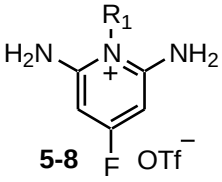

5-8

	E_1	E_2
6-1	S	S
6-2	S	Se
6-3	Se	S
6-4	Se	Se

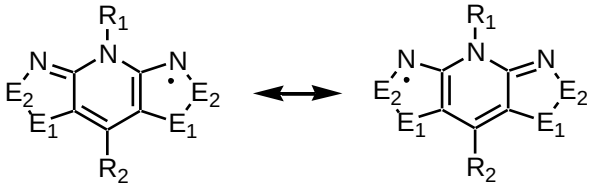

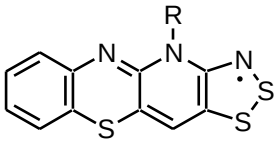

6-5

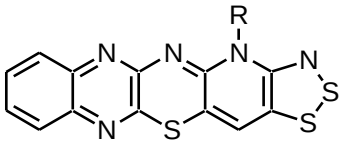

6-6

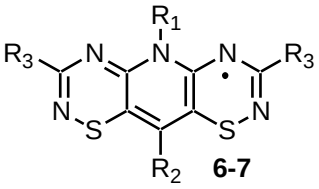

6-7

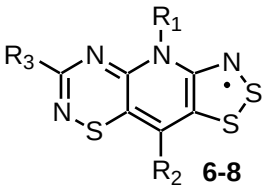

6-8

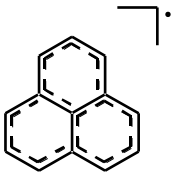

6-9

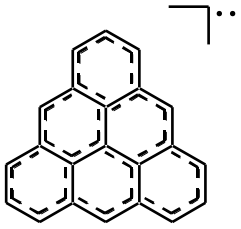

6-10

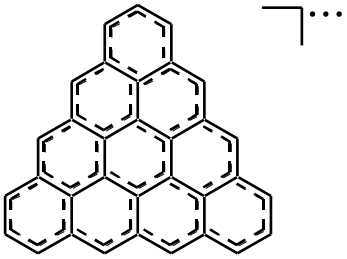

6-11

List of Abbreviations

4c–6e	4-center 6-electron
6-31G(d,p)	a split valence plus polarization basis set
a	crystallographic unit cell axis; hyperfine coupling constants
act	activation
AFM	antiferromagnetism
Å	Angstrom
Anal.	analysis
b	crystallographic unit cell axis
B3LYP	hybrid B3 including an HF exchange term and the LYP correlation functional
BEDT	*bis*(ethylenedithio)
br	broad (IR peak descriptor)
BSS	broken symmetry singlet
Bu	butyl group
BTEAC	benzyltriethylammonium chloride
C	Curie constant
^{o}C	degree centigrade
c	crystallographic unit cell axis
calcd.	calculated
CDW	charge density wave
cm^{-1}	reciprocal centimeters
CO	crystal orbital
CT	charge transfer
CV	cyclic voltammetry
d	doublet (NMR peak descriptor)

D	dimensionality, as in 1D or 3D
DAC	diamond anvil cell
DCE	dichloroethane
DCM	dichloromethane
dec.	decomposition
deg	degrees
DFT	Density Functional Theory
DMFc	*bis*(pentamethylcyclopentadienyl)iron
DTA	dithiazolyl
DTDA	dithiadiazolyl
DSDA	diselenadiazolyl
E	chalcogen, either sulfur or selenium
E_1	chalcogen in the 1-position of the bisdithiazolyl framework, sulfur or selenium
E_2	chalcogen in the 2-position of the bisdithiazolyl framework, sulfur or selenium
E	energy
ΔE	change in energy
$E_{1/2}$	half-wave potential
E_{act}	activation energy
EA	electron affinity
E_{cell}	peak to peak potential separation
EHT	Extended Hückel Theory
emu	electromagnetic unit
E_{pa}	anodic peak potential
E_{pc}	cathodic peak potential
EPR	electron paramagnetic resonance
ET	*bis*(ethylenedithio) tetrathiafulvalene

ESI	electrospray ionization
Et	ethyl
EtOH	ethanol
eV	electron volt
f	fraction of band filled
FM	ferromagnetism
FMO	frontier molecular orbital
FMR	ferromagnetic resonance
g	gram
g	Landé factor (g-factor)
GPa	gigapascal, unit of pressure
GSAS	General Structure Analysis System
$\mathbf{H'}$	effective Hamiltonian
^{1}H	proton
h	hour
H	magnetic field
H_c	coercive field
ΔH_{disp}	disproportionation enthalpy
ΔH_{diss}	bond dissociation enthalpy
Hx	hexyl group
HOAc	acetic acid
HOMO	highest occupied molecular orbital
Hz	Hertz
IP	ionization potential
IR	infrared
$\boldsymbol{J}$	exchange energy

J	valence bond exchange integral
j, j'	electrostatic terms of the valence bond exchange integral
J_π	exchange energy along the π-stack direction
J_{12}	Coulomb integral
k	a quantum number, direction in reciprocal space
k_B	Boltzmann constant
K	Kelvin
kHz	kilohertz
kJ	kilojoule
L	litre
LIESST	Light Induced Excited Spin State Trapping
LT	low temperature
LUMO	lowest unoccupied molecular orbital
LW	linewidth
M	molarity, magnetization
m	multiplet (NMR descriptor)
min	minute
MIT	metal-to-insulator transition
Me	methyl
MeCN	acetonitrile
MeOH	methanol
mL	millilitre
mmol	millimole
MO	molecular orbital
mol	mole
mp	melting point

MS	mass spectrometry
mT	millitesla
NBMO	nonbonding molecular orbital
NMR	nuclear magnetic resonance
Nβ	Avogadro's number multiplied by the Bohr magneton – unit of magnetization
OAH	odd alternate hydrocarbon
Oe	Oersted
OMFc	*bis*(tetramethylcyclopentadienyl)iron
OTf	triflate (trifluoromethanesulfonate) anion
ORTEP	Oak Ridge thermal ellipsoid parameter
param.	parameters
PCC	piston cylinder cell
Ph	phenyl group
PLY	phenalenyl radical
ppm	parts per million
Pr	propyl group
Pn	pentyl group
PXRD	powder X-ray diffraction
K (or Q)	valence bond Coulomb integral
r	radius, van der Waals radius, distance (Å)
R	general substituent group
R	agreement index (crystallography)
RDI	radical-to-dimer interconversion
rem	remanent
ref.	referenced
restr.	restraints

RIC	radical ion conductor
ROTf	alkyl triflate
R_p	agreement index- profile (crystallography)
RT	room temperature
R_w	weighted agreement index
RVB	resonating valence bond
s	strong (IR peak descriptor); singlet (NMR peak descriptor); second
S	Siemens ($1S = 1\Omega^{-1}$); singlet state
S	spin
S^2	overlap density integral
$<S>^2$	expectation value
sat	saturation
SCE	saturated calomel electrode
SCF	self consistent field
SCO	spin crossover
SHMO	Simple Hückel Molecular Orbital Theory
SOMO	singly occupied molecular orbital
SMM	single molecule magnet
SIM	single ion magnet
SW	sweep width
t	triplet (NMR peak descriptor)
T	temperature; triplet state
T^*	critical temperature for MIT
T_c	Curie temperature
TCNQ	tetracyano-*p*-diquinomethane
TCNE	tetracyano ethylene

TDAE	tetrakis(dimethlyamino)ethylene
temp	temperature
TEMPO	2,2,6,6-tetramethylpiperidine-N-oxyl
TM	transition metal
TMPDA	N,N,N',N'-tetramethyl-*p*-phenylenediamine
T_N	Néel temperature
Torr	unit of pressure = 133.32 Pa
TMS	trimethylsilyl group
TMTSF	tetramethyltetraselenafulvalene
TTF	1,1',3,3'-tetrathiafulvalene
U	on-site Coulomb repulsion energy
V	Volt
V	volume
VASP	Vienna Ab initio Structure Package
VB	valence bond
vs	very strong (IR peak descriptor)
vs	versus
vw	very weak (IR peak descriptor)
w	weak (IR peak descriptor)
W	bandwidth
wR_p	weighted agreement index - profile (powder crystallography)
X	halogen group
x	Cartesian coordinate
y	Cartesian coordinate
Z	number of asymmetric units per unit cell
z	Cartesian coordinate

ZFC	zero field cooled
^{o}	degree
α	crystallographic axis angle; coulombic parameter
β	crystallographic axis angle; resonance parameter
γ	crystallographic axis angle
δ	chemical shift in ppm; mean separation of molecules in a slipped stack
ε	orbital energy
μ	absorption correction
μA	microamps
π	orbital symmetry
τ	angle between the mean plane of the heterocyclic backbone and the stacking axis
υ	frequency
ρ	electrical resistivity; spin density
σ	electric conductivity; orbital symmetry
σ_{RT}	room temperature conductivity
λ	wavelength
ϕ	atomic orbital
χ	magnetic susceptibility
ψ	wavefunction

"Of all the frictional resistances, the one that most retards human movement is ignorance – what Buddha called 'the greatest evil in the world.' The friction which results from ignorance can be reduced only by the spread of knowledge and unification of the heterogeneous elements of humanity. No effort could be better spent."

Nikola Tesla

"The Problem of Increasing Human Energy" (The Century Magazine, June, 1900)

Chapter 1

Introduction to Neutral Radicals as Conductive and Magnetic Materials

1.1 Stable Radicals: a Brief History

The classical textbook definition of a *radical* is that it is a molecule containing at least one unpaired electron, and therefore possesses an open-shell electronic configuration.[1] The majority of these species are highly reactive and exist only as transient intermediates in various chemical processes.[2] This is primarily due to the fact that their major reactivity pathways such as dimerization, hydrogen abstraction and disproportionation are strongly favored thermodynamically. These processes also tend to have a small or non-existent activation barrier.[3] However, it is possible to design radicals that are remarkably stable by using either steric or electronic control. Such species can exist in solution or in the solid state "on the bench top" for indefinite periods.

There are certain chemical characteristics that support stability, and hence there are a number of families of stable radicals.[3,4] The current definition of a *stable* radical is one which can be isolated and handled as a pure compound and is preferably inert to both oxygen and moisture. *Persistent* radicals, on the other hand, cannot be isolated but are sufficiently long-lived to be observed spectroscopically.[5]

Although closed-shell materials are diamagnetic, that is, they slightly repel an applied magnetic field, free radicals are paramagnetic and are attracted to a magnetic field. This inherent property of radicals provides a powerful tool for their detection and study, as well as giving rise to their technological relevance. Radicals have been used for spin labeling,[6] spin trapping,[7] electron paramagnetic resonance (EPR) imaging,[8] and living free radical polymerization catalysis,[9] and they are key players in many biological processes.[10]

The focus of this thesis is primarily the synthesis and characterization of new, stable heavy atom heterocyclic radicals and their dimers, as well as an exploration of solid state structures under applied

physical pressure. Before reporting my results and analyses, it is instructive to begin with the history of families of stable molecular radicals leading to the thiazyls. Following that, relevant theory for the understanding of molecular magnetism and conductivity will be introduced, in addition to examples of molecular materials displaying these properties. Lastly, recent results from the Oakley group will be summarized as a logical prelude to my own research.

1.2 Families of Stable Molecular Radicals

1.2.1 Triphenylmethyl Radicals

The history of stable radicals begins at the turn of the 20th century, when Moses Gomberg boldly announced the formation of the first persistent free radical triphenylmethyl **1-1**.[11] It was initially met with a great deal of skepticism, but was ultimately accepted by the chemical community.[12] This discovery, with its immediate impact, set the stage for rapid discovery of more stable radicals throughout the 20th century. It was determined many years later that, although the radical **1-1** was persistent in solution, desolvation led to the formation of a dimer in the solid state. The unpaired electron in this system is sterically and electronically stabilized by the propeller-like conformation of the phenyl rings leading to its persistence in solution, although it has been established that the radical is in equilibrium with its σ-bonded dimer.[13] Despite a few initial guesses of the dimer structure, it was elucidated to be the head-to-tail configuration as in **1-2**.[14] This dimerization process is the typical fate of most carbon-centered radicals, particularly ones that are not sufficiently protected by bulky substituents.[15]

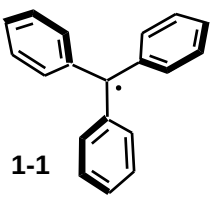

1-1

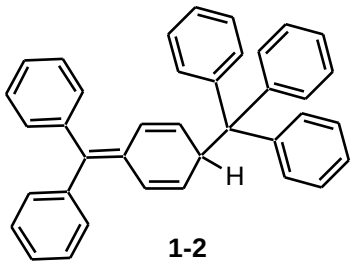

1-2

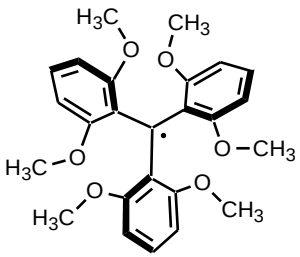

1-3

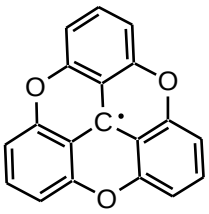

1-4

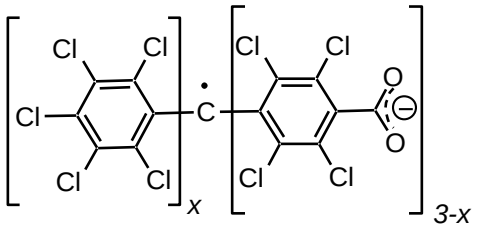

1-5

Further attempts to isolate stable, carbon-based radicals have led, for example, to **1-3** and **1-4**. Despite the planar geometry of **1-4**, and thus potential for full π-delocalization of the unpaired spin, these radicals form insoluble dimers.[16] On the other hand, extreme steric protection of the unpaired spin in **1-3** stabilizes the open shell monomer species in a twisted form, both in solution and in the solid state.[15a,17] The possibility of linking these radicals *via* coordination or non-covalent interactions, such as the *para* carboxylate substituted radicals **1-5** (x = 0–2), has been a particularly interesting direction in which triphenylmethyl chemistry has taken over the last 10 years.[18] These systems are as stable as the parent perchlorinated triphenylmethyls, and hold potential for binding to transition metals in discrete complexes[19] as well as metal organic frameworks.[20] They can also be employed as supramolecular synthons in the generation of hydrogen bonded networks with tunable pore sizes and functionalities.[21]

1.2.2 Phenalenyl and Related Radicals

The phenalenyl radical **1-6** was synthesized over 50 years ago,[15c] but more recently has been investigated as a potential molecular conductor, a topic discussed further in Section 1.4.5. In solution, this radical is very oxygen sensitive and in equilibrium with its σ-bonded dimer.[22] However, in dilute, deoxygenated solution, most radicals of this type persist indefinitely.[23] This stability is attributed to electronic effects, *i.e.*, a large resonance stabilization energy, in contrast to the steric control demonstrated by the triphenylmethyl radical family.

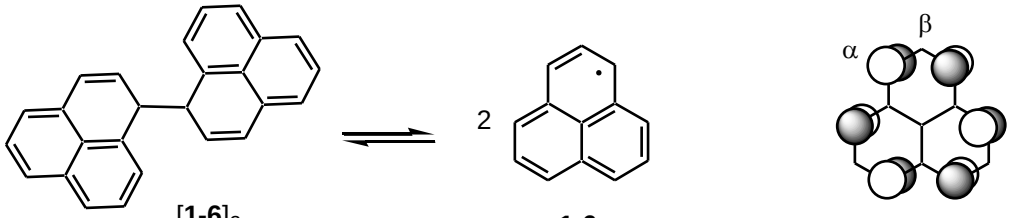

[**1-6**]$_2$ **1-6** **1-7**

The spin density of the unpaired electron is mostly distributed around the α carbon atoms, despite the fact that the structure is commonly drawn with the unpaired spin on the central carbon. This spin distribution can be understood on the basis of the singly occupied molecular orbital (SOMO) **1-7**, an orbital that is a non-bonding molecular orbital (MO) with coefficients solely on the α carbon atoms. The spin density distribution suggests that the unpaired electron resides almost entirely on the periphery of the ring, thus rationalizing the ease with which this species forms carbon-carbon σ-dimers [**1-6**]$_2$ in solution.[24]

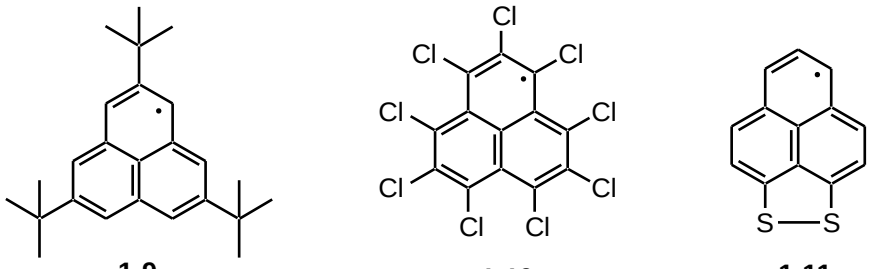

1-9 **1-10** **1-11**

Although the bond energy of these σ-dimers has been found *via* computation to be weak, most simple phenalenyl radicals dimerize reversibly in this way.[25] Methods to block this dimerization pathway include the introduction of steric bulk in the form of *t*-butyl groups on half of the α carbon atoms (**1-9**),[25b,26] perchlorination (**1-10**),[27] and the execution of electronic control with the addition of sulfur atoms to the ring system (**1-11**).[28,29] All three of these strategies successfully block σ-dimerization through carbon, yet only **1-10** forms discrete radicals in the solid state with a buckled phenalenyl skeleton to accommodate the repulsive interactions between *peri* chlorine substituents. The *t*-butyl substituted radical **1-9** associates in an alternative mode – through π-π dimerization, a mode that is a common fate for most flat, delocalized π-radicals. In this case, the two radicals are stacked face-to-face and out of phase with respect to the *t*-butyl groups to avoid steric repulsion. The plates are 3.2 Å apart

in the solid state, which is significantly shorter than non-bonded π-stacking distances (~ 3.4 Å). The first phenalenyl radical to be stabilized against σ-dimerization without bulky substituents is **1-11**. Despite the fact that only two α carbon positions have been sterically protected, these radicals do not associate *via* C-C σ-bonds, demonstrating that stabilization has been affected electronically through the presence of heteroatoms. In solution, the radicals are fully dissociated, but they do form π-dimers in the solid state.[29] Whether or not these so-called "pancake dimers" are truly closed-shell species or strongly antiferromagnetically (AFM) coupled open-shell singlets is a matter of some debate.[30,31]

1.2.3 Nitrogen and Oxygen Organic Radicals

Due to the propensity of carbon-based radicals to dimerize, both through σ- and π-bonds, the natural trajectory of radical science led to the development of organic radicals possessing heteroatoms (N, P and O, P) within the ring systems. It has long been known that small heteroatomic radicals such as nitric oxide (NO), nitrogen dioxide (NO_2) and molecular oxygen (O_2) are monomeric under standard conditions. With a long-standing history, they remain of considerable biological, industrial, and chemical importance.[32] In the realm of synthetic chemistry, it has been found that many radicals can be stabilized when containing N, O or a combination of both atoms. Unpaired electrons centered on these atoms enjoy increased stability due to the electron richness of these atoms, termed the alpha-effect,[33,34] that is, the repulsion between lone pairs on neighbouring molecules tends to inhibit σ-bond formation, in addition to the high *s*-character and electronegativity. The galvinoxyl radical **1-12** is a prime example, where the combination of an oxygen-based radical possessing resonance delocalization of the spin leads to a stable, monomeric structure in the solid state.[35] Intriguingly, it is essentially insensitive to oxygen and has unusual solid state magnetic properties.[36] Other well-known families of N- and O-containing stable radicals are the nitroxyls **1-13**, nitronyl nitroxides **1-15**, verdazyls **1-16** and oxoverdazyls **1-17**.

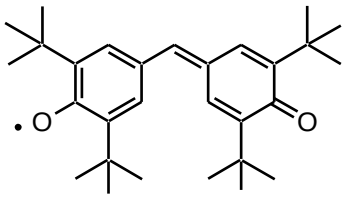

1-12

1-13

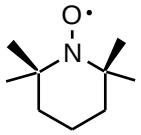

1-14

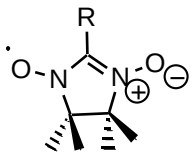

1-15

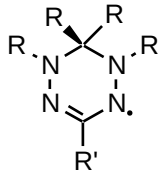

1-16

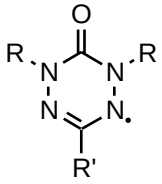

1-17

Nitroxyl (or nitroxide) radicals **1-13** are possibly the most well-known family of stable radicals.[37] There are many variations containing the N-O radical unit, where *many* of them are stable with respect to dimerization, air, water and other radical-based reactions, and stability depends on the R substituents. For example, TEMPO (2,2,6,6-tetramethylpiperidine-N-oxyl) **1-14** is very stable and is used as a building block for spin labeling studies.[38] Incorporating resonance delocalization into the framework affords the nitronyl nitroxide subclass **1-15**, where the unpaired spin is equally distributed over both N-O units. A wide range of applications for these radicals and the parent stable nitroxyls **1-13** include their use in spin-trapping devices,[39] pH-sensitive spin probes,[40] prefluorescent probes,[41] polymerization initiation,[42] Magnetic Resonance Imaging (MRI)[43] and organic synthesis.[44] Due to their inherent stability and thus open shell nature, the nitronyl nitroxide radicals are particularly interesting with respect to their magnetic properties, a topic that will be discussed further in Section 1.3.2.

Furthermore, heterocyclic radicals based on nitrogen, such as verdazyls **1-16**[45] and oxoverdazyls **1-17**[16,46] have intrinsic stability. In these radical families, there is little steric bulk around the unpaired spin, and the stability is supported by the delocalization of the electron around the electron-rich ring system. Like the nitroxyls, many of these materials are stable indefinitely, while some are modestly (hours) persistent.[4a,47]

1.2.4 Nitrogen and Sulfur Radicals: The Thiazyls

Considering the fact that sulfur is directly below oxygen in Group 16, one might infer that stable radicals analogous to the ones containing N and O could easily be developed for N and S, yet the chemistry of sulfur differs greatly from oxygen. The most fundamental distinction can be found in the common forms of the two elements (O_2 *vs*. S_8), and the fact that stable open shell species O_2, NO, and NO_2 do not have stable sulfur analogues.[48] Take for example the thionitroxides **1-18**, which are directly related to the nitroxides **1-13**. At room temperature, these radicals mainly exist as their disulfide dimers [**1-18**]$_2$, although they do dissociate upon heating due to the weakness of the S−S bond (ΔH_{diss} [a] ~ 43 kcal mol^{-1}).[49,50] The drastic differences in S/N radical chemistry *versus* that of N/O can be attributed to the larger size and hence polarizability of sulfur, which leads to a diminished alpha effect in heavier elements.

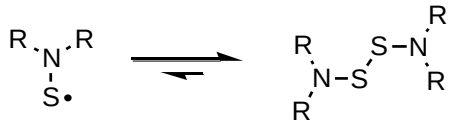

1-18 [**1-18**]$_2$

Despite this tendency for simple sulfur radicals to associate, sulfur-nitrogen chemistry has been at the frontier of molecular radical research for years. Many of the systems that have been developed since the 1970s are functional materials displaying intriguing physical properties such as conductivity and magnetism. The basic S/N subunit consists of a 2-center 3-electron bond, which has considerable strength compared to a carbon-carbon π-bond (Figure 1.1).[51] Conjugated systems containing the –S=N– subunits have been coined as "electron rich" because, like nitroxyls, they have more π-electrons than atoms.[52] However, the higher electronegativity of S and N with respect to carbon leads to some stabilization despite the "electron richness."

[a] Dimerization/dissociation enthalpies (ΔH_{diss}) will be quoted with respect to the following equation throughout this thesis: R–R → 2 R• .

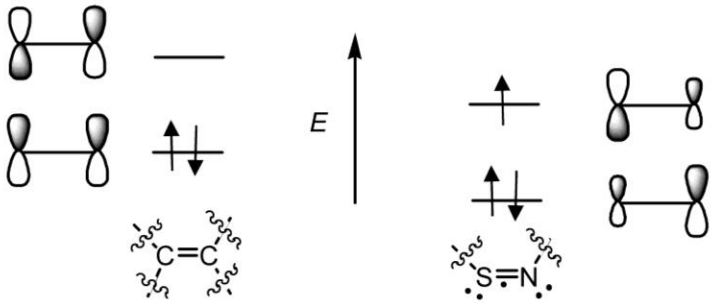

Figure 1.1 Qualitative energy level diagram showing relative energies of the frontier molecular orbitals (MOs) of C−C and S−N π-bonds.

One particularly famous material containing the –S=N– subunit is poly(sulfur-nitride), $(SN)_x$, which was the first example of a synthetic metal.[53] It was originally made *via* the solid state polymerization of S_2N_2 **1-20**, which is generated by heating S_4N_4 **1-19** over silver wool (Scheme 1.1). The procedure generates a highly crystalline material, forming fibrous golden needles,[54] but alternative methods were developed due to the shock sensitivity of both S_2N_2 and S_4N_4.[55,56]

Scheme 1.1

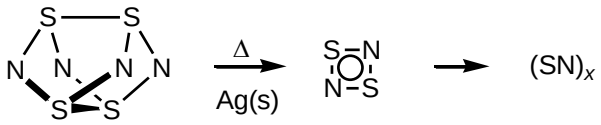

1-19 **1-20**

The crystal structure of the polymer consists of parallel planar, puckered (*cis-trans*) chains of covalently linked SN units tightly packed to allow for close interchain interactions (Figure 1.2). The two covalently linked SN atoms are very closely bound; atomic separations are 1.59 and 1.63 Å, indicating the presence of significant, delocalized π-bonding along the chains. There are also numerous interchain interactions that are well within the van der Waals separation for S and N (~ 3.1 Å).[57,58] These help provide structural stability down to low temperatures.[59] Since modifications to the $(SN)_x$ backbone, other than selenium replacement of sulfur, were not possible, the tendency toward the development of radical heterocycles containing the –S=N– subunit and an unpaired electron in the

singly occupied molecular orbital (SOMO) was natural. In principle, these systems would also enjoy stabilization with respect to the σ-dimerization trap that plagued the carbon-based radicals.

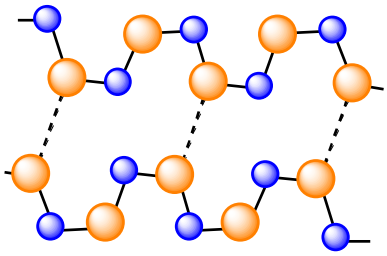

Figure 1.2 Schematic drawing of $(SN)_x$ crystal structure showing bonds and interchain contacts (dashed lines).

The early target building blocks were the 1,2,3,5-dithiadiazolyl radicals (DTDA) **1-21**, first discovered in the 1970s,[60] the related 1,2,3,5-diselenadiazolyls (DSDA) **1-22**,[61] and the 1,3,2- and 1,2,3-dithiazolyls (DTA) **1-23** and **1-24**, respectively.[48] Their SOMOs are all antibonding in character (π*), and in the case of the DTDAs **1-21a**, DSDAs **1-22a** and the 1,2,3-DTAs (**1-24a**), possess nodes going through carbon atoms to which R groups are attached. This prevents direct electronic conjugation of the substituent R with these orbitals. By contrast, substituents are able to communicate electronically with the unpaired spin in the DTAs as there are small coefficients on the ring carbons in SOMOs **1-23a** (R_1 and R_2) and **1-24a** (just R_2).

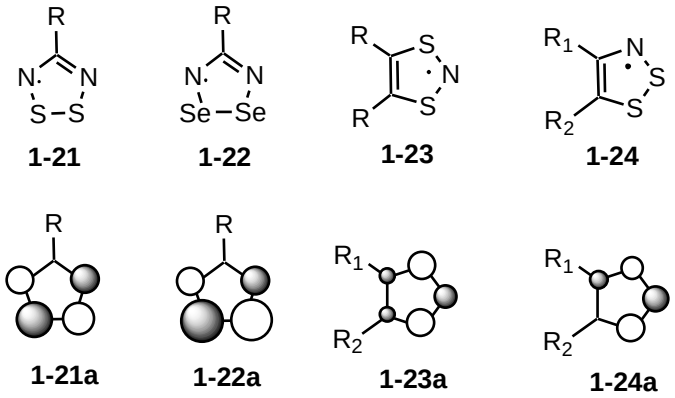

1.2.5 Modes of Dimerization of Simple Thiazyl Radicals

Unfortunately, most thiazyl and selenazyl radicals associate as π-dimers in the solid state. In fact, all of the early DTDAs **1-21** form π-dimers in the absence of steric protection.[48,56] The symmetry of the π* SOMO allows various approaches of the two magnetic π* orbitals in the solid state. An in-phase combination results in a bonding MO available for spin pairing of the two nominally unpaired electrons (Figure 1.3).

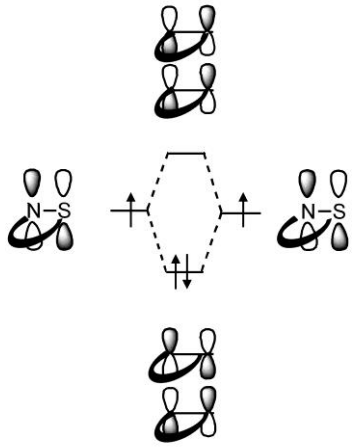

Figure 1.3 A simple molecular orbital diagram depicting the coupling of two magnetic π* SOMOs, resulting in a spin-paired π-dimer. Adapted from reference 48.

Due to the numerous options for the approach of these two orbitals, DTDA dimers can take various forms depending on the steric requirements of substituent R, as shown in Figure 1.4. The most typical structure in the series, the *cis*-cofacial dimer (Figure 1.4a), is found for 4-phenyl-1,2,3,5-DTDA and other derivatives with simple aromatic substituents.[62,63] This structure gives rise to short intradimer S···S' contacts of 3.0 – 3.1 Å, which lie between the sum of the van der Waals contacts for sulfur (3.6 Å) and that of a S–S covalent bond (~ 2.1 A). The other typical arrangement for DTDAs is the twisted cofacial structure, Figure 1.4b, found for structures where R is a non-planar substituent such as CF_3, Me, NMe_2, Cl, and adamantyl.[64] The other two arrangements, shown in Figure 1.4c[63] and d,[65] are much more rare.

The selenium analogues of DTDAs, the DSDAs **1-22**, mainly associate in the *cis*-cofacial arrangement,[63,66] although a peculiar T-shaped mode (Figure 1.4e and f) has been found when R = *p*-chloro- and *p*-bromo-tetrafluorophenyl.[67] The observation of diamagnetism in the samples has been rationalized by the spin-paired spiroconjugated SOMOs shown in Figure 1.4f. Despite a large dimerization enthalpy for DTDAs (ΔH_{diss} ~ 35 kJ mol^{-1}), there are a few derivatives that are paramagnetic in the solid state, namely those with fluorinated phenyl substituents.[61] A few of these derivatives possess interesting magnetic properties, discussed in more detail in Section 1.3.2.

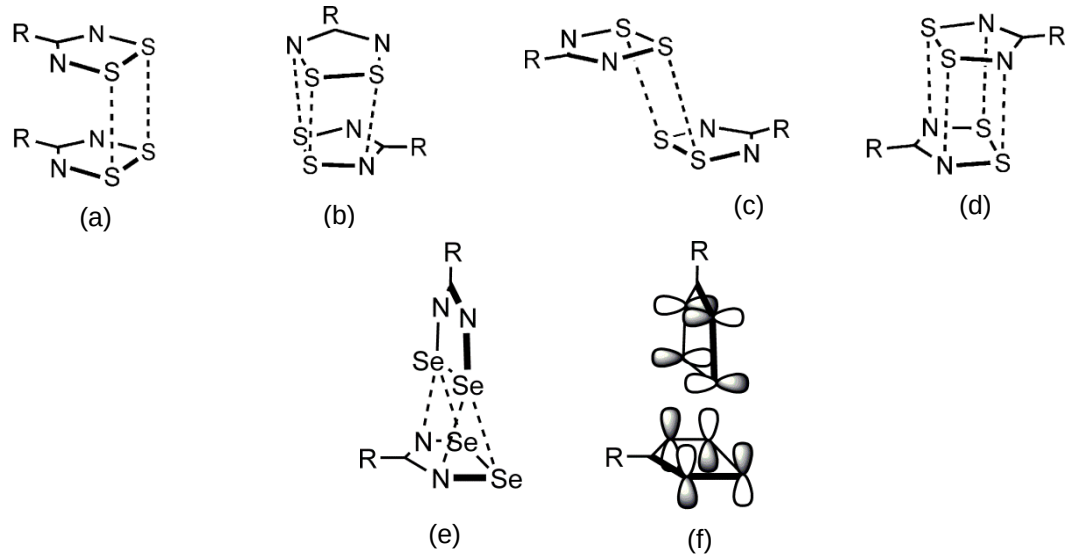

Figure 1.4 Modes of dimerization of radicals **1-21** and **1-22**, including (a) *cis*-cofacial, (b) twisted cofacial, (c) *trans*-antarafacial, (d) *trans*-cofacial, and (e) T-shaped with (f) the corresponding $\pi^* - \pi^*$ interaction. Adapted from reference 3.

1.2.6 Bistability in 1,3,2-DTAs

In contrast with the DTDA radicals, the enthalpy of dimerization of 1,3,2-DTAs **1-21** is almost negligible (ΔH_{diss} ~ 0 kJ mol^{-1})[68] and a large number of these radicals are monomeric in the solid state.[69] Nonetheless, some derivatives do associate as π-dimers,[70] turning out to be more interesting than their monomeric counterparts. At low temperatures, the dimeric species are all diamagnetic, yet some of these can "pop" open (dissociate) with increasing temperature.[71] Most of the variants do so gradually

with temperature, such as QDTA **1-25**, reaching about 40 % free Curie spins by 350 K.[72] However, a few of the variations, such as TDP-DTA **1-26**,[73] displays hysteretic behavior with respect to this spin liberating transition, giving rise to a metastable open-shell state between 150–200 K. A wide region of bistability near room temperature was discovered for PDTA **1-27**[69b,74] and TTTA **1-28**[75].

As defined by Rawson,[61]

> "A material is structurally bistable if it can exist in two stable forms (polymorphs) under the same range of external parameters."

Typically, at any given temperature, one polymorph or phase is more stable than the other, and there exists an energetic barrier between the two phases. The less stable phase, then, is metastable with respect to the more stable one, and the range within which both phases are observed is the bistability region. In the solid state, lattice reorganization is usually the factor that gives rise to this energetic barrier in DTA radicals **1-23**, therefore the more dramatic a structural change, the larger is the region of bistability.

Understanding the mechanisms by which these transitions occur in the solid state requires having detailed structural information at temperatures above and below the phase transition. In cases where hysteresis is not observed, the structural change is a simple uncoupling of the π-dimers, leading to a regular π-stacked radical array and strongly antiferromagnetically coupled free Curie spins. When hysteresis in the magnetic susceptibility measurements is observed, the structural change is much more dramatic, giving rise to an energetic barrier between the two states. In the case of QDTA **1-25** and TDP-DTA **1-26**, the plates slip laterally at higher temperatures (Figure 1.5a). The most activated of the transitions, though, leading to the largest barriers and thus widest regions of bistability, is *via* the Venetian blind mechanism observed for PDTA **1-27** and TTTA **1-28** (Figure 1.5b). In the case of **1-28**, the temperature range of the bistability is 92 K, encompassing room temperature. One notable, and rare, example of a radical in the DTDA family that does much the same thing is 1,3-phenylene-bridged bis-

DSDA **1-29**.[76] This material crystallizes as a co-facial π-dimer under ambient conditions, but with increasing temperature demonstrates hysteretic liberation of free Curie spins.

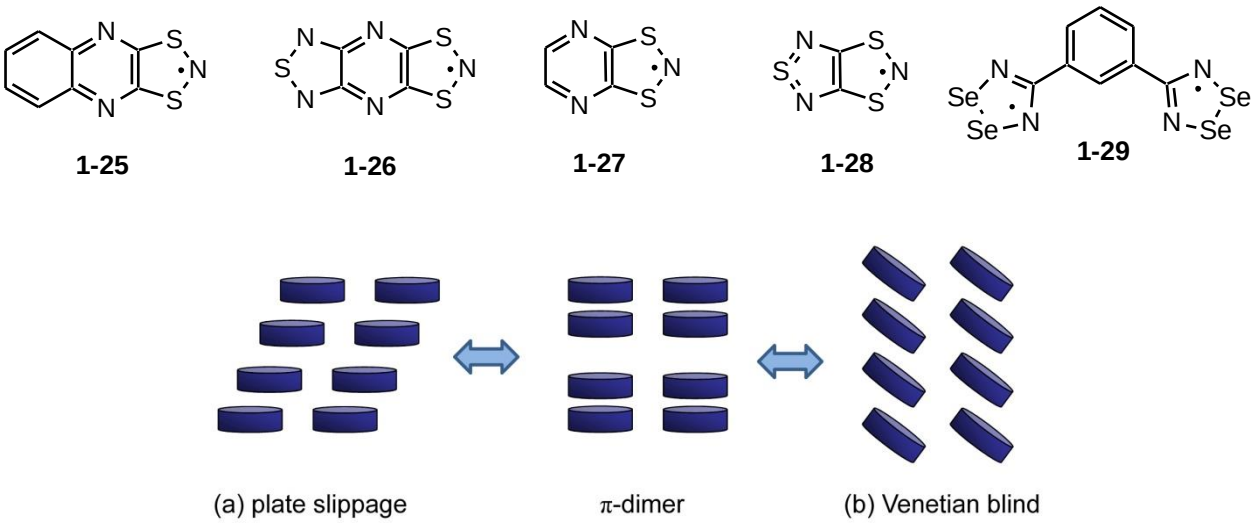

Figure 1.5 Mechanisms by which a π-dimer may reversibly uncouple leading to (a) plate slippage or (b) a Venetian blind structure.

Materials exhibiting wide regions of bistability, particularly those that encompass room temperature, are exciting for the development of new molecular switching devices. This has been explored extensively with transition metal complexes and their spin crossover (SCO) transitions,[77] using both temperature[78] and light[79] to switch between phases. A novel radical undergoing hysteretic interconversion with its σ-dimer under the influence of temperature, pressure and light will be presented in Chapter 4, a transition that is fundamentally different from the behavior of the aforementioned DTAs. The hysteresis observed in the DTA materials is attributed solely to cooperative solid state effects,[80] while the new radicals exhibit a radical to dimer interconversion (RDI) as a result of a symmetry forbidden transition at the molecular level.[81]

1.2.7 Resonance Stabilization and the Bisdithiazolyl Family

The next generation of radicals, the 1,2,3-DTAs **1-24** pioneered by the Oakley group, are isomers of the 1,3,2-DTAs and involve a slightly larger degree of delocalization of the unpaired spin than previous

systems. The π-SOMO **1-24a** of these radicals is antibonding, and there is a node through one of the carbon atoms in the backbone. The other carbon atom, however, possesses a substantial coefficient, and thus electron density can "bleed" away from the thiazyl ring and onto R_1 (of **1-24**) or a fused ring. Over the years, many examples of these radicals were synthesized and the family includes a great deal of structural diversity.[82] Recently, the first metal coordination complex with a 1,2,3-DTA heterocyclic ligand was reported. The undimerized radicals act as bridging ligands between three Mn(II) centers, mediating ferromagnetic coupling between the metal ions and exhibiting ferrimagnetism in the complex.[83]

One of the early attempts to make a 1,2,3-DTA involved the reduction of Appel's salt,[84] **1-24** ($R_1 = R_2$ = Cl), resulting in the fulvalene-based structure **1-30** in which a double bond is formed through the active carbon atoms (ones possessing spin density in the SOMO).[85] The simple benzo-fused derivative **1-31** has been known for many years,[82] and was characterized in solution *via* EPR and cyclic voltammetry. Its solid state structure is not known. Attempts to generate selenium and tellurium variants of **1-31** gave rise to strongly associated dications $[\mathbf{1\text{-}32}]_2^{2+}$ (E = Se, Te) in solution.[86] The corresponding selenium radicals were found to be persistent in solution, while the tellurium radicals were unattainable due to the surprisingly strong 4-center centrosymmetric interaction between cation pairs.

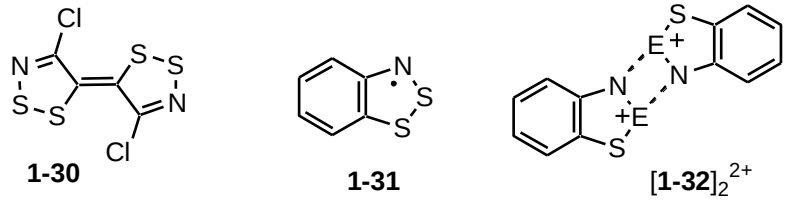

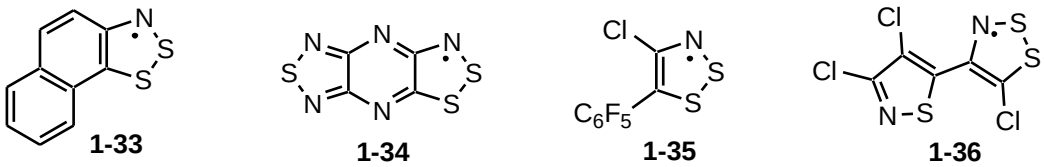

To date, only four mono-1,2,3-DTA radicals have been characterized in the solid state, and three of them form π-dimers. Radicals **1-33**,[87] **1-34**[88] and **1-35**[89] form *cis*-cofacial, *centrosymmetric* cofacial and

twisted (gauche) dimers, respectively. Dithiazolyl **1-36** is unique in that it is monomeric in the solid state, and forms slipped π-stacked arrays.[90] Nonetheless, its performance as a molecular material is somewhat disappointing, as the measured room temperature conductivity is on the order of 10^{-7} S cm^{-1}, although this is much higher than that seen for DTDAs.

A major shift in the thiazyl radical paradigm occurred when the Oakley group began to synthesize and characterize the resonance stabilized bisdithiazolyl DTA radicals **1-37** – **1-40**.[91] These systems consist of two 1,2,3-DTA rings fused through a pyridine core, and possess unpaired spin that is conjugated throughout the whole π-system, as shown in the SOMO **1-37a**, with a large amount of spin density on the thiazyl wings. The majority of these materials are *not* associated in the solid state and enjoy interesting magnetic and conductive properties as a result. Modification of the R_1 and R_2 substituents can fine-tune the solid state packing, and hence charge and spin transport properties. Replacement of the sulfur atoms in **1-37** with the heavier chalcogen selenium affords three more variations of the building blocks, and again, strides have been made in the generation of functional molecular materials. There is a great deal of structural diversity within this family of thiazyl radicals, as well as an array of functional properties, topics which will be discussed further along in this, and subsequent chapters.

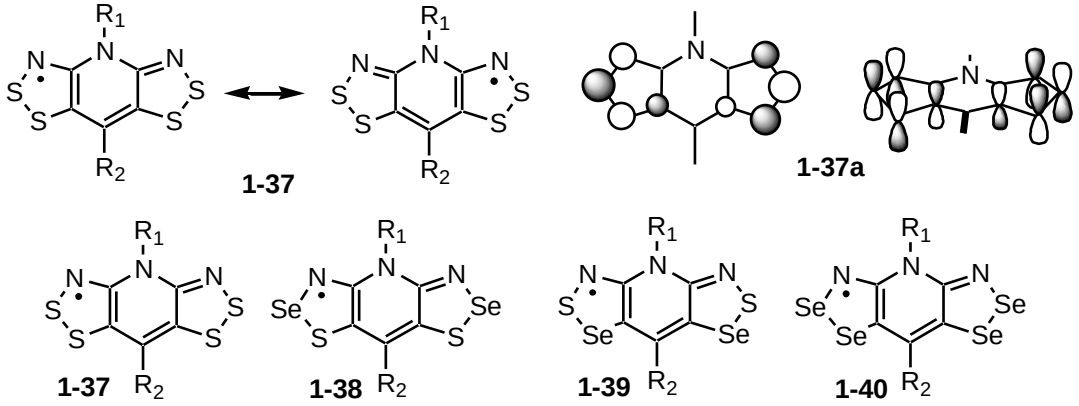

In recent years, there has been a push for the development of molecular materials exhibiting properties useful for device applications, such as conductivity, magnetism, or both (*i.e.*, magnetoresistance). At this stage in the introduction, it is pertinent to develop the theory behind

molecular conductivity and magnetism before discussing the properties of these and other materials.

1.3 Radicals as Molecular Magnetic Materials

There are many examples of inorganic ferromagnets[92] or transition metal-based complexes with organic ligands displaying ferromagnetic ordering,[93] however, a true organic ferromagnet is rare. Joel Miller, [94] one of the key players in the field, describes an organic magnet as,

> "A material exhibiting bulk magnetic ordering, and possessing unpaired electron spins residing in *p*-orbitals that contribute to magnetic ordering."

Some of the thiazyl and selenazyl radicals prepared in the Oakley Group fulfill these criteria. The undimerized radicals are all paramagnetic materials at ambient temperature with magnetic communication between the localized radical centers.

1.3.1 Theory and Computation

The requirements for magnetic exchange in any material are (i) unpaired electrons, which naturally possess a magnetic moment and (ii) a magnetic exchange pathway. The strength and type of the magnetic communication between neighbouring molecules is highly sensitive to the spin density distribution within the molecules and the extent of orbital overlap between them. We can employ quantum mechanics to understand when ferromagnetic (FM, ↑↑) or antiferromagnetic (AFM, ↑↓) coupling will be observed between unpaired electrons on two separate sites. For FM exchange to prevail, the triplet state must be lower in energy than the open-shell singlet state. In the limit of weakly-interacting centers (such as the Oakley radicals described above), the Heitler-London Valence Bond (VB) wavefunction can be written as (eqn. **1**), where ϕ_a and ϕ_b are the active orbitals of the two interacting radicals. Application of the Variational Principle and solving the resulting secular determinant affords wavefunctions for the triplet (eqn. **2**) and singlet states (eqn. **3**) and their relative energies (eqn. **4**) and (eqn. **5**), respectively (Figure 1.6).

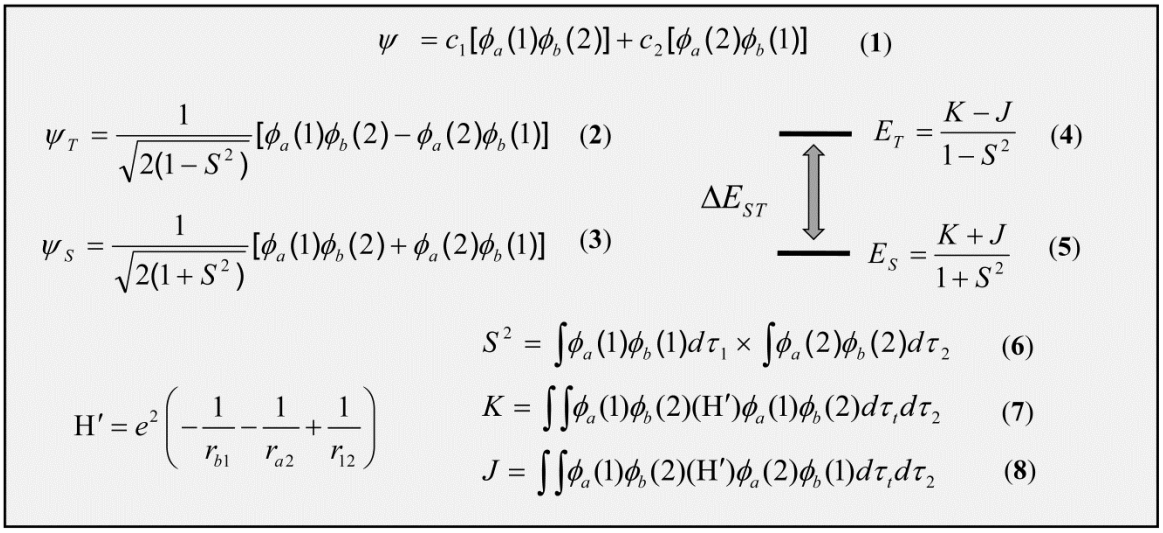

Figure 1.6 The energy difference between the singlet and triplet states, ΔE_{ST}, of two weakly interacting radicals.

In the present sense, S^2 is the overlap density integral (eqn. **6**), K is the VB Coulomb integral (eqn. **7**) and $\boldsymbol{J}$ is the VB Exchange Integral (eqn. **8**).[33,95] In the limit where $S^2 << 1$, that is, orbital overlap is small (such as in the absence of a chemical bond between the two centers), the difference between the two states reduces to $2\boldsymbol{J}$ (eqn. **9**), where $\boldsymbol{J}$ is the difference between j and $2j'|S|$ (eqn. **10**) (Figure 1.7). Here, j' (eqn. **11**) is an integral describing the attraction of the overlap density *between* the two centers *to* the two individual centers, that is, the origin of the chemical bond. The integral j (eqn. **12**) describes the repulsion of the overlap density with itself and thus it opposes the formation of a chemical bond. Both of these integrals carry positive signs. The relative energy of the triplet and open-shell singlet states depends on the magnitude and sign of $2\boldsymbol{J}$. By convention, $\boldsymbol{J}$ is positive for FM coupling and negative for AFM.[96] As a result, in the context of magnetic exchange, the $2j$ term is often called the FM term because it stabilizes the triplet state and hence promotes ferromagnetic coupling, while the $-4j'|S|$ term stabilizes the singlet state and is called the AFM term. These expressions determine when one type of exchange will occur over the other between pairs of radicals. For example, it is evident that FM coupling is observed when $|S| \approx 0$ and j is large. This can occur only when there is orthogonal overlap of two deeply penetrating orbitals. In contrast, AFM coupling is observed when there is simply strong net orbital overlap, *i.e.*, $|S| >> 0$.

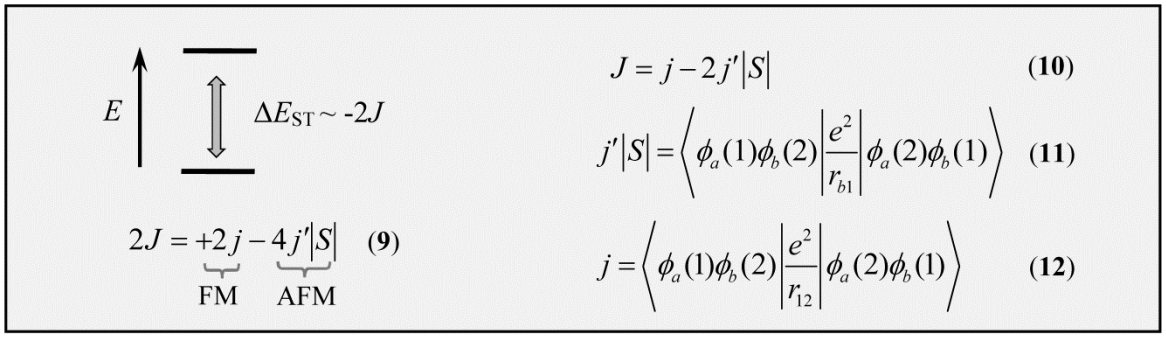

Figure 1.7 The energy difference, ΔE_{ST}, as a function of the exchange integral ***J***.

The extent of orbital overlap between arrays of molecules in the solid state can be studied using Extended Huckel (tight-binding) Theory (EHT) band structure calculations. The results are then plotted as the crystal orbital (CO) energies as a function of *k*-space, which arise from the radical SOMOs in the unit cell. The shape of the resulting dispersion curves depends on the nature of the intermolecular orbital interaction, as shown in Figure 1.8 for a model system consisting of a 1D-array of π-stacked thiazyl radicals, each possessing a simple two-site antibonding π* SOMO.

In the case where the SOMOs along a π-stack are superimposed (Figure 1.8a), the overlap integral *S* is large and antibonding (at $k = 0$), $\Delta E_k < 0$, and thus the solid state bandwidth $W > 0$. This is similar to a 1D array of σ-bonded *p*-orbitals, that is, dE_k/d_k is negative. When the stacks are severely slipped such that adjacent *p*-orbitals of the same sign align vertically in a σ fashion (Figure 1.8c), *S* is also large, however the interaction is bonding and the dispersion curve is characterized by a positive dE_k/d_k and $W > 0$. In both cases, AFM exchange along the π-stacks is expected, and the magnitude of ΔE_k, *W*, and as an extension the exchange parameter ***J***, is dependent upon the extent of the orbital overlap. When the slippage of the radicals is somewhere between these two extremes, destructive interference of the orbital overlap begins to decrease the overlap integral *S* and the overall dispersion *W*. At some point along the slippage coordinate, perfectly orthogonal overlap is possible (Figure 1.8b), a condition that nullifies CO dispersion and gives $W = 0$. At this point, magnetic exchange is expected to be FM, as long as there is orthogonal overlap of strongly *interpenetrating* orbitals, that is, *j* is large.

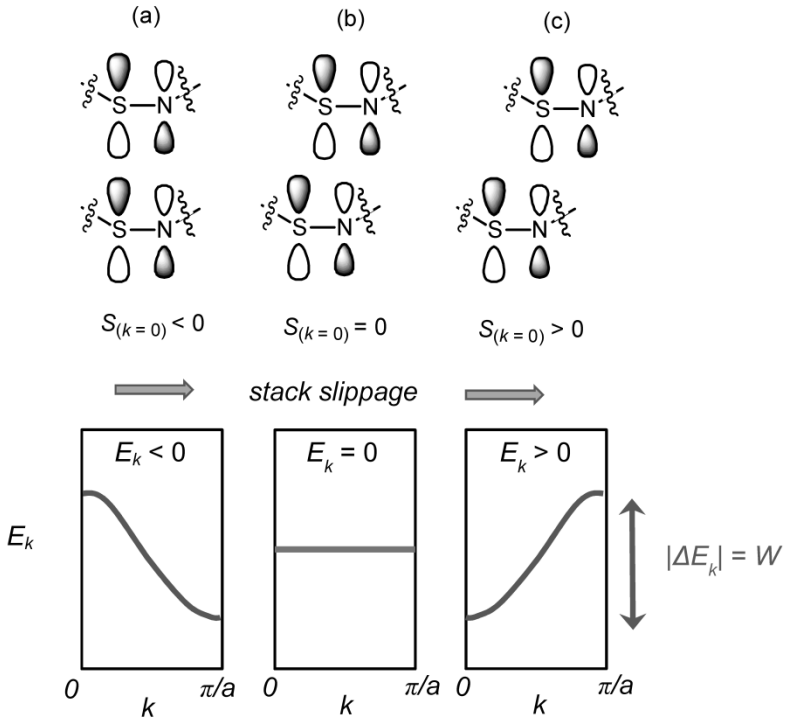

Figure 1.8 Dispersion curves of a model 1D π-stack of thiazyl radicals as a function of stack slippage.

Although it is common to observe short-range FM interactions, long-range ferromagnetic ordering is a three-dimensional phenomenon for which there are few examples in the field of molecular materials. One way in which the magnetic behaviour of a molecular material can be understood is to consider the bulk magnetic susceptibility to be representative of a composite of the individual exchange interactions (***J***) arising from all pairwise combinations of a radical and its nearest neighbors in the lattice. These pairwise exchange energies ***J*** can be estimated using Density Functional Theory (DFT) methods.[97] A useful way in which this can be accomplished is to employ the broken symmetry method,[98] which bypasses the need to calculate the energy of the open-shell singlet state (E_s) by calculating the energy of the hypothetical broken symmetry singlet (E_{BSS}) instead. The relative energies of these states are shown in Figure 1.9. With reference to the Heisenberg Hamiltonian (eqn. **13**),[99] where ***J*** is the magnetic coupling constant between two magnetic centers and *S* is the total spin operator, the magnetic exchange parameter ***J*** may be calculated using equation **14** for any pair of interacting radicals. In this equation, E_T and E_{BSS} are the calculated energies of the two spin states using DFT, and $<S^2>$ are their respective spin

expectation values. This method has been utilized for a variety of magnetically active organic radicals, including nitrogen-centered radicals,[100] thiazyls[101] and selenazyls,[102] as well as phenalenyls.[103] The advantage of this approach is that once it is established which of the interactions is the most influential on the bulk property, changes in the susceptibility can be correlated with modification of solid-state geometries.

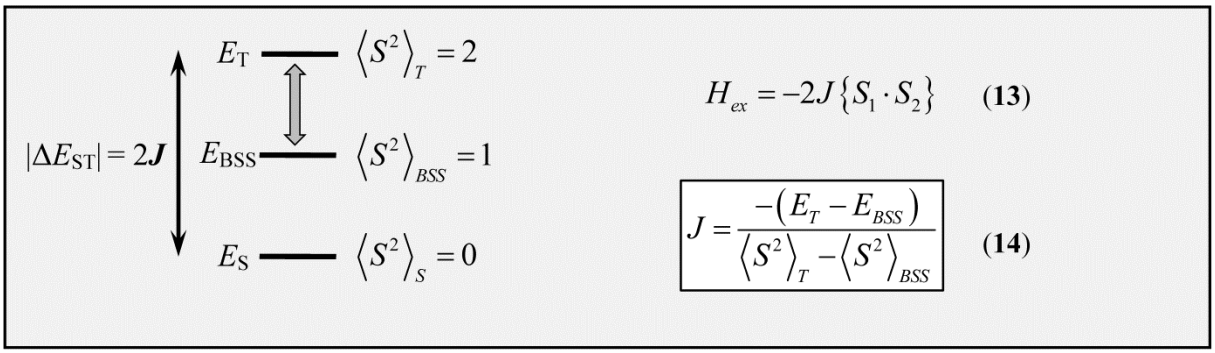

Figure 1.9 Relative energies of the triplet (E_T), broken symmetry singlet (E_{BSS}) and singlet (E_S) states, as well as the expression for the magnetic exchange energy ***J*** (eqn. **14**) for the broken symmetry method.

1.3.2 Magnetic Ordering of Molecular Materials

Open-shell species, by definition, possess unpaired electrons available to act as magnetic couplers within a lattice. Historically, chemists and physicists alike have focused their studies on metal-based systems such as transition metal (TM) alloys,[104] which order as bulk ferromagnets at high ordering temperatures with large coercivities (hysteretic behaviour in their magnetization as a function of field, *i.e.*, how well the material can remain magnetized upon the removal of the external field. However, the advantages of using open-shell molecular materials, over systems in which the unpaired electron is associated with an atomic unit, are abundant. The structural versatility and flexibility of organic compounds make them ideal candidates for systems exhibiting exciting new magnetic behavior. Molecular magnets may be based on TM complexes in which the unpaired electrons are provided by the metal itself, such as in the vast field of single-molecule magnet (SMM),[105] single-chain magnet

(SCM),[106] and single-ion magnet (SIM)[107] chemistry. In the former systems, clusters of TMs are linked together *via* diamagnetic or paramagnetic[108] organic spacers, producing a single molecule or chain with a large cumulative spin count. The textbook example of this phenomenon is the 'Mn_{12}–acetate' compound, $[Mn^{III}_8Mn^{IV}_4O_{12}(O_2CMe)_{16}(H_2O)_4]\cdot 4H_2O_2\cdot MeCO_2H$, which has a spin of S = 10 (Figure 1.10a).[109,110] Single-ion magnets rely on the spin of a sole lanthanide ion with a complex ligand network surrounding it, such as the $[LnP_5W_{30}O_{110}]^{12-}$ ion shown in Figure 1.10b.[107b] At best, these materials demonstrate a measurable hysteresis below 2 K, and blocking temperatures in the same range. Despite a plethora of new SMM and SCM materials, modification to the molecular units including the use of lanthanide elements[111] has improved magnetic properties only marginally – the ordering temperatures have plateaued at ~ 14 K in recent years.[112]

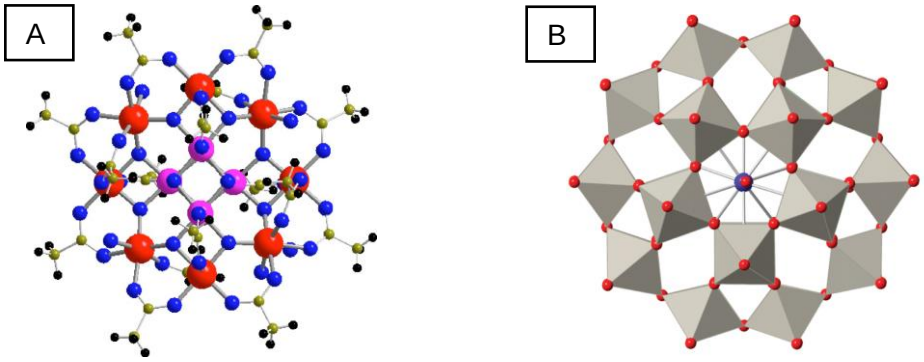

Figure 1.10 (a) Structure of 'Mn_{12}–acetate', a single molecule magnet (SMM). (b) Structure of the $[LnP_5W_{30}O_{110}]^{12-}$ anion, a single-ion magnet (SIM).

Another way by which unpaired electrons may be generated in molecular materials is *via* charge transfer. Noteworthy systems of this type are Miller's TCNE (tetracyanoethylene) salts, such as V[TCNE] and $[Fe(C_5Me_5)_2][TCNE]$, for which the solid state structures are unknown.[93a,113] Although the ordering temperatures of these materials reach up to 300 K, only a few examples exhibit large coercivity.[93b]

In 2002, Awaga demonstrated that TMs are not necessary to mediate magnetic coupling and main group elements may be used exclusively in molecular magnets.[114] This was realized with the

observation of ferromagnetic ordering at 6.7 K of [BBDTA][$GaCl_4$] **1-41**. This radical salt crystallizes in a known geometry as an acetonitrile solvent and is diamagnetic. However, upon desolvation *in vacuo*, the material becomes ferromagnetic with a vanishingly small hysteresis, and the structure of the unsolvated salt is unknown. The charge transfer salt TDAE·C_{60} **1-42** is an example of a truly organic ferromagnetic material, ordering at 16.1 K, the highest T_c in its class prior to 2007.[115] The crystal structure of this material was established years later down to 7 K.[116]

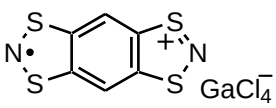

1-41

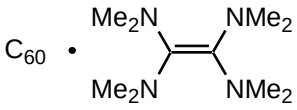

1-42

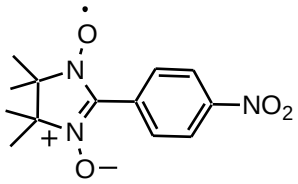

1-43

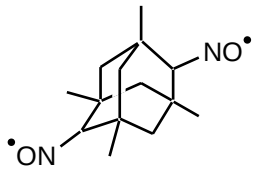

1-44

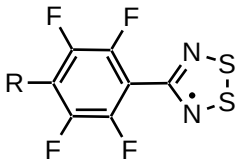

1-45

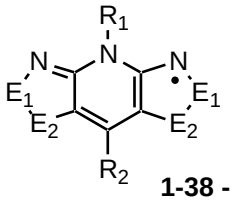

1-38 - 1-40

As a logical alternative to TM-based or charge transfer salts, neutral radicals possessing magnetically active unpaired electrons also possess great potential as molecular magnetic materials. Prior to 2007, the ordering temperatures (T_c) of all neutral radicals displaying bulk ferromagnetism were below 2 K. In 1991, Kinoshita reported the onset of bulk ferromagnetic ordering in a nitronyl nitroxide radical **1-43** at 0.65 K.[117] Shortly thereafter, Chiarelli observed the same phenomenon in a nitroxide diradical **1-44** at 1.48 K.[118] Rawson showed that the DTDA radical **1-45** (R = NO_2) orders ferromagnetically below 1.3 K[101a,119] and a second derivative of this system **1-45** (R = CN) orders as a canted antiferromagnet with an unprecedented Néel temperature (T_N) of 36 K.[120] The latter discovery was the first example of magnetic ordering in a thiazyl radical and high pressure measurements indicated a dramatic increase in T_N to ~ 70 K at 1.6 GPa.[121] Two variants of Oakley radicals **1-39** and **1-40** (R_1 = Et; R_2 = H) also display canted AFM ordering, with T_N values of 18 K and 27 K, respectively.[122] Despite their ability to order magnetically, all of the above materials exhibit negligible hysteresis. By contrast, the selenazyl

radicals **1-38** and **1-40** (R_1 = Et; R_2 = Cl)[123] reported by the Oakley group between 2007-2008 demonstrate a dramatic improvement in the properties of organic magnetic radicals as well as in the ability to correlate property with solid state structure. Not only is the onset of a phase transition to a ferromagnetically ordered state observed at the new record-high T_c of 17 K for **1-40**, but the coercivity of this material is 1370 Oe (at 2 K). This is three orders of magnitude larger than that observed in conventional light atom ferromagnets. Pressurization of these materials will be discussed in Chapter 2, including changes to their structure, ferromagnetic coupling and conductivity under these conditions.

Modifications to the molecular selenazyl building blocks of **1-38** resulted in a deeper understanding of the origin of the ferromagnetic ordering. In 2008, the Oakley group carried out a systematic study of the solid-state structures and transport properties of the series of tetragonal (space group $P\bar{4}2_1m$) bisthiaselenazyl radicals **1-38**.[102a] It was demonstrated that minor changes in packing occasioned by the differing steric requirements of the *N*-alkyl substituent R_1 gives rise to major changes in magnetic properties. While three of the radicals within the series **1-38** (R_1= Et; R_2 = Me, Br, Cl) ordered as ferromagnets with similar T_c and H_c (coercive field) values, the other two variants **1-38** (R_1 = CH_2CF_3, Pr; R_2 = Cl) showed no indication of ordering above 2 K. It was determined that these radicals possess an acute sensitivity to the nature of ligands R_1 and R_2 and hence solid state packing, a topic discussed in more detail in subsequent sections. This initial study illustrated the use of *chemical pressure*, that is, the introduction of a small perturbation by synthetic means to a known system, to modify structure and hence property. The effects of chemical pressure are further explored in Chapter 2 with the completion of the halogen-substituted series of **1-38** (R_1 = Et, R_2 = F, Cl, Br, I). In Chapter 5, a novel series of bisdithiazolyls **1-37** with long alkyl substituents in place of R_1, and where R_2 = F, will be described. The topological ladder-like packing gives rise to a novel network of interactions not previously observed for materials of this type. These so-called spin ladders are formed *via* strong magnetic coupling along the π-stacks and between pairs of stacks.[124]

In probing the series of S = ½ neutral radical ferromagnets **1-38** and **1-40**, it was established that increasing selenium content within the radical framework leads to an increase in the ferromagnetic ordering temperature and magnetic hysteresis. While it is somewhat straightforward to understand the increase in T_c with selenium incorporation, as it is a result of the enhancement of isotropic through-space magnetic exchange through the larger, more diffuse selenium orbitals (*versus* sulfur), the origin of the magnetic anisotropy leading to the extremely large hysteresis is not as obvious. To rationalize this phenomenon, a series of experiments were performed using ferromagnetic resonance (FMR) absorption. The results demonstrated that ferromagnetic ordering was certainly not an artifact or the result of an impurity, but the result of spin-orbit effects from the presence of selenium orbitals.[125] Strong coupling within the magnetic lattice produces anisotropy leading to an easy *c*-axis, and a hard *ab*-plane, thus giving rise to a large barrier to the reversal of the alignment of spins, *i.e.*, a large coercive field. This is in line with Heisenberg's early recipe for the observation of long-range ferromagnetic order, where he stated that the magnetic lattice requires *heavy* ($n \geq 3$) elements.[99,126]

1.4 Models of Molecular Conductivity

As with the field of molecular magnetism, the discovery of electrical conductivity through molecular media has been a hot topic in science for decades. As early as 1911,[127] McCoy and Moore proposed that,

> "If the electron theory of the metallic state is as fundamental as it seems to be, there would be little reason to doubt that the aggregate of such free radicals would be a body having metallic properties; for such a hypothetical body would be made up of radicals which, analogous to metallic atoms, could easily lose electrons."

Although the radicals these physicists originally envisioned were far simpler than the synthetic materials available today, the initial hypothesis is nonetheless historically valuable.[128] It was not until the 1950s that the first highly conductive organic charge transfer salts were synthesized,[129] spurring years of in depth research into these novel compounds.[130] Thereafter, many new classes of molecular

conductors emerged, including conducting polymers, for which a Nobel Prize was awarded in 2000 to Heeger, MacDiarmid, and Shirakawa,[131] radical ion conductors (RICs),[132] closed shell conductors,[133] and of course, neutral radical conductors, which are the topic of this thesis.[134]

1.4.1 Charge Transfer Salts

There are two critical requirements for any material to conduct and they are (i) possession of charge carriers such as unpaired electrons or ions, and (ii) the existence of a conduction pathway. Most closed-shell organic molecules are insulators as they do not fulfill either of these criteria. Certain modifications to these systems, however, can induce charge mobility. Charge-transfer (CT) salts are the prime example of this, and the history of organic conductors *is* the history of charge-transfer salts. In 1973, it was discovered that co-crystallization of a molecule of tetrathiafulvalene (TTF **1-46**) with tetracyanoquinodimethane (TCNQ **1-47**) gives rise to an organic solid with metallic conductivity down to 60 K (Figure 1.11).[135] By 1977, over 400 TCNQ-based CT salts had been prepared.[136,137]

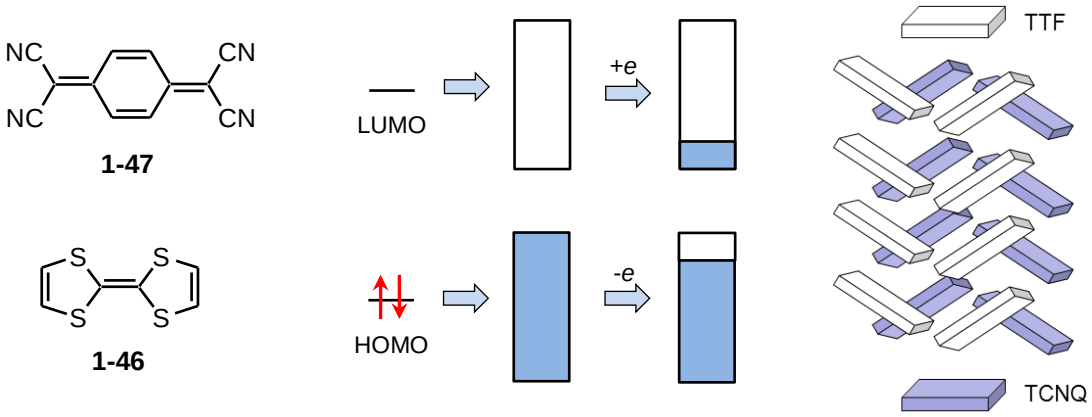

Figure 1.11 Charge transfer salt TTF-TCNQ (left), partial charge transfer between units generating partially filled energy bands (middle), and the solid state packing motif (right).

Conductivity is possible in these salts because (i) charge carriers are generated by electron transfer between a donor and an acceptor molecule, and (ii) a conduction pathway is generated through the segregated π-stacks of partially ionized molecules providing good intrastack orbital overlap. Replacement of sulfur with its heavier congener selenium gave the tetraselenafulvalene donor **1-48** and

its derivative TMTSF (tetramethyltetraselenafulvalene) **1-49**, one of which (in a 1:1 ratio with TCNQ) remained highly conducting to extremely low temperatures.[138] Interest in these materials grew exponentially as they engaged both organic and physical chemists, as well as solid-state physicists. A new class of CT salts, the RICs, was developed with a view to better control the extent of charge transfer, where a π-donor **1-49** was crystallized as a radical ion salt in the form $[TMTSF]_2[X]$, where, for example, X = PF_6^-, AsF_6^-, NO_3^-.[139] Another group of RICs that were generated were based on the BEDT-TTF (bis(ethylenedithio)tetrathiafulvalene or ET) donor **1-50**, to give the $[ET]_2X$ salts, where X is a monovalent anion such as I_3^-.[140] There was (and still is) a great interest among researchers to find a high-temperature superconductor, thus a large number of physical experiments were done on CT salts in the pursuit of an organic superconductor. While some examples of these materials do indeed exhibit superconducting behaviour, their critical temperatures are extremely low.[141]

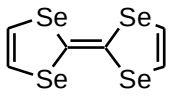

1-48

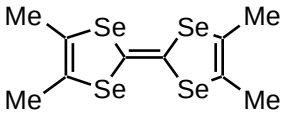

1-49

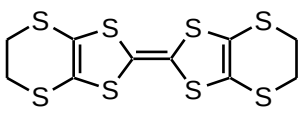

1-50

Although these organic compounds show metallic and even superconducting behavior, a true molecular metal was yet to be realized. In principle, a metallic conductor should be a single-component material, such as sodium and copper, possessing one partially filled energy band and displaying conductivity down to 0 K. In a clever response to this challenge, Kobayashi *et al.* reported the synthesis and conductive properties of an internal CT salt made of a single molecule **1-51**. This compound houses donor (a TTF-like ligand) and acceptor (nickel) components in one molecule, a configuration that gives rise to metallic conductivity down to 0.6 K and room temperature conductivity of 400 S cm^{-1}.[142] Other derivatives have been developed with alterations to the ligand and using different metals for the complexes.[133] This series of materials are highly conductive internal CT salts, possessing HOMO and LUMO energy levels that are not well separated, generating valence and conduction bands that overlap and allow for internal charge transfer in the solid state.

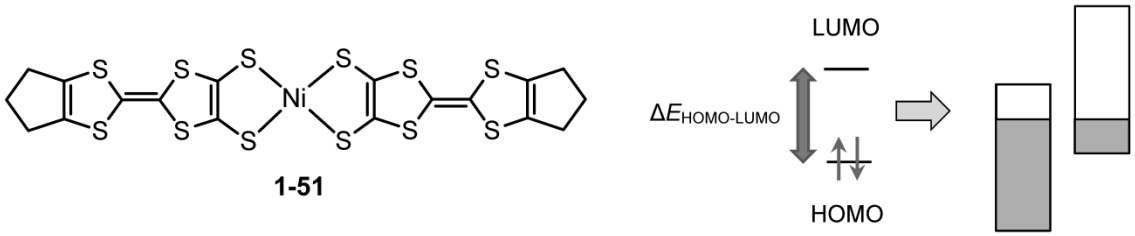

1-51

Figure 1.12 Internal charge transfer complex **1-51** (left) exhibiting internal, partial CT due to a very small molecular HOMO-LUMO gap leading to overlapping bands in the solid (right).

1.4.2 Electron Correlation and Mott Insulating States

It was recognized early on that incomplete charge transfer was vital for CT salts to display these remarkable conductive properties.[143] Complete transfer of electrons generates a half-filled (f = ½) energy band and results in insulating behaviour. This electron localization occurs mainly due to the Coulombic repulsion experienced by two electrons on the same site, a phenomenon called the on-site Coulomb repulsion U. This repulsion is easily understood within the context of the Hopping Model of Conduction,[144] where electron migration from one site to the next in an f = ½ system results in a doubly-occupied site (Figure 1.13a). The repulsion of these two electrons (U) is much greater than the electron-electron repulsions (V) in a partially filled band, for example f = ¼ (Figure 1.13b), where the electron can migrate to the next available unoccupied site without hindrance. Materials with very large U values are trapped in Mott insulating ground states,[145] unless the solid-state bandwidth W is great enough to overcome this barrier.[146]

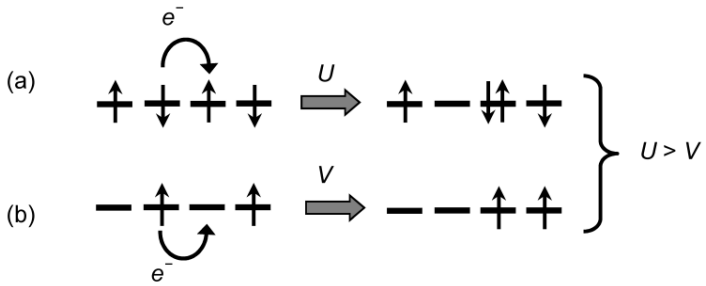

Figure 1.13 On-site Coulomb repulsion energy (U) of systems with (a) f = ½, and (V) for a system with (b) f = ¼.

In order to determine the conditions necessary for a metallic ground state to prevail, let us consider a simple Molecular Orbital (MO) model.[147] Accordingly, the issue of metallic *versus* Mott insulating states can be related to differences between a low-spin and a high-spin state of a simple diatomic molecule, for example, H_2 (Figure 1.14). We will use this analogy to deduce the relationship between U and W.[148]

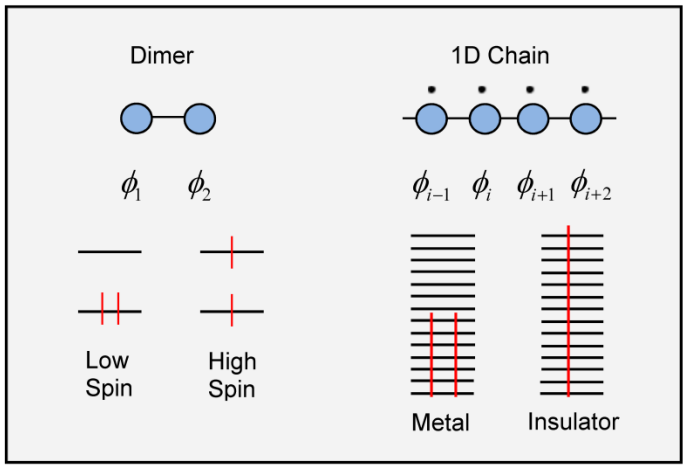

Figure 1.14 The low-spin and high-spin states of a dimer (left) and the analogous metal and insulator states of a 1D chain of radicals (right).

In Simple Hückel molecular orbital (SHMO) theory, when two orbitals (ϕ_1, ϕ_2) within a dimer overlap, two new molecular orbitals are formed, in-phase ψ_1 (eqn. **15**) and out-of-phase ψ_2 (eqn. **16**), with corresponding expectation values, ε_1 and ε_2 (Figure 1.15). At the SHMO level, the difference in energy between the two MOs is equal to 2β, where β is the resonance integral and given by equation **17**. In this system, the orbitals may be occupied in such a way as to give a triplet (high spin) or singlet (low spin) state.

If the SHMO effective Hamiltonian[149] is replaced by one in which electron repulsion is explicitly included, and the antisymmetrized versions of ϕ_1 and ϕ_2 are employed, the singlet and triplet energy states, E_S and E_T respectively, are obtained (Figure 1.16). These energies are expressed in terms of the orbital energies ε_1 and ε_2, and the Coulomb integral J_{ij}. The energy difference, ΔE_{ST} (eqn. **18**), is then a function of the ε_1 and ε_2 energies and the repulsion integral J_{12}. To obtain a simpler way of expressing

the repulsion between the two electrons the integral J_{12} is expanded by substituting the full expressions for the wavefunctions ψ_1 (ϕ_1 + ϕ_2) and ψ_2 (ϕ_1 - ϕ_2) giving an expression that expands further into many terms. If we make the approximation that repulsion between the electrons is zero, except for the on-site Coulomb repulsion ($\phi_i\phi_i$, not $\phi_i\phi_j$), then the integral reduces to equation **19**.

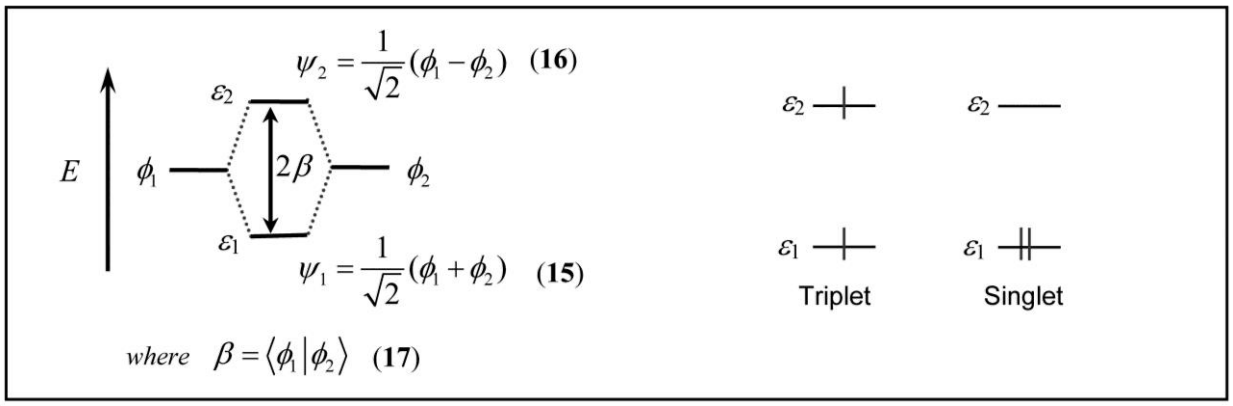

Figure 1.15 The energy level diagram of a dimer using SHMO theory, with triplet and singlet energy states.

Combining equations (**18**) and (**19**) provides a singlet-triplet splitting given by (eqn. **20**), demonstrating the relationship between the resonance integral, β, and the onsite Coulomb repulsion for discrete dimers. Keeping in mind that, by definition, $\beta < 0$ and $U > 0$, the ground state energy (singlet or triplet) may be determined by the sign of ΔE_{ST}. Therefore, if $|2\beta| > |U/2|$, then $\Delta E_{ST} < 0$ and the singlet, or low spin, state is the ground state (Figure 1.17). Alternatively, if $|2\beta| < |U/2|$, then $\Delta E_{ST} > 0$ and the triplet, or high spin, state will be lowest in energy.

If we extend these principles into the solid state such that the discrete dimer energy levels spread into solid state bands, as illustrated in Figure 1.17, we come up with an energy difference of $4\beta + U$ between the metallic (low-spin) and Mott insulating (high-spin) states. The bandwidth W of an array of molecules is defined as 4β, hence giving the following condition: if $W > U$, a metallic ground state will prevail (Figure 1.18 right). Otherwise, the material will have a Mott insulating ground state due to electron correlation effects (Figure 1.18 left). Since β is a function of the extent of the SOMO-SOMO

interaction, a high degree of orbital overlap in the solid state is necessary to generate a high *W* material. In the case of $f = ½$ systems, where *U* is a maximum, a significant amount of orbital overlap, and hence a large *W*, is necessary for metallic conductivity. This is the strategy used in developing molecular metals from neutral radicals.

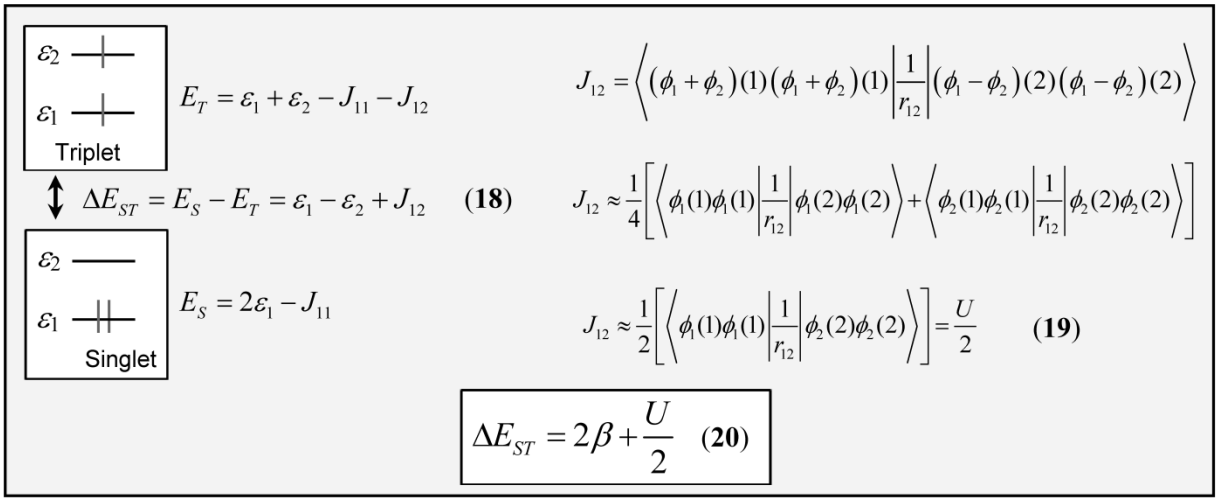

Figure 1.16 The energy difference between the singlet (low spin) and triplet (high spin) energy states (ΔE_{ST}), as well as the definition of the Coulomb integral J_{12}.

Between these two extremes, there is a point at which $U \sim W$ and the two states are approximately equal in energy. Within this region, the phase transition between a Mott insulator and a metal, is an area with rich potential for highly interesting solid state physics. The field of metal-to-insulator transition (MIT) research has seen remarkable growth due to the realization that the transition is not as clean and abrupt as once predicted. In fact, a sharp distinction between a metal and an insulator only exists at $T = 0$ K. As shown in Figure 1.19a, the critical temperature T^* separates the insulator and metal with a more complex critical region encompassing "bad insulator" and "bad metal" states, as a function of the relationship *W*/*U*.[150]

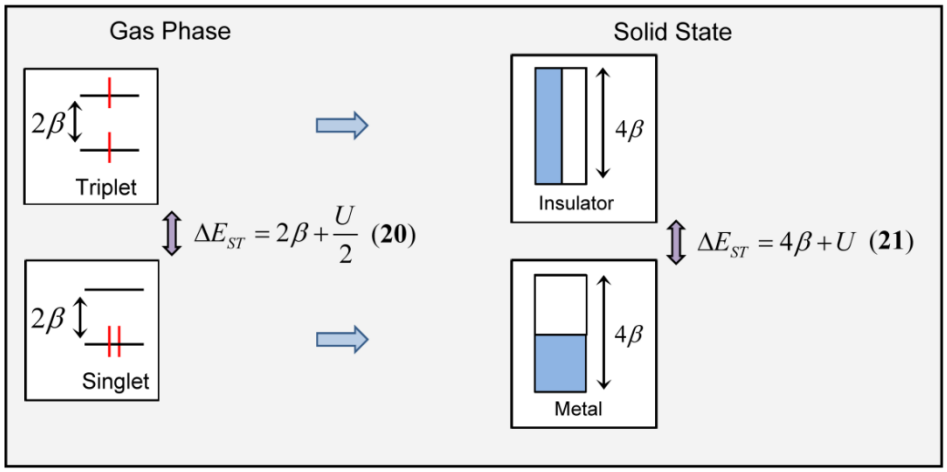

Figure 1.17 Extension of the singlet and triplet states of a dimer into the solid state Mott insulating and metallic states.

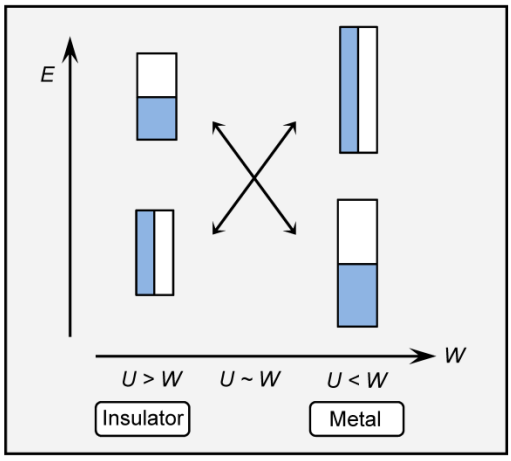

Figure 1.18 Crossover between a Mott insulating ground state to a metallic ground state as a function of the solid state bandwidth *W* for a 1D chain.

Experimentally, these transitions have been probed for molecular materials such as the κ-(BETD-TTF)$_2$Cu[N(CN)$_2$]Cl salt and numerous phase diagrams depicting the states have been established.[151] For example, Figure 1.19b shows the separation between the antiferromagnetic insulator, Mott insulator, semiconductor, bad metal and Fermi liquid metallic regimes as a function of temperature and pressure.[152] In this material, pressure broadens the bands, and thus increases *W*, favoring the metallic state. The first-order Mott transition extends up to the critical point of ~ 40 K through the shaded region. At low temperatures (T < 40 K), the transition is more defined and the material displays

hysteresis in charge transport within the shaded region.[153]

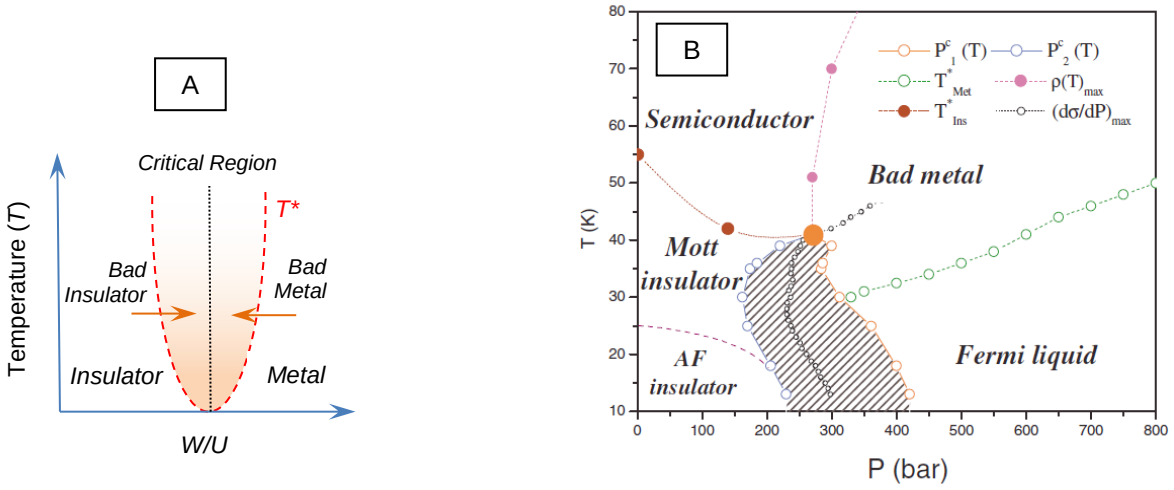

Figure 1.19 (a) Metal-to-insulator (MIT) transition with increasing *W/U*. (b) Phase diagram for κ-(BETD-TTF)$_2$Cu[N(CN)$_2$]Cl as a function of temperature and pressure. Reprinted figure with permission from the American Physical Society as follows: Limelette, P.; Wzietek, P.; Florens, S.; Georges, A.; Costi, T. A.; Pasquier, C.; Jérome, D.; Mèziére, C.; Batail, P. *Phys. Rev. Lett.* 91, 1, 2003. Copyright 2003 by the American Physical Society.

1.4.3 The Neutral Radical Conductor Model

In the 1970's, there were many converging theories on how to design an organic metal, all of them based on the charge-transfer paradigm. In 1975, Robert Haddon proposed an alternative to this approach, one that involved the use of neutral radicals as the building blocks for molecular metals.[154] His idea is based on the principle that an array of molecular π-radicals, each possessing one unpaired electron (Figure 1.20a), should generate a half-filled energy band and give rise to metallic conductivity (Figure 1.20b). These molecules would function like atoms in an elemental metal, like sodium. Knowing that an f = ½ system possesses a very large on-site Coulomb repulsion and thus a tendency towards highly correlated Mott insulating ground states (Figure 1.20c), this idea was in conflict with conventional wisdom. However, neutral radicals with minimized values of U and maximized W were nonetheless pursued, as they could potentially be the only materials characterized as true molecular metals.

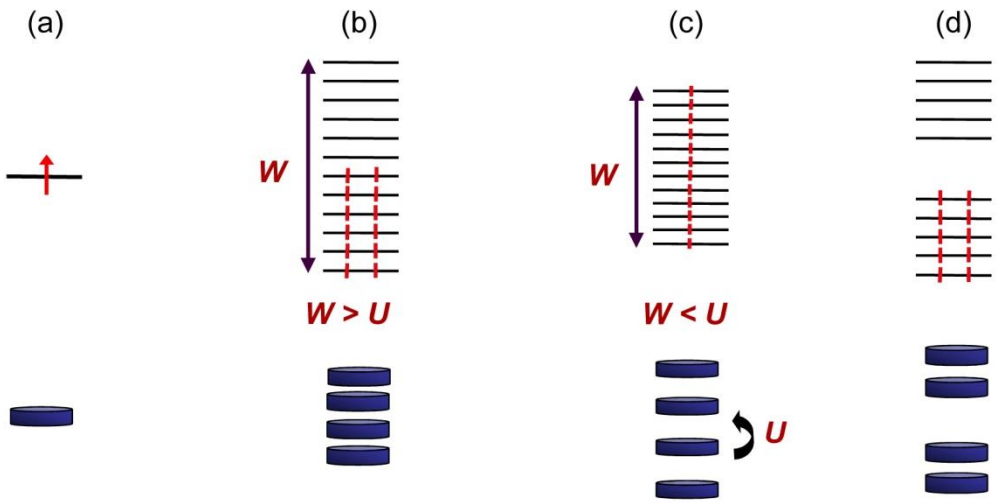

Figure 1.20 Energy levels of (a) a single π-radical, (b) a metallic state, (c) a Mott insulating π-stack and (d) a Peierls distorted π-stack.

Besides the potential for localization of spins and electron correlation, this model possessed another short-coming. One-dimensional half-filled energy bands are prone to a Peierls distortion,[155] that is, the radicals will π-dimerize, which results in the opening of a band gap at the Fermi level (Figure 1.20d). In order to suppress this propensity to dimerize, bulky substituents can be incorporated into the molecule, but this tends to decrease orbital overlap and thus bandwidth *W*.[134]

In order to prepare molecular radicals with high conductivity, the factors affecting both the bandwidth *W*, and the barrier to electron transfer, *U*, must be understood and controlled. For any system, *W* can be approximated using Extended Hückel Theory. However, *U* is a solid state property that is not as easy to assess.[156] For a hypothetical neutral radical (R·), the movement of an electron from one site to the next results in one cationic (R^+) and one anionic (R^-) species, as shown in Figure 1.21. In the gas phase, the energy associated with the removal of one electron is the ionization potential (*IP*), and the electron affinity (*EA*) is the enthalpy gained as a result of the addition of an electron. Therefore, the overall enthalpy of the process of moving one electron is defined as the disproportionation enthalpy, $\Delta H_{disp} = IP - EA$. In the solution phase, this process is related to the electrochemical cell potential, E_{cell}, which is the difference between the electrochemical half-wave potentials of the oxidation ($E_{½}^{(0/+1)}$) and reduction ($E_{½}^{(-1/0)}$) processes of the radical. As an extension of that, the value of *U* is approximated by monitoring

the gas-phase disproportionation enthalpy ΔH_{disp} and solution-based electrochemical cell potential E_{cell} (= $E_{½}^{(0/+1)}$ - $E_{½}^{(-1/0)}$) of the molecules, as trends in these two parameters are very effective in reflecting trends in U in the solid. Thus, neutral radicals with lower ΔH_{disp} and E_{cell} values have lower U values, and are better candidates for use as neutral radical conductors.

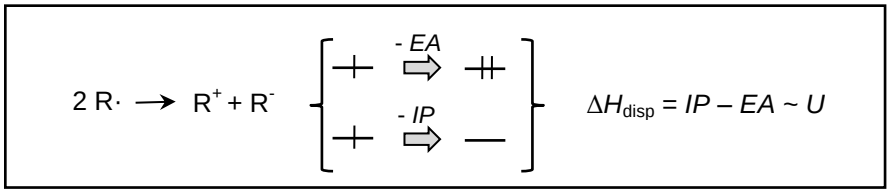

Figure 1.21 Relating U to the disproportionation enthalpy (ΔH_{disp}) of a radical (R·) system.

1.4.4 Odd-Alternant Hydrocarbons as Neutral Radical Conductors

Central to Haddon's 1975 proposal was the importance of low values of U in conductive radicals, thus he suggested that odd-alternant hydrocarbons (OAHs) should be able to serve as useful building blocks for organic metals and superconductors.[154] They possess one unpaired electron in a non-degenerate, non-bonding molecular orbital (NBMO) and display a relatively low U due to the lack of electronic reorganization accompanied by the removal of the unpaired electron (*IP*) or the addition of one more (*EA*) (Figure 1.22). It was expected that these molecules would adopt a superimposed π-stacking motif with maximum SOMO orbital overlap leading to very high conductivity. The OAHs of choice were phenalenyl **1-6**, which is unstable as a radical in the solid state, and its derivatives **1-10** and **1-11**. Radical **1-10** is monomeric and open shell in the solid state, however, it is trapped in a Mott insulating ground state due to poor orbital overlap along the π-stacks.[27] Dithiophenalenyl **1-11** crystallizes as a π-dimer, the structure of which was discussed in Section 1.2.2, and exhibits semiconducting behavior with a wide band gap.

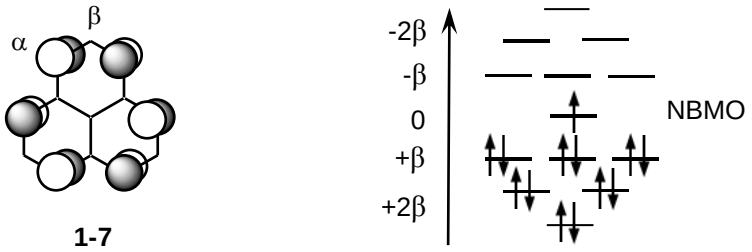

1-7

Figure 1.22 SHMO diagram depicting the energy levels of the orbitals of phenalenyl, including the non-bonding molecular orbital (NBMO).

High conductivity using the phenalenyl moiety was eventually achieved with the spiro-conjugated *bis*-phenalenyl **1-52a** (σ_{RT} = 10^{-1} S cm^{-1}) as a result of a decrease in solid-state band-filling (f = ¼) and thus a lower U.[157] This decreased the requirement for a large W and led to good conductivity. Of the numerous spirobisphenalenyls prepared, many do not associate in the solid state, and crystallize in a rich array of structural motifs.[158] Derivatives of **1-52b** (R = hexyl, benzyl) exist as discrete radicals in the solid state, and the hexyl derivative exhibits high conductivity with σ_{RT} = 0.5 S cm^{-1}.[159] Two examples of great significance are **1-52b** (R = cyclohexyl, cycloheptyl), which form continuous π-stacks in the solid state, with C···C' intermolecular contacts *within* the sum of the van der Waals radii for C atoms.[157,160] Although these materials display activated conductivity, room temperature conductivity is exceptionally high (σ_{RT} = 0.3 S cm^{-1}) and Pauli paramagnetism has been observed. To rationalize these results, Anderson's Resonating Valence Bond (RVB) model has been employed. The spirotriphenalenyl radical complex **1-53**, although promising, has a complex structural arrangement with low conductivity (σ_{RT} = 10^{-6} S cm^{-1}).[161]

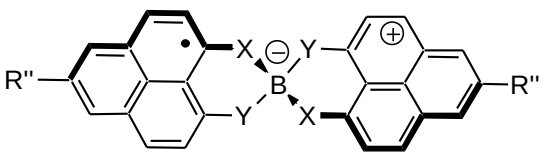

1-52

a X = O, Y = O, R'' = Me, H
b X = NR, Y = O, R'' = H
c X = NR, Y = NR', R'' = H

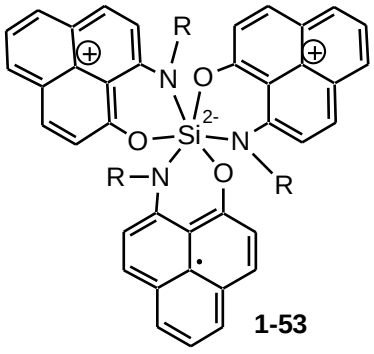

1-53

Other noteworthy derivatives of these spirobisphenalenyls are radicals **1-52b** (R = ethyl, butyl), which undergo a phase transition with temperature between diamagnetic and a paramagnetic states, shown in Figure 1.23.[162] In the case of the butyl compound, this phase change is observable *via* three different channels, that is, through IR transmittance, electrical conductivity and magnetic susceptibility. Results show that with increasing temperature at around 350 K, the structure changes to that of the open shell radicals, and stays "locked in" this phase with decreasing temperature until around 325 K when it relaxes back to the original, closed shell dimer. This bistability, which is not observed for the ethyl derivative, gives rise to potential for the development of magnetic switching devices, although a wider region of bistability, and one which hovers around room temperature, is desired.

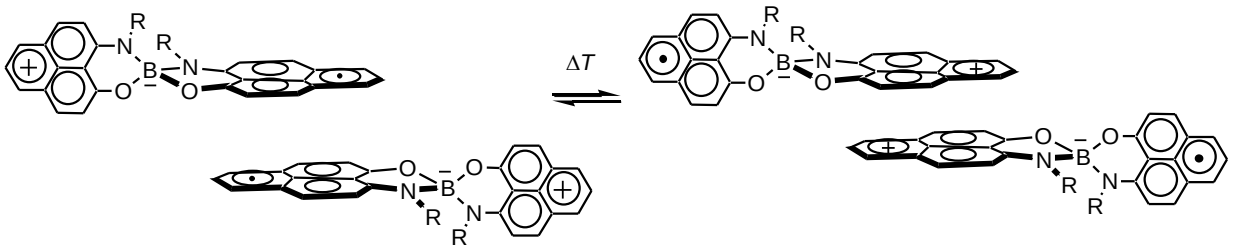

Figure 1.23 Interconversion between the low- (left) and high-temperature (right) structures for spirobisphenalenyl radicals **1-52b** (R = butyl). Adapted from ref. 162.

Tactical manipulation of the band filling has recently been explored by Mori *et al.*, with the development of the internal charge transfer salt shown in Figure 1.24.[163] The TTF-based units are linked together by hydrogen bonds, providing a unique structure involving resonance delocalization of the unpaired electron through a purely organic single-component molecular conductor. Dimerization of two of these units gives rise to an overall band that is ¼−filled with holes. However, the large splitting between the upper and lower bands leads to half-filled character of the conduction band. Moreover, this material metallizes at ~ 1 GPa, and future derivatives are expected to be the first single-component molecular metals under ambient conditions.

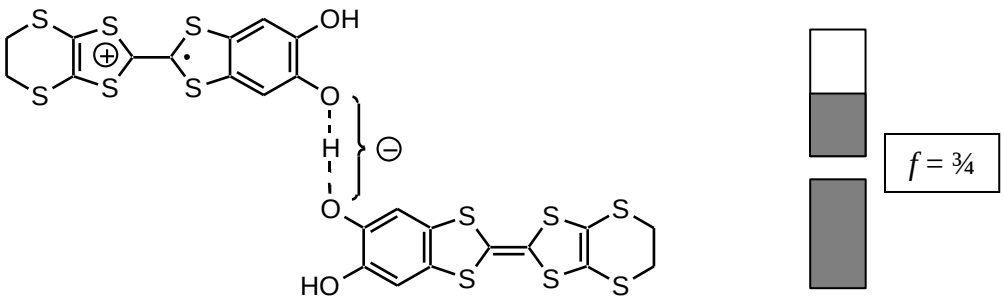

Figure 1.24 The structure of a new type of single-component molecular conductor and a schematic drawing of its f = ¾ band filling.

A new approach toward the development of future target molecules for applications in molecular electronic devices and magnetic materials called "synthethic organic spin chemistry" has recently been developed, in which molecular engineering can be employed to tailor the electronic structure of phenalenyl-based radicals.[164] It involves the development of target molecules based on open-shell graphene fragments, of which phenalenyl is a prime example (Figure 1.25).

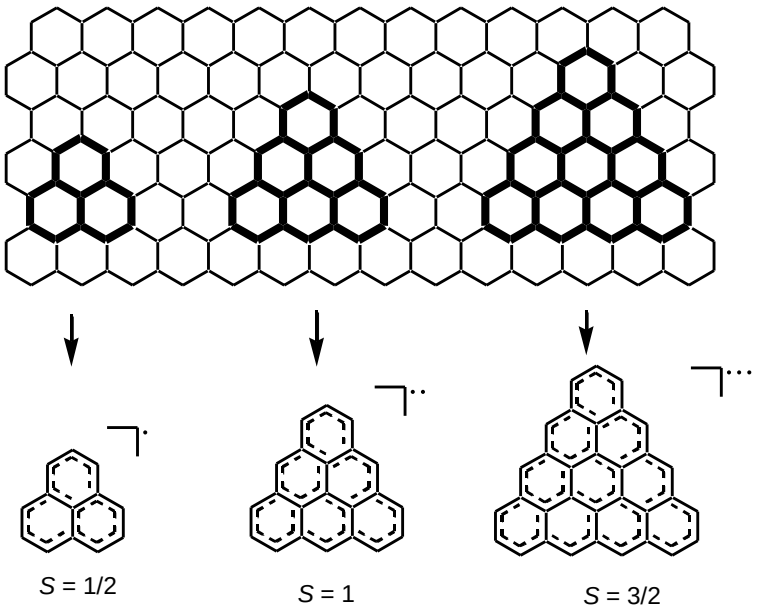

Figure 1.25 Phenalenyl derivatives based on open-shell triangular graphene fragments. Adapted from reference 164.

Both phenalenyl and triangulene may be viewed as triangular fragments of a graphene[165] sheet with extended π-delocalization of the unpaired electron(s) throughout the planar molecule. Theoretical calculations reveal that, like phenalenyl, the spin density of larger fragments is distributed throughout the whole molecule, but it is mainly located on the periphery.[166] This drawback leads to the kinetic instability of phenalenyl-based radicals towards C−C σ-dimerization, although judicious choice of peripheral substituents will likely suppress this pitfall. The tri-*tert*-butylated derivative of triangulene has been synthesized by Morita *et al.*, and a triplet ground state has been detected by EPR spectroscopy,[167] almost 60 years after its structure was first postulated.

1.5 Thiazyl Radicals as Neutral Radical Conductors

The evolution of thiazyl radical chemistry through several generations of radical building blocks has been arguably pioneered by the Oakley group. For many years, the main goals of the research program has been to develop functional materials, those displaying conductive and/or magnetic properties, based on the aforementioned thiazyl radical ring systems that, in principle, give rise to a half-filled band in the solid state. Great strides were made in developing the synthetic pathways towards these systems and a large number of monofunctional heterocycles were crystallized and characterized. However, all of the early generations of radicals were plagued by the propensity to form π-dimers in the solid state, and thus only a handful were open shell radicals. In the few cases where dimerization did not occur, poor intermolecular orbital overlap in the solid state kept the bandwidth, *W*, low, and insufficient π-delocalization of the unpaired spin meant that the onsite Coulomb repulsion energy, *U*, was high. Room temperature conductivity values for selenium dimers (semiconductors) peaked at around 10^{-5} S cm^{-1}, whereas that of the open-shell Mott insulators measured at around 10^{-7} S cm^{-1} at best for the early generations.[168]

1.5.1 Packing and Slippage

The development of the highly delocalized systems based on the bisdithiazolyl framework **1-37**,[91] as well as the selenium variants **1-38** – **1-40**, has been revolutionary in this field. In this latest generation of radicals, only a handful of examples dimerize,[169] whereas most are open shell, stable species.[134] A large number of derivatives have been generated over the years, displaying novel physical properties and demonstrating remarkable stability in the solid state. The symmetry of the antibonding π-SOMO **1-37a** is such that there is a nodal plane through the center of the molecule. As a result, modification of the substituents R_1 and R_2 does not result in any first order electronic effects, but it leads to a great deal of diversity in their solid state structures. Due to the presence of the central ligands R_1 and R_2, the structures typically consist of slipped π-stack arrays to avoid steric repulsion. As shown in Table 1.1, space groups within a given family (same R_1/R_2 or selenium/sulfur content) vary significantly with minor changes to the molecular structure. Even within a particular space group, the slipped π-stack arrangement of undimerized radicals may change from system to system, giving rise to rich diversity in interesting magnetic properties, including bulk ferromagnetic ordering,[123] canted antiferromagnetism,[122] and metamagnetism.[170] Conductive behavior ranges from highly electron correlated Mott insulators,[171] to semiconductors[169] and weak metals.[172] The improvement in conductivity of the Mott insulators has resulted in some radicals reaching room temperature (ambient pressure) conductivity of 10^{-3} S cm^{-1}, and activation energies as low as 0.17 eV, properties that have been shown to improve further with the application of slight physical pressure.

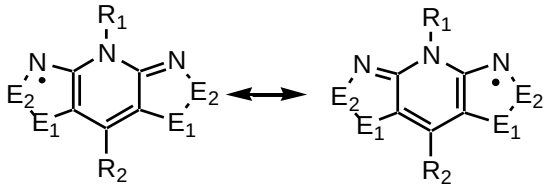

	E_1	E_2
1-37	S	S
1-38	S	Se
1-39	Se	S
1-40	Se	Se

Table 1.1 Space Groups for a Selection of Characterized Radicals **1-37** – **1-40**.

R_1	R_2	**1-37**	**1-38**	**1-39**	**1-40**
Me	H[a]	$P2_12_12_1$	$P2_1/c$ *	$P2_12_12_1$	$P2_12_12_1$
Et	H[b]	$P2_1/c$	$P2_1/c$ *	$P2_1/c$	$P2_1/c$
Me	Cl[c]	$P2_12_12_1$	$P2_1/n$	$P2_12_12_1$	$P2_1/n$
Et	Cl,[d] Br[e]	$P\bar{4}2_1m$	$P\bar{4}2_1m$	$P\bar{4}2_1m$	$P\bar{4}2_1m$
Et	Me[f]	$P\bar{4}2_1m$	$P\bar{4}2_1m$	---	---
Me	Ph[g]	$P3_121$	$P3_121$	---	---
Et	Ph[h]	$P3_221$	$P3_221$	---	---

[a] Ref. 171, 173. [b] Ref. 122, 171. [c] Ref. 91, 102b. [d] Ref. 91, 123. [e] Ref. 174. [f] Ref. 102a. [g] Ref. 175a,c. [h] Ref.175 * For the σ-bonded dimers, see Ref. 169.

The main strategy used towards the improvement of properties in these highly delocalized thiazyl radicals was the incorporation of selenium, a larger, softer chalcogen with more diffuse π-orbitals. These more spatially extensive orbitals have the ability to enhance orbital overlap and provide a greater solid-state bandwidth. Knowing that all selenazyl radicals have dimerized in the past, the synthesis of these systems was expected to be a challenge. The first two bisthiaselenazolyls **1-38** (R_1 = Me, Et; R_2 = H) formed a new type of Se−Se hypervalent σ-dimer in the solid state, and there was concern that all future selenium variants would also associate in this way (a topic covered in more detail in Section 1.4.2). Serendipitously, shortly thereafter, the first examples of these selenium radicals that did *not* associate in the solid state were generated, and contained a bulky substituent in the R_2 position (**1-38**, R_1 = Me, Et; R_2 = Ph). They crystallize in the high symmetry $P3_121$ and $P3_221$ space groups and the packing of the radicals about the three-fold screw axes eliminates the potential for Se−Se σ-bond formation. Other monomeric materials have been made that crystallize in the high-symmetry $P\bar{4}2_1m$ space group (**1-38 – 1-40**; R_1 = Et; R_2 = Cl, Br) or form Se---Se' clusters within orthorhombic or monoclinic space groups (**1-38 – 1-40**; R_1 = Me; R_2 = Cl).

It has become clear over the years that different combinations of R_1/R_2 substituents have significant implications on the physical properties of these materials. From a synthetic standpoint, we needed a rational design plan in order to improve the conductive and magnetic behavior of this radical framework, and an in-depth theoretical inquiry into their structure-property relationships was carried out.[102b] Numerous calculations have revealed that while there are important lateral magnetic interactions in these structures, it is the intrastack exchange interactions that are the most influential and subject to the largest variation with substituent modification.[102a] Changes to the structure modify the degree of slippage of the radical plates along the π-stack and hence orbital overlap between the SOMOs. Both electronic and magnetic interactions have been calculated and correlated as a function of the direction and extent of slippage, displayed as a function of internal molecular coordinates *x* and *y* in Figure 1.26. Slippage coordinates are denoted [*x*, *y*], where the [0.0, 0.0] point corresponds to direct superposition of the two radicals. The types of calculations that were performed are (i) EHT calculations of the 1D *π*-SOMO dispersion energy ΔE_k (Figure 1.27) and (ii) DFT (UB3LYP/6-31G(d,p)) calculations of the pairwise intrastack exchange energy $\boldsymbol{J}_\pi$ (Figure 1.28). Both series of calculations considered the effects of all possible translations (slippage) along the *x* and *y* directions, using an interplanar separation (δ) of 3.5 Å. The results are summarized in the form of surface plots for the two representative systems **1-37** and **1-40**.

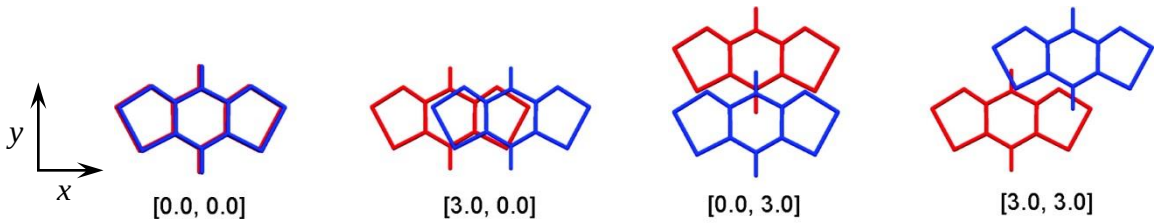

Figure 1.26 Slippage of π-stacks of model radicals **1-37 – 1-40** ($R_1 = R_2 = H$) as a function of [*x*, *y*]. Adapted from reference 102b.

The dispersion energy plots (Figure 1.27) show that the maximum bandwidth ($W = |\Delta E_k|$) along the π-stacking direction is observed when the radicals are superimposed [0.0, 0.0] and at position [1.5, 2.5] on the green "hill". The SOMO-SOMO interactions for these two situations is depicted in Figure 1.29.

Between these two areas, there are regions of varying *W*, including a line where ΔE_k goes from positive (green) to negative (blue), indicating orthogonal overlap between SOMOs (Figure 1.29b). The magnetic exchange energy plot (Figure 1.28) consists of an AFM "lagoon" around [1.5, 2.5] and a deep minimum at [0.0, 0.0]. These two regions are separated by a region where $\boldsymbol{J}_\pi$ is positive and magnetic exchange is expected to be ferromagnetic.

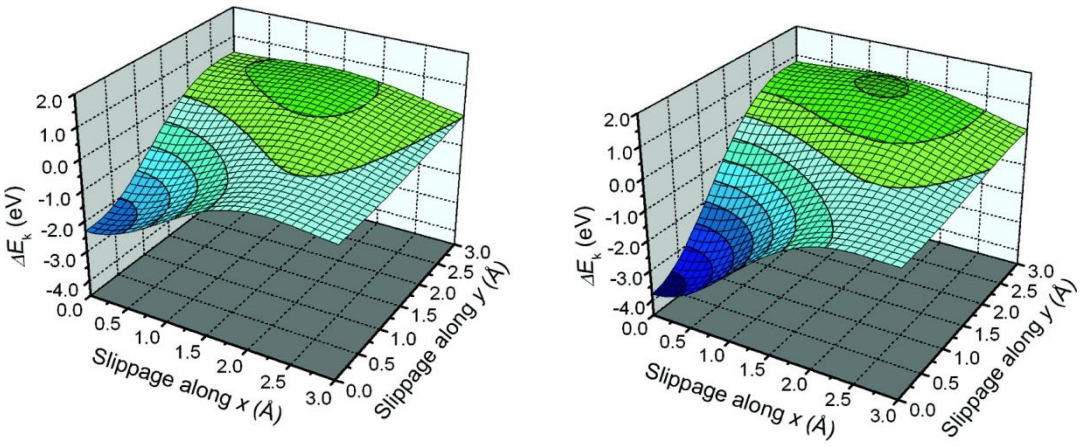

Figure 1.27 Surface plots of the dispersion energy ΔE_k (eV) as a function of *x* and *y* for **1-37** (left) and **1-40** (right) ($R_1 = R_2 = H$) with $\delta = 3.5$ Å. Contour lines are drawn at intervals of 0.5 eV. Adapted from reference 102b.

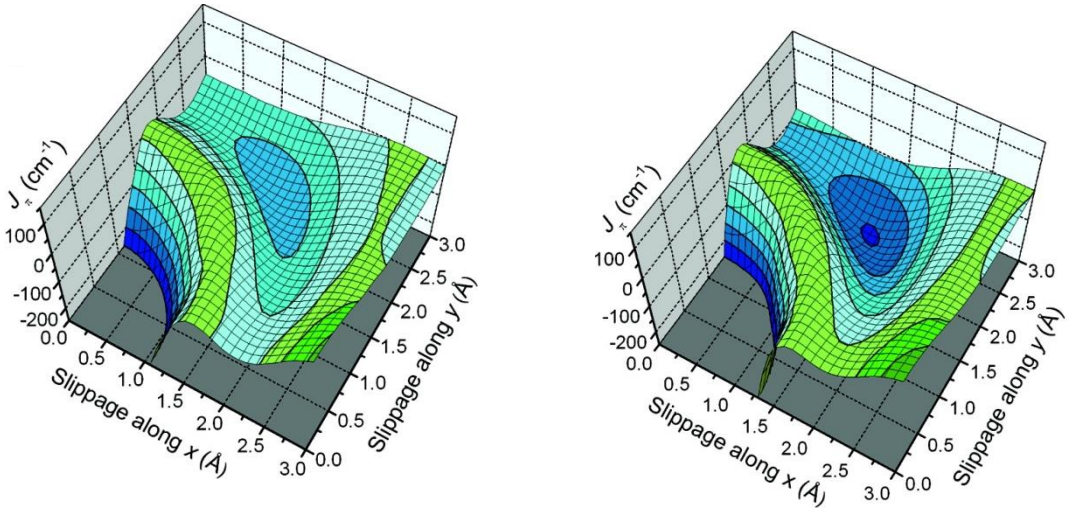

Figure 1.28 Surface plots of $\boldsymbol{J}_\pi$ (cm^{-1}) as a function of *x* and *y* for **1-37** (left) and **1-40** (right) ($R_1 = R_2 = H$) with $\delta = 3.5$ Å. Contour lines are drawn at intervals of 50 cm^{-1}. Adapted from reference 102b.

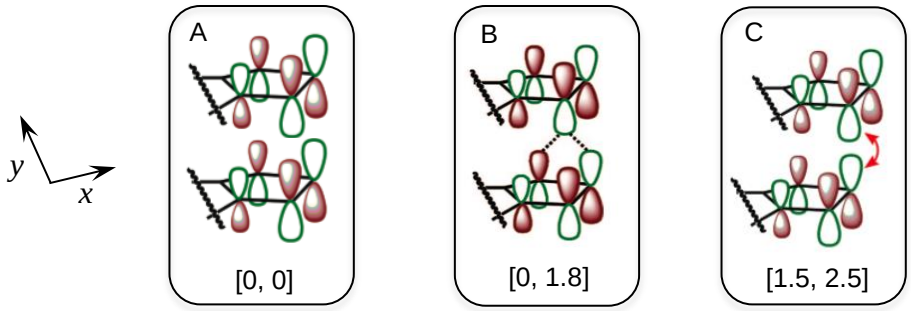

Figure 1.29 SOMO-SOMO interaction along the π-stack as a function of internal slippage coordinates [*x*, *y*].

With reference to the expression for the magnetic exchange integral 2***J*** (eqn. **9**), it is possible to correlate the two series of calculations. Where $|\Delta E_k|$ is a maximum, and hence $|S| >> 0$, AFM exchange along the stack is strong as evidenced by the regions of large, positive $\boldsymbol{J}_\pi$ at [0.0, 0.0] and [1.5, 2.5]. On the other hand, where $|S| \sim 0$ and overlap is orthogonal, we expect to observe FM exchange along the green "ridge".

The trends in both the dispersion and energy exchange plots for all-sulfur **1-37** and all-selenium **1-40** radicals are the same. The incorporation of selenium atoms into the rings increases orbital overlap, and enhances the magnitudes of both *W* and $\boldsymbol{J}_\pi$. Essentially, the "hills" get higher and the "valleys" get deeper in the 3D plots. Materials which we have made thus far map well onto these model calculations. Experimentally, we observe the greatest conductivity of any neutral radical in compound **1-40** (R_1 = Me; R_2 = Cl), whose coordinates [1.49, 1.64] approach the local maximum in the dispersion map (Figure 1.27).[102b] Moreover, the ferromagnetically ordered materials **1-38** (R_1 = Et; R_2 = Cl, Br, Me) and **1-40** (R_1 = Et; R_2 = Cl, Br) are slipped in such a way that they possess orthogonal overlap along the π-stack giving rise to FM exchange in this direction.[102a,123] Their coordinates hover around [0.0, 2.5] where slippage is solely along the *y* direction. Favourable (FM) exchange energies are only found in a narrow range of inclination angles (degree of slippage). The slipped π-stacks of those that *do not* order

ferromagnetically in this family, such as **1-38** ($R_1 = CF_3CH_2$, Pr; R_2 = Cl), fall well outside this window, while the other three are close to if not inside it.

As a result of these studies, we have been in a position not only to rationalize physical properties of existing systems, but to anticipate the transport properties of any new radical we synthesize. These structure maps, as we like to call them, will be referred to in Chapter 2, as the radicals presented there further demonstrate the sensitivity of magnetic and electronic exchange to the degree of slippage of π-stacks. In Chapter 5, a series of bisdithiazolyls **1-37** with novel ladder-like exchange interactions will be presented, demonstrating that F···S' intermolecular interactions that knit pairs of π-stacks may mediate strong lateral magnetic exchange in addition to typical interactions along the slipped π-stacks.

1.5.2 Sulfur and Selenium σ-Dimers – the 4c-6e Bond

As was previously mentioned, some of the early selenium containing radicals based on the bisdithiazolyl framework **1-37** form hypervalent σ-bonded dimers [**1-38**]$_2$ – a sharp contrast to the modes of dimerization demonstrated historically by the simple selenazyl radicals (Figure 1.4 in Section 1.2.5). This lateral mode of association (Scheme 1.2) was, at the time, without precedent. In order to determine whether bisthiaselenazolyl σ-dimers were going to be the rule or the exception, theoretical studies were performed. Density Functional Theory calculations (B3LYP/6-31G(d,p)) of the bond dissociation enthalpies, ΔH_{diss}, for model dimers of the type [**1-37**]$_2$ to [**1-40**]$_2$ (R_1 = H; R_2 = H) revealed that σ-dimerization is most favorable for dimers [**1-38**]$_2$, as shown in Table 1.2 and illustrated in Scheme 1.2.[176] The results suggest that σ-dimers should be the rule based on the high dissociation energy. However, it is clear from the numerous radicals synthesized over the years that the most significant factor impacting the solid state packing, and thus whether or not these radicals dimerize is in fact the nature of the ligands R_1 and R_2.

Scheme 1.2

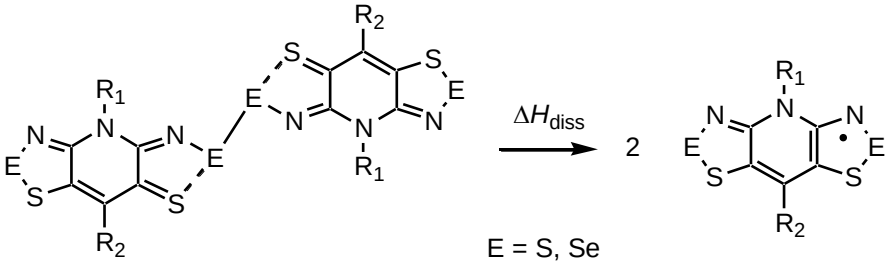

Table 1.2 (U)B3LYP/6-31G(d,p) Bond Dissociation Enthalpies, ΔH_{diss}, for [**1-37**]$_2$ to [**1-40**]$_2$.[a]

Compound	[**1-37**]$_2$	[**1-38**]$_2$	[**1-39**]$_2$	[**1-40**]$_2$
ΔH_{diss} [b] (kcal mol^{-1})	11.12	18.19	-1.12	8.87

[a] ΔH_{diss} values from reference 176 and for $R_1 = R_2 = H$. [b] For the reaction in Scheme 1.2.

The most appropriate way to describe the bonding in these σ-dimers is as 4-center 6-electron (4c–6e) bonds, which are extended hypervalent bonds arising from interactions caused by direct orbital overlap between nonbonded atoms. Hypervalent dichalcogenides of the type E'···E−E···E' (where E = S/Se) have been known for quite some time, and have been studied extensively in the naphthyl systems **1-54**.[177] The driving force of the 4c–6e arrangement is the electron donation from two *p*-type orbitals of the "outside" E' atom to the σ* E−E orbital. Figure 1.30 shows the qualitative MO depiction of this interaction, where σ_2 may correspond to the stabilizing 4c–6e interaction.

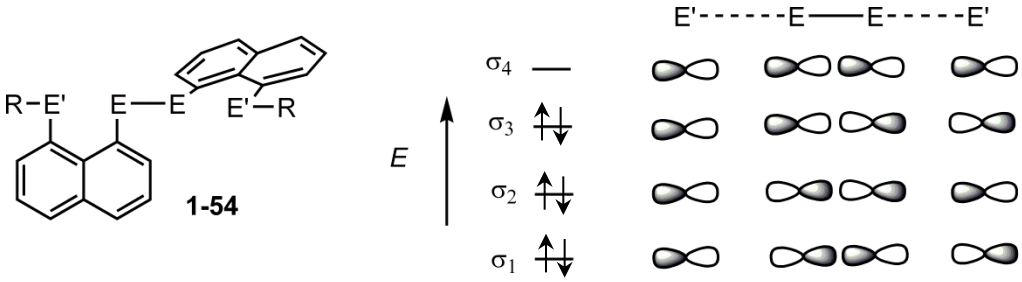

Figure 1.30 Qualitative molecular orbital diagram for a simple 4c–6e bond.

To date, four bisthiaselenazolyl σ-dimers [**1-38**]$_2$ have been found, where R_1 = Me, R_2 = H, Me, F and R_1 = Et, R_2 = H.[169,176] Although, initially, their discovery was considered a bane since their spins are

quenched, they have proven themselves to be arguably just as significant as their open-shell counterparts. In Chapter 3, the pressurization of bisdithiazolyl and bisthiaselenazyl dimers will be presented, in which compression of the stacks is monitored by powder X-ray crystallography and correlated to the resulting improvement in conductivity towards metallization.

Early studies showed that the diamagnetic dimers are small bandgap semiconductors, with $\sigma_{RT} = 10^{-6}$ $S \cdot cm^{-1}$ and E_{act} as low as 0.32 eV. Although these results were notable, the dependence of the conductivity and activation energy to pressure is what made the compounds remarkable. Specifically, [**1-38**]$_2$ (R_1 = Me, R_2 = H), hereby termed [**1-55**]$_2$, displayed an increase in conductivity by five orders of magnitude, and a decrease in E_{act} to 0.03 eV with only 5 GPa of applied pressure.[172] For closed shell molecular compounds, such sensitivity is rare and typically materials require much higher pressures for a strong response. For example, the E_{act} of single crystals of pentacene can be reduced to 0 eV upon the application of 27 GPa of pressure, and even higher pressures are required on powdered samples.[178]

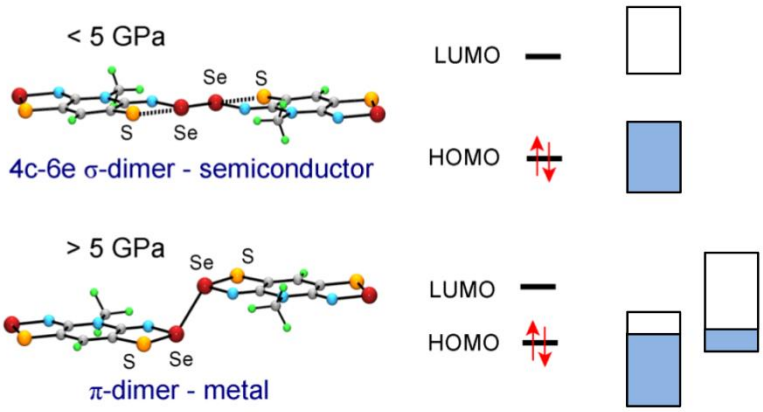

Figure 1.31 Molecular transformation from a σ- to a π-dimer [**1-55**]$_2$ (left), and frontier molecular orbital considerations with pressure (right). Adapted from ref. 172.

An in-depth structural analysis was performed on [**1-55**]$_2$, and the nature of the remarkable response was established. While at pressures below 5 GPa the unit cell is simply compressed, above 5 GPa there is a structural change at the molecular level. The once planar molecules "buckle" under pressure (see Figure 1.31), the space between the two new molecular planes increases and the new arrangement is best described as a π-dimer. At the molecular level, the diselenide bond Se−Se' that binds the dimers

actually lengthens, the hypervalent Se···S interactions revert to values more in keeping with a covalent Se−S bond, and the C−S bonds lengthen, suggesting they should no longer be described as terminal thiones. The molecular reorganization accompanying the abrupt bulk structural changes of [**1-55**]$_2$ lead to the closure of the HOMO-LUMO gap near 5 GPa and the onset of a weakly metallic state. As expected, this phenomenon is not observed for the related σ-dimers.

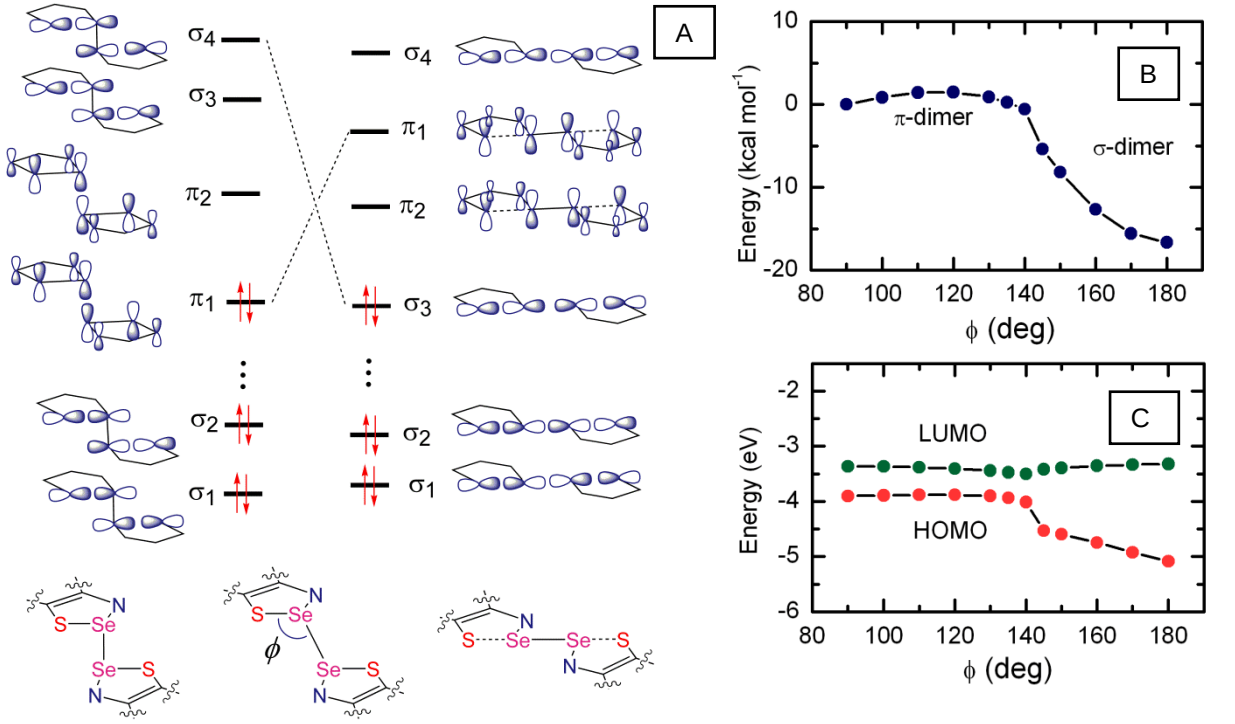

Figure 1.32 (a) Evolution of the frontier MOs from a σ- to a π-dimer of a simple model radical. (b) B3LYP/6-31G(d,p) energy and (c) the calculated HOMO-LUMO energies as a function of evolution angle ϕ. Adapted from ref. 172.

In order to address the closure of the HOMO-LUMO gap in [**1-55**]$_2$ with applied pressure, it is necessary to consider the changes in the frontier molecular orbitals (FMOs) as a result of the structural reorganization. With reference to the simple 4c–6e model in Figure 1.30, we know the nature of the σ-type FMOs of the hypervalent dimer. In order for conversion to a π-dimer to occur, electrons from one of these σ-orbitals must move into the π-system. As may be seen in the FMO correlation diagram of a simple 7π−electron system, the basic building block of [**1-55**]$_2$ (Figure 1.32a), movement of the two dimer halves from a linear σ-dimer to a π-dimer is accompanied by an evolution of the pertinent

orbitals. The σ_3 level, the HOMO of the σ-dimer, rises high in energy in the π-dimer arrangement, whereas the π_{4b} level becomes the new HOMO. The avoided crossing results in an energy barrier between the two states, which is overcome by the external (*PV*) work done on the system with applied pressure. Further theoretical studies (Figure 1.32b and c) confirmed that this change leads to a closure of the HOMO-LUMO gap, and thus an abrupt switch from a molecule to a metal with a "warm hug" of applied pressure.

1.5.3 Oxobenzene-bridged Materials – the Fluorine (and Oxygen) Difference

The advantage of developing the structure maps for bisdithiazolyls **1-37** and their variants **1-38**, **1-39** and **1-40** was two-fold: (i) the physical properties of existing structures could be rationalized based on the model calculations and (ii) improvement in charge transport could be effected by strategic crystal engineering. Since the common packing motif for the pyridine-bridged family of radicals **1-37** – **1-40** is the herringbone π-stack (Figure 1.33a), a couple of different strategies have been developed to move the structures toward superposition of adjacent radicals in the π-stacks. One method by which this has been effected will be explored in detail in Chapter 2, and involves the pressurization of tetragonal radicals **1-40** (R_1 = Et; R_2 = Cl, Br) causing the stacks to become less slipped and for metallization to occur.[174]

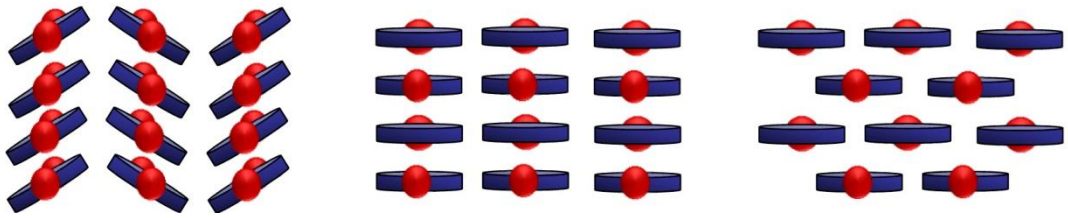

(a) herringbone π-stacks (b) superimposed (ABAB) π-stacks (c) layered π-stacks

Figure 1.33 π-Stacking motifs of planar bisdithiazolyl radicals.

Knowing that the location on the structure maps where one would find the greatest bandwidth, *W*, is at the point of SOMO-SOMO superposition, a new bisdithiazolyl framework was conceived in which one of the basal substituents (R_2) was replaced by a N atom. Due to a smaller degree of steric bulk, these pyrazine-bridged radicals **1-56** (R_1 = Me) broke out of the herringbone slipped π-stack mold and

crystallized in superimposed ABAB π-stacks (Figure 1.33b).[179] Extended Hückel Theory calculations based on the crystal structure at room temperature revealed that this material should possess a bandwidth of ~ 2 eV. The conductivity of **1-56** (R_1 = Me) was the highest (at the time) for a bisdithiazolyl radical, with $\sigma_{RT} \sim 10^{-3}$ S·cm^{-1} rivaling even the selenium-based pyridine-bridged radicals, yet the presence of an activation barrier of E_{act} = 0.19 eV demonstrated that a metallic ground state had not yet been achieved. Further structural work revealed that with decreasing temperature, the space group symmetry of the lattice was sequentially lowered, changes that gave rise to an opening of a band gap at the Fermi level and the formation of a semiconducting ground state.

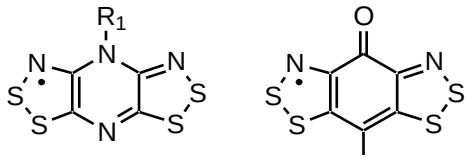

1-56 **1-57**

More recently, work in the Oakley group has evolved to focus on the development of oxobenzene-bridged bisdithiazolyls **1-57**.[180] These radicals enjoy a lower value of *U*, as well as possess supramolecular sythons, that is, structure makers within the molecular framework. The ability of O···S' interactions to direct packing of these planar radicals in the solid state lead to ribbon-like arrays, which form layered π-stacks (Figure 1.33c) instead of the typical herringbones.[181] The multidimensional network of intermolecular interactions, as well as the shift away from ABAB superposition, stabilizes these materials with respect to spin pairing. As a result, all variations (R_2 = Ph, Cl, H, F) known thus far *do not* dimerize, exhibit some of the highest conductivity of neutral thiazyl (and selenazyl) radicals and possess strong magnetic coupling that leads to canted AFM ordering in most cases, with T_N values ranging from 4.5 K to 13 K.[182]

Under ambient conditions, **1-57** (R_2 = F), or FBBO, possesses the best conductivity of a neutral f = ½ radical known to date, with $\sigma_{RT} \sim 2 \times 10^{-2}$ S·cm^{-1}, even better than the best selenium-based variant of **1-40** (R_1 = Me; R_2 = Cl) where $\sigma_{RT} \sim 4 \times 10^{-3}$ S·cm^{-1}. In addition to its high conductivity, FBBO orders as a canted antiferromagnet with T_N ~ 13 K. Remarkably, this radical metallizes under a mere 3 GPa of

applied pressure, which has been confirmed by both conductivity measurements and infrared spectroscopy, showing the closure of the Mott-Hubbard gap under pressure. Superior charge transport in FBBO over other neutral radicals is attributed to its unique sheet-like architecture, directed by F···S' as well as O···S' intermolecular interactions, and the resulting interlayer π-SOMO overlap (Figure 1.34).

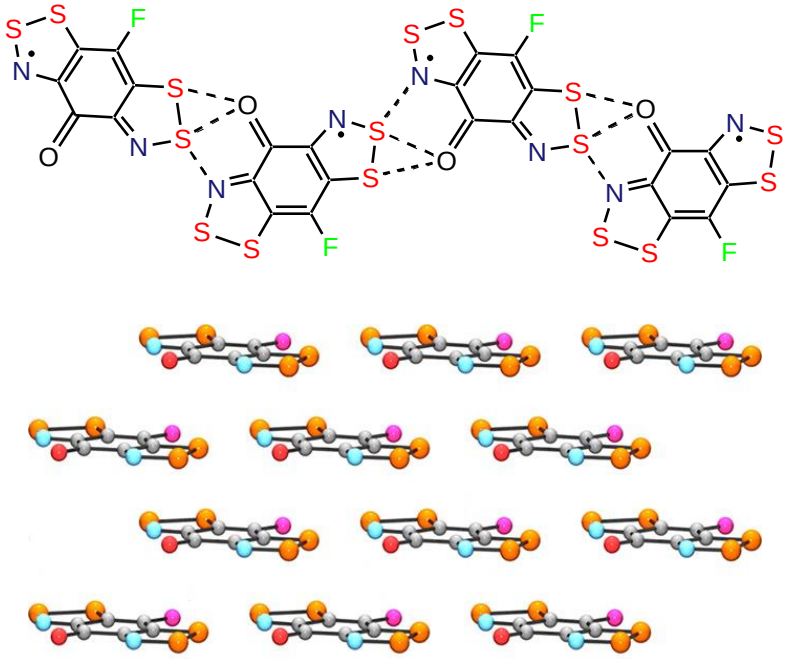

Figure 1.34 A single ribbon generated by O···S' and N···S' (top), and brick wall-like architecture of π-stacks (bottom) in **1-57** (R_2 = F). Adapted from reference 182.

In recognition of its structure-making abilities, many of the radicals I have worked on, and their respective σ-dimers, possess a fluorine atom in the basal R_2 substituent on the pyridine-bridged ring system. As a result, most of the structures discussed in Chapters 3–5 are knit together *via* these F···S' supramolecular synthons, giving rise in most cases to unique structural, as well as physical, properties.

1.6 Thesis Scope

Shortly before the beginning of my graduate studies in 2008, the Oakley group had started to investigate the synthesis, properties and solid state structures of bisdithiazolyls **1-37** and their selenium

variants **1-38**, **1-39**, and **1-40**. In my early days in the research group, we were coming to understand the effects of *chemical pressure* on these materials, and learning to rationalize properties such as magnetic ordering and high conductivity in a systematic way. The bulk of my graduate work involved the synthesis and characterization of new radicals within this family, as well as an in-depth examination of the effect of external *physical pressure* on the solid state structures and physical properties. In all cases, the radicals in this thesis are substituted by a basal halogen atom, and the later chapters describe the properties of solely fluorine-substituted thiazyl and selenazyl radicals.

The addition of fluorine to the molecular structure has provided strong F···S' intermolecular interactions that serve to knit structures together in advantageous ways. In some cases, these structures may change in unanticipated ways under the influence of external pressure, temperature and light. In addition to chemical pressure studies on the ferromagnetic family of radicals, this thesis presents work on three new, fluorine-substituted 4c–6e σ-dimers that demonstrate the rich functionality of these materials. In recognition of this potential, my work on these dimers has led to a departure from a traditional feeling of disappointment associated with the discovery of a new spin-paired radical dimer instead of the corresponding open-shell species.

Firstly, though, **Chapter 2** of this thesis describes the effect of chemical and physical pressure on chalcogen-substituted bisthiaselenazolyl **1-38** (R_1 = Et; R_2 = F, Cl, Br, I) and bisdiselenazolyl **1-40** (R_1 = Et; R_2 = Cl, Br) radical ferromagnets. As described in the present chapter, charge and spin transport are highly sensitive to the solid state structure and, specifically, the degree of π-stack slippage. Determination of the complete set of ambient pressure crystal structures of the halogen-substituted series **1-38** led to structure-property mapping of the halogen effect on ferromagnetic ordering. With a view to explore the magnetic and conductive properties with physical pressure, the highest T_c ferromagnets **1-40** (R_1 = Et; R_2 = Cl, Br) were examined.

In **Chapter 3**, these pressure studies were extended to bisthiaselenazolyl 4c–6e σ-dimers [**1-38**]$_2$ (R_1

= Me; R_2 = F) and their sulfur counterparts [**1-37**]$_2$ (R_1 = Me; R_2 = F). These structures were examined under pressure as a comparison study to the dimer that "buckles" and metallizes under pressure, [**1-55**]$_2$ (Scheme 1.3). The structural dichotomy leads to a sharp contrast in the conductive properties. By contrast, metallization of [**1-38**]$_2$ (R_1 = Me; R_2 = F) at P ~ 13 GPa is a result of band spreading in the absence of a phase transition, which leads to an eventual coalescence of the valence and conduction bands.

Scheme 1.3

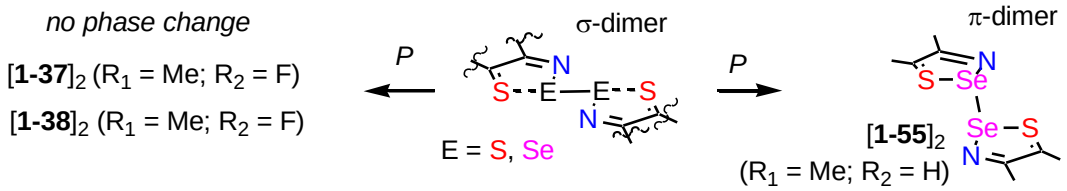

In **Chapter 4**, a novel 4c–6e bisdithiazolyl σ-dimer [**1-37**]$_2$ (R_1 = Et; R_2 = F) is presented, which undergoes a reversible radical-to-dimer interconversion (RDI),[b] that is, a S = 0 ↔ 2 (S = ½) transition. This process can be initiated thermally, optically and with mild pressure. The hysteretic phase change in the thermal experiment, observed through the magnetic channel, gives rise to a metastable S = ½ state with a 5 K region of bistability near 375 K. This phase change can be observed at room temperature with the application of ~ 0.7 GPa of pressure. In all cases, the structures of the high spin states were elucidated and demonstrate the same metastable phase independent of the stimuli. The σ-dimer to π-radical pair conversion is the result of a configurational crossover at the molecular level, which is fundamentally different from the bistability arising for 1,3,2-DTAs described in section 1.2.6.

Scheme 1.4

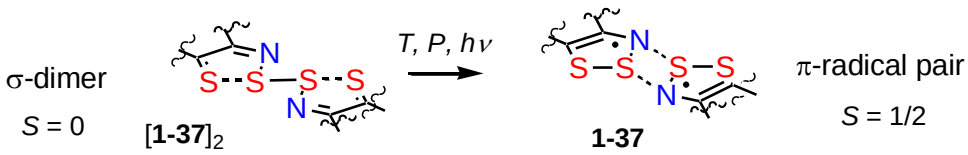

[b] "'When I use a word,' Humpty Dumpty said in rather a scornful tone, 'it means just what I choose it to mean - neither more nor less.'" ~ Lewis Carroll

In the pursuit of even more σ-dimers exhibiting bistability, I extended the family of fluorine-substituted bisdithiazolyls by elongating the alkyl chain further and generating the series **1-37** (R_1 = Pr, Bu, Pn, Hx; R_2 = F), discussed in **Chapter 5**. Instead of dimers, however, the pinning effect of the F···S' interactions leads to a topological ladder structure type facilitated by the buffering effect of the alkyl substituents. Magnetic exchange through S···S' atoms between the π-stacks in addition to the intrastack interactions gives rise to spin ladders in three of the four radicals presented in **Chapter 5**.

This highly interdisciplinary research required a network of collaborators in order to be brought to fruition. In this thesis, I present a composite of work performed here in the Oakley lab as well as the labs of Drs. Dube, Tse, Secco, Shatruck, Mito and Jin from around the world. Certain experiments (particularly those under pressure) required instrumentation that simply is not available at the University of Waterloo. In each case, data was collected off site by collaborators and worked up, analyzed and interpreted by myself in the Oakley lab under the guidance of my supervisor and with input from my fellow lab mates.

Chapter 2

Changing Chemical and Physical Pressure in Selenium Radicals: Structural Implications and Metallic Conductivity

2.1 Introduction

As discussed in Chapter 1, during the last few years, our work on radical-based materials in the Oakley lab has evolved towards the development of resonance stabilized heterocycles of the type **2-1** – **2-4** (Chart 2.1). These highly delocalized spin systems enjoy low gas phase disproportionation energies ΔH_{disp} and electrochemical cell potentials E_{cell}, indicative of a low onsite Coulomb potential U. They were designed to allow for alteration in both intermolecular magnetic and electronic interactions either through variations in the exocyclic substituents R_1 and R_2,[1] or through replacement of the heteroatom sulfur by its heavier (and softer) congener selenium.[2]

Chart 2.1

	E_1	E_2
2-1	S	S
2-2	S	Se
2-3	Se	S
2-4	Se	Se

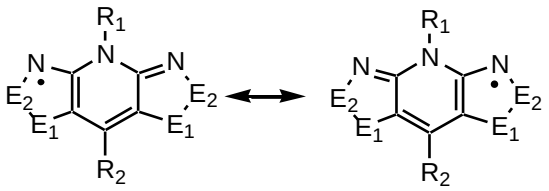

R_1	Et	Et	Et	Et
R_2	**F**	**Cl**	**Br**	**I**
2-1	2-1a	2-1b	2-1c	2-1d
2-2	2-2a	2-2b	2-2c	2-2d
2-3		2-3b	2-3c	
2-4		2-4b	2-4c	

The latter strategy, which was predicated on the idea that S/Se replacement would afford isostructural mapping in the solid state, was sometimes hindered by the tendency of radicals of type **2-2** (and occasionally **2-1**) to crystallize as dimers bound by hypervalent 4-center 6-electron S···E-E···S bonds.[3,4] Examples of these will be further discussed in Chapters 3 and 4. It was nonetheless apparent, from the earliest reports of undimerized examples of **2-2**, **2-3** and **2-4**, that selenium incorporation within an isostructural series affords improved conductivity, as expected given the greater spatial extension of 4*p*-orbitals on selenium relative to 3*p*-orbitals on sulfur. Somewhat accidentally we also discovered that S/Se incorporation could give rise to remarkable magnetic effects. Compounds **2-3** and

2-4 (R_1 = Et, R_2 = H), for example, were found to order as spin-canted antiferromagnets with T_N values of 18 K and 27 K respectively,[5] while **2-2b** and **2-4b** (R_1 = Et, R_2 = Cl) were observed to order as bulk ferromagnets with T_c values of 12.8 and 17 K respectively (Chart 2.2).[6] In addition to their high ordering temperatures, the latter two materials display coercive fields (H_c at 2 K) of 250 and 1370 Oe, values 2 to 3 orders of magnitude greater than those found in light atom ferromagnets.[7]

Chart 2.2

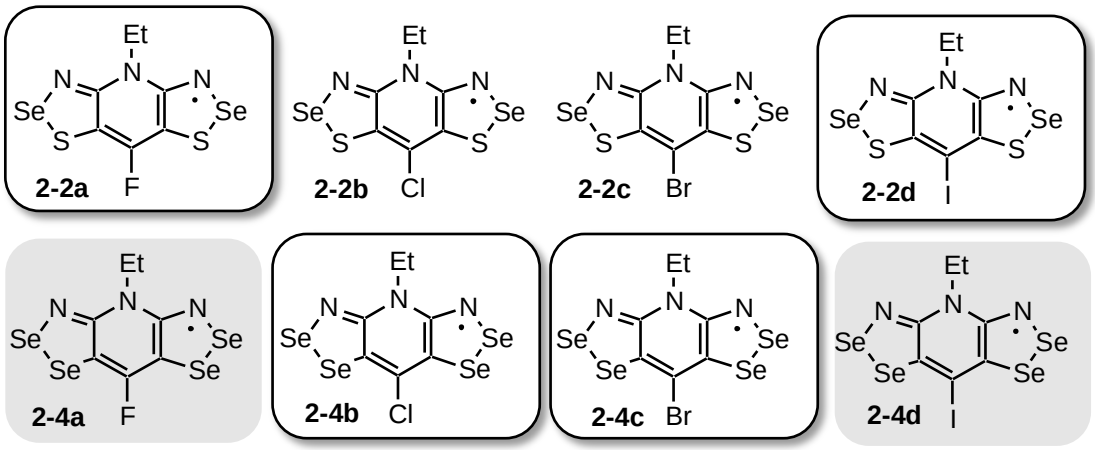

While the observation of a single component molecular material displaying ferromagnetic ordering along with conductivity, albeit not metallic, represents a significant advance in the development of molecular magneto-electronics, improvements in conductivity, ordering temperature and coercivity require a better understanding of the relationship between crystal structure, electronic structure and bulk property. To address the point regarding the relationship between crystal structure and property, we have explored the effect of variations of the molecular packing found for **2-2b**, by using sufficiently small modifications of the R_1/ R_2 groups such that the tetragonal space group ($P\bar{4}2_1m$) was preserved.[8] This investigation of the effect of *chemical pressure* on magnetic ordering was discussed in detail in Chapter 1.

Within the aforementioned study, the conclusion reached was that when the substituent on the framework R_1 is an ethyl group and the R_2 is a halogen atom (Cl or Br at the time), the material

crystallizes in such a way that orthogonal overlap of adjacent SOMOs in the π-stacks give rise to ferromagnetic exchange in this direction and hence bulk ferromagnetic ordering. The present chapter explores the effects of halogen substitution on structure and magnetic exchange in the present framework when R_1 = Et (Chart 2.2). This is possible with the completion of the bisthiaselenazolyl series *via* the synthesis of **2-2a** (R_2 = F) and **2-2d** (R_2 = I) (Chart 2.2). Further selenium incorporation has led to stronger magnetic exchange, and thus higher T_c and H_c, in **2-4b** over **2-2b** (and **2-4c** over **2-2c**), which prompted us to attempt to complete the full series of halogen-substituted compounds and include **2-4a** and **2-4d**. However, despite our best efforts, we were unable to synthesize the desired compounds.

An alternative strategy to probing changes in the charge transport properties of these systems is to invoke the use of *physical pressure*,[9] effects of which will be further explored in the present and subsequent chapters. One of the hypotheses of the latter type of study is that with continued compression of the π-stacks of these tetragonal structures, there should be a marked increase in intermolecular overlap and hence electronic bandwidth. To explore this possibility we have examined the effect of increased pressure (0–15 GPa) on the crystal structure and physical properties, including magnetic ordering and conductivity, of our two best ferromagnets **2-4b** and **2-4c** (Chart 2.2). In addition to a preliminary communication,[10] a full report was published on a large portion of this work.[11]

2.2 Synthesis

2.2.1 Synthesis of 2-2a (R_1 = Et; R_2 = F)

The procedure for the preparation of **2-2a**, outlined in Scheme 2.1, begins with the alkylation of commercially available 2,4,6-trifluoropyridine with ethyl trifluoromethanesulfonate (triflate). This produces *N*-ethyl-2,4,6-trifluoropyridinium triflate **2-5** which, upon treatment with gaseous ammonia, affords the corresponding 2,6-diaminopyridinium triflate **2-6**. Double Herz cyclization[12] of the latter with sulfur monochloride (S_2Cl_2) in refluxing acetonitrile (MeCN) then furnishes the desired

bisdithiazolylium framework in the form of the triflate salt [**2-1a**][OTf]. Selenium selectively replaces sulfur in the 2-position of the DTA ring using SeO_2 in pressurized acetonitrile at 110 ºC.[6,8] This tricky step produces the triflate salt of [**2-2a**]$^+$ in reasonable yield; the resulting material is recrystallized from acetonitrile before proceeding to the final reduction step. Reduction of the cation [**2-2a**]$^+$ to the desired radical **2-2a** may be effected at this stage in acetonitrile with a reducing agent. This step was attempted with a number of reducing agents, including *N*,*N*,*N*',*N*'-tetramethyl-*p*-phenylenediamine (TMPDA), decamethylferrocene (DMFc) and octamethylferrocene (OMFc). Two different methods by which we readily generate radicals were also utilized, that is, slow solution diffusion *via* H-cells or careful, slow bulk reduction. We were unsatisfied with the phase purity from all methods, noting the presence of a mystery contaminant by FTIR (Figure 2.1) and powder X-ray crystallography (Figures 2.4 and 2.5).

Scheme 2.1

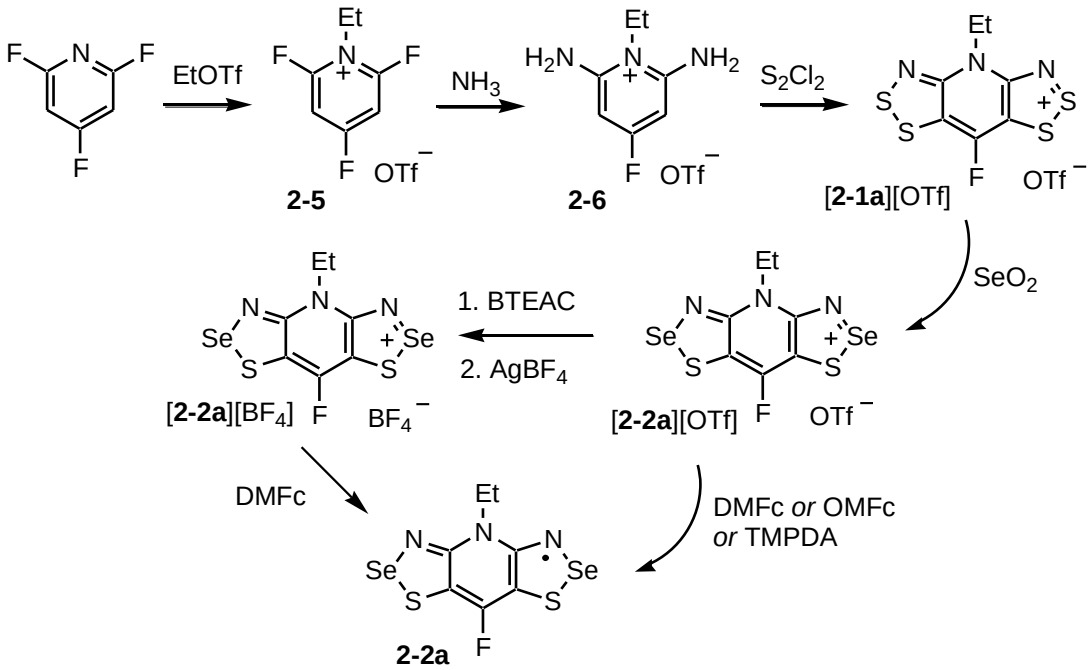

To further purify the cation [**2-2a**]$^+$ prior to reduction, with the intention of hopefully obtaining phase-pure radical **2-2a**, we proceeded to metathesize the OTf^- salt to the corresponding BF_4^- salt. This switch typically produces salts that are slightly less soluble in MeCN, which we predicted would help

the recrystallization of the cation [**2-2a**]$^{+}$. The [**2-2a**][OTf] salt was first converted to its corresponding Cl^{-} salt with the addition of benzyltriethylammonium chloride (BTEAC) in MeCN solution. The purple precipitate was then treated with $AgBF_4$, and the resulting material [**2-2a**][BF_4] was much more easily recrystallized from MeCN. The radical used for structural and physical property measurements was obtained *via* reduction of the [**2-2a**][BF_4] salt with DMFc to generate *almost* phase-pure material **2-2a** in reasonable yields. Despite our best efforts, it was impossible to isolate one phase of **2-2a**, which we attribute to the presence of small amounts of σ-dimerized radicals [**2-2a**]$_2$, akin to those discussed in Chapter 1.

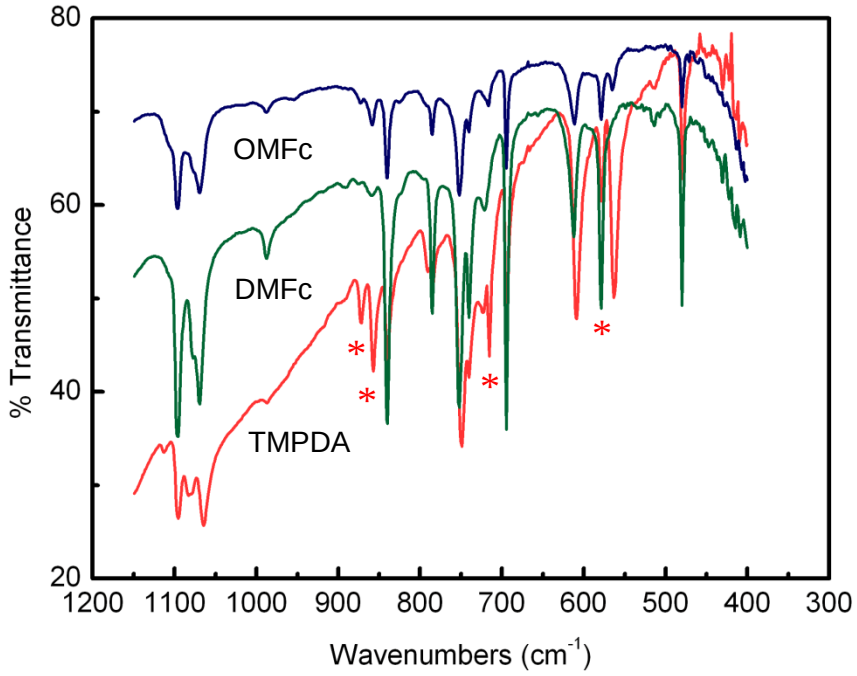

Figure 2.1 FTIR spectra of the products of reduction of [**2-2a**][OTf] with TMPDA (bottom), DMFc (middle) and OMFc (top) resulting in varying levels of phase purity. Starred peaks are evidence of contamination.

2.2.2 Synthesis of 2-2d (R_1 = Et; R_2 = I)

The procedure for the generation of radical **2-2d**, outlined in Scheme 2.2, is somewhat analogous to the above sequence. The starting point is commercially available 2,6-dichloro-4-iodopyridine, which is first alkylated with ethyl triflate, followed by an amination with NH_3 to generate *N*-ethyl-2,6-

diaminopyridium triflate **2-8**. At this point is where the sequence for the iodo compound begins to diverge from that used previously for the fluoro-substituted material. In this case, the double Herz reaction is done under much gentler conditions to avoid replacement of the basal iodo-substituent with a chlorine atom. It is evident, then, that the fluoro-substituted material is not at all susceptible to chlorination, while the analogous, weaker C−I bond *is* susceptible to substitution with chlorine. This issue complicated the synthesis of **2-2d**, as the gentle conditions required for ring closure to [**2-1d**][Cl] led to a low yield of the desired product. To analyze the chloro-contamination of the [**2-2d**][Cl] salts produced from the initial double Herz step, FTIR spectroscopy was mainly used, as shown in Figure 2.2. Note the absence of absorption at ~ 770 cm^{-1} in the (top) blue spectrum *versus* the green one below. The strength of this peak varied with the amount of chloro-contamination, finally reaching a minimum when the conditions of the double Herz reaction were perfected.

Scheme 2.2

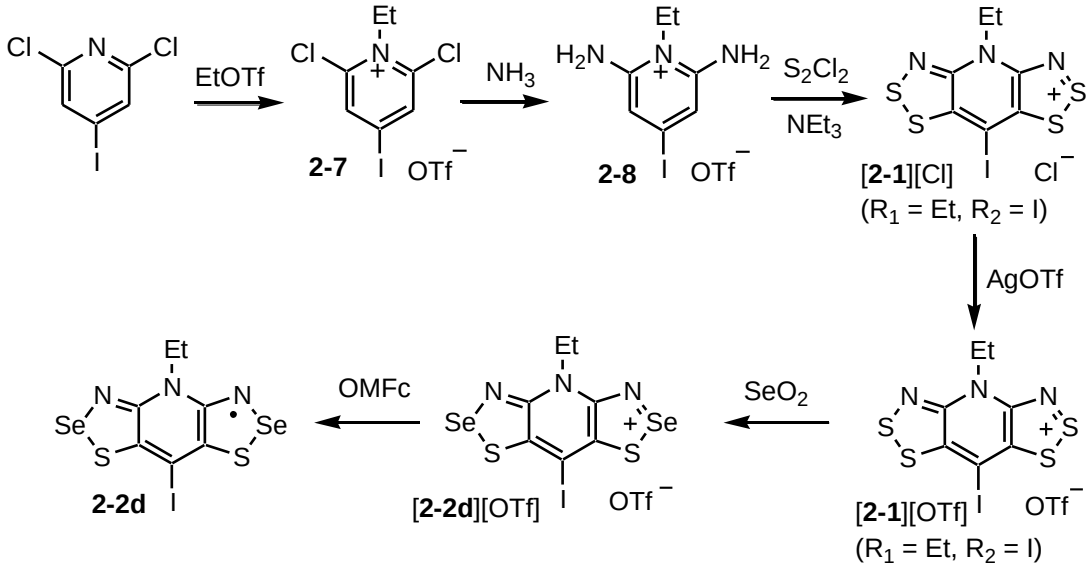

Since the first few steps of this procedure produce an insoluble chloride salt of [**2-1d**]$^{+}$, purification by anion exchange followed by recrystallization is necessary. Metathesis with AgOTf in acetonitrile provides the soluble salt [**2-1d**][OTf], while AgCl precipitates out of solution. The resulting product is much easier to work with and purification is straightforward. It is subsequently treated with SeO_2 to

form the bisthiaselenazolylium cation [**2-2d**]$^{+}$. After purification of this salt, it is reduced with OMFc to generate radical **2-2d** either by bulk reduction or slow diffusion in H-cells producing microcrystalline material at best suitable for physical property measurements and powder X-ray crystallography.

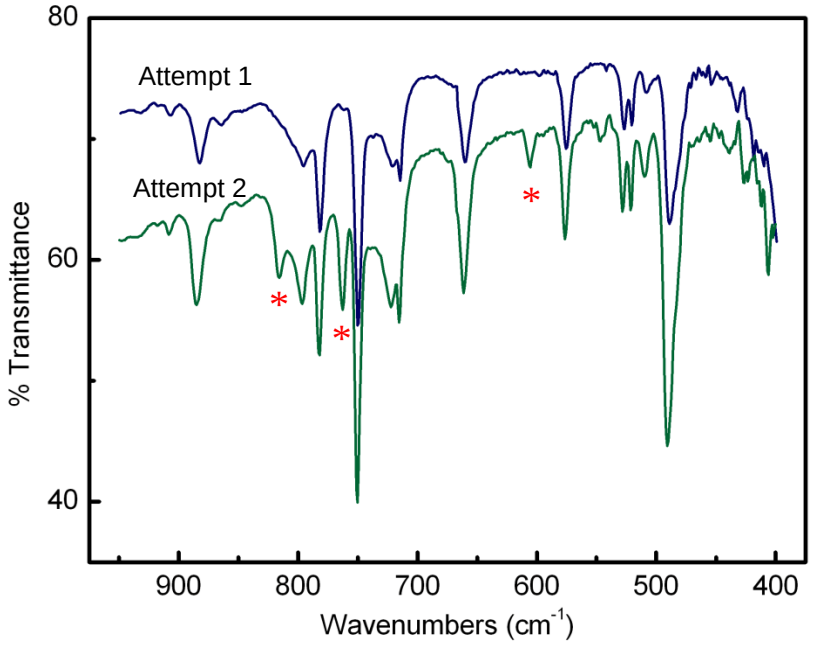

Figure 2.2 FTIR spectra of the [**2-1d**][Cl] salts produced by double Herz cyclization. Attempt 1 is from material that has little-to-no contamination with R_2 = Cl (note absence of peak at ~ 770 cm^{-1}, for example), whereas these impurities are present in Attempt 2. Starred peaks are evidence of contamination.

2.2.3 Synthesis of 2-4b,c (R_1 = Et; R_2 = Cl, Br)

The synthesis of bisdiselenazolyls **2-4b,c** begins with commercially available 2,6-diaminopyridine (Scheme 2.3).[19] This material is treated with bromine and KSeCN to obtain the *bis*-selenocyanate **2-9**. Reduction with $NaBH_4$, followed by alkylation of the exposed selenolates with iodomethane, affords the *bis*-selenomethyl pyridine derivative **2-10**. The organic solid is condensed with thionyl chloride ($SOCl_2$) in the presence of triethylamine (NEt_3) to generate the bisdithiazolylium framework [**2-3**][Cl] (R_1, R_2 = H) as a chloride salt in the form of a black, insoluble powder. Subsequent metathesis firstly with $GaCl_3$ to afford the $GaCl_4^-$ salt, followed by tetrabutylammonium triflate (Bu_4NOTf) to generate

[**2-3**]$^+$ as a triflate salt, gives a product that is more soluble and easier to work with than the initial chloride salt. As previously reported, removal of the apical proton (R_1) with Proton Sponge gives a highly insoluble zwitterionic product, which is subsequently alkylated with ethyl triflate to form the triflate salt of the *bis*-1,2,3-selenathiazolylium cation [**2-3**]$^+$ (R_1 = Et; R_2 = H).[6b,13]

Scheme 2.3

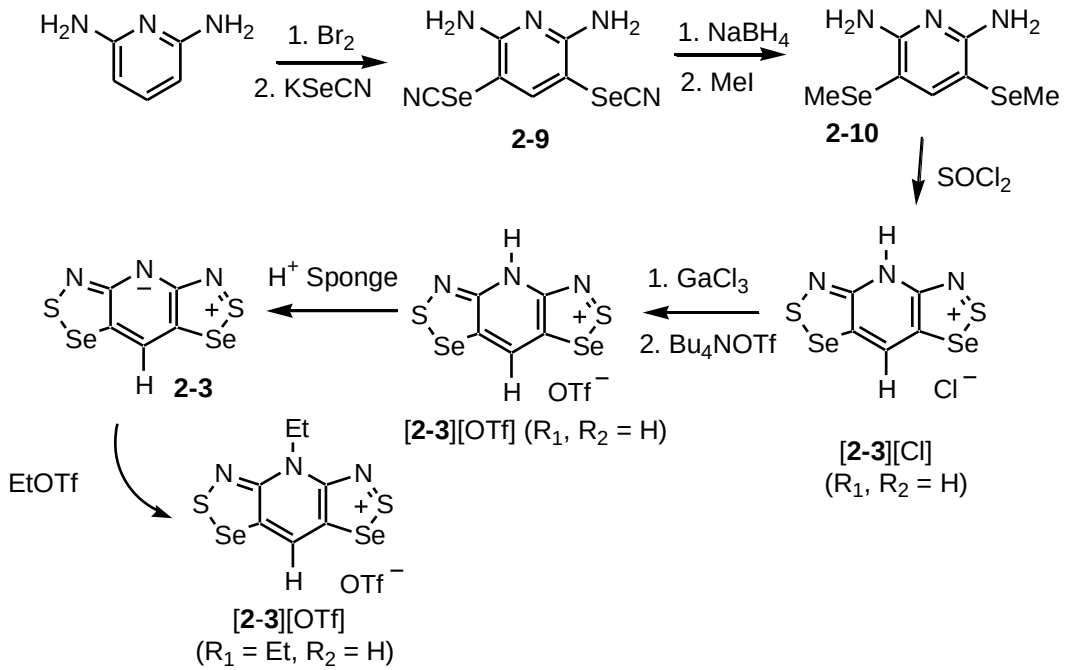

The triflate salt [**2-3**][OTf] (R_1 = Et, R_2 = H) is the starting material for both compounds **2-4b** and **2-4c**. Oxidation of this material with iodobenzene dichloride (Scheme 2.4) affords the triflate salt of the chloro-substituted cation [**2-3b**]$^+$, while the use of bromine or *N*-bromosuccinimide yields the bromo-substituted derivative [**2-3c**][OTf]. Subsequent treatment of either of these two salts with selenium dioxide in boiling acetic acid leads to a sulfur/selenium exchange and the formation of the triflate salt of the respective bisdiselenazolylium cations [**2-4b,c**]$^+$. Bulk reduction of the salts to produce the radicals **2-4b,c** in microcrystalline form suitable for ambient and high pressure transport property measurements was conveniently effected using OMFc or the metal-free agent TMPDA. Crystals of the radicals used for single crystal diffraction were grown by electrocrystallization methods.

Scheme 2.4

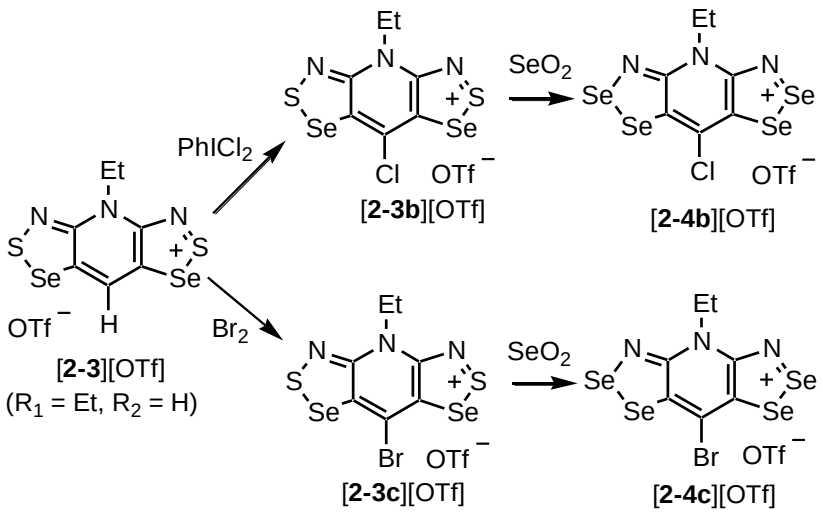

2.3 Ambient Pressure Results

2.3.1 Crystallography under Ambient Conditions

Single crystal X-ray diffraction has established that crystals of **2-1 – 2-4** (R_1 = Et; R_2 = Cl, Br) form an isostructural set (see Chart 2.1).[6] Using powder X-ray methods, we have now also established that solid state structures of new radicals **2-2a** and **2-2d** are members of this set as well. All of these compounds belong to the tetragonal space group $P\bar{4}2_1m$.

We were unable to grow single crystals of **2-2a** as it quickly became apparent that the quality of the material produced was dependent on the reducing agent used to generate the radical. For example, Figure 2.3 shows two diffraction patterns collected at room temperature for **2-2a**, the top one being from material generated in a TMPDA reduction, which is a relatively weak reducing agent, and the bottom pattern is from material generated by reduction with DMFc, with a much stronger potential. It is evident that the latter pattern is cleaner, and visibly absent are contaminant peaks at $2\theta \sim 12°$ and 23° that are present in the sample when reduced slowly with TMPDA. Despite our best efforts, we were unable to make material better than microcrystalline quality. Growth of good quality crystals typically requires slow co-diffusion in an H-cell apparatus (see Appendix), a method that inevitably produces contaminated material in this case. Other methods, such as recrystallization of the radical from an

organic solvent, or sublimation in a vacuum furnace, are unsuitable for selenium-containing radicals of this type as lattice energies are simply too high to allow vaporization.

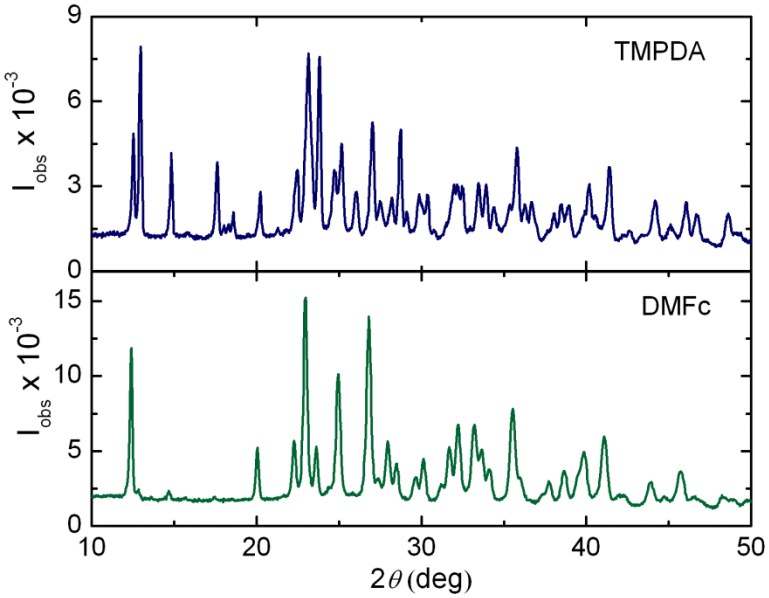

Figure 2.3 Powder diffraction patterns of **2-2a** from material produced by reduction with TMPDA and DMFc (λ = 1.54056 Å).

Fortunately, we were able to solve the structure from the powder diffraction pattern for material reduced with DMFc (Figure 2.4). Starting with the molecular model of **2-2** (R_1 = Et; R_2 = Cl), the chlorine atom was changed for a fluorine (the C–F bond length was adjusted accordingly and later refined), and a model structure was produced by indexing and simulated annealing using DASH.[14] During the initial Rietveld refinement, performed using DASH, a rigid-body constraint was maintained. The final Rietveld[15] refinement of the unit cell, performed using fixed atomic positions and isotropic thermal parameters, was carried out with GSAS, providing an excellent fit to the experimental pattern.[16]

In the case of the iodine-substituted material **2-2d**, we were unable to grow single crystals due to the lack of solubility of the radical compared to related radicals. Instead, we resorted to powder diffraction methods again to observe the crystal packing. The diffraction pattern for **2-2d** was collected at room temperature with λ = 1.54056 Å. Using simulated annealing methods in DASH, a model of the crystal packing of **2-2d** was generated starting with a molecular model based on **2-2c**. This was then refined to

provide a satisfactory fit to the experimental data using the same procedure as for **2-2a**. Figure 2.5 shows the experimental, simulated and difference diffraction patterns from GSAS.

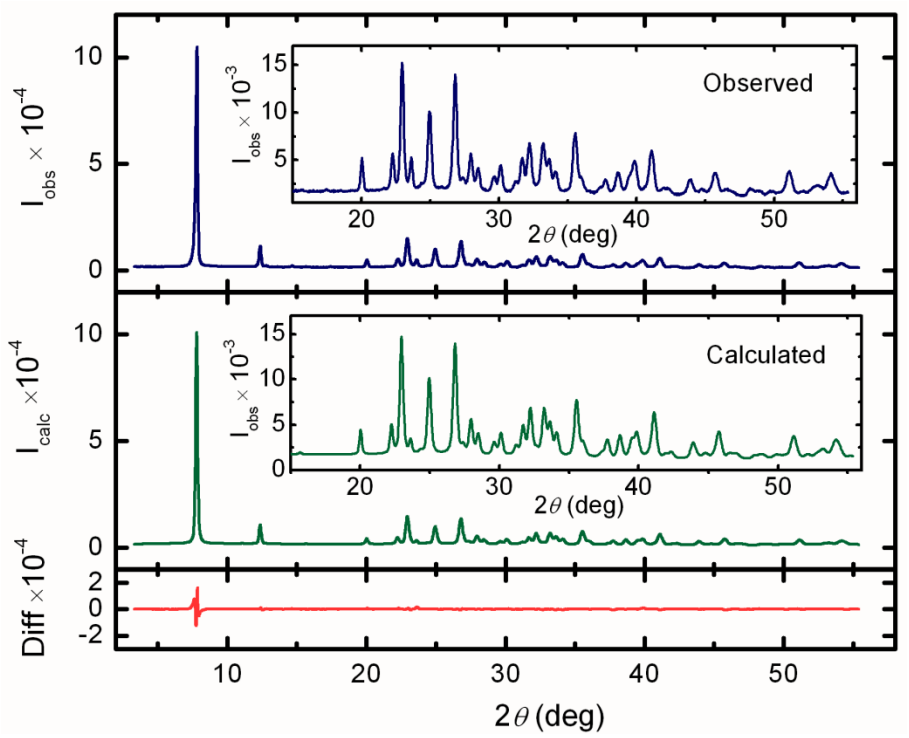

Figure 2.4 Observed, calculated and difference powder X-ray diffraction patterns for **2-2a** (λ = 1.54056 Å). Inserts show an expansion of the 2θ = 15–55° that is 10 times the original scale.

The crystal structures of all of these tetragonal radicals, including the aforementioned **2-2a,b,c,d** and **2-4b,c**, consist of undimerized radicals bisected by mirror planes and arranged in pinwheel-like clusters about the $\bar{4}$ centers of the unit cell. The radicals are not dimerized, but pack into slipped π-stack arrays running parallel to the *c*-axis, as may be seen in Figure 2.6, which illustrates the crystal structure of **2-2d** viewed parallel and perpendicular to the stacking direction. Crystal metrics for the six compounds **2-2a,b,c,d** and **2-4b,c** at ambient pressure are provided in Table 2.1 for comparison. While none of these radicals are dimerized, there are numerous intermolecular Se···Se' contacts within the nominal van der Waals separation for selenium (3.8 Å).[17] Of these, d_1, d_2, and d_3, defined in Figure 2.6 and Table 2.1, will be discussed below.

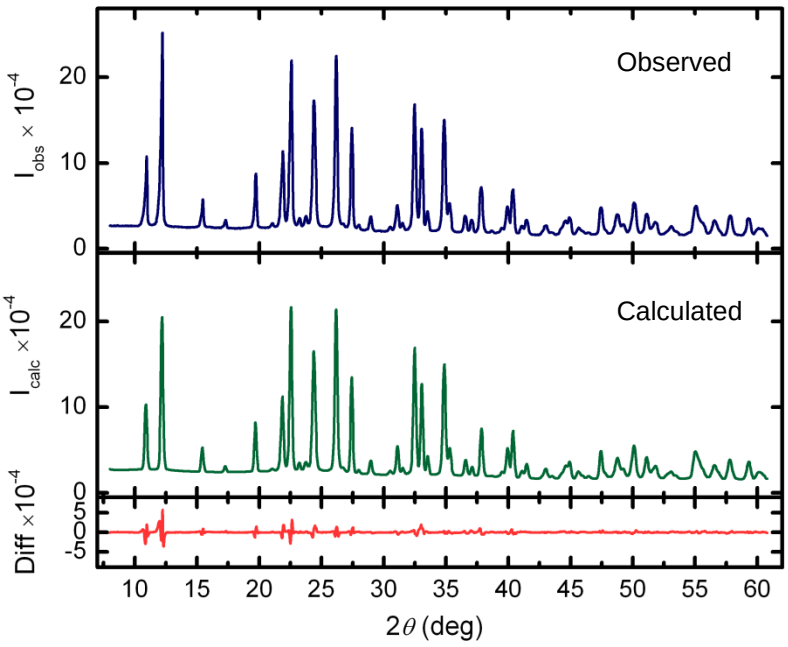

Figure 2.5 Observed, calculated and difference powder X-ray diffraction patterns for **2-2d** (λ = 1.54056 Å).

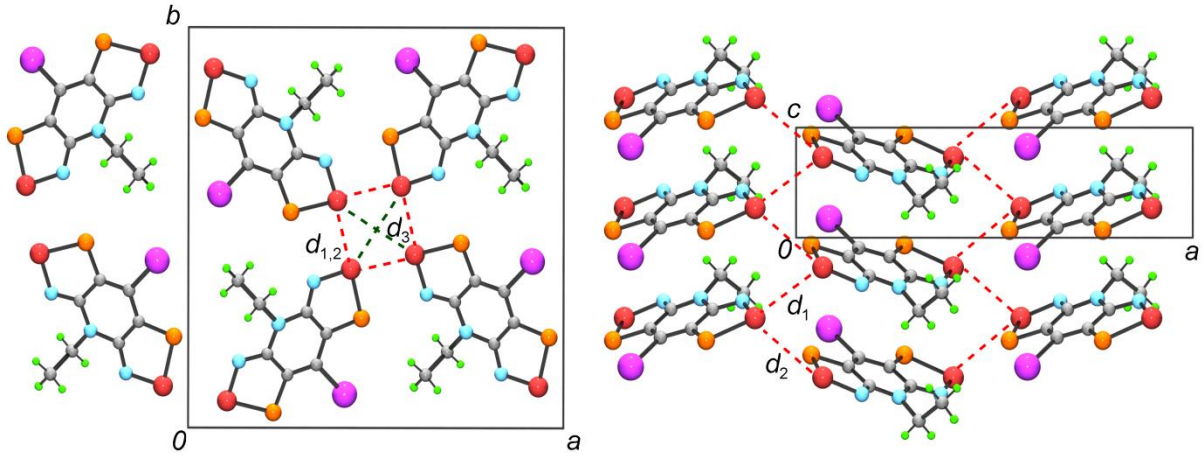

Figure 2.6 Crystal packing of **2-2d**, viewed parallel to the *c*-axis (A) and *a*-axis (B).

It is useful to examine the pertinent intermolecular distances in these structures at ambient temperature and pressure. Interestingly, when the chlorine in the R_2 position of **2-4b** is substituted with a bromine atom as in **2-4c**, the structure changes ever so slightly. Intermolecular contacts d_1 – d_3 lengthen by only a small factor, and the mean interplanar separation increases from 3.545 to 3.563 Å.

Additionally, the values for the slippage along the internal *y*-direction for the π-stacks (*dy*), as well as the interplanar separation (δ), as defined in Figure 2.7, are very similar for **2-4b** and **2-4c** (Figure 2.8).

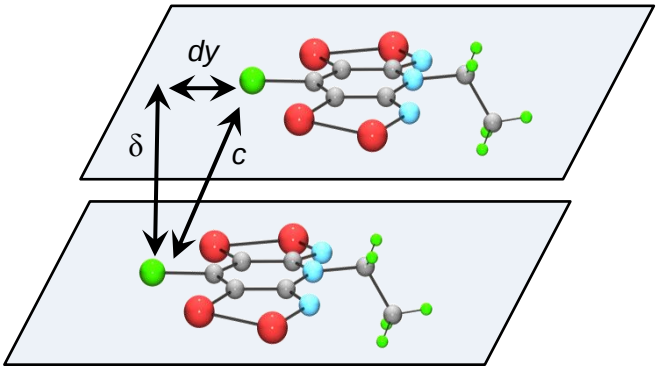

Figure 2.7 Definitions of the slippage (*dy*) and interplanar separation (δ) of adjacent radicals along the π-stacks.

Within the series of radicals **2-2a,b,c,d**, some deviations from the ideal trends are observed. Once again, halogen substitution from a Cl to a Br atom in the R_2 position results in very little change in the intermolecular contacts, *dy* and δ. However, a small nudge to the structure in either direction, whether with a slightly smaller atom such as fluorine (**2-2a**), or a larger one like iodine (**2-4d**) can cause the molecules to shift quite significantly. For example, the plate-to-plate separation δ = 3.499 Å and the Se···Se' interaction d_1 = 3.280 Å are both much smaller for **2-2a** than for the others within the series (Table 2.1). Furthermore, when a much larger halogen atom like iodine is introduced into the structure such as in **2-2d**, an even more significant change in the packing results, albeit within the same space group. In this case, there is a dramatic increase in the length of the pertinent intermolecular contacts about the $\overline{4}$ center ($d_1 - d_3$), as well as a significant jump in the interplanar separation δ (3.517 Å for **2-2c** *versus* 3.622 Å for **2-2d**) to accommodate the much larger iodine atoms within the stacks. Surprisingly, this extra space was sufficient for the packing of π-radicals **2-4d**, as the slippage along the *y*-direction did *not* change, with *dy* = 2.17 Å for both **2-2c,d**, in line with the rest of the series. This subtle change in packing within a given set of related radicals is the effect of *chemical pressure* on the

system. It often has significant implications within the scope of physical property measurements and can alter behaviour dramatically.

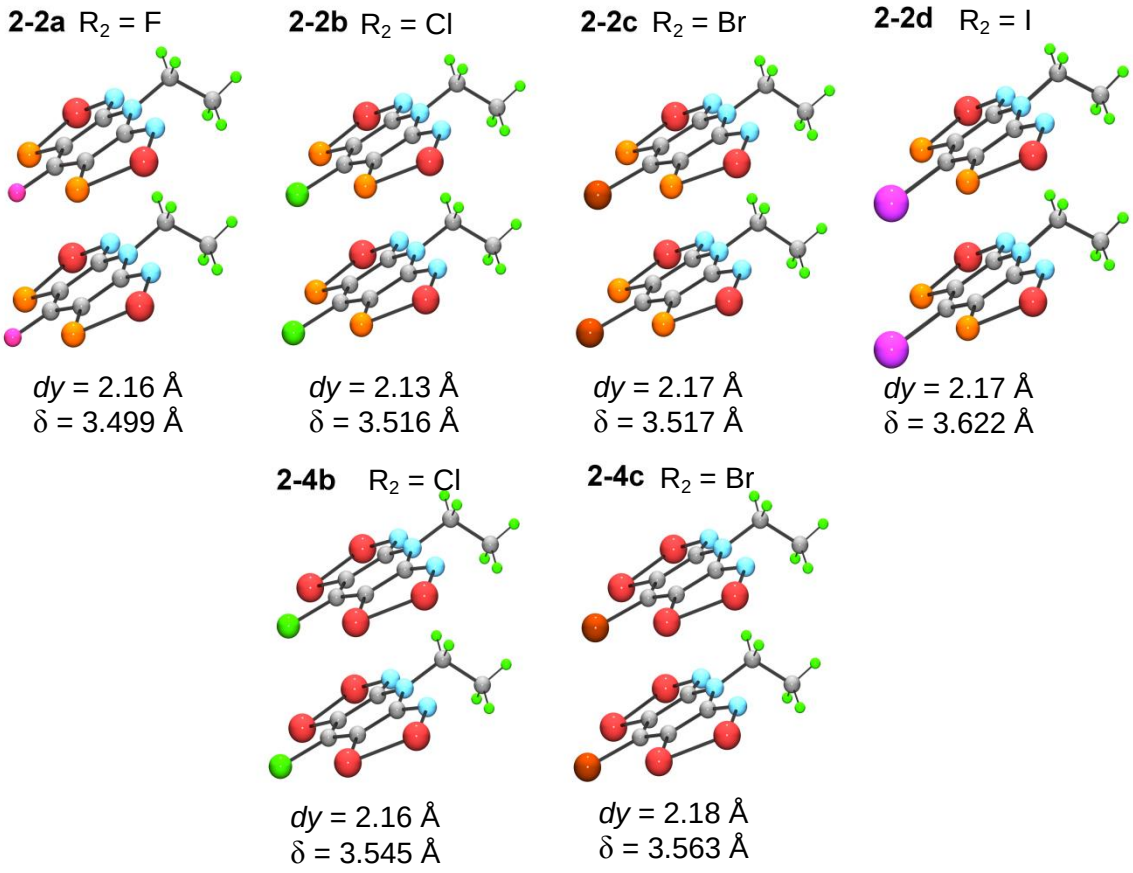

Figure 2.8 Slippage (*dy*) and plate-to-plate separation (δ) illustrated for π-stacks of all six **2-2a,b,c,d** and **2-4b,c**.

Table 2.1 Crystal Data and Metrics for **2-2a,b,c,d** and **2-4b,c**

	2-2a	**2-2b** [a]	**2-2c** [b]	**2-2d**	**2-4b** [c]	**2-4c** [d]
Formula	$C_7H_5FN_3S_2Se_2$	$C_7H_5ClN_3S_2Se_2$	$C_7H_5BrN_3S_2Se_2$	$C_7H_5IN_3S_2Se_2$	$C_7H_5ClN_3Se_4$	$C_7H_5BrN_3Se_4$
M	372.20	388.64	433.09	480.08	482.43	526.89
a (Å)	15.9870(10)	16.0334(8)	16.0885(7)	16.2434(4)	16.2708(5)	16.3109(14)
c (Å)	4.1152(6)	4.1090(4)	4.1339(3)	4.2220(3)	4.1720(3)	4.1753(7)
V (Å^3)	1051.77(17)	1056.30(13)	1070.02(10)	1113.95(7)	1104.49(9)	1110.80(2)
ρ_{calcd} (g cm^{-3})	2.351	2.444	2.688	2.332	2.901	3.151
space group	$P\bar{4}2_1m$	$P\bar{4}2_1m$	$P\bar{4}2_1m$	$P\bar{4}2_1m$	$P\bar{4}2_1m$	$P\bar{4}2_1m$
Z	4	4	4	4	4	4
temp (K)	296	296(2)	296(2)	296	296(2)	296(2)
μ (mm^{-1})	--	7.61	11.00	--	13.494	16.774
λ (Å)	1.54056	0.71073	0.71073	1.54056	0.71073	0.71073
data/restr./ parameters	--	1150/0/76	1166/0/76	--	1209/0/76	1211/0/76
solution method	powder methods	direct methods	direct methods	powder methods	direct methods	direct methods
R, R_w (on F^2)	0.0768, 0.1356	0.0447, 0.1003	0.0173, 0.0402	0.0688, 0.1081	0.0374, 0.0635	0.0307, 0.0504
d_1 (Å)	3.280	3.328(1)	3.344(1)	3.433	3.404(1)	3.411(1)
d_2 (Å)	3.498	3.459(1)	3.490(1)	3.637	3.502(1)	3.519(1)
d_3 (Å)	3.803	3.818(1)	3.845(1)	4.005	3.891(1)	3.910(1)
δ (Å)	3.499	3.516	3.517	3.622	3.545(6)	3.563
dy (Å)	2.16	2.13	2.17	2.17	2.16	2.18
dev. from plane (Å)[e]	--	0.087	0.093	--	0.0843	0.0287

[a] Data from reference 6a. [b] Data from reference 8. [c] Data from reference 6b. [d] Data from reference 11. [e] Mean value of deviations of all atoms from plane of heterocyclic framework.

2.3.2 Physical Property Measurements under Ambient Pressure of 2-4b,c.

Ambient pressure magnetic susceptibility χ measurements on compounds **2-4b,c** reveal very similar results. Plots of the product χT (field cooled) *versus* temperature at a field of H = 100 Oe (Figure 2.9) confirm that both radicals behave as paramagnets between 50 K and 300 K, with χT(300 K) values of 0.432 emu·K·mol^{-1} (**2-4b**) and 0.420 emu·K·mol^{-1} (**2-4c**). Curie-Weiss fits to the data (corrected for diamagnetic contributions)[18] afford Curie constants C of 0.369 emu·K·mol^{-1} and 0.387 emu·K·mol^{-1} respectively (Table 2.4), that is, near the value expected (0.375 emu·K·mol^{-1}) for an S = ½ system with g nominally equal to 2. The large positive Weiss constants θ of 22.9 K (**2-4b**) and 23.2 K (**2-4c**) indicate the presence of strong local ferromagnetic exchange interactions. Upon cooling both compounds there is a slow rise in χT, in keeping with the positive θ-values, followed by a dramatic surge just below 20 K, with χT reaching a maximum near 14 K of 244 emu·K·mol^{-1} for **2-4b** and of 232 emu·K·mol^{-1} for **2-4c**. This response is consistent with a phase transition to a ferromagnetically ordered state. At temperatures below these maxima there is a steady drop-off in χT for both compounds, as would be expected from low temperature magnetization saturation. Variable temperature AC susceptibility measurements at different frequencies allowed us to pinpoint and compare the ordering temperatures T_c of the two compounds. As shown in Figure 2.9, both radicals display sharp, well-defined maxima in the real (in-phase) χ' and imaginary (out-of-phase) χ'' components at 17.0 K (**2-4b**) and 17.5 K (**2-4c**). The invariance of T_c with changes in the cycling frequency (from 100 Hz to 5 kHz) establishes that these materials are not spin glasses.

Magnetization (M) measurements as a function of field show that for both compounds M rises sharply with H, reaching a maximum (at 2 K) at H = 10 kOe, after which there is no further change up to H = 55 kOe. The corresponding saturation magnetization values M_{sat} are 1.03 Nβ (**2-4b**) and 1.02 Nβ (**2-4c**).[19] Reversal and cycling of the field sweep leads to hysteresis. Plots of M *versus* H, from measurements at 2 K (Figure 2.12), show that while the remnant magnetization M_{rem} of the two compounds is virtually the same, the coercive field H_c for **2-4c** (1600 Oe) is significantly greater than

that found for **2-4b** (1370 Oe), a difference that may be a reflection of an increased magnetic anisotropy occasioned by larger spin-orbit coupling from bromine.

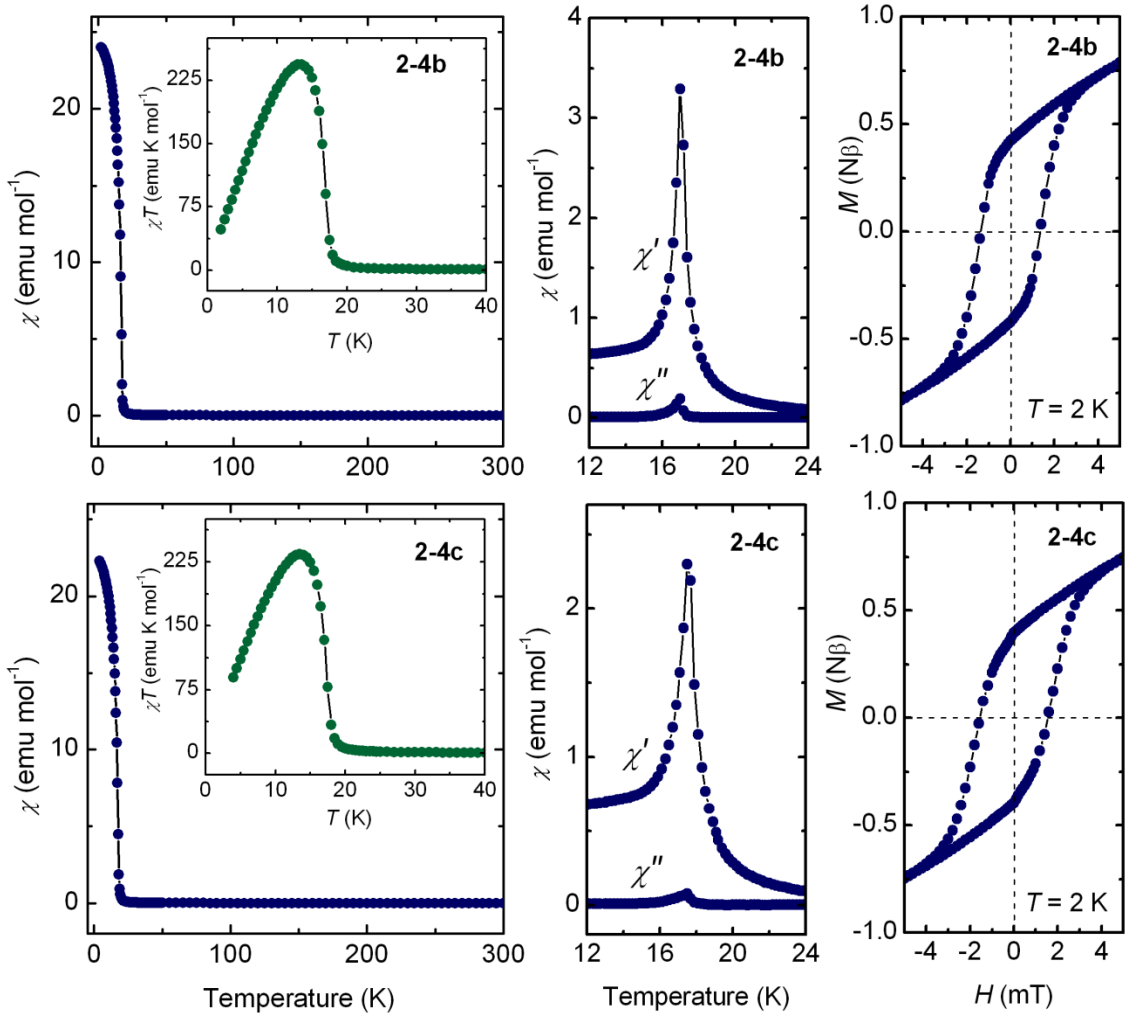

Figure 2.9 Plots of χ (field-cooled) and the product χT (insert) *versus* temperature at 100 Oe (left), AC susceptibility χ' and χ'' *versus* temperature at 1 kHz (center), and magnetization M *versus* field at T = 2 K (right).

We have measured the ambient pressure conductivity σ of **2-4b** and **2-4c** over the temperature range 200–300 K, using the 4-probe method on a pressed pellet sample. The variation in σ as a function of inverse temperature for the two compounds is illustrated in Figure 2.10, and the values of σ(300K) and the thermal activation energy E_{act} derived from an Arrhenius fit are listed in Table 2.2. These values

demonstrate slightly lower conductivity and higher activation energy than that observed in other related bisdiselenazolyl radicals.[2b,4a] Unsurprisingly, the conductivity increases considerably and activation energy decreases under the influence of chemical pressure. In this case, the change involves the incorporation of two more selenium atoms into each framework (**2-4** *versus* **2-2** series), giving rise to better orbital overlap and bandwidth.

Table 2.2 Ambient Pressure Magnetic and Conductivity Data

	2-4b	**2-4c**
C (emu·K·mol^{-1})	0.392	0.387
θ (K)	22.9	23.2
T_c (K)	17	17.5
M_{sat} (Nβ) at 2 K	1.03	1.02
M_{rem} (Nβ) at 2 K	0.41	0.4
H_c (Oe) at 2 K	1370	1600
σ(300 K) (S cm^{-1})	3.0 ×10^{-4}	6.0 ×10^{-4}
E_{act} (eV)	0.19	0.23

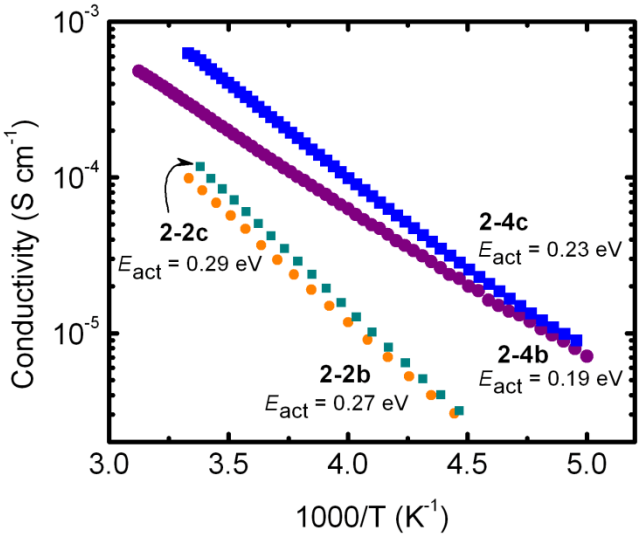

Figure 2.10 Ambient pressure four-probe conductivity measurements on **2-2b,c** and **2-4b,c**, with calculated activation energies (E_{act}).

2.3.3 Magnetic Measurements under Ambient Pressure of 2-2a,d

Ambient pressure magnetic susceptibility χ measurements on **2-2a** and **2-2d** reveal similar results to those previously reported for **2-2b,c**, with some peculiar differences.[6,8] Plots of the magnetic susceptibility χ (field cooled) and of the product χT *versus* temperature at a field of H = 1000 Oe for **2-2a** and 100 Oe for **2-2d** (Figure 2.11) confirm that both compounds behave as paramagnets between 20 K and 300 K.[20] Below 20 K, a dramatic surge in magnetization is observed, indicating a transition to a ferromagnetically ordered state. Curie-Weiss fits to the high temperature data (corrected for diamagnetic contributions) revealed Curie constants C of 0.291 emu·K·mol^{-1} for **2-2a** and 0.475 emu·K·mol^{-1} for **2-2d**. Both of these values are quite different from the expected value of 0.375 emu·K·mol^{-1} for an ideal S = ½ system. The low value observed for **2-2a** is attributed to the presence of a diamagnetic impurity, possibly the related σ-bonded dimer, which is consistent with the FTIR and powder X-ray crystallography results (Section 2.2.1 and 2.3.1).[21] The abnormally high C value for **2-2d** is possibly due to contamination with the chloro-substituted compound **2-2b**, which would affect the actual molar mass of the sample.

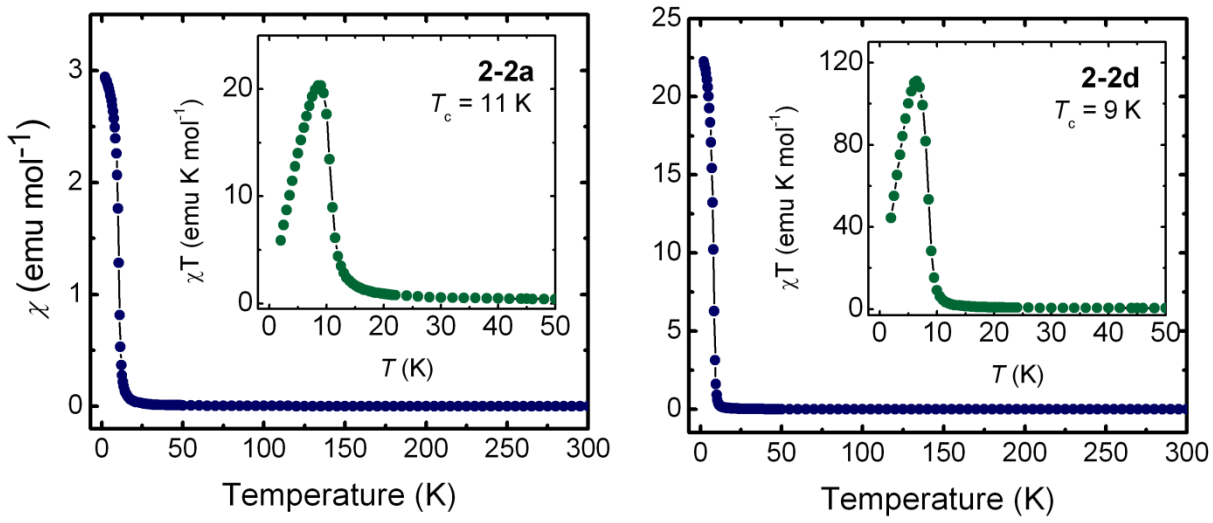

Figure 2.11 Plots of χ (field-cooled) *versus* temperature at H = 1000 Oe for **2-2a** (left) and H = 100 Oe **2-2d** (right) from 0–300 K. Inserts show low temperature (0–50 K) data of the product χT *versus* temperature.

The ferromagnetic ordering temperatures for **2-2a**,**d** are in the same range as in the related bisthiaselenazolyl radicals **2-2b,c**. The T_c for **2-2a** is 11 K in keeping with the trend, which is just slightly below the value of 12 K measured for **2-2b** and 14 K for **2-2c**. It would appear, then, that the value of T_c increases as the mass of the halogen atom (and thus the strength of spin-orbit coupling ~ Z^4) increases within this structural framework. This naïve hypothesis is challenged by the fact that the T_c for **2-2d** is only 9 K, much lower than the value of 16–17 K one would expect if this radical were to follow the established trend, in the absence of structural effects. This effect is explored more thoroughly in the Discussion section.

The weaker magnetic coupling in **2-2a** and **2-2d** under ambient conditions led us to cease the pursuit of further measurements and focus our efforts on the best ferromagnets we were able to synthesize. The remainder of this chapter will deal with primarily **2-2b** and **2-4c**, and their response to applied physical pressure.

2.4 High Pressure Measurements

2.4.1 High Pressure Crystallography on 2-4b,c

Having established the crystal structures of both **2-4b** and **2-4c** at ambient pressure, we wished to explore the effect of *physical pressure* on the molecular packing, in order to rationalize any changes in properties with pressure as a function of the crystal packing of our two best ferromagnets. To this end, high pressure powder diffraction data on both bisdiselenazolyls **2-4b** and **2-4c** were collected at room temperature as a function of *increasing* pressure using synchrotron radiation and a diamond anvil cell (DAC), with helium as the pressure transmitting medium. Two series of data sets up to 15 GPa were indexed and the structures solved in DASH using molecular models derived from the ambient pressure single crystal solutions. By way of illustration, the data sets collected on **2-4c** over the range 2–14 GPa are shown in Figure 2.12. Representative experimental and refined (in GSAS) powder patterns, along with the difference between the two for **2-4b** (2.16 and 7.97 GPa) and **2-4c** (2.20 and 8.91 GPa) are also

shown in Figure 2.14. Changes in the unit cell parameters as a function of pressure of **2-4b**,**c** are illustrated in Figure 2.13.

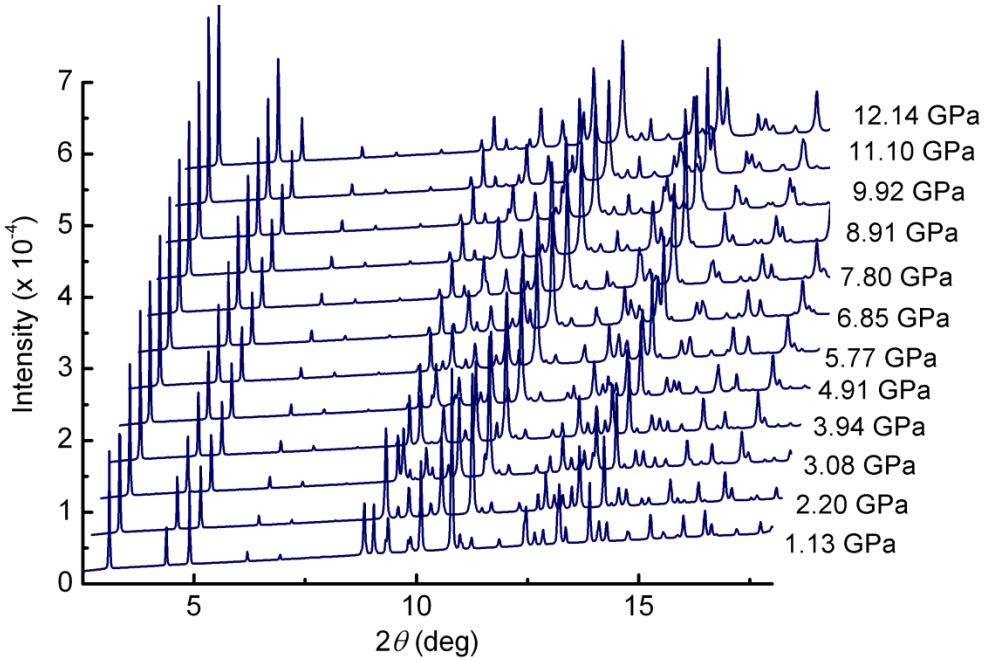

Figure 2.12 Powder diffraction data (λ = 0.61795 Å) for **2-4c** as a function of applied pressure.

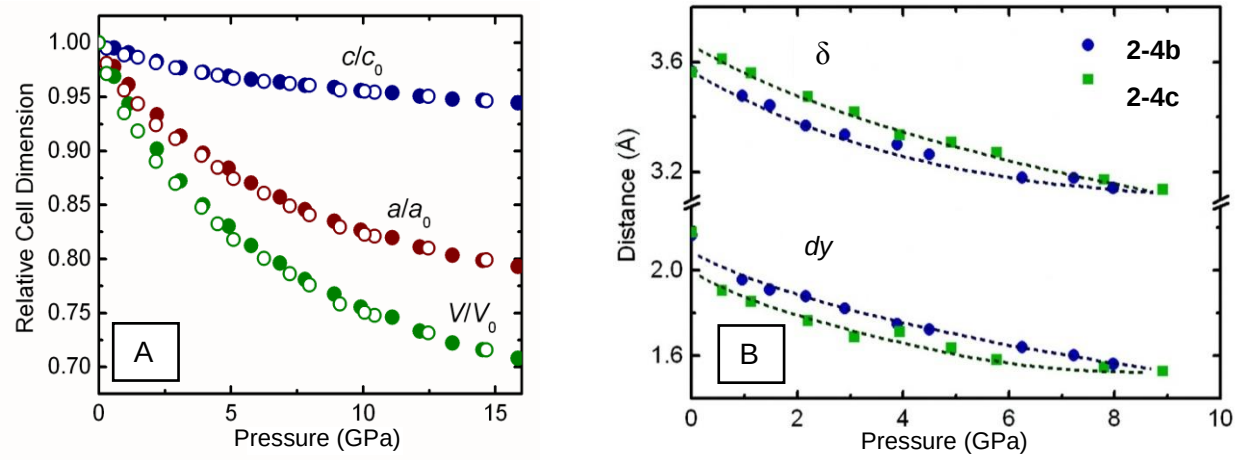

Figure 2.13 (a) Relative unit cell parameters of **2-4b** (open circles) and **2-4c** (closed circles), and (b) variations in the intermolecular metrics of **2-4b** and **2-4c** as a function of pressure.

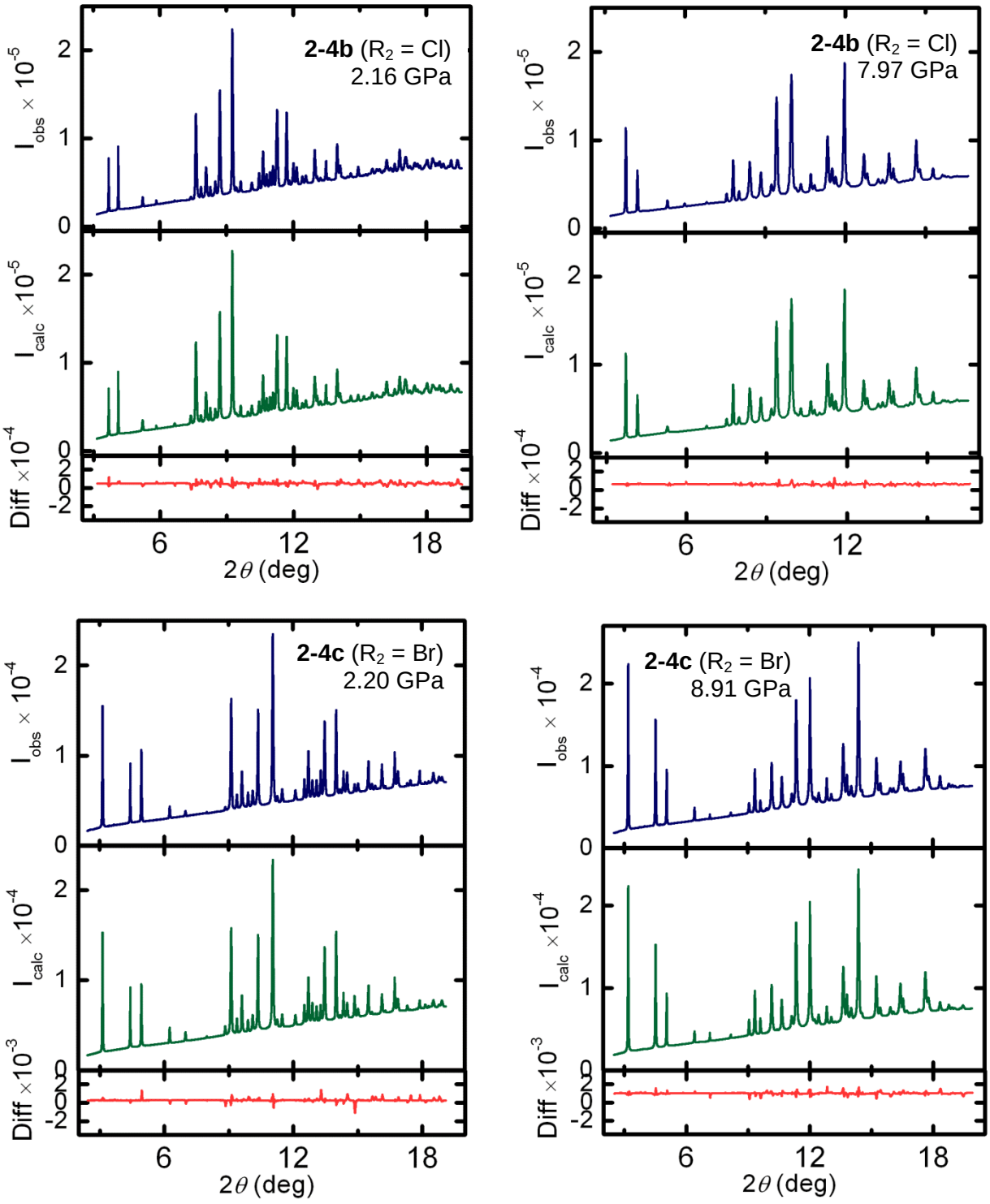

Figure 2.14 Representative plots of observed, calculated and difference powder patterns for **2-4b** and **2-4c** at low and high pressures.

Table 2.3 Crystal Data of **2-4b** as a Function of Pressure.

Press, GPa	0.96[a]	1.48[a]	2.16	2.90[a]	3.89[a]	4.50[a]	6.25	7.23	7.97
a, Å	16.09457(26)	16.07661(18)	15.96595(27)	15.90088(27)	15.83767(24)	15.78087(28)	15.63059(27)	15.72090(24)	15.61515(21)
c, Å	3.98958(8)	3.94232(6)	3.85717(8)	3.80246(8)	3.73814(7)	3.69090(8)	3.57744(8)	3.55860(7)	3.50758(6)
V, Å^3	1033.44(2)	1018.92(2)	983.24(3)	961.41(2)	937.64(2)	919.17(2)	874.02(3)	879.50(14)	855.26(2)
space group	$P\bar{4}2_1m$	$P\bar{4}2_1m$	$P\bar{4}2_1m$	$P\bar{4}2_1m$	$P\bar{4}2_1m$	$P\bar{4}2_1m$	$P\bar{4}2_1m$	$P\bar{4}2_1m$	$P\bar{4}2_1m$
Temp, K	293(2)	293(2)	293(2)	293(2)	293(2)	293(2)	293(2)	293(2)	293(2)
λ, Å	0.51446	0.51446	0.51446	0.51446	0.51446	0.51446	0.51446	0.51446	0.51446
Solution method	powder data	powder data	powder data	powder data	powder data	powder data	powder data	powder data	powder data
R_p	0.0164	0.0123	0.0158	0.0168	0.0120	0.0150	0.0176	0.0143	0.0117
R_{wp}	0.0313	0.0197	0.0244	0.0269	0.0196	0.0242	0.0261	0.0224	0.0184

Table 2.4 Crystal Data of **2-4c** as a Function of Pressure.

Press, GPa	0.58	1.13	2.20	3.08	3.94	4.91	5.77	7.80	8.91
a, Å	16.23481(16)	16.16020(20)	16.03132(20)	15.93675(16)	15.86977(16)	15.81103(17)	15.76088(15)	15.67329(19)	15.63466(14)
c, Å	4.08300(5)	4.01327(6)	3.89682(7)	3.81437(5)	3.74821(5)	3.69185(6)	3.63360(6)	3.52999(6)	3.48795(6)
V, Å^3	1076.15(2)	1048.07(2)	1001.50(2)	968.77(2)	943.99(2)	922.92(2)	902.61(1)	867.15(2)	852.60(2)
space group	$P\bar{4}2_1m$	$P\bar{4}2_1m$	$P\bar{4}2_1m$	$P\bar{4}2_1m$	$P\bar{4}2_1m$	$P\bar{4}2_1m$	$P\bar{4}2_1m$	$P\bar{4}2_1m$	$P\bar{4}2_1m$
Temp, K	293(2)	293(2)	293(2)	293(2)	293(2)	293(2)	293(2)	293(2)	293(2)
λ, Å	0.61795	0.61795	0.61795	0.61795	0.61795	0.61795	0.61795	0.61795	0.61795
Solution method	powder data	powder data	powder data	powder data	powder data	powder data	powder data	powder data	powder data
R_p	0.0119	0.0137	0.0128	0.0116	0.0109	0.0118	0.0111	0.0115	0.0104
R_{wp}	0.0204	0.0231	0.0237	0.0190	0.0178	0.0194	0.0182	0.0197	0.0169

2.4.2 High Pressure Magnetic Studies on 2-4b,c

We have explored the effect of physical pressure on the magnetic properties on **2-4b** and **2-4c** by means of AC magnetic susceptibility measurements (χ') performed over the pressure range 0–5 GPa under hydrostatic conditions using a piston cylinder cell (PCC) and a diamond anvil cell (DAC) in a SQUID magnetometer (Figure 2.15).[22] The initial results on **2-4b** indicate first an increase in the T_c, which reached a maximum value of 21 K near 0.9 GPa. Beyond this pressure T_c retreated, so that by 1.6 GPa its value was near 18 K. Similar results were obtained using the quasi-hydrostatic compression afforded by a DAC. The latter technique also allowed access to pressures above 1.6 GPa, and revealed a continued decrease in T_c to 16 K at 2 GPa, with little change thereafter to the limit of the experiment (4 GPa). The magnetic response also weakened significantly at higher pressures, suggesting partial collapse of the long range ferromagnetic network.[22] As illustrated in Figure 2.15, the dependence of T_c on pressure follows a similar profile for both **2-4b** and **2-4c**, although the increase in T_c is more gradual and the maximum value near 24 K, observed over a broad plateau between 2–4 GPa, is substantially higher for **2-4c**.

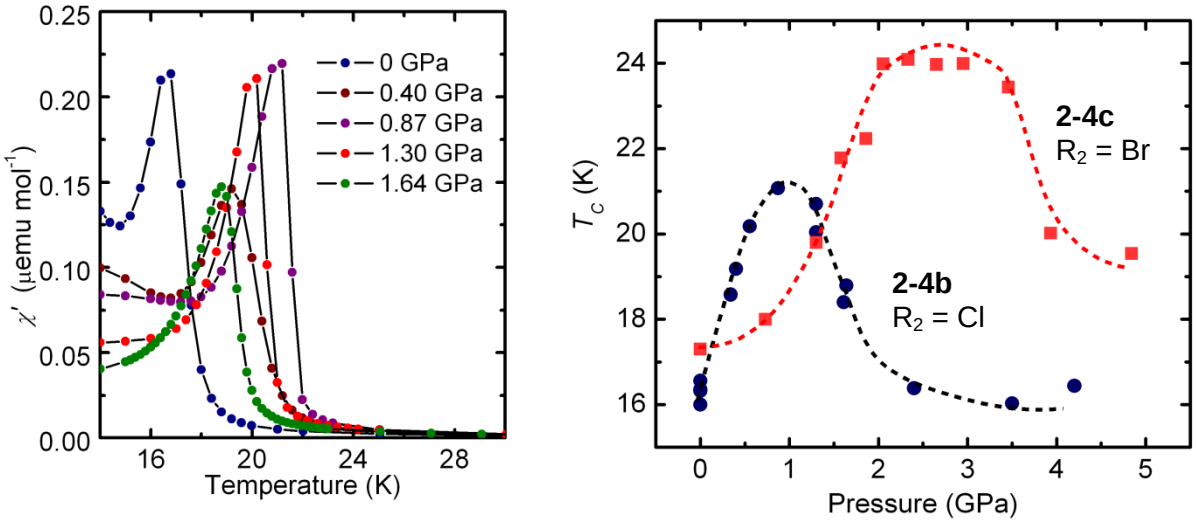

Figure 2.15 Plots of χ', the in-phase component of the AC susceptibility (at 1 kHz), *versus T* for **2-4b** at different pressures (left) and of T_c *versus* pressure for both **2-4b** and **2-4c** (right).

Pressure dependent magnetization (*M*) measurements as a function of field (*H*) were also performed on **2-4b** under hydrostatic conditions in a PCC. The coercive field H_c (1250 Oe) obtained from the *M versus H* hysteresis loop at 0 GPa and T = 2 K (Figure 2.16) undergoes little or no change up to 0.55 GPa. With further compression to 1.6 GPa, the saturation moment at 50 kOe remains essentially constant, but the hysteresis loop contracts and H_c drops to 880 Oe, consistent with the notion that the long-range ferromagnetic exchange pathways are compromised by pressure.[22]

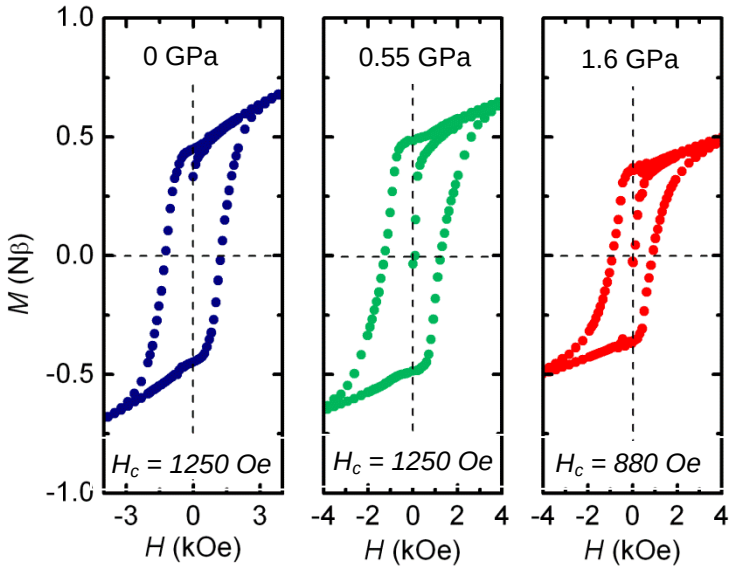

Figure 2.16 Magnetization *M* as a function of *H* under pressure at T = 2 K on **2-4b**.

2.4.3 High Pressure Conductivity Measurements on 2-4b,c

In order to explore the changes in both conductivity and activation energy with pressure we again turned to the use of DAC techniques. These measurements did not afford conductivity values directly, as it was not possible to obtain accurate measurements of sample dimensions, but we were nonetheless able to effect the conversion by calibrating the DAC resistance data with the conductivity values taken from the ambient pressure measurements. As may be seen in Figures 2.17 and 2.18 (left), the decrease in log σ with $1/T$ for **2-4b** is approximately linear from 300–200 K over the pressure range 0–5GPa, while for **2-4c** this pseudo-linear range extends out to about 8 GPa. Arrhenius fits to the data within these confines affords thermal activation energies E_{act} that decrease steadily with pressure (Figures 2.17

and 2.18, right), and extrapolation suggests that their values would reach 0 eV near 7 GPa for **2-4b** and near 9 GPa for **2-4c**. The theoretical and experimental challenge then becomes one of establishing whether the apparent elimination of a thermal barrier to activation heralds the onset of a metallic ground state.

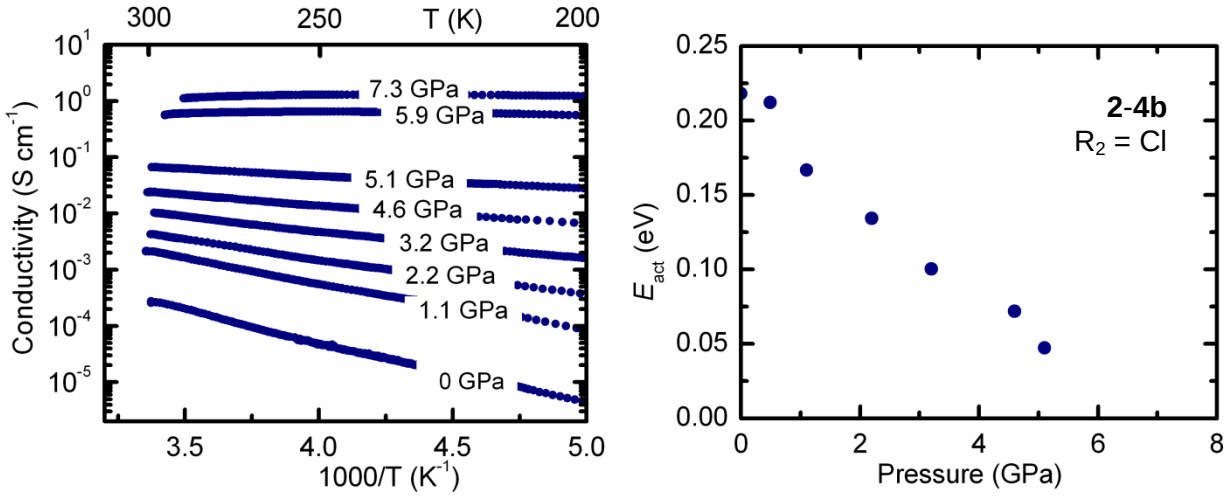

Figure 2.17 (Left) Log plots of σ *versus* 1/*T* for **2-4b** with increasing pressure. (Right) Thermal activation energy E_{act} as derived from the conductivity data measured above 200 K.

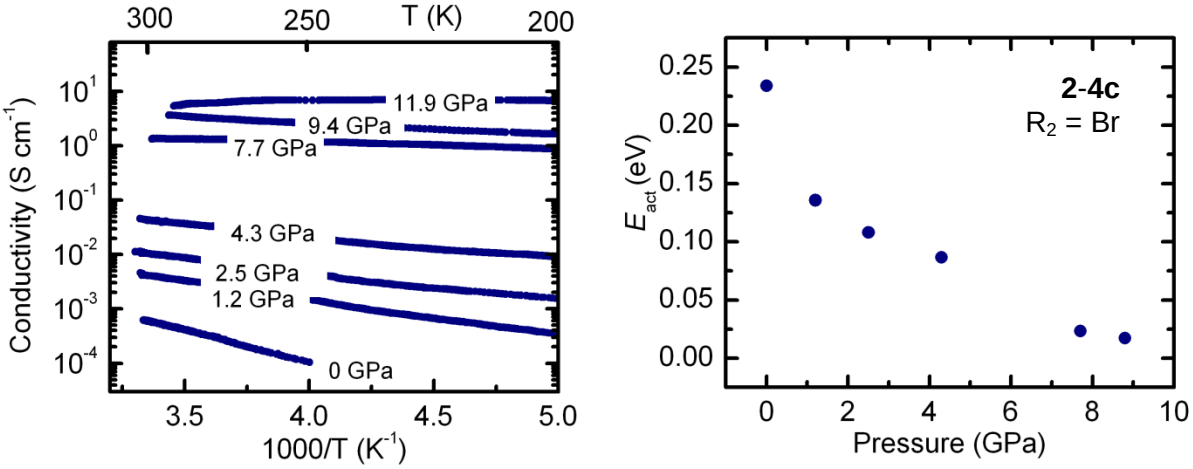

Figure 2.18 (Left) Log plots of σ *versus* 1/*T* for **2-4c** at increasing pressures. (Right) Thermal activation energy E_{act} as derived from the conductivity data measured above 200 K.

To explore this issue, we examined the conductivity of both compounds in the low temperature region. As may be seen in Figure 2.19, which expands the log σ *versus* 1/*T* plots for **2-4b** over the

temperature range 10−300 K, the conductivity drops rapidly with decreasing temperature for pressures ≤ 5.9 GPa, as would be expected for activated (nonmetallic) conductivity; for **2-4c** this range extends out to 7.7 GPa (not shown). By contrast, at more elevated pressures, that is ≥ 7.3 GPa for **2-4b** (and ≥ 9.4 GPa for **2-4c**), log σ does not tend to zero, but instead settles to a plateau value in the low temperature limit. This phenomenon, the apparent loss of thermal activation, can also be illustrated by means of a plot of the resistivity ρ against temperature in the critical pressure region where E_{act} approaches zero. As is apparent in Figure 2.19 (right), the resistivity rises asymptotically with decreasing temperature for all pressures ≤ 5.9 GPa for **2-4b**, as would be expected for a nonmetallic material in which all charge carriers are lost at 0 K. However, at pressures near and above 7.3 GPa, ρ appears to saturate as the temperature is decreased. In fact, below 25 K the rate of increase in ρ diminishes and extrapolation of the data indicates convergence to a finite value of ρ at T = 0 K, an observation consistent with the onset of a weakly metallic state, that is, one in which charge carriers are present at 0 K. A similar situation is found for **2-4c**, only the crossover from a formally nonmetallic to weakly metallic state occurs somewhere between 7.7 and 9.4 GPa.

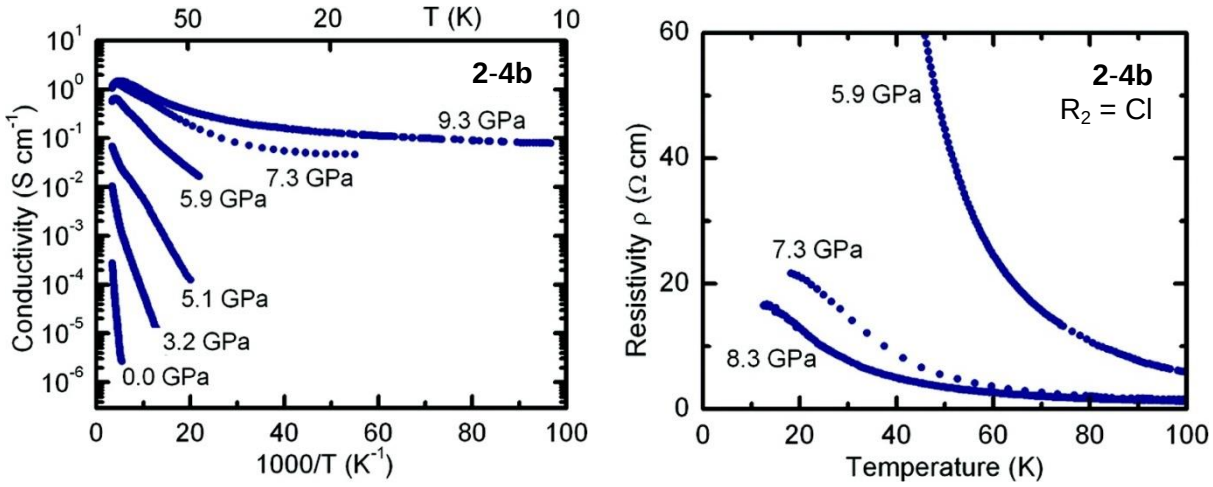

Figure 2.19 Log plots of σ *versus* 1/*T* for **2-4b** at different pressures, for *T* = 10−300 K (left). Plots of resistivity ρ *versus T* for **2-4b** at different pressures (right).

2.5 Discussion

Physical pressure has been widely used to explore the Mott insulator-to-metal transition (MIT) in metal oxides and chalcogenides[23] and also in organic charge transfer compounds such as the κ-phase salts of BEDT-TTF and Bechgaard salts $[TMTSF]_2[X]$ and more recently the hydrogen-bonded H_2Cat-EDT-TTF (κ-S) and H_2Cat-EDT-ST (κ-Se) internal charge transfer salts.[24] In these latter systems, where the Mott energy gap can be quite small, a rich array of phases, ranging from paramagnetic insulating to antiferromagnetic, metallic and even superconducting can be accessed, often with relatively mild (< 1 GPa) compression (see Chapter 1 for a sample phase diagram).[25] More recently, pressure has been utilized on a magnetic thiazyl radical, *p*-NCC_6F_4-DTDA, to enhance magnetic exchange and magneto-structural correlations have been established.[26] Under ambient conditions, this material orders as a canted antiferromagnet at 36 K. Upon the application of physical pressure, the structure contracts, magnetic exchange interactions strengthen, and concomitantly the T_c value increases steadily to 70 K at 1.6 GPa.

In this chapter, it has been shown that both chemical *and* physical pressure can be used to influence the magnetic properties in predictable ways for this family of tetragonal radicals. Within the bisthiaselenazolyl series of halogen substituted radicals **2-2a** – **2-2d**, ferromagnetic ordering has been found in all cases. The first three radicals in the series **2-2a,b,c** display a small, yet steady, increase in T_c with increasing size of the basal halogen atom. However, with the substitution of an iodine atom onto the heterocycle, the solid state structure expands more dramatically to make space for the largest halogen, and the magnetic response is concomitantly affected. Whereas the value of the plate-to-plate separation is $\delta \sim 3.5$ Å for **2-2a,b,c**, the value expands to 3.622 Å for **2-2d**. This change is not accompanied by an increase in the slippage of the radical with respect to the rest of the series.

The reason for the decrease in T_c of **2-2d** *versus* **2-2a,b,c** can be understood, at least qualitatively, in terms of the variations in the intrastack pairwise magnetic exchange energy $\boldsymbol{J}_\pi$, which arises when the

SOMO-SOMO interaction between adjacent radicals moves through a region of orthogonal overlap. These ideas, which we developed using a broken symmetry DFT-based approach[27] to estimate the magnitude of J_π within a 1D array of bisthiaselenazolyl radicals **2-2** (R_1 = R_2 = H), are illustrated in Figure 2.20 and discussed in more detail in Chapter 1. Evidently, when *dx* = 0, the value of J_π is ferromagnetic (> 0 cm^{-1}) over a relatively small range of π-stack slippage, expressed in terms of *dy*, one which corresponds to a region where the EHT bandwidth *W* moves through a null point (near *dy* = 1.8 Å). When the value of δ increases, the strength of intrastack exchange decreases and, as a result, the height of the ferromagnetic "hill" decreases. Therefore, the increase in δ > 3.5 Å for **2-2d**, and hence the decrease in orbital overlap between the SOMOs, leads to a diminished value of both J_π and T_c for this compound.

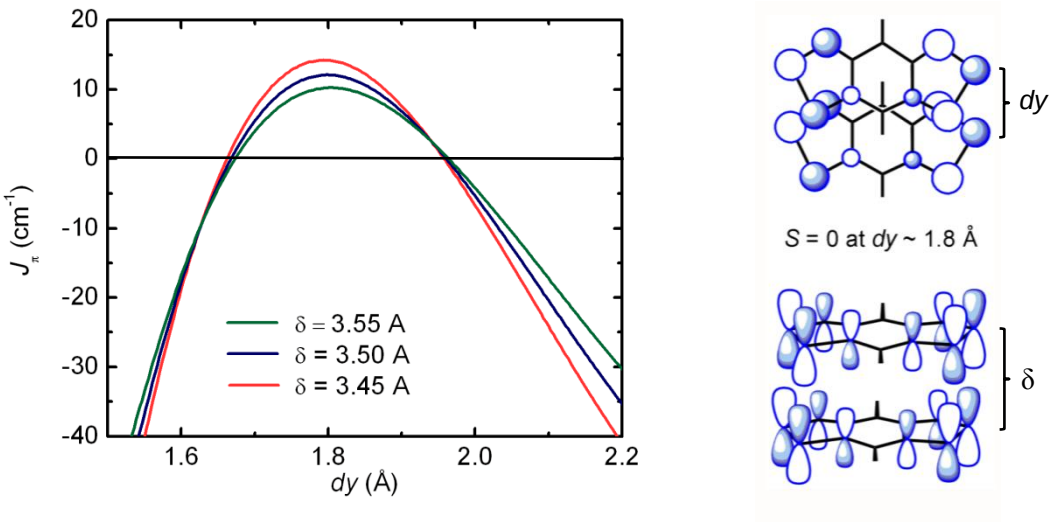

Figure 2.20 DFT estimated J_π values for a 1D π-stack of a model radical **2-4** (R_1 = R_2 = H) as a function of *dy* with δ = 3.45, 3.50 and 3.55 Å (left). Also shown (right) are cartoons of the SOMO-SOMO overlap *S* at *dy* ~ 1.8 Å viewed from above (top) and side (below).

Further incorporation of selenium into the bisthiaselenazolyl ring system has, in the past, led to enhanced conductivity and magnetic ordering. This knowledge led to the pursuit of radicals **2-4a** – **2-4d** to complete the family of halogen substituted bisdiselenazolyl radicals. Synthetically, the challenge was too great for both **2-4a** and **2-4d** and various attempts at generating the radicals have failed. However,

we have fully characterized the two best ferromagnets we have on hand, and examined their magneto-structural response to pressure. In this chapter it has been shown that metallization in **2-4b** and **2-4c** requires the application of greater pressures than the aforementioned κ-phase charge transfer salts, in the region of 7–9 GPa, but *en route* their magnetic properties undergo a series of changes. For both compounds the initial pressure-induced decrease in the slippage of the π-stacks leads to an increase in T_c, one more pronounced for **2-4c**, which displays a maximum and, to our knowledge, record value of T_c = 24 K at 2 GPa. With further compression, however, T_c retreats, so that by 5 GPa the magnetic response of the both materials is completely quenched.

To extend the use of the structure-property relationships, we have performed a series of DFT broken symmetry calculations at the UB3LYP/6-31G(d,p) level in order to estimate variations in the magnetic exchange interaction $\boldsymbol{J}_\pi$ between neighboring radicals along the π-stacks of **2-4b** as a function of pressure, using experimentally obtained crystallographic coordinates. The results, shown in Figure 2.21 (right), indicate an initial increase in $\boldsymbol{J}_\pi$ with pressure, that is, a stronger ferromagnetic interaction. This change, which can be related to a loss of overlap between adjacent SOMOs occasioned by slippage of the π-stacks (a decrease in the value of *dy*), is consistent with the observed increase in T_c with pressure (Figure 2.21, left). However, with continued compression, the slippage of the π-stacks moves past the position of minimum (orthogonal) overlap, and $\boldsymbol{J}_\pi$ begins to decrease, as does the experimental T_c. While the maxima in the $\boldsymbol{J}_\pi$ and T_c plots as a function of pressure do not coincide, the qualitative correspondence between the two profiles is appealing and suggests that physical pressure, like chemical pressure,[8] can be used to alter the degree of π-stack slippage in radicals of this type.

Orbital overlap-based arguments for correlating structure with magnetic property, which mesh so appealingly with the classical orbital orthogonality conditions for ferromagnetic exchange provided by Kahn,[28] also afford a qualitative insight into the changes in conductivity that occur with continued compression. Thus, comparison of the changes in *dy* in **2-4a** and **2-4b** induced with increased pressurization with the estimated 1D-bandwidths *W* shown in Figure 1.27 suggests that pressures

beyond 5 GPa should lead to a significant enhancement in *W*. This increase, when coupled with the band broadening induced by a compression of the π-stacks, *i.e.*, a reduction in the plate-to-plate separation δ, suggests that the loss of ferromagnetic ordering, be it followed or not by the onset of AFM ordering, should eventually lead to metallization. Experimentally, we observe the onset of metallization at about 7 GPa for **2-4a** and 9 GPa for **2-4b** for $T > 200$ K, which we attribute to the transition to a "bad metal" state, characterized typically by an anomalously high resistivity for a metallic conductor ($d\sigma/dT < 0$). The possibility that this material might exhibit a phase transition to a highly conducting Peierls distorted (π-dimerized) state is refuted by the fact that a low temperature (~ 7.3 K) and high pressure (~ 9.01 GPa) structure has been solved[29] and shows *no* evidence for a charge density wave (CDW) driven distortion.

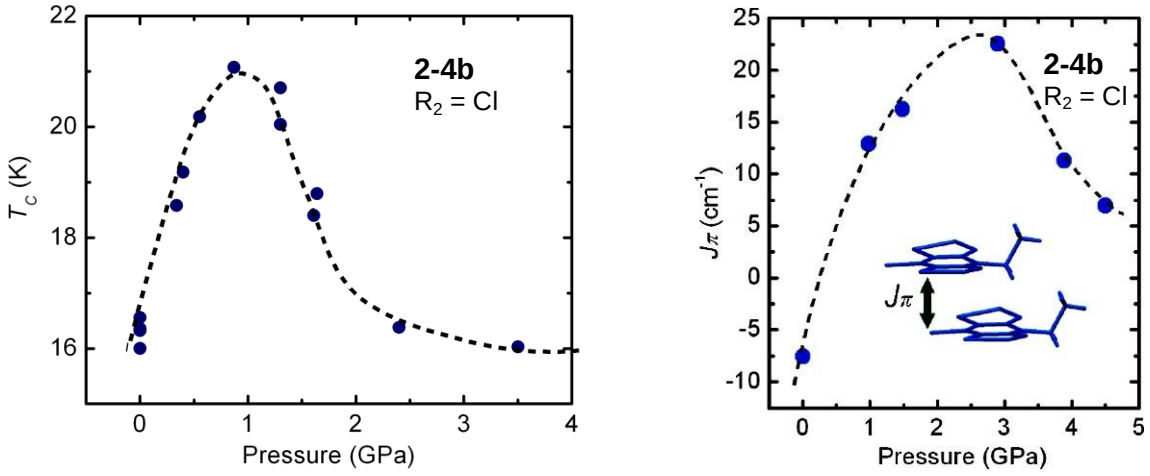

Figure 2.21 Plot of the T_c values obtained for **2-4b** under increasing pressure (left) and DFT calculated J_π values for **2-4b** as a function of crystal structure geometry at increasing pressure (right).

2.6 Summary

The magnetic and charge transport properties of radicals **2-4b** and **2-4c** are unique. At ambient pressure both materials are bulk ferromagnets with the highest T_c values found outside of transition-metal based materials, display coercive fields that are several orders of magnitude greater than other

radical ferromagnets, and also possess appreciable, albeit activated, conductivity. The high pressure structural measurements presented in this chapter provide a clear view of the response of the crystal structure of both materials to physical pressure and have allowed for the development of a qualitative understanding of the evolution of their solid state electronic and magnetic properties with compression.

At ambient pressure, slippage of the radical π-stacks of all six radicals **2-2a,b,c,d** and **2-4b,c** produces almost perfectly orthogonal overlap between adjacent SOMOs. The consequent FM exchange interactions along the π-stacks, when combined with FM exchange interactions lateral to the π-stacks, give rise to ferromagnetically ordered systems. Changes in slippage and plate-to-plate separation of the π-stacks occasioned by chemical changes such as halogen substitution lead to minor changes in the magnetic response, except when the halogen size exceeds a threshold value accompanied by a larger structural expansion.

In the case of the two best ferromagnets, **2-4b,c**, compression and consequent plate slippage, first enhances and then destroys the orthogonal overlap condition, so that exchange interactions along the π-stacks become strongly antiferromagnetic. As a result ferromagnetic ordering is lost, and possibly replaced by an AFM ordered state at intermediate pressures. Continued pressurization eventually generates sufficient bandwidth *W* to overcome the onsite Coulomb repulsion energy *U*. Metallization for **2-4b** and **2-4c** at pressures near 7 and 9 GPa, respectively, represent, one of few instances for the observation of a pressure-induced MIT for a neutral radical (f = ½) material. We have since observed that further chemical modifications of related radicals have allowed for the metallization condition ($W > U$) to be met at even lower pressures, such as in **1-57** (Chapter 1). The possibility that superconductivity may be found in these kinds of materials, with or without the need for applied pressure, provides an additional incentive for further exploration.

2.7 Experimental Section

General methods and procedures are described in Appendix A.

Preparation of *N*-Ethyl-2,6-dichloro-4-iodopyridinium Trifluoromethanesulfonate, 2-7. Ethyl triflate (3.07 mL, 23.8 mmol) was added to 2,6-dichloro-4-iodopyridine (5.00 g, 18.3 mmol) in 10 mL of DCE and the reaction mixture was stirred for 16 h at 80 ºC to afford a heavy white precipitate. Diethyl ether (35 mL) was added to fully precipitate the product and the entire mixture was kept at –20 ºC for 1 hour. The product was collected on a fine (E porosity) glass frit and recrystallized from hot DCE; yield, 7.85 g (17.4 mmol, 95%); mp, 152 - 154 ºC. IR: 3054 (s), 1578 (vs), 1530 (vs), 1479 (m), 1347 (w), 1260 (vs), 1226 (s), 1148 (vs), 1110 (m), 1093 (m), 1029 (vs), 975 (w), 890 (w), 866 (m), 839 (s), 803 (s), 637 (s), 574 (m), 550 (w), 516 (m), 433 (w) cm^{-1}. ^1H NMR (δ, CD_3CN): 8.52 (s, 2H), 4.82 (*q*, 2H, *J* = 7.29 Hz), 1.49 (*t*, 3H, *J* = 7.29 Hz). Anal. Calcd for $C_8H_7Cl_2F_3INO_3S$: C, 21.26; H, 1.56; N, 3.10. Found: C, 21.46; H, 1.66; N, 3.10.

Preparation of *N*-Ethyl-2,6-diamino-4-iodopyridinium Trifluoromethanesulfonate, 2-8. Solid **2-7** (4.35 g, 9.62 mmol) was dissolved in 100 mL MeCN, through which NH_3(g) was bubbled for 15 min. The mixture was sealed in a glass pressure vessel and heated at 80 ºC for 16h. The vessel was then vented and the solution refluxed at 100 ºC for 2h to release excess ammonia. After cooling to room temperature, NH_4Cl was filtered off on a Büchner funnel and the filtrate evaporated. The resulting yellow crystalline solid was recrystallized from 1:3 MeCN/DCE to afford colourless needles; yield, 2.30 g (5.57 mmol, 58%); mp, 236 – 239 ºC. IR: 3416 (s), 3355 (s), 3242 (s), 3089 (w), 1677 (s), 1645 (s), 1615 (s), 1564 (s), 1520 (w), 1489 (m), 1323 (w), 1263 (vs), 1225 (s), 1178 (s), 1088 (w), 1030 (s), 960 (w), 855 (m), 801 (s), 762 (w), 731 (m), 639 (s), 586 (m), 513 (m) cm^{-1}. ^1H NMR (δ, CD_3CN): 6.55 (s, 2H), 3.87 (*q*, 2H, *J* = 7.37 Hz), 1.29 (*t*, 3H, *J* = 7.37 Hz). Anal. Calcd for $C_8H_{11}F_3IN_3O_3S$: C, 23.26; H, 2.68; N, 10.17. Found: C, 23.50; H, 2.88; N, 10.29. **NOTE:** This recrystallization was problematic due to the very high solubility of the product and a strange insoluble yellow powder which was sometimes soluble and other times not. Removal of this mystery substance by many hot filtrations resulted in a clean baseline in the IR and the absence of a broad absorbance in the 3500 cm^{-1} region. All

of the filtrates were saved and then recovered by recrystallization from HOAc and then MeCN/DCE once again. The yield is low but most of the product was salvaged over time.

Preparation of 8-Iodo-4-ethyl-4H-bis[1,2,3]dithiazolo[4,5-*b*:5',4'-*e*]pyridin-2-ium Chloride, [2-1][Cl] (R_1 = Et, R_2 = I). Triethylamine (2.94 g, 29.1 mmol) was added to a solution of **2-8** (1.50 g, 3.63 mmol) in 150 mL MeCN. The mixture was cooled to -40 ºC on a $CO_{2(s)}$/$EtOH_{(l)}$ bath and to it a solution of S_2Cl_2 (1.96 g, 14.5 mmol) was added dropwise over 1h 10min (1 drop / 4 sec). The cold bath was removed and the mixture allowed to warm up to room temperature over 2h. The resulting fine, dark blue precipitate was collected on a large, fine (E porosity) glass frit and backwashed with MeCN (3 x 60 mL), hot DCE (2 x 90 mL), and DCM (1 x 60 mL); yield, 1.80 g. This was used in the next step without further purification.

Preparation of 8-Iodo-4-ethyl-4H-bis[1,2,3]dithiazolo[4,5-*b*:5',4'-*e*]pyridin-2-ium Trifluoro-methanesulfonate, [2-1][OTf] (R_1 = Et, R_2 = I). Crude [**2-2d**][Cl] (1.74 g, 4.13 mmol) and AgOTf (1.27 g, 4.94 mmol) were refluxed in 230 mL MeCN for 20 min. The mixture was cooled to room temperature and AgCl was filtered off on a Büchner funnel. To the blue solution, 115 mL of chlorobenzene was added and the solvent was slowly removed on a rotovap until the volume was ~ 100 mL. The resulting blue/red sparkly precipitate was collected on a glass frit and washed with DCM; yield 1.73 g (3.23 mmol, 89% overall). The crude material was recrystallized once from hot HOAc (3.3 g from 100 mL). mp, dec > 255 ºC. IR: 1518 (m), 1480 (m), 1274 (s), 1238 (vs), 1184 (m), 1172 (m), 1080 (w), 1025 (s), 1003 (w), 886 (w), 788 (m), 752 (s), 719 (m), 667 (m), 638 (s), 580 (w), 574 (w), 534 (w), 516 (w), 475 (m) cm^{-1}. Anal Calcd for $C_8H_5F_3IN_3O_3S_5$: C, 17.95; H, 0.94; N, 7.85. Found: C, 18.12; H, 0.79; N, 7.69. **NOTE:** The amount of S_2Cl_2 and NEt_3, along with the rate of addition is *critical* to the success of this reaction. A careless reaction results in chlorination at the 4-position of the pyridine ring.

Preparation of 8-Iodo-4-ethyl-4H-bis[1,2,3]thiaselenazolo[4,5-*b*:5',4'-*e*]pyridin-2-ium Trifluoro-methanesulfonate, [2-2d][OTf] (R_1 = Et, R_2 = I). The salt [**2-1**][OTf] (R_1 = Et, R_2 = I) (1.07 g, 2.00 mmol) and finely ground selenium dioxide (0.666 g, 6.00 mmol) were added to a large glass pressure vessel along with 80 mL MeCN, and the mixture stirred and heated in an oil bath at 110 ºC for 68 h.

The reaction was continued until analysis of the mixture by ESI mass spectrometry showed complete and specific formation of [**2-2d**]+. The flask was cooled to room temperature, and the dark green solution filtered through a glass Büchner funnel to remove a small amount of black precipitate. To the filtrate was added 50 mL of chlorobenzene and the entire mixture was rotovapped until the volume reached ~ 40 mL. The resulting crystalline solid was filtered and washed with DCM and dried in air. The product was recrystallized three times from MeCN as red plates; yield 578 mg (0.919 mmol, 46 %). mp, dec > 260 ºC. IR: 1499 (m), 1426 (s), 1360 (s), 1280 (s), 1242 (s), 1222 (m), 1170 (w), 1156 (s), 1086 (w), 1067 (w), 1025 (s), 996 (w), 773 (w), 757 (w), 731 (s), 721 (w), 636 (s), 595 (m), 572 (w), 516 (w), 470 (w) cm^{-1}. Anal. calcd for $C_8H_5F_3IN_3O_3S_3Se_2$: C, 15.27; H, 0.80; N, 6.68. Found: C, 15.40; H, 0.69; N, 6.83.

Preparation of 8-Iodo-4-ethyl-4H-bis[1,2,3]thiaselenazolo[4,5-*b*:5',4'-*e*]pyridin-2-yl, 2-2d (R_1 = Et, R_2 = I). Degassed solutions (4 freeze-pump-thaw cycles) of OMFc (70 mg, 2.35 mmol) in 50 mL MeCN and [**2-2d**][OTf] (140 mg, 2.25 mmol) in 150 mL MeCN were combined and after 20 mins the gold-brown precipitate of **2-2d** was filtered off and washed with 6 x 15 mL MeCN, yield 104 mg (2.16 mmol, 96 %), dec > 120 ºC. IR: 1401 (w), 1351 (w), 1314 (w), 1224 (m), 1168 (w), 1061 (w), 997 (w), 885 (w), 837 (w), 719 (m), 692 (m), 564 (w), 503 (w), 448 (w) cm^{-1}. Anal. Calcd for $C_7H_5IN_3S_2Se_2$: C, 1751; H, 1.05; N, 8.75. Found: C, 17.70; H, 1.01; N, 9.04.

Preparation of *N*-Ethyl-2,4,6-trifluoropyridinium Trifluoromethanesulfonate, 2-5. A mixture of ethyl triflate (2.74 mL, 24.0 mmol) and 2,4,6-trifluoropyridine (2.66, 20.0 mmol) was stirred for 16 h at 60 ºC to afford a heavy white precipitate. DCE (10 mL) and diethyl ether (35 mL) was added and the product **2-5** was filtered off, washed with diethyl ether, and dried in *vacuo*. Yield, 5.73 g (18.4 mmol, 92%); mp 122-124 ºC. IR: 3063 (s), 1673 (vs), 1600 (vs), 1538 (m), 1508 (s), 1424 (w), 1271 (vs), 1228 (s), 1208 (m), 1168 (vs), 1095 (w), 1033 (vs), 881 (m), 759 (w), 639 (vs), 575 (w), 518 (s), 410 (w) cm^{-1}. ^{1}H NMR (δ, CD_3CN): 7.65 (*dd*, 2H, *J* = 6.89, 2.59 Hz), 4.57 (*qt*, 2H, *J* = 7.35, 2.72 Hz), 1.51 (*t*, 3H, *J* = 7.35 Hz). ^{19}F NMR (*d*, CD_3CN): 69.7 (*t*, 1F, *J* = 30 Hz), 77.7 (*d*, 2F, *J* = 30 ppm). Anal. Calcd for $C_8H_7F_6NO_3S$: C, 30.88; H, 2.27; N, 4.50. Found: C, 30.83; H, 2.36; N, 4.36.

Preparation of *N*-Ethyl-2,6-diamino-4-fluoropyridinium Trifluoromethanesulfonate, 2-6. Anhydrous ammonia gas was passed over a solution of **2-5** (4.70 g, 0.0151 mmol) in 50 mL MeCN at 0 ºC for 5-10 min. The yellow mixture was stirred at room temperature for 30 min, and the resulting white precipitate of NH_4F was filtered off. Evaporation of the solvent from the filtrate afforded a white solid that was recrystallized from a 1:5 mixture of MeCN/DCE as off-white flakes of **2-6**. Yield, 3.34 g (0.0109 mmol, 72 %); mp 132-134 ºC. IR: 3419 (s), 3361 (s), 3248 (s), 3116 (w), 1672 (s), 1649 (s), 1604 (s), 1548 (w), 1517 (s), 1448 (m), 1339 (m), 1280 (s), 1257 (s), 1226 (s), 1180 (s), 1166 (s), 1091 (m), 1069 (w), 1032 (s), 1015 (m), 811 (s), 793 (w), 761 (w), 642 (s), 598 (w), 580 (w), 573 (w), 515 (m) cm^{-1}. ^1H NMR (δ, CD_3CN): 6.38 (*s*, 4H), 5.96 (*d*, 2H, *J* = 9.63 Hz), 3.91 (*q*, 2H, *J* = 7.36 Hz), 1.31 (*t*, 3H, *J* = 7.36 Hz). Anal. Calcd for $C_8H_{11}F_4N_3O_3S$: C, 31.48; H, 3.63; N, 13.77. Found: C, 31.83; H, 3.40; N, 13.58.

Preparation of 8-Fluoro-4-ethyl-4*H*-bis[1,2,3]dithiazolo[4,5-*b*:5',4'-*e*]pyridin-2-ium Trifluoromethanesulfonate, [2-1a][OTf] (R_1 = Et, R_2 = F). A solution of sulfur monochloride (9.20 g, 0.0681 mol) in 20 mL MeCN was added to a solution of **2-6** (5.22 g, 0.0171 mol) in 90 mL MeCN. The solution was heated at a gentle reflux for 90 mins and the resulting deep blue solution was cooled to room temperature and then at –20 ºC for 2 h. The red, microcrystalline precipitate of crude [**2-1a**][OTf] was filtered off, washed with 4 × 40 mL hot DCE, 20 mL CS_2 and 20 mL DCM, after which the product was dried *in vacuo*, yield 5.52 g (0.0129 mol, 75 %). Red blocks were isolated by recrystallization from MeCN, mp 291-293 ºC IR: 1512 (s), 1461 (s), 1279 (s), 1239 (s), 1224 (w), 1197 (w), 1121 (w), 1025 (s), 856 (w), 790 (m), 786 (m), 716 (w), 678 (w), 671 (w), 650 (w), 635 (m), 516 (w), 479 (m), 472 (m). Anal. Calcd for $C_8H_5F_4N_3O_3S_5$: C, 22.48; H, 1.18; N, 9.83. Found: C, 22.60; H, 1.23; N, 9.66.

Preparation of 8-Fluoro-4-ethyl-4*H*-bis[1,2,3]thiaselenazolo[4,5-*b*:5',4'-*e*]pyridin-2-ium Trifluoromethanesulfonate, [2-2a][OTf] (R_1 = Et, R_2 = F). Compound [**2-1a**][OTf] (855 mg, 2.00 mmol) and finely ground selenium dioxide (0.666 g, 6.00 mmol) were added to a large glass pressure vessel along with 80 mL of MeCN, and the mixture was stirred and heated in an oil bath at 110 °C for 48−72 h. The reaction was continued until analysis of the mixture by ESI-MS showed complete and specific

formation of [**2-2a**]$^+$. The flask was cooled slightly and then filtered warm. The solution was then concentrated to 30 mL, 30 mL of DCE was added and the mixture was cooled to −20 °C overnight. Black powder of crude [**2-2a**][OTf] was filtered off, dissolved in 150 mL MeCN and hot filtered. To the filtrate, 50 mL of PhCl was added and the whole mixture was slowly rotovapped down to ~ 40 mL to leave a dark, red microcrystalline material. These crystals were filtered off, washed with DCM, and dried in air. The product was recrystallized from MeCN red needles of pure [**2-2a**][OTf], yield 510 mg (0.978 mmol, 49 %). IR: 1455 (s), 1362 (m), 1278 (s), 1234 (vs), 1189 (w), 1174 (m), 1163 (m), 1114 (w), 1074 (w), 1025 (s), 864 (w), 799 (w), 776 (w), 762 (m), 718 (w), 635 (s), 598 (s), 575 (w), 516 (w). Anal. Calcd for $C_8H_5F_4N_3O_3S_3Se_2$: C, 18.43; H, 0.97; N, 8.06. Found: C, 19.30; H, 0.93; N, 8.77.

Preparation of 8-Fluoro-4-ethyl-4*H*-bis[1,2,3]thiaselenazolo[4,5-*b*:5',4'-*e*]pyridin-2-ium Tetrafluoroborate, [2-2a][BF$_4$] (R_1 = Et, R_2 = F). The triflate salt [**2-2a**][OTf] (765 mg, 1.47 mmol) was dissolved in 200 mL refluxing MeCN and a small amount of black insoluble material was filtered off. To the remaining solution, $NBzEt_3Cl$ (a source of chloride ion, 501 mg, 2.20 mmol) was added and a purple precipitate formed immediately. The solid was filtered off, washed 2 x 30 mL MeCN and dried in *vacuo*, yield 598 mg. This material was then boiled in 150 mL MeCN with $AgBF_4$ (343 mg, 1.76 mmol) to generate a dark green solution. The white precipitate (AgCl) was filtered off, and the solution concentrated to 12 mL. The product was recrystallized from MeCN as red crystalline blocks, yield 540 mg (1.18 mmol, 71 % overall), dec > 295 ºC. IR: 1505 (vs), 1495 (vs), 1456 (vs), 1286 (w), 1112 (s), 1075 (s), 863 (w), 794 (m), 779 (w), 760 (s), 719 (m), 628 (w), 599 (s), 522 (w) cm^{-1}. Anal. Calcd for $C_7H_5BF_5N_3S_2Se_2$: C, 18.32; H, 1.10; N, 9.15. Found: C, 18.51; H, 1.30; N, 9.37.

Preparation of 8-Fluoro-4-ethyl-4*H*-bis[1,2,3]thiaselenazolo[4,5-*b*:5',4'-*e*]pyridin-2-yl, 2-2a (R_1 = Et, R_2 = F). Degassed solutions (3 freeze-pump-thaw cycles) of DMFc (212 mg, 0.650 mmol) in 132 mL MeCN and [**2-2a**][BF_4] (284 mg, 0.619 mmol) in 95 mL MeCN were combined and after 20 mins the gold-brown precipitate of **2-2a** was filtered off and washed with 5 x 15 mL MeCN, yield 203 mg (0.545 mmol, 88 %), dec > 120 ºC. IR: 1438 (s), 1428 (m), 1328 (m), 1245 (s), 1181 (w), 1096 (m), 1065 (m), 987 (w), 840 (m), 785 (m), 752 (m), 740 (m), 694 (m), 612 (w), 579 (m), 480 (m) cm^{-1}. Anal. Calcd for $C_7H_5FN_3S_2Se_2$: C, 22.59; H, 1.35; N, 11.29. Found: C, 22.66; H, 1.14; N, 11.34.

Ambient Pressure Powder X-ray Measurements. X-ray diffraction data were collected on a powder diffractometer with a position sensitive detector (INEL) using Cu $K\alpha_1$ radiation (λ = 1.5406 Å). The total 2θ range was 2–112º, measured in steps of 0.029º. The powder diffraction patterns for **2-2a** and **2-2d** were indexed using DASH 3.1, from which it was evident that the $P\bar{4}2_1m$ space group of the related structures **2-2b,c** was a suitable starting point. For **2-2a**, we started with the molecular coordinates for **2-2b**, with the Cl atom replaced by an F and the C-F bond length adjusted and then modeled the crystal structure using DASH 3.1. For **2-2d**, the starting point was molecular coordinates of **2-2c**, with Br replaced by I and the corresponding C-I bond length adjusted. Again, the crystal structure was modeled using DASH 3.1. During the initial Rietveld refinement in DASH a rigid-body constraint was maintained. The powder solutions from DASH were refined by Rietveld[16] methods using the GSAS[16] program package. Final Rietveld indices R_p and R_{wp} are listed in Table 2.1. Atomic positions were not further refined and, as a result, standard deviations for atomic coordinates are not available.

High Pressure X-ray Measurements. High pressure X-ray diffraction experiments on **2-4b** and **2-4c** were performed at BLX10U, SPring-8, using synchrotron radiation (λ = 0.51446 Å) and a powdered sample mounted in a DAC, with helium as the pressure transmitting medium. The diffraction data were collected at room temperature and as a function of *increasing* pressure. A series of data sets (from 0–15 GPa) were indexed with XRDA[30] and the cell parameters later refined using DICVOL,[31] as provided in DASH 3.01.[14] It was evident that both compounds **2-4b** and **2-4c** at all pressures were isomorphous with the ambient pressure structures, and the space group $P\bar{4}2_1m$ was selected. Starting with the molecular coordinates for **2-4b** taken from the 100 K, ambient pressure data set,[19b] and those of **2-4c** taken from the ambient temperature and pressure data set described here, as the initial models, the structures were solved and refined using DASH. The powder solutions from DASH were refined by Rietveld[16] methods using the GSAS[16] program package. Final Rietveld indices R_p and R_{wp} are listed in Table 2.3 and 2.4. Atomic positions were not further refined and, as a result, standard deviations for atomic coordinates are not available. Isotropic thermal parameters were only refined for the selenium atoms, where possible. Data from 2θ = 3–20° were refined with fixed atomic positions and isotropic thermal parameters with an assigned value of 0.025. Measurements were taken by Drs. J. S. Tse and S. Desgreniers from the University of Saskatchewan and the University of Ottawa, respectively.

High Pressure Magnetic Measurements. Piston cylinder cell (PCC) AC magnetic susceptibility measurements on samples of **2-4b** were performed over the pressure range 0–1.6 GPa in a SQUID magnetometer. The crystals were mixed with a pressure transmitting medium, Apiezon J oil, and held with a piece of lead as the manometer. Pressure calibration was performed using the superconducting transition of lead. Diamond anvil cell (DAC) AC magnetic measurements were carried on both **2-4b** and **2-4c** using techniques described in Reference 32. Measurements were taken by Dr. M. Mito at the Faculty of Engineering, Kyushu Institute of Technology, Kitakyushu, Japan.

High Pressure Conductivity Measurements. The variation of the electrical resistance of **2-4a** and **2-4b** with pressure was investigated by the four-probe technique in a diamond anvil cell. Pressure was generated by a pair of diamonds with a 600 μm diameter culet. A sample hole of 300 μm diameter was drilled in the gasket after its thickness was reduced from 250 to 30 μm by pre-indentation. It was then covered with a thin layer of cubic boron nitride BN for electrical insulation between the gasket and the electrodes. Gold wire of 18 μm diameter was used as electrode leads. The pressure was determined by the ruby fluorescence method at room temperature before and after each cooling cycle. Raw resistance measurements were converted into conductivity values by calibration with the ambient pressure measurements. Measurements were taken by S. Zhang, Q. Liu, and Dr. C. Jin, from the Institute of Physics at the Chinese Academy of Sciences in Beijing.

Chapter 3

Structural Changes under Pressure of Isostructural Hypervalent σ-Dimers

3.1 Introduction

In the previous chapter, a thorough investigation into the effect of halogen substituent replacement on bisthiaselenazolyls **3-2** was presented, where R_1 = Et, in addition to high pressure studies on two of our best ferromagnetically ordered materials. The present chapter will focus on related materials that have been subject to a small modification with respect to the aforementioned radicals – the R_2 substituent is solely a fluorine atom and R_1 = Me. This seemingly minor change leads to an entirely different architecture at the molecular level as well as in the solid state, where bisthiaselenazolyl [**3-2a**]$_2$ and its sulfur counterpart [**3-1a**]$_2$ crystallize as 4-center 6-electron (4c–6e) σ-dimers (Chart 3.1).

Chart 3.1

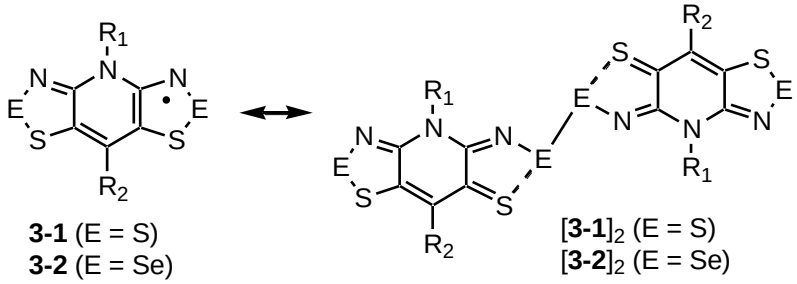

3-1 (E = S)
3-2 (E = Se)

[**3-1**]$_2$ (E = S)
[**3-2**]$_2$ (E = Se)

	E	R_1	R_2
α-**3-1a**	S	Me	F
β-[**3-1a**]$_2$	S	Me	F
[**3-2a**]$_2$	Se	Me	F
[**3-2b**]$_2$	Se	Me	H

When dimers [**3-2**]$_2$ (R_1 = Me, Et; R_2 = H) were first isolated in 2005,[1] these compounds represented the first example of heterocyclic selenazyl radicals to associate in the solid state through hypervalent 4c–6e σ-bonds.[2] While dimerization of selenazyl radicals is ubiquitous, association usually takes place *via* π-π interactions, as was discussed in Chapter 1.[3,4] The radical spins were nonetheless quenched, and the resulting closed shell molecules displayed transport properties expected for small band gap semiconductors, with room temperature conductivity σ(300 K) near 10^{-6} S·cm^{-1}. However, with relatively mild compression (to 5 GPa), the value of σ(300 K) surged upwards by 5-6 orders of magnitude, and concomitantly the thermal activation energies E_{act} dropped to near zero. In comparison to typical materials studied under applied physical pressure,[5] the response of the conductivity of these

radical dimers is quite dramatic.

To obtain a better understanding of the origin of the response to pressure of the aforementioned dimers, a detailed investigation was carried out on structurally related systems **3-2** (R_1 = Me; R_2 = Me, F).[6] At the time, only the crystal structures under ambient conditions were known; the three dimers [**3-2**]$_2$ (R_1 = Me; R_2 = H, Me, F) form an isomorphous set. It was found that the conductivity of all three dimers increases sharply with pressure, although materials with R_2 = H, F perform slightly better under these conditions than when R_2 = Me.[7] Until recently, the origin of the effect remained unclear and whether it involved the closure of a band gap or a molecular rearrangement needed to be determined.

To understand the origin of the response of [**3-2b**]$_2$ to pressure, a detailed investigation of its crystal structure over the pressure range 0–11 GPa was carried out, using synchrotron radiation and diamond anvil cell techniques.[7] This work confirmed that metallization did not occur by decomposition, for example, by extrusion of elemental selenium,[8] and showed that the application of pressure caused the linear S···Se–Se···S arrangement of the σ-dimer to "buckle" into a motif best described as a highly distorted π-dimer. As was described at length in Chapter 1, while the conversion of a σ-dimer to a π-dimer was, in itself, a novel finding, what made the process remarkable was the fact that the σ- to π-dimer rearrangement caused a sharp reduction in the HOMO–LUMO gap. As a result, the broadening of the valence and conduction bands induced by compression was sufficient to induce closure of the band gap, affording a weakly metallic state. In essence, metallization appeared to arise as much from changes in molecular structure as in solid state packing.

A potential corollary to this interpretation is that, in the absence of molecular buckling, sudden band gap closure and metallization should not be observed. To test this possibility, however, structurally related systems need to be examined. In this regard, the high pressure response of related dimer [**3-2a**]$_2$ has been studied and is presented in this chapter. The conductivity of this material also increases sharply with pressure, like that of [**3-2b**]$_2$, and our initial thought was that a similar structural

rearrangement might be at play. To clarify the structural and electronic changes induced by compression of these dimers, a study was carried out of the crystal and electronic structure of fluoro-substituted [**3-2a**]$_2$ as a function of pressure using synchrotron radiation and diamond anvil cell (DAC) techniques. We have found that the slipped π-stacks are compressed without significant change in the molecular structure of the dimer itself, unlike the buckling observed for [**3-2b**]$_2$. Density functional theory (DFT) calculations have been used to replicate the pressure induced changes for [**3-2a**]$_2$, and to predict the electronic band gap as a function of pressure. The results indicate a gradual decrease of the band gap with increasing pressure, with full closure not anticipated until P > 13 GPa. These studies then provide a baseline for the way in which a pressurized σ-dimer behaves, in the absence of a phase change.

Although sulfur analogues of these σ-dimers are rare, the phenomenon has been observed on a few occasions.[9,10,11] In particular, where R_2 = F as in **3-1a**, the radical crystallizes in two forms under ambient conditions; the open-shell form α-**3-1a** and the 4c–6e σ-dimer β-[**3-1a**]$_2$. In this chapter, the structure and properties of both phases are presented under ambient conditions, and applied pressure studies are performed on the dimer phase β-[**3-1a**]$_2$. The results for bisdithiazolyl radical dimer β-[**3-1a**]$_2$ under applied pressure are compared to the related bisthiaselenazolyls [**3-2a**]$_2$ and [**3-2b**]$_2$. A full paper was recently published on the high pressure response of [**3-2a**]$_2$,[12] and a manuscript is currently in preparation on the polymorphic sulfur material **3-1a** at ambient and high pressure.[13]

3.2 Results

3.2.1 Synthesis of α-3-1a, β-[3-1a]$_2$ and [3-2a]$_2$

Similarly to the synthesis of **2-2a** in Chapter 2, the formation of the sulfur and sulfur/selenium radicals in this series begins with the alkylation of commercially available 2,4,6-trifluoropyridine with methyl trifluoromethanesulfonate (triflate) (Scheme 3.1). Once [**3-1a**][OTf] is produced *via* familiar chemistry,[9,14] reduction with DMFc may be effected under kinetic conditions to obtain near-pure α-**3-1a**

in crude, microcrystalline form. When reduced carefully, this material is suitable for physical property measurements. Single crystals of α-**3-1a** were obtained, with a great deal of difficulty, *via* slow reduction in an H-cell apparatus.

Scheme 3.1

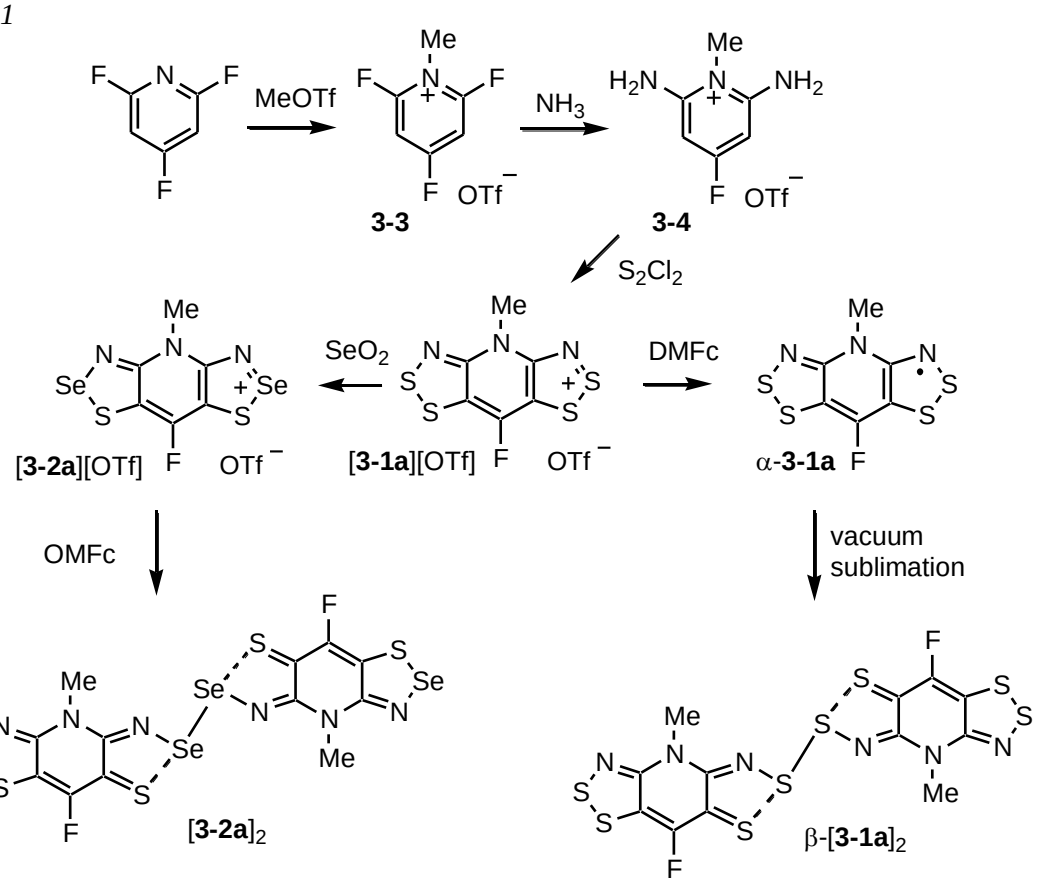

When **3-1a** was sublimed under vacuum (10^{-4} Torr) in a gradient tube furnace, a mixture of green needles and bronze blocks were obtained. Over time, the green needles tend to resublime and condense as pure bronze blocks of β-[**3-1a**]$_2$ that are suitable for single crystal X-ray diffraction, as well as bulk physical property measurements.[15] Alternatively, and *en route* to the formation of [**3-2a**]$_2$, transformation of the bisdithiazolylium cation [**3-1a**][OTf] to its mixed S/Se analogue [**3-2a**][OTf] was effected by heating a solution of [**3-1a**][OTf] with selenium dioxide in MeCN in a glass pressure vessel, a method developed some years ago for the introduction of selenium into the 2-position of simple 1,2,3-dithiazolylium salts.[16]

3.2.2 Ambient Pressure Crystallography

The crystal structures of both α-**3-1a** and β-[**3-1a**]$_2$ have been determined at ambient temperature and pressure by single-crystal X-ray diffraction, which established that **3-1a** is indeed polymorphic. The inability to grow single crystals of [**3-2a**]$_2$ forced us to determine its crystal structure under ambient conditions using powder data collected from synchrotron radiation (λ = 0.51446 Å). Details of the structural refinements are given in section 3.2.4. Crystal metrics for the two polymorphs of **3-1a** and the selenium analogue [**3-2a**]$_2$ are provided in Table 3.1, and drawings of the molecular building blocks, showing atom numbering schemes, are illustrated in Figure 3.1.[17]

Crystals of α-**3-1a** belong to the monoclinic $P2_1/n$ space group, and possess two molecules in the asymmetric unit, denoted A and B in the numbering scheme. Each of the two radicals provides the basis for a slipped π-stack array running along the *y*-direction. The mean interplanar separations δ are 3.506 Å (A) and 3.446 Å (B), and the inclination angles τ of the mean molecular plane with respect to the stacking axis are 59.8º (A) and 58.1º (B). Views of the unit cell of α-**3-1a** along directions parallel and perpendicular to the stacking axis are shown in Figure 3.2 (left). While the radicals are not dimerized, there are intermolecular S···S' contacts, d_1 (3.398 Å) and d_2 (3.329 Å) within the nominal van der Waals separation for sulfur (3.6 Å) between the A and B π-stacks. Additionally, there are weak 4-center S···N' interactions (3.151 Å) between B-type molecules, a common feature of the packing of thiazyl and selenazyl heterocycles.[18] These 4-center S···N' interactions are very characteristic of 4c–6e σ-bonded structures, and indeed, they are present in β-[**3-1a**]$_2$ as well, albeit marginally shorter (d_5 = 3.092 Å) than in α-**3-1a**. As observed in related structures, these contacts generate an extensive lattice-wide network of electronic and magnetic interactions.

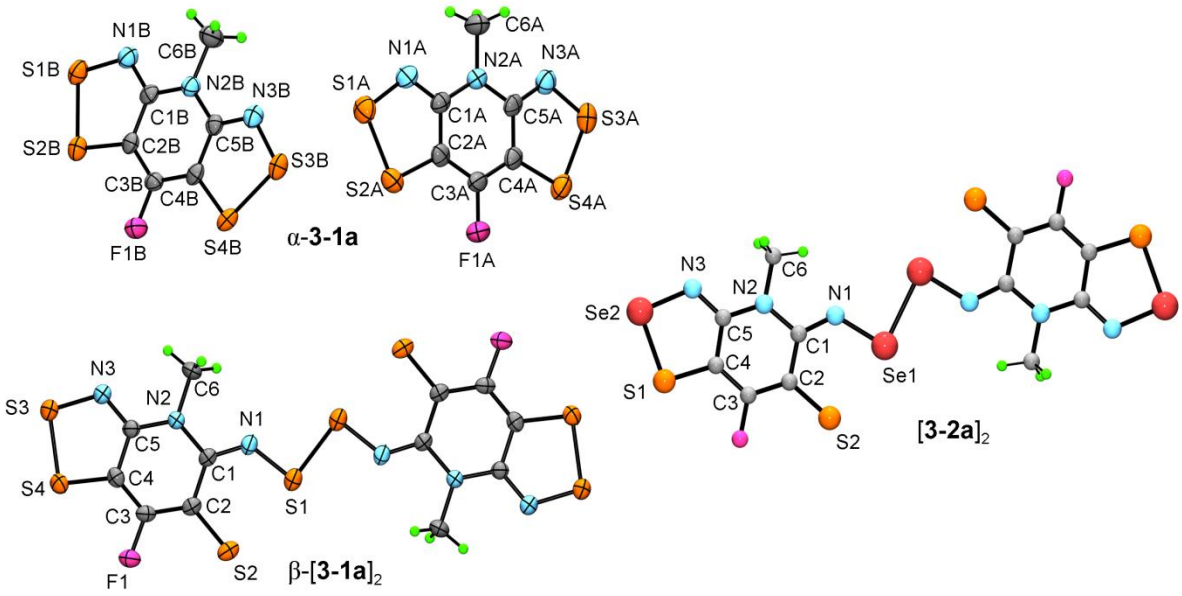

Figure 3.1 ORTEP drawings (50% probability ellipsoids) of α-**3-1a** and β-[**3-1a**]$_2$ and ball and stick drawing of [**3-2a**]$_2$ at ambient pressure and temperature, showing atom numbering.

By contrast, crystals of β-[**3-1a**]$_2$ and [**3-2a**]$_2$ belong to the monoclinic space group $P2_1/c$ and form an isostructural pair. They are also isostructural with other previously reported thiazyl[9] and selenazyl[1,6] dimers. At the molecular level, the radicals are dimerized in a nearly coplanar arrangement, as demonstrated by the small interplanar separation δ_2 (Figure 3.3) of 0.369 Å for β-[**3-1a**]$_2$ and 0.367 Å for [**3-2a**]$_2$. The two radicals within each dimer unit are linked by a 4c–6e S···E–E···S interaction, which leads to a lengthening of the S–E bond to a value intermediate between the sum of the covalent radii[19] and the expected van der Waals contact,[20] in keeping with a hypervalent description. At the same time, the N1–C1, N3–C5, and C4–S2 bonds contract in a manner that is consistent with the valence bond formulation shown in Chart 3.1. As illustrated in the representative packing diagram in Figure 3.2, there are two centrosymmetric dimers per unit cell, each bridged by a single E–E' bond and packed in cross-braced slipped π-stacks that run parallel to the *a* axis. The dimers are also linked laterally into ribbons by 4-center Se···N' contacts d_5. Comparison of the distances indicates that the contacts in the selenium structure [**3-2a**]$_2$ (d_5 = 2.849 Å) are much shorter (d_5 = 3.092 Å) than β-[**3-1a**]$_2$, where E = S.

The inclination of the slipped π-stacks with respect to the stacking direction τ = 49.4° for β-[**3-1a**]$_2$ and 54.1° for [**3-2a**]$_2$ under ambient conditions (Figure 3.3).

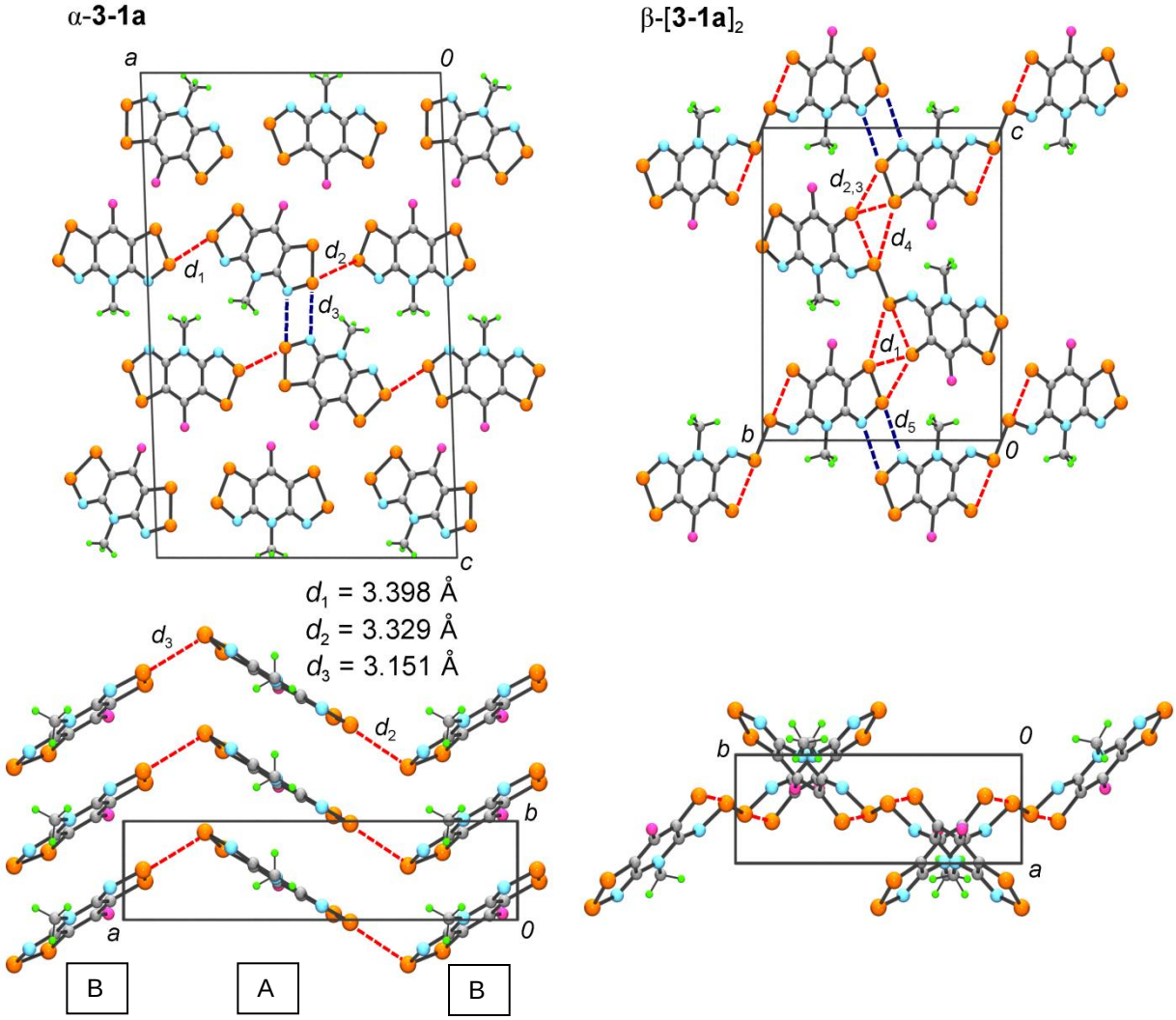

Figure 3.2 Crystal structures of α-**3-1a** (left) and β-[**3-1a**]$_2$ (right) under ambient conditions, viewed along the *b* (above) and *c* (below) axes for α-**3-1a**, and *a* (above) and *c* (below) axes for β-[**3-1a**]$_2$.

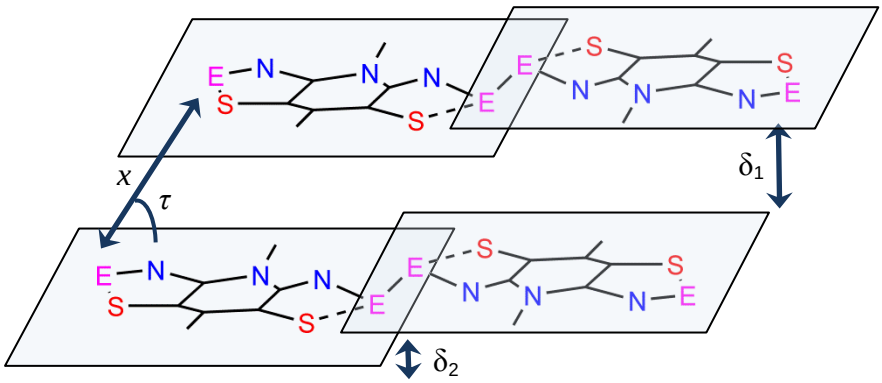

Figure 3.3 Intermolecular structural parameters δ_1, δ_2 and τ for σ-dimers where E = S, Se.

Table 3.1 Crystal data for α-**3-1a** and β-[**3-1a**]$_2$, and [**3-2a**]$_2$ under Ambient Conditions.

	α-**3-1a**	β-[**3-1a**]$_2$	[**3-2a**]$_2$
formula	$C_6H_3FN_3S_4$	$C_6H_3FN_3S_4$	$C_6H_3FN_3S_4Se_2$
fw	264.35	264.35	358.15
pressure (GPa)	0	0	0
a, Å	17.301(3)	4.6011(7)	4.28423(11)
b, Å	4.0582(7)	12.7317(19)	13.4658(4)
c, Å	26.249(4)	15.9122(19)	15.8983(17)
β, deg	92.074(4)	78.949(4)	79.300(4)
V, Å^3	1841.8(5)	914.8(2)	901.24(9)
space group	$P2_1/n$	$P2_1/c$	$P2_1/c$
Z	8	4	4
temp, K	296(2)	293(2)	293(2)
λ, Å	0.71073	0.71073	0.51446
solution method	direct methods	direct methods	powder methods
R_p	0.0526	0.0486	0.0086
R_{wp}	0.0993	0.0758	0.0130
δ (Å)	3.506 (A), 3.446 (B)	3.491	3.469
τ (deg)	59.8 (A), 58.1 (B)	49.4	54.1

3.2.3 Magnetic Measurements

Magnetic susceptibility (χ) measurements have been performed on the α- and β-phases of **3-1a** over the temperature range 2–300 K using a SQUID magnetometer operating at H = 1000 Oe. Figure 3.4 shows the results of data collected over the range T = 2–300 K, presented in the form of plots of χ (corrected for diamagnetic contributions) and χT against T. The monoclinic phase α-**3-1a** behaves as a Curie-Weiss paramagnet, and a fit to the 50–300 K data affords values of C = 0.346 emu K mol^{-1} and θ = −14.9 K, indicating the presence of strong local antiferromagnetic interactions.

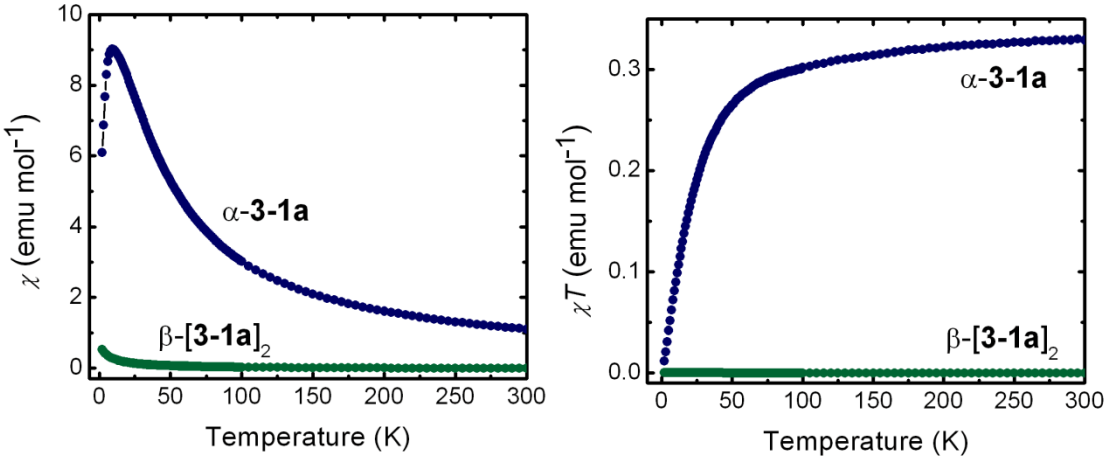

Figure 3.4 Plots of χ (left) and χT (right) *versus* T for α-**3-1a** and β-[**3-1a**]$_2$ from T = 2–300 K.

As expected from the presence of a covalent bond between the two radicals in the dimeric unit in β-[**3-1a**]$_2$, the near base-line plot (Figure 3.4) of χ *versus* T indicates that the material is essentially diamagnetic over the temperature range 2–300 K; the small Curie "tail" observed at low temperatures may be ascribed to radical defects.[1a,6] In a separate experiment, the magnetic susceptibility of β-[**3-1a**]$_2$ was measured in the range 300–400 K to observe whether or not the paired spins uncouple. This showed that the material does not crossover to a paramagnetic radical below 400 K (the limit of the experiment).[21] In Chapter 4, a bisdithiazolyl dimer whose spins *do* uncouple under the influence of temperature, pressure and light will be presented.

Table 3.2 Crystal Data for β-[**3-1a**]$_2$ and [**3-2a**]$_2$ as a Function of Pressure.

Dimer	β-[**3-1a**]$_2$			[**3-2a**]$_2$		
formula	$C_6H_3FN_3S_4$	$C_6H_3FN_3S_4$	$C_6H_3FN_3S_4$	$C_6H_3FN_3S_2Se_2$	$C_6H_3FN_3S_2Se_2$	$C_6H_3FN_3S_2Se_2$
fw	264.35	264.35	264.35	358.15	358.15	358.15
P, GPa	0	2.53	4.88	0	4.38	8.40
a, Å	4.6011(7)	4.12168(24)	3.86543(33)	4.28423(11)	3.82021(12)	3.59910(17)
b, Å	12.7317(19)	13.2722(11)	13.4994(21)	13.4658(4)	13.82056(34)	13.88062(35)
c, Å	15.9122(19)	14.8586(10)	14.4694(12)	15.8983(17)	15.0366(14)	14.5372(15)
β, deg	78.949(4)	84.318(5)	86.261(7)	79.300(4)	82.973(6)	84.851(6)
V, Å^3	914.8(2)	808.83(5)	753.42(8)	901.24(9)	787.93(7)	723.31(7)
space group	$P2_1/c$	$P2_1/c$	$P2_1/c$	$P2_1/c$	$P2_1/c$	$P2_1/c$
Z	4	4	4	4	4	4
temp, K	293(2)	293(2)	293(2)	293(2)	293(2)	293(2)
λ, Å	0.71073	0.509175	0.509175	0.51446	0.51446	0.51446
soln method	direct methods	powder data	powder data	powder data	powder data	powder data
R_p, R_{wp}	0.0486, 0.0758	0.0105, 0.0158	0.0099, 0.0142	0.0086, 0.0130	0.0100, 0.0142	0.0117, 0.0169

3.2.4 High Pressure Crystallography on σ-Dimers

High pressure diffraction data on β-[**3-1a**]$_2$ and [**3-2a**]$_2$ were collected at room temperature as a function of increasing pressure using synchrotron radiation (λ = 0.509175 and 0.51446 Å, respectively) and DAC techniques. A total of nine data sets from 0 GPa to 11.2 GPa on [**3-2a**]$_2$ and five data sets from 2.53 to 7.69 GPa on β-[**3-1a**]$_2$ were indexed using DICVOL, as supplied with DASH. In the case of β-[**3-1a**]$_2$, all five of these were solved starting from the molecular model based on the ambient pressure crystal structure. Due to the inability to produce single crystals of [**3-2a**]$_2$, the molecular model used to solve six of the indexed data sets (including the 0 GPa data)[22] came from the ambient pressure crystal of [**3-2b**]$_2$ (R_1 = Me; R_2 = H) with the basal proton replaced by a fluorine atom. During the initial

Rietveld refinement, performed using DASH, a rigid-body constraint was maintained, but for the high pressure structures the sulfur and selenium (when present) positions were later released to optimize within the plane of the molecule. A final refinement of the unit cell, using fixed atomic positions and isotropic thermal parameters, was performed using GSAS on two data sets for β-[**3-1a**]$_2$ and three in the case of [**3-2a**]$_2$. Unit cell and refinement parameters for these are listed in Table 3.2, while summaries of pertinent inter- and intramolecular distances as a function of pressure are presented in Table 3.3. Representative powder patterns (observed and calculated) are shown in Figure 3.5 at low and high pressures for each dimer.

Table 3.3 Selected Distances[a] and Angles[b] in β-[**3-1a**]$_2$ and [**3-2a**]$_2$ as a Function of Pressure.

Dimer	β-[**3-1a**]$_2$			[**3-2a**]$_2$		
P, GPa	0	2.53	4.88	0	4.38	8.40
E–E'	2.169	2.243	2.212	2.497	2.486	2.557
E---S	2.797	2.801	2.799	2.785	2.808	2.755
δ_1	3.491	3.119	3.017	3.469	3.182	3.036
δ_2	0.369	0.531	0.504	0.367	0.335	0.398
τ	49.4	49.2	51.3	54.1	56.4	57.5
d_1	3.976	3.704	3.645	3.910	3.666	3.369
d_2	4.084	3.556	3.499	3.667	3.485	3.211
d_3	3.231	3.160	3.224	3.165	3.064	2.896
d_4	4.300	3.951	3.854	4.144	3.795	3.567
d_5	3.092	3.084	2.751	2.849	2.541	2.450

[a] Distances in Å. [b] Angles in degrees.

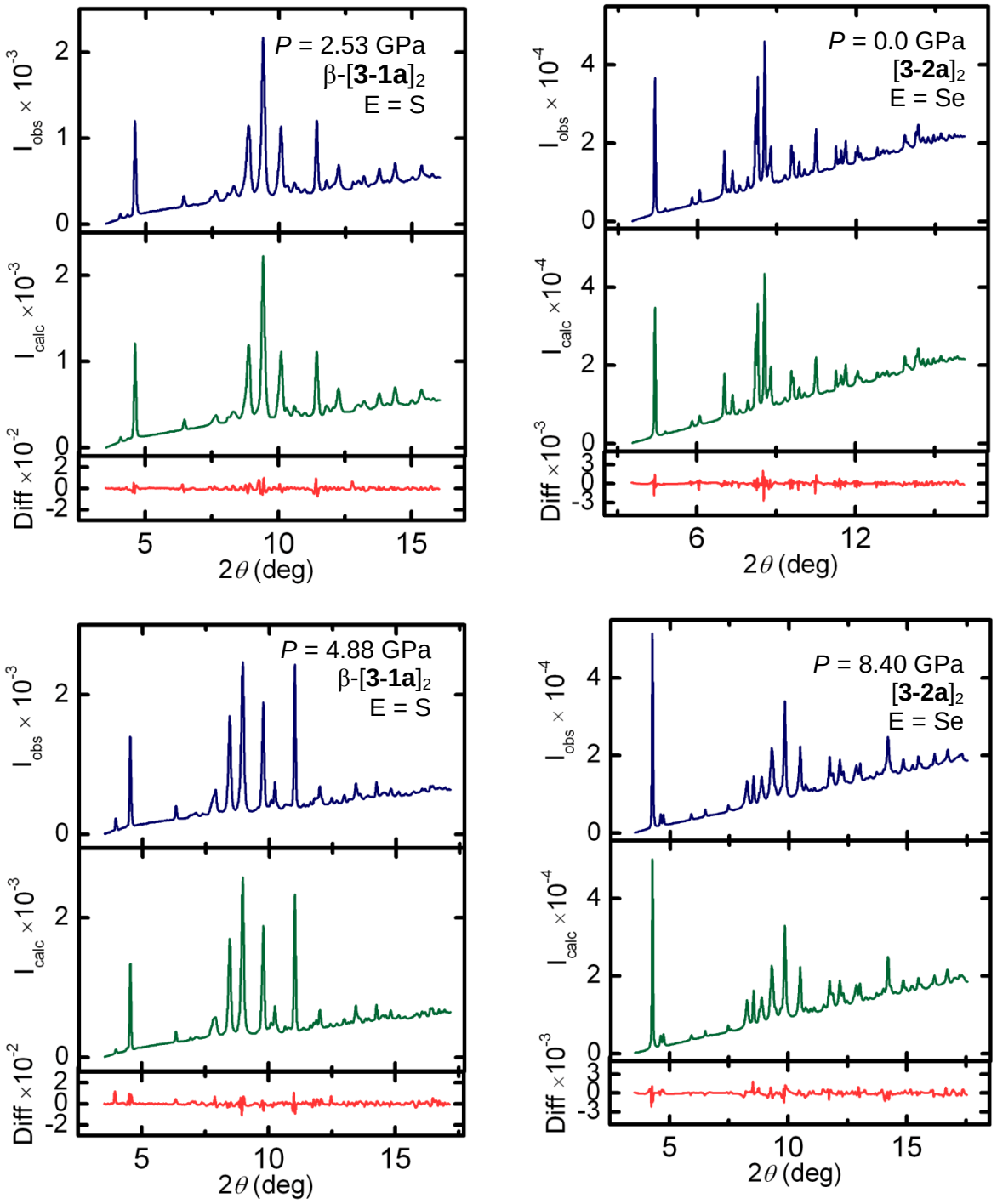

Figure 3.5 Representative powder X-ray diffraction patterns (observed and calculated) for β-[**3-1a**]$_2$ (λ = 0.509175 Å) and [**3-2a**]$_2$ (λ = 0.51446 Å) at low (above) and high (below) pressures.

With the application of pressure the dimer structures display a similar response. As may be seen in Figure 3.6, which illustrates the relative changes in cell parameters and volume as a function of pressure, the *a* and *c* axes contract slightly, while the *b* axis becomes marginally longer in both cases. As expected, the cell volume compresses for both β-[**3-1a**]$_2$ and [**3-2a**]$_2$, although the S–S' σ-dimer appears to be slightly more compressible. The value of δ_1, the plate-to-plate separation along the π-stacks, decreases slightly, as would be expected, and the inclination of the π-stacks, measured in terms of the tilt angle τ, also decreases marginally (as reflected in the increase of the value of τ), so that the molecular plates become more nearly superimposed (Table 3.3). The dimer units themselves also remain much the same as at ambient pressure. The interannular E–E' σ-bond, the hypervalent S···E σ-bonds and the C4–S4 bonds show small but unexceptional variations. Likewise the value of δ_2, the interplanar separation of the two halves of the dimer, also remains essentially constant. By contrast, all of the intermolecular interactions $d_{1\text{-}5}$ decrease significantly under pressure, other than d_3 in the case of β-[**3-1a**]$_2$ (Figure 3.7).

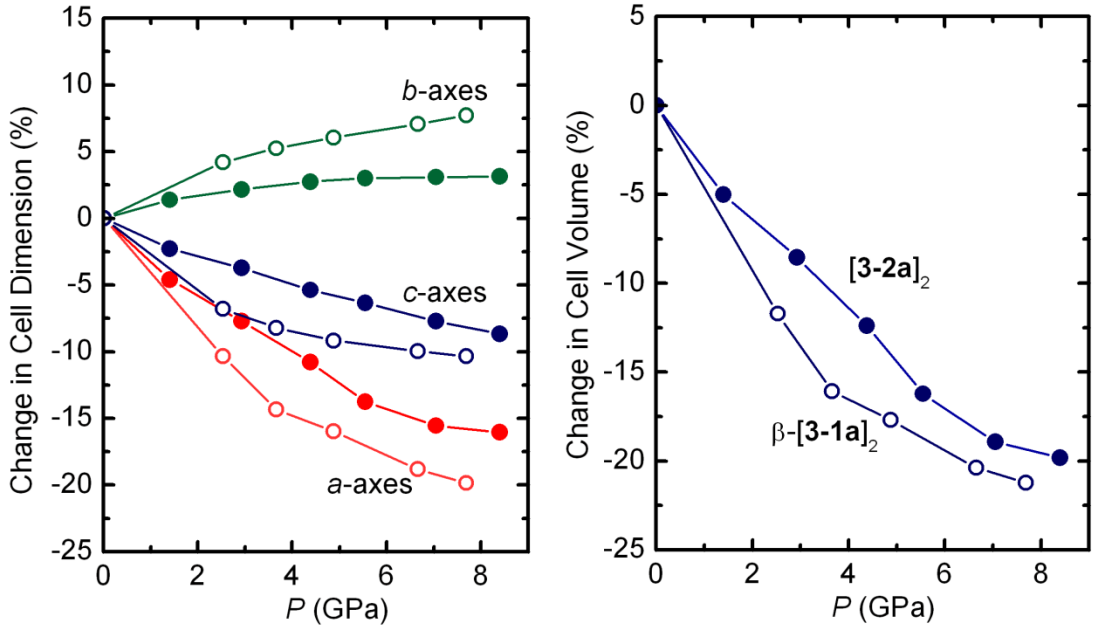

Figure 3.6 Relative changes in cell dimensions (left) and cell volume (right) of β-[**3-1a**]$_2$ (open circles) and [**3-2a**]$_2$ (closed circles) with increasing pressure.

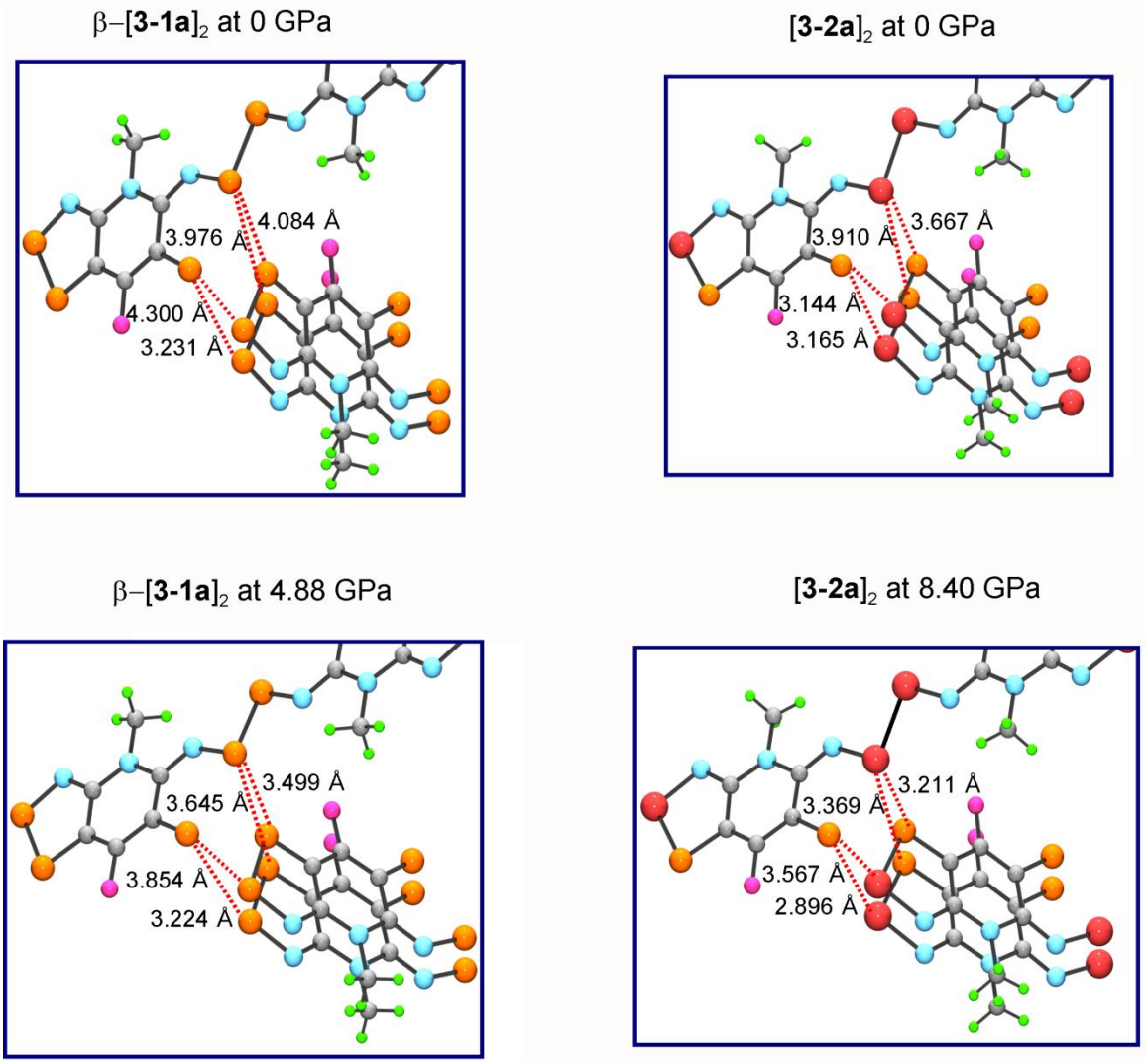

Figure 3.7 Coordination and contact distances about the dichalcogenide core in dimers β-[**3-1a**]$_2$ and [**3-2a**]$_2$ as a function of pressure.

3.2.5 Conductivity Measurements

In previous work, the room temperature conductivity of [**3-2a**]$_2$ was determined to be on the order of 10^{-6} S·cm^{-1} at ambient pressure. We also explored the variation in conductivity with pressure, by means of a cubic anvil press, and established that the conductivity could be increased by 5-6 orders of magnitude by the application of 5 GPa pressure, much like that of related E = Se σ-dimers.[1,6] The same experiments were recently performed on β-[**3-1a**]$_2$ in order to compare the high pressure response of the E = S/Se variations (Figure 3.8). Although the room temperature conductivity of the sulfur dimer β-[**3-**

1a]$_2$ increases by 5 orders of magnitude over the pressure range, the value of the conductivity reaches a maximum of almost 10^{-1} S·cm^{-1}. This is over an order of magnitude lower than the selenium analogue [**3-2a**]$_2$, which displays conductivity at 5 GPa greater than 1 S·cm^{-1}. Variable temperature conductivity measurements on β-[**3-1a**]$_2$ and [**3-2a**]$_2$ indicate that the value of the thermal activation energy E_{act} is reduced at 5 GPa to near 0.2 eV and 0.1 eV, respectively. This occurs in a uniform, non-precipitous fashion to the limit of the experiment. Extrapolation of the data to higher pressures suggests that loss of activation would require pressures well above 10 GPa for both dimers.

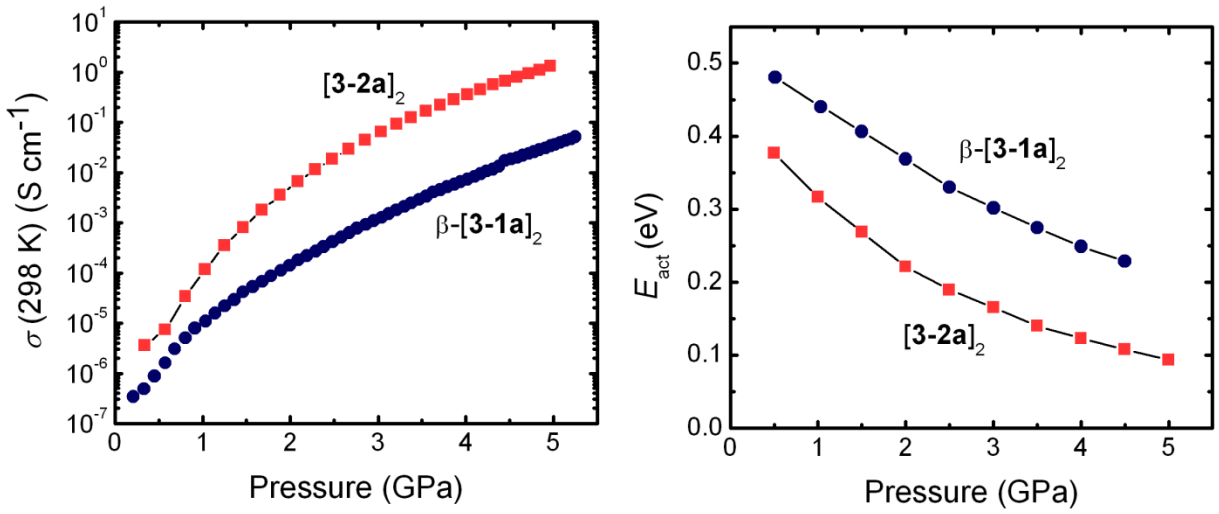

Figure 3.8 Pressure dependence of the conductivity at 298 K (left) and activation energy E_{act} for conductivity (right) of β-[**3-1a**]$_2$ and [**3-2a**]$_2$ over the range T = 300–360 K, as measured using a cubic anvil press.

3.3 Discussion

The application of physical pressure to crystalline solids can have a profound impact on their structure and electronic properties.[5] Although significant changes to ionic materials may require pressures in excess of 200 GPa, molecular elemental solids, notably the heavier chalcogens and halogens, can respond quite dramatically to relatively low pressures (20–30 GPa). Generally, however, the structural transformations involve bond cleavage. For example, the metallization of molecular iodine[23] is associated with several phase transitions, with complete separation of the atoms occurring

near 30 GPa.[24] Bond dissociation also occurs for elemental sulfur under pressure,[25] leading to opening of the S_8 rings of the orthorhombic phase and formation of a helical chain (trigonal) structure which, in turn, re-cyclizes to a rhombohedral structure based on S_6 rings.[26] Analogous trigonal[27] and rhombohedral[28] phases are known for selenium.

In light of these findings, reports of pressure-induced changes in the electronic properties of closed shell molecular compounds, particularly those containing heavier chalcogens and halogens, require careful scrutiny, as in many cases, metallization has been suggested to arise from products of decomposition.[29] Enhancement of the conductivity of sulfur-,[30] selenium-,[31] and tellurium-based[32] polyacenes has also been observed, with metal-like behavior emerging near or above 20 GPa. However, for these chalcogen-based compounds, crystallographic studies have established that the molecular framework remains intact under compression, and density functional theory (DFT) calculations have confirmed that metallization can be attributed in large part to closure of the electronic band gap.[33]

In recent years there has been a surge in interest in the development of structure-property correlations for organic magnetic and conductive materials as a function of pressures < 10 GPa. The critical challenge is to establish whether the function of molecular materials under mild pressure can be understood, and hence fine-tuned. The ability to pursue this goal has been driven in large part by the increasing availability of synchrotron radiation and DAC techniques. These allow for a detailed mapping of the associated structural changes, which are often very subtle. Variations in magnetic properties,[34] conductivity enhancements,[35] and phase transitions associated with the coordination geometry[36] have been effectively correlated with pressure-induced structural changes. In the present case the pair of dimers β-[**3-1a**]$_2$ and [**3-2a**]$_2$ provide an example of two isostructural molecular materials that display similar responses to physical pressure. The observation of bulk structural compression and enhancement of conductivity are changes that one would expect with increasing pressure. In essence, the dimer structures are compressed under pressure, but not altered.

The story would conclude here, were it not for the striking comparison of the behavior of these dimers to their isostructural relative [**3-2b**]$_2$ (R_1 = Me; R_2 = H), where the subtle changes discussed above are in marked contrast to that previously observed for [**3-2b**]$_2$. As reported earlier and discussed thoroughly in Chapter 1, [**3-2b**]$_2$ undergoes a phase change between 3.74 and 5.09 GPa, and the divergence in the cell parameters becomes far more pronounced; the values of *a* and *c* drop rapidly, to differing degrees, while *b* rises sharply (Figure 3.9).[7] Collectively, these unit cell changes translate into a concertina-like compression of the cross-braced π-stack framework. The plate-to-plate separation δ_1 decreases significantly, as would be expected, but in addition, individual ribbons appear to buckle under pressure, as a result of which the planes of the two halves of the dimers separate (*i.e.*, δ_2 increases). Between 5.09 GPa and 9.37 GPa, the cell changes become more gradual, and all packing and molecular adjustments are, by comparison, minor.

The molecular reorganization accompanying the abrupt bulk structural changes of [**3-2b**]$_2$ lead to the closure of the HOMO-LUMO gap near 5 GPa and the onset of a weakly metallic state, a transformation discussed in Chapter 1 in more detail. As expected, this phenomenon is not observed for related dimers β-[**3-1a**]$_2$ and [**3-2a**]$_2$. Compression does, however, significantly enhance the intermolecular interactions and thus bandwidth of these materials in the absence of a phase transition.

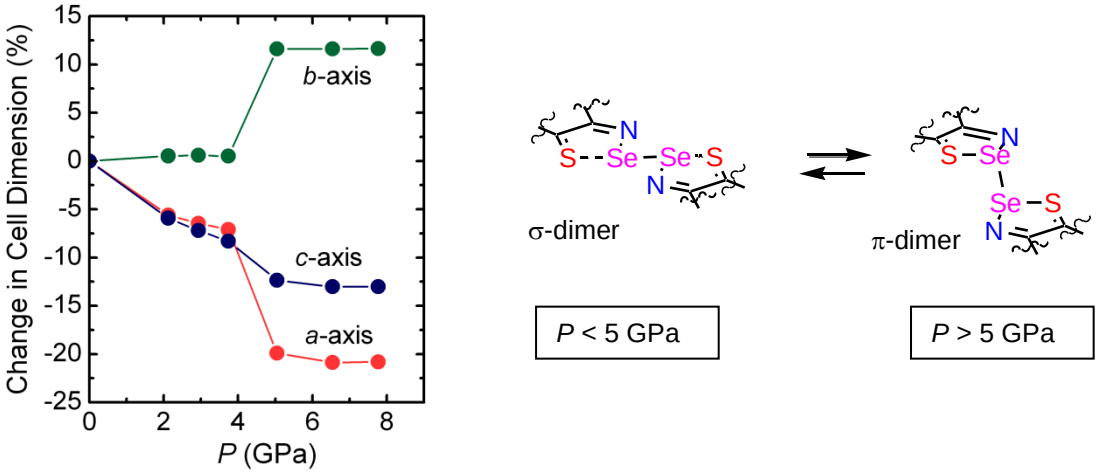

Figure 3.9 Summary of structural changes in [**3-2b**]$_2$. Evolution of the unit cell dimensions as a function of pressure (left) and transformation from a σ- to a π-dimer at the molecular level (right). Adapted from reference 7.

3.3.1 Band Electronic Structures

The room temperature electronic structure of [**3-2a**]$_2$ has been probed as a function of pressure by a series of *ab initio* calculations with the VASP package in order to compare the results to those reported for [**3-2b**]$_2$. Using the experimental structures at various pressures as starting points, complete optimizations of both geometry and pressure were performed. As illustrated in Figure 3.10, plots of the calculated cell parameters over the pressure range 0–13.7 GPa are in good agreement with those obtained experimentally for [**3-2a**]$_2$, supporting the conclusion that pressurization does not induce a phase transition for [**3-2a**]$_2$, as it does for [**3-2b**]$_2$.

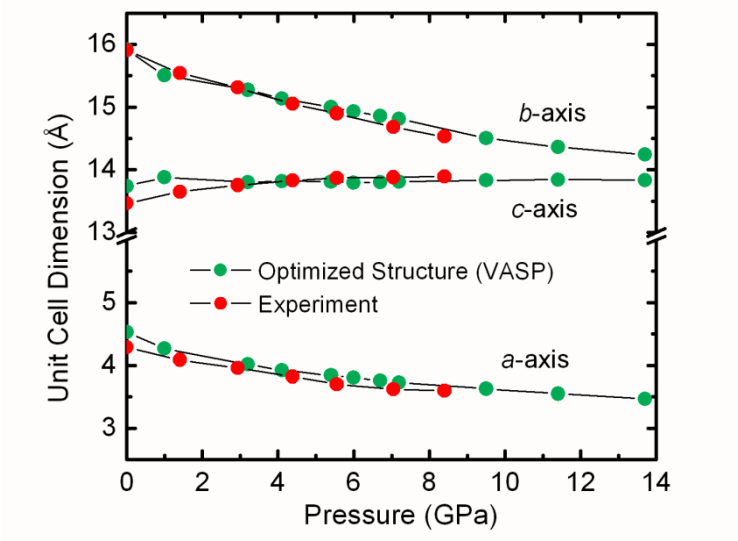

Figure 3.10 Calculated (VASP optimized) and experimental cell dimensions for [**3-2a**]$_2$ as a function of pressure.

Based on the success of the VASP package in replicating the observed geometry of [**3-2a**]$_2$ as a function of pressure, we have examined its band electronic structure as a function of pressure using the same computational method. The results are illustrated in Figure 3.11 (top), in the form of crystal orbital dispersion diagrams at three well-separated pressures in the range 0–10 GPa. As may be seen, there is a well-defined energy gap E_g between the valence and conduction bands at ambient pressure, as expected for a closed shell semiconductor (for which $E_g \sim 2\ E_{act}$). With increasing pressure the valence

and conduction bands are broadened, as a result of increased intermolecular overlap, and there is a concomitant decrease in E_g, which reaches a value of 0.08 eV at 9.5 GPa. However, final coalescence of the valence and conduction bands does not take place until > 13 GPa. This is in marked contrast to the behavior of [**3-2b**]$_2$ (Figure 3.11, bottom), for which the band gap closes by 5.27 GPa.

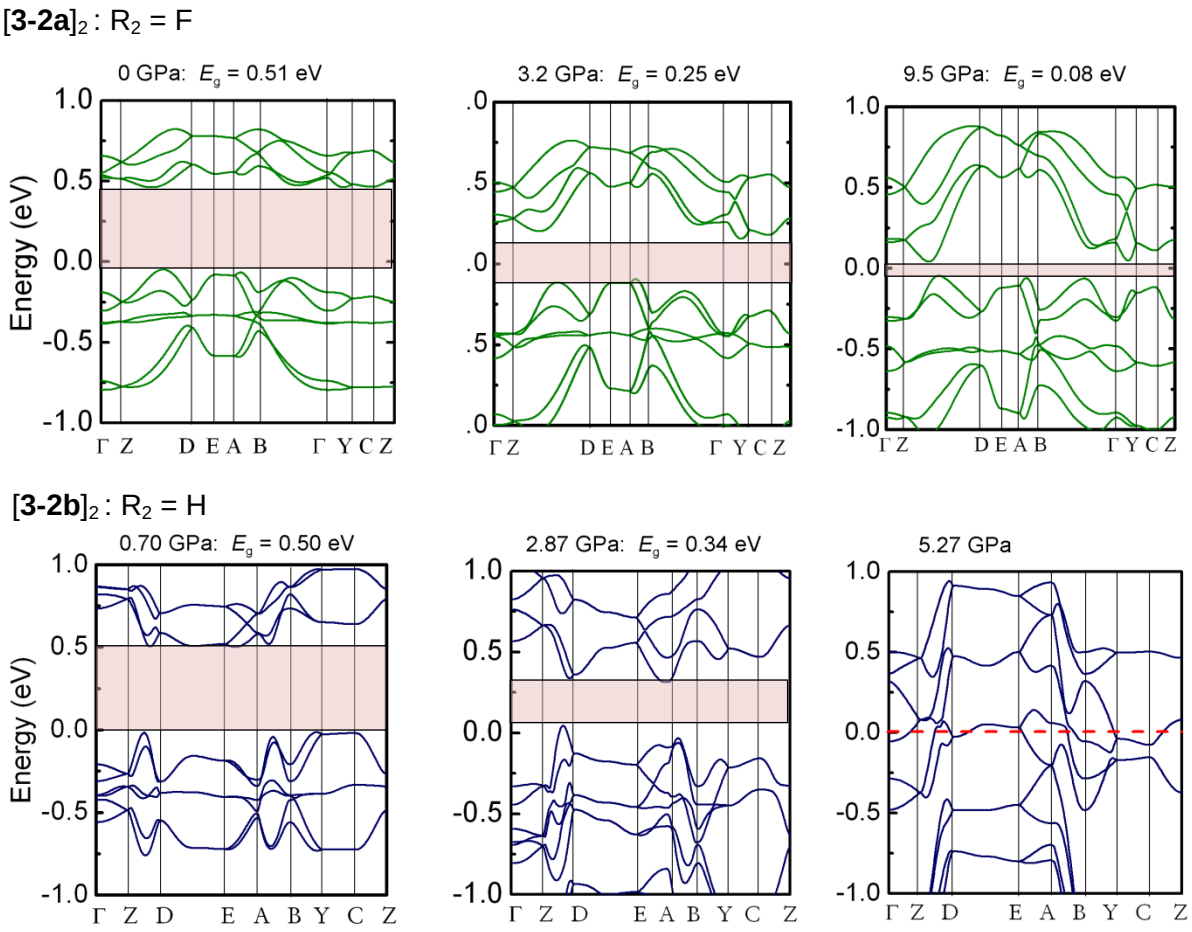

Figure 3.11 VASP band dispersion diagrams for [**3-2a**]$_2$ (above), and [**3-2b**]$_2$ (below) as a function of pressure. The hatched zone (in blue) denotes the indirect band gap E_g.

In order to contrast the behavior more directly, a comparison of the pressure dependence of the calculated band gap for the two compounds where E = Se is provided in Figure 3.12. The slow, steady decrease in E_g for [**3-2a**]$_2$ is in sharp contrast to that seen for [**3-2b**]$_2$, which undergoes a rapid drop in E_g in the region of the phase transition from σ-dimer to π-dimer. As a result, the band gap of [**3-2a**]$_2$ is not expected to close before 14 GPa.

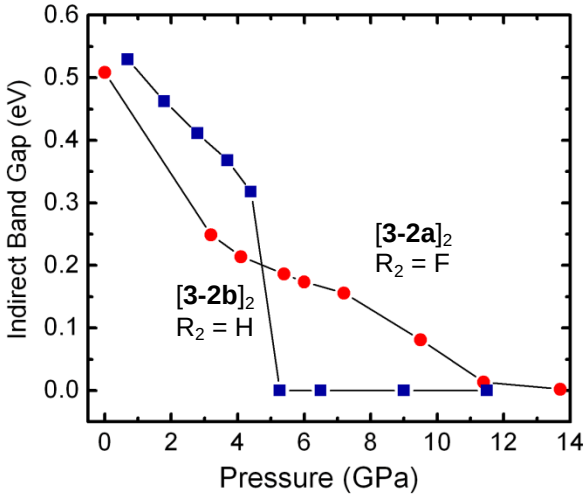

Figure 3.12 Band gaps E_g obtained from VASP optimized structures of [**3-2a**]$_2$ (circles), and [**3-2b**]$_2$ (squares) as a function of pressure. The data for [**3-2b**]$_2$ are from ref 7.

3.3.2 Structural Considerations

DFT calculations provide an impressive replication of the structural evolution and the associated changes in molecular and band electronic structures of the two selenium compounds. What the computational results do not reveal, however, is why the pressure induced dichotomy exists at all. While we do not have a definitive answer to this question, a qualitative understanding of the issues can, we believe, be developed by comparing the ambient pressure structures of the sulfur dimer β-[**3-1a**]$_2$ and the two selenium dimers [**3-2a**]$_2$ and [**3-2b**]$_2$. As illustrated in Figure 3.13, the most notable difference between them at 0 GPa is the degree of inclination of the mean planes of dimers with respect to the stacking direction, that is, the angle τ defined in Figure 3.2. In [**3-2b**]$_2$, τ is much smaller (46.0°) than in [**3-2a**]$_2$ (54.1°). Given that the two molecules differ only in the replacement of the basal fluorine in [**3-2a**]$_2$ with a proton atom in [**3-2b**]$_2$, this significant change in π-stack slippage is at first surprising, since their van der Waals radii (r_H = 1.20 Å, r_F = 1.47 Å) are comparable (Figure 3.12).[20] However, close inspection of the overlay of adjacent dimers along the π-stacks leads to the conclusion that the difference in π-stack inclination is not a steric issue, but rather one associated with the electronegativity of fluorine, which (i) leads to potential electrostatic interactions within the π-stacks, and (ii) allows for

the development of structure-strengthening F···H_3C contacts that influence the interlocking of neighboring π-stacks. The observation of similar F···S intrastack contacts for both [**3-2a**]$_2$ and β-[**3-1a**]$_2$ supports this explanation.

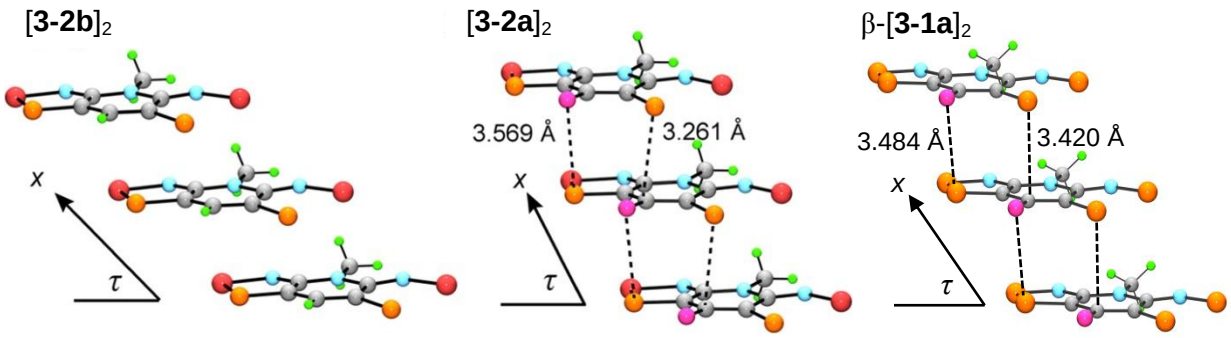

Figure 3.13 π-Stack slippage and interlayer contacts in [**3-2a**]$_2$ and [**3-2b**]$_2$, and β-[**3-1a**]$_2$ at ambient pressure.

The first of these two effects is explored in Figure 3.14, which compares the charge density distribution in the heterocyclic core of selenium dimers [**3-2a**]$_2$ and [**3-2b**]$_2$, as calculated at the B3LYP/6-31G(d,p) level. As can be seen, there is a significant polarization of charge away from the C3 carbon in [**3-2a**]$_2$ (relative to [**3-2b**]$_2$) induced by the presence of the ligated fluorine. Although this difference may not be the root cause of the reduced slippage of the π-stacks in [**3-2a**]$_2$, it is interesting to observe (in Figure 3.13) that in this structure the C3 carbons are aligned almost perfectly below the negatively charged thione sulfurs S2, with d(C3–S2) = 3.261 Å. At the same time, on the other side of the molecule, there is a close interlayer contact (3.569 Å) between fluorine and the positively charged endocyclic sulfur S1. A similar situation with close intrastack electrostatic interactions is observed for β-[**3-1a**]$_2$, where the d(C3–S1) = 3.420 Å and d(F1–S4) = 3.484 Å. By contrast, these interactions are not present in [**3-2b**]$_2$.

The second issue noted above concerns the possibility that the close CH_3···F(aryl) contacts in [**3-2a**]$_2$ and β-[**3-1a**]$_2$ may be serving as supramolecular synthons[37] which control the degree of slippage of the π-stacks. The potential for covalently bound fluorine atoms to enter into weak "hydrogen bridge" interactions is well-known in organic structures.[38,39] Such donor/acceptor CH_3···F(aryl) contacts are

strongest when the hybridization at the donor carbon is sp^2 or sp. When sp^3 hybrids are involved, the hydrogen is less acidic, and $CH_3\cdots F$(aryl) interactions are weaker still, but their influence can still be observed, as in the π-stacking of benzimidazolyl-nitronyl nitroxides.[34b] Given these precedents, it is noteworthy that the more nearly superimposed stacking in [**3-2a**]$_2$ and β-[**3-1a**]$_2$ is associated with, if not actually induced by, two close $CH_3\cdots F$(aryl) contacts (Figure 3.15).[40] By contrast, the increased slippage seen in [**3-2b**]$_2$ gives rise to only one short $CH_3\cdots H$(aryl) approach. In the latter case, this feature may indeed be desirable, as these $CH_3\cdots H$(aryl) interactions are likely repulsive.

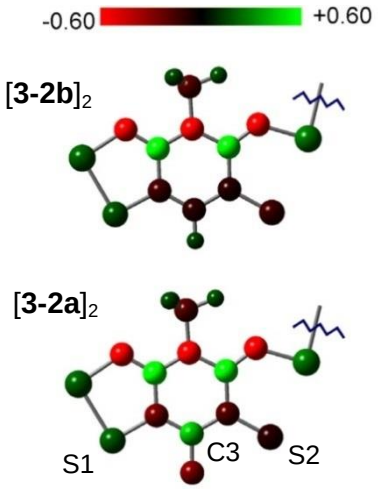

Atom	[**3-2a**]$_2$	[**3-2b**]$_2$
H/F	-0.258	0.132
C1	0.573	0.555
C2	-0.170	-0.083
C3	0.397	-0.093
C4	-0.232	-0.129
C5	0.605	0.580
N1	-0.571	-0.564
N2	-0.581	-0.576
N3	-0.557	-0.549
S1	0.184	0.162
S2	-0.084	-0.120
Se1	0.238	0.236
Se2	0.190	0.188

Figure 3.14 B3LYP/6-31G(d,p) charge distribution in [**3-2a**]$_2$ and [**3-2b**]$_2$ at ambient pressure.

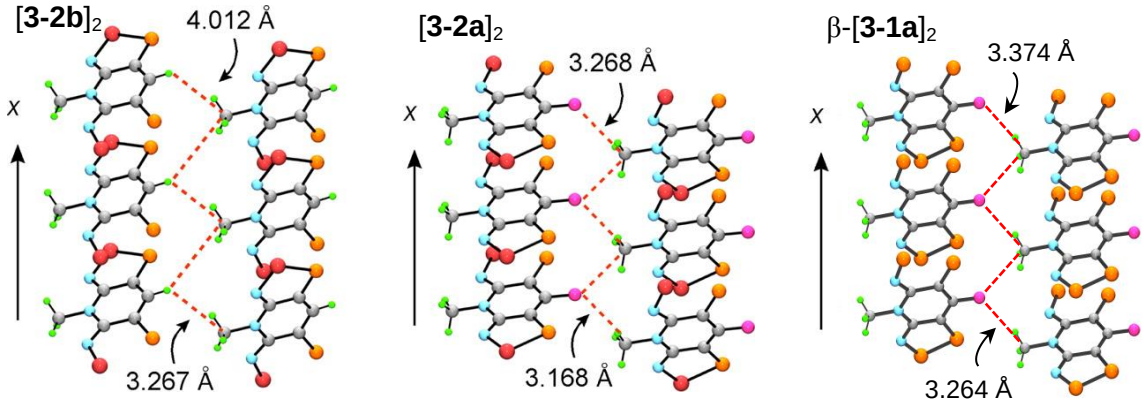

Figure 3.15 Interstack $CH_3\cdots H$(aryl) and $CH_3\cdots F$(aryl) contacts in [**3-2b**]$_2$, [**3-2a**]$_2$, and β-[**3-1a**]$_2$ at ambient pressure.

3.3.3 Energetics of Compression with and without Buckling

The marked difference in the response of [**3-2a**]$_2$ and [**3-2b**]$_2$ to pressure prompts one final question. If it were possible to probe the compression of [**3-2b**]$_2$ in the absence of buckling, what would be the energy and electronic properties of the undistorted structure in the high pressure regime? To address this question, a series of VASP calculations on [**3-2b**]$_2$ were performed invoking gradual *isostructural compression* of the experimental ambient pressure structure. In this way, the phase change was effectively bypassed. Figure 3.16a compares the VASP unit cell volume V_{cell} of the two modifications of [**3-2b**]$_2$, that is, the experimental π-dimer phase and a hypothetical σ-dimer phase derived using isostructural compression to suppress the phase transition. It is readily apparent that the hypothetical σ-dimer form undergoes a steady compression across the entire pressure range examined (0–14 GPa), but with formation of a π-dimer there is a contraction near 5 GPa. The enthalpy H of each phase as a function of pressure was estimated from the identity expression $H = E + PV$, using the total electronic energy E from the VASP calculations.

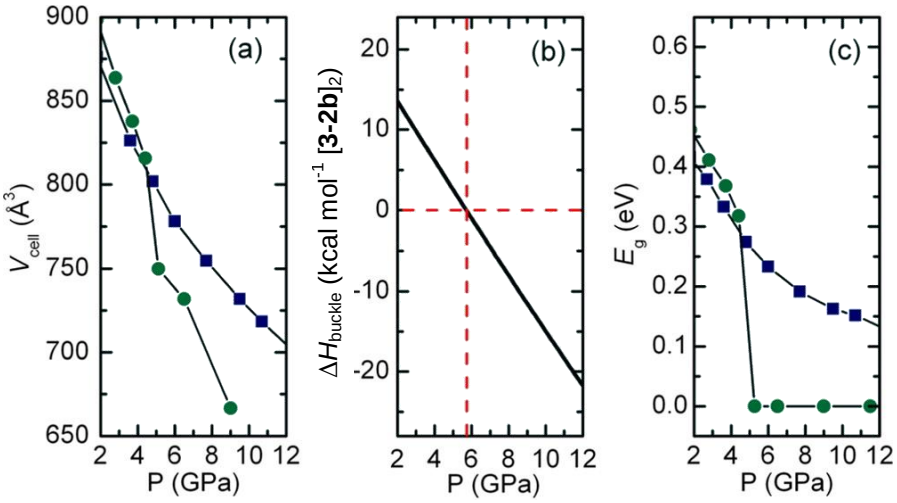

Figure 3.16 (a) Calculated cell volume V_{cell} of (hypothetical) σ-dimer and π-dimer phases, (b) calculated enthalpy difference ΔH_{buckle} for the σ-dimer to π-dimer phase conversion, and (c) calculated band gap E_g of the σ-dimer and π-dimer phases of [**3-2b**]$_2$ as a function of pressure. In parts a and c, data for the σ-dimer and π-dimer phases are represented respectively by blue squares and green circles.

The difference between the enthalpy values derived for each phase, *i.e.*, the enthalpy change ΔH_{buckle} for the buckling process, is plotted in Figure 3.16b. As expected, the uniformly compressed (σ-dimer) structure is predicted to be more stable at low pressures, with the buckled π-dimer taking over at higher pressures. Given the size of the computational problem, the predicted transition pressure of 5.7 GPa (the vertical line in Figure 3.16b) is in good agreement with experiment. Finally, Figure 3.16c provides a visual comparison of the indirect band gap E_g of the buckled and unbuckled forms as a function of pressure. Perhaps not surprisingly, the results for the σ-dimer modification of [**3-2b**]$_2$ are reminiscent of those illustrated in Figure 3.12 for [**3-2a**]$_2$. Essentially, without buckling, the band gap of [**3-2b**]$_2$ is predicted not to occur until well above 14 GPa.

3.4 Summary and Conclusions

Predicting or even modifying the crystal structures of molecular solids is never easy, as changes in molecular structure can often have a significant effect on crystal structure.[41] The rich variety of space groups observed for bisthiaselenazolyl radicals **3-1** with different R_1/R_2 groups[23] provides a clear demonstration of how relatively minor molecular tinkering can induce completely different crystal packing patterns and hence alter physical and electronic properties. Examples of **3-1** and **3-2** that dimerize are few, but when solid state association does occur, as in [**3-2a**]$_2$ and β-[**3-1a**]$_2$, the two radicals are linked *via* hypervalent 4c–6e S···E−E···S interactions. The resulting σ-dimers are isostructural at ambient pressure, crystallizing in the monoclinic space group $P2_1/c$ and packing in cross-braced slipped π-stacked arrays. Pairing of the spins affords a diamagnetic ground state and both materials behave as small band gap semiconductors.

With the application of physical pressure, the crystal structures compress significantly and charge transport improves such that room temperature conductivity increases by 5–6 orders of magnitude. The activation energies for the dimers decrease to 0.1 eV ([**3-2a**]$_2$) and 0.2 eV (β-[**3-1a**]$_2$) at 5 GPa, which is the limit of the experiment. Band structure calculations on [**3-2a**]$_2$ reveal that, although the band gap

diminishes considerably with pressure, closure of the gap is not expected until well over 10 GPa.

The significance of the present work lies in the fact that it demonstrates the similarity in the structure and transport properties of fluorine-substituted dimers β-[**3-1a**]$_2$ and [**3-2a**]$_2$, yet it breaks down under pressure when R_2 = H. Dimer [**3-2b**]$_2$ undergoes a phase transition near 5 GPa in which the unit cell experiences a "pancake-like" collapse, and the σ-dimer molecular structure buckles into a distorted π-dimer. By contrast the unit cells of [**3-2a**]$_2$ and β-[**3-1a**]$_2$ undergo a relatively uniform compression, with no change in the structure of the molecular dimers. Variable pressure conductivity measurements demonstrate that the phase transition in [**3-2b**]$_2$ gives rise to a metallic state near the phase transition, whereas the activation energy slowly diminishes for [**3-2a**]$_2$ and β-[**3-1a**]$_2$. Taken as a whole, the differing response of the structures of [**3-2a**]$_2$ and β-[**3-1a**]$_2$ *versus* [**3-2b**]$_2$ to applied pressure emphasizes the need to appreciate the subtlety within a molecular arrangement, which can have a deep impact on the bulk structure and properties of a material upon a slight perturbation.

3.5 Experimental Methods

General methods and procedures are described in Appendix A.

Preparation of 8-Fluoro-4-methyl-4H-bis[1,2,3]dithiazolo[4,5-b:5,4-e]pyridin-3-yl, 3-1a. Before use, all glassware was soaked overnight in dilute HNO_3, washed with deionized water followed by distilled water, and finally dried at 100 °C overnight. Magnetic stir bars were glass-covered. A sample of [**3-1a**][OTf] (700 mg, 1.69 mmol)[6] and DMFc (585 mg, 1.79 mmol) were combined in 20 mL of degassed (four freeze−pump−thaw cycles) MeCN at 0 °C. After the mixture was stirred for 4 h at room temperature, the black-green microcrystalline product (α-[**3-1a**]) was filtered off and washed with 5 × 10 mL of MeCN. Yield, 405 mg (1.51 mmol, 84 %). IR: 1510 (s), 1462 (s), 1352 (s), 1280 (s), 1238 (s) 1161 (m), 1125 (m), 1059 (w), 1026 (s), 937 (w), 867 (m), 791 (s), 760 (w), 713 (m), 678 (s), 653 (w), 637 (s), 577 (w), 559 (w), 516 (m), 500 (w), 472 (s). Radical phase α-**3-1a**: Crystals suitable for crystallographic work were obtained by slow diffusion across an H-cell between degassed (four freeze-

pump-thaw cycles) solutions of [**3-1a**][OTf] (28 mg, 0.0677 mmol) in 10 mL MeCN and DMFc (23 mg, 0.0705 mmol) in 15 mL MeCN. After 30 minutes, the long, thin needles of α-**3-1a** were prepared for single crystal diffraction experiments. Dimer phase β-[**3-1a**]$_2$: Crystals suitable for crystallographic work, as well as transport property measurements, were obtained by vacuum sublimation of the bulk material at 10^{-4} Torr in a three-zone furnace along a temperature gradient of 120 to 40 °C. This gave pure metallic bronze blocks of β-[**3-1a**]$_2$ after numerous trials and, often, manual separation of the two phases. IR: 1538 (s), 1508 (m), 1443 (s), 1396 (w), 1212 (w), 1100 (m), 1045 (m), 869 (w), 840 (m), 772 (s), 709 (w), 661 (s), 616 (w), 561 (w), 517 (w), 473 (m). Anal. Calcd for β-[**3-1a**]$_2$, $C_6H_3FN_3S_4$: C, 27.26; H, 1.14; N, 15.89. Found: C, 26.96; H, 1.61; N, 15.61.

High Pressure Crystallography. High pressure, ambient temperature diffraction experiments on [**3-2a**]$_2$ were performed at BLX10U, SPring-8, using synchrotron radiation (λ = 0.51446 Å) and a powdered sample mounted in a DAC, with helium as the pressure transmitting medium. The diffraction data were collected at room temperature and as a function of *increasing* pressure. A total of nine data sets from 0 GPa to 11.21 GPa were indexed and the cell parameters refined using DASH 3.1.[42] Six of these data sets were solved in DASH starting from a model half-dimer based on the atomic coordinates of [**3-2b**]$_2$ with the H-substituent replaced by a fluorine atom (with d(C-F) = 1.30 Å). During the Rietveld[43] refinement in DASH a rigid-body constraint was maintained. At this point the space group settings were adjusted so as to allow a direct comparison of all the cell parameters with those published for [**3-2b**]$_2$. For three data sets (Table 3.2) the settings and atomic coordinates from the DASH solution were then taken into GSAS[44] for a final Rietveld refinement. Data from 2θ = 3-20° were refined with fixed atomic positions and isotropic thermal parameters with an assigned value of 0.025.

High pressure, ambient temperature diffraction experiments on β-[**3-1a**]$_2$ were performed at High Energy X-ray Materials Analysis (HXMA) beamline of the Canadian Light Source using synchrotron radiation (λ = 0.509175 Å) and a powdered sample mounted in a diamond anvil cell, with low-viscosity (1 cst) polydimethylsiloxane as the pressure-transmitting medium. The diffraction data were collected at room temperature and as a function of *increasing* pressure. A total of five data sets from 2.53 to 7.69 GPa were indexed and the cell parameters refined using DASH 3.1. Two of these data sets were solved

in DASH starting from a model half-dimer based on the atomic coordinates of β-[**3-1a**]$_2$ collected at ambient pressure on a single crystal. During the Rietveld refinement in DASH a rigid-body constraint was maintained. For these two data sets (Table 3.2) the settings and atomic coordinates from the DASH solution were then taken into GSAS for a final Rietveld refinement. Data from 2θ = 3-20° were refined with fixed atomic positions and isotropic thermal parameters with an assigned value of 0.025. Measurements were taken by Drs. J. S. Tse and S. Desgreniers.

High Pressure Conductivity Measurements. High pressure conductivity experiments on β-[**3-1a**]$_2$ and [**3-2a**]$_2$ were carried out in a cubic anvil press[45] using pyrophyllite ($Al_4Si_8O_{20}(OH)_4$) as the pressure transmitting medium. Sample pressure was determined from previous calibrations of the applied hydraulic load against pressures of structure transformations in standards at room temperature (Hg L ↔ I at 0.75 GPa, Bi I ↔ II at 2.46 GPa, Tl 1 ↔ III at 3.70 GPa, and Ba 1 ↔ II at 5.5 GPa).[46] Two Pt electrodes contacted the pre-compacted, powder samples which were contained in a boron nitride ($\sigma_{BN} \approx 10^{-11}$ S cm^{-1}) cup. Four-wire AC (Solartron 1260 Impedance Analyzer) resistance measurements were made at a frequency of 1 kHz. The contiguous disk-shaped sample was extracted from the recovered pressure cell and the sample geometry was measured to convert resistance to conductivity. Measurements were taken by Dr. R. Secco at the University of Western Ontario, London, Ontario.

Electronic Structure Calculations. Charge densities for [**3-2a**]$_2$ and [**3-2b**]$_2$ were calculated using the UB3LYP functional and the split-valence double-ζ basis set 6-31G(d,p), as contained in the Gaussian 09W suite of programs.[47] Full geometry optimization was invoked.

All solid state electronic structure calculations were performed with the electronic code VASP (Vienna Ab initio Structure Package)[48] employing projector augment wave potentials[49] (PAW) to replace the core orbitals of all elements except H. The Perdew-Burke-Ernzerhof exchange and correlation functionals[50] within the generalized gradient approximation were used. The wavefunctions were expanded in plane wave basis sets. A grid of 4 × 2 × 2 *k*-points was used in the SCF and geometry optimization calculations. A more dense 16 × 4 × 4 *k*-point set was used for the calculation of the electron density of states. For [**3-2a**]$_2$ the crystal geometry at different pressures was used as a starting point for geometry optimizations. The VASP calculations were performed by collaborator Dr. J. S. Tse.

Chapter 4

Thermal, Optical and Pressure-Induced Radical-to-Dimer Interconversion

4.1 Introduction

In previous chapters, the effect of pressure on the structure and properties of a variety of bisdithiazolyl and bisthiaselenazolyl radicals was presented. Chapter 2 described the changes induced in unassociated ferromagnetic Mott insulators, while Chapter 3 provided details of the response of semiconducting hypervalent σ-dimers. In the previous chapter, the structure and properties of two S···E–E···S σ-dimers [**4-2**]$_2$ and [**4-3**]$_2$ (previously called β-[**3-1a**]$_2$ and [**3-2a**]$_2$) under pressure were thoroughly examined (Scheme 4.1). The results demonstrated that the slow and steady closure of the band gap in these intrinsic semiconductors is a result of band broadening.[1] This provided a baseline for what occurs under pressure in the absence of a phase transition, and provided a dramatic contrast to work that preceded my own on [**4-4**]$_2$,[2] which buckles to produce a structure with an abrupt closure of the HOMO-LUMO gap forming a metallic state near 5 GPa.

Scheme 4.1

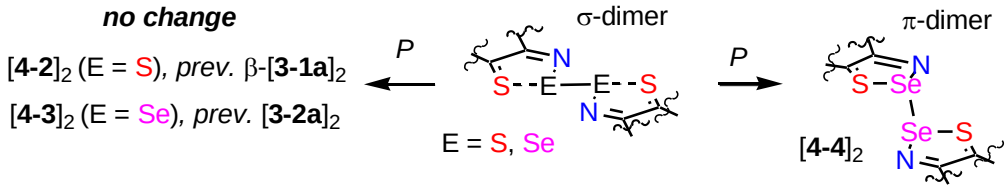

In the present chapter, radical dimers of this type will be further explored in the context of the structurally related compound β-[**4-1**]$_2$ (E = S; R_1 = Et; R_2 = F), which exhibits behavior under pressure that is in sharp contrast to all of the above dimers. This σ-dimer "pops" open to a pair of S = ½ radicals under the influence of temperature, pressure and light (Scheme 4.2).

Scheme 4.2

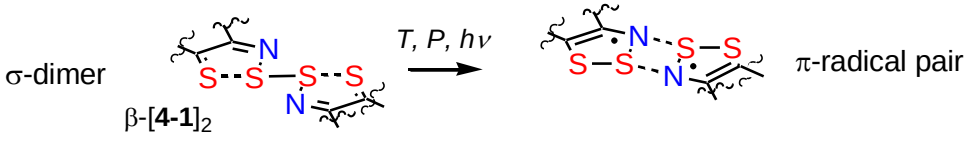

This sulfur-based material **4-1** is dimorphic, crystallizing in one case (α-**4-1**) as π-stacked radicals and in the other (β-**4-1**) as π-stacked dimers; in the latter structure the dimers consist of pairs of radicals laced together by hypervalent 4c–6e S···S–S···S σ-bonds, as shown in Chart 4.1.[3] Although this dimerization mode is rare for sulfur-based radicals,[4] it has been known for selenium radicals such as [**4-3**]$_2$ and [**4-4**]$_2$ for many years.[5] The remarkable response of the conductivity to pressure for these systems prompted further inquiries and a desire to correlate properties to their crystal structures.

Chart 4.1

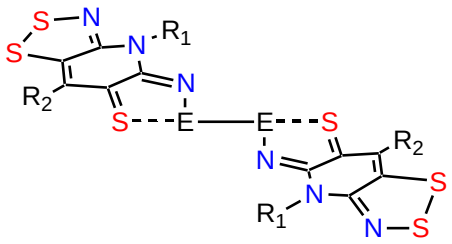

β-[**4-1**]$_2$: E = S, R_1 = Et, R_2 = F

	E	R_1	R_2
β-[**4-1**]$_2$	S	Et	F
[**4-2**]$_2$	S	Me	F
[**4-3**]$_2$	Se	Me	F
[**4-4**]$_2$	Se	Me	H

Dimerization of neutral π-radicals, particularly those based on the DTDAs, their selenium counterparts (DSDAs), as well as simple DTAs has been known for decades.[6] The various modes of dimerization are associated with the coupling of two magnetic π-orbitals, and the structural variations these may exhibit were presented in Chapter 1. The consequent pairing of spins, which is facilitated at low temperatures, quenches magnetic interactions and, to the extent that an electronic band model applies, gives rise to the opening of a band gap at the Fermi level. The resulting diamagnetic materials may have a lower conductivity than the parent radical, but there are cases where association actually improves conductivity.[7] There are also a few reports of magnetically bistable radicals, that is, systems which display temperature regimes within which the dimer (S = 0) and radical (S = ½) states can co-exist.[8,9] The magnetic hysteresis that is observed with these spin crossover phase transitions has led to interest in the potential use of bistable radicals in information storage devices.[10] In some cases, hysteresis is apparent in several channels (magnetic, electronic and optical), and these discoveries have fueled the pursuit of multifunctional materials.[11] In addition to the phase changes associated with

radical-to-dimer interconversions (RDI), there are numerous examples of radicals and radical dimers that crystallize as non-interconvertable polymorphs.[4,12]

The β-phase dimer of radical **4-1** crystallizes as crossbraced π-stacks of σ-dimers under ambient conditions. At elevated temperatures (~ 120 °C), the spin-paired dimer pops open abruptly to generate two open-shell radicals. This transformation has also been confirmed to occur under the application of mild external pressure (~ 0.7 GPa) and optically (~ 650 nm) *via* the so called LIESST (Light Induced Excited Spin State Trapping) effect. Although the reported bistability of the simple thiazyl radicals, such as the 1,3,2-DTAs, is a result of cooperative solid state effects, the process is fundamentally different from that which occurs for β-[**4-1**]$_2$. The present molecular rearrangement is also in contrast to the σ- to π-dimer interconversion of [**4-4**]$_2$ under pressure, which has been shown to lead to coalescence of the HOMO and LUMO bands and gives rise to a weakly metallic state.[2] These two processes will be compared in light of DFT calculations of the frontier molecular orbitals. A full paper on the majority of this work has been published,[13] however, a communication has been submitted on the more recent results of the optical experiments.[14]

4.2 Results

4.2.1 Synthesis and EPR Spectroscopy

The procedure (Scheme 4.3) for the preparation of **4-1** is based on methods developed for related radicals, and very similar to that shown in Chapter 3 for sulfur radical **4-2**.[15] Alkylation of 2,4,6-trifluoropyridine **4-5** with ethyl triflate produces *N*-ethyl-2,4,6-trifluoropyridinium triflate **4-6** which, upon treatment with gaseous ammonia, affords the corresponding 2,6-diaminopyridinium triflate **4-7**. Double Herz cyclization of the latter with sulfur monochloride (S_2Cl_2) in refluxing acetonitrile (MeCN) then furnishes the desired bisdithiazolylium framework in the form of the triflate salt [**4-1**][OTf].

Scheme 4.3

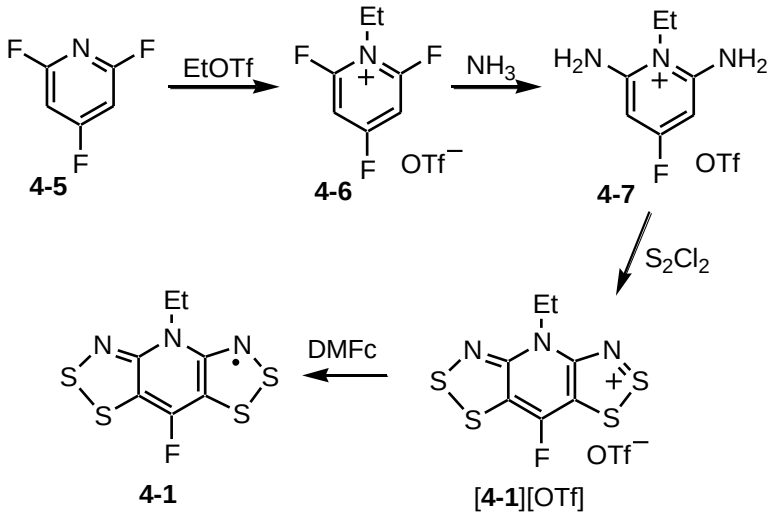

Cyclic voltammetry on solutions of this salt in MeCN, with 0.1 M *n*-Bu_4NPF_6 as supporting electrolyte and Pt wire electrodes, confirms the expected series (−1/0, 0/+1, +1/+2) of redox processes, and the half-wave potentials of these couples, which are listed in Table 4.1, are consistent with those seen for related radicals.[15] Based on these potentials, chemical reduction of [**4-1**][OTf] was conveniently effected using DMFc ($E_{½}$ (ox) = −0.13 V *vs*. SCE) in MeCN.[16] This afforded radical **4-1** as a black microcrystalline precipitate.

Subsequent purification and single crystal X-ray diffraction analysis of **4-1** (*vide infra*) established the existence of two polymorphs. The material prepared as described above, which can be recrystallized in small quantities as metallic green needles from hot dichloroethane, constitutes the tetragonal phase α-**4-1**. This phase can also be obtained by sublimation of the crude material in *vacuo*, but dark brown blocks of a second polymorph, subsequently established to be the monoclinic dimer phase β-[**4-1**]$_2$, are also produced in the process. Initially, crystals of the two phases were separated manually, but it was later discovered that β-[**4-1**]$_2$ could be generated almost exclusively by slow sublimation at a pressure of 10^{-4} Torr along a temperature gradient of 60−120 °C.[17] The infrared spectra of the two phases, shown in Figure 4.1, are very different, a feature which provides a simple method for assessing phase purity. The X-band EPR spectrum obtained by dissolving either phase of **4-1** in CH_2Cl_2 at 293 K consists of a seven-line pattern with additional fine structure (Figure 4.2). This is a somewhat different pattern to that

observed for the related chloro-substituted derivative **4-1** (R_1 = Et; R_2 = Cl),[15 a] which displays a quintet structure arising from hyperfine coupling to two equivalent DTA nitrogens ($I(^{14}N) = 1$), the value of a_N being approximately one-half of that observed in monofunctional 1,2,3-DTAs (Table 4.1).[18] Spectral simulation for **4-1** confirms that a_N remains much the same, but there is also coupling to fluorine ($I(^{19}F) = ½$), in addition to weaker coupling to the pyridine nitrogen and the methylene protons of the *N*-ethyl group.

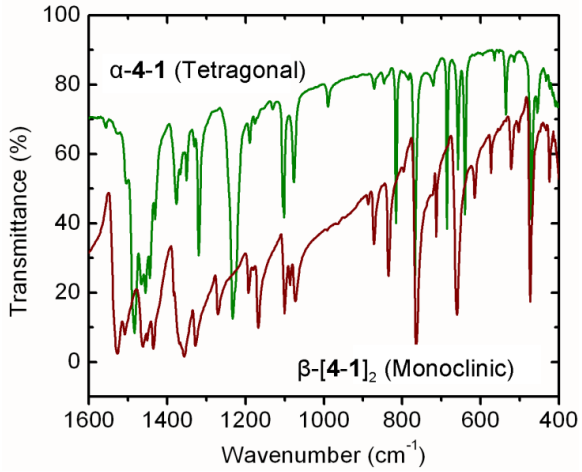

Figure 4.1 FTIR spectra of α- and β-phases of **4-1**.

Table 4.1 Electrochemical Half-Wave Potentials[a] and EPR Parameters for Derivatives of **4-1**.

R_1, R_2	Et, H [b]	Et, Cl [c]	Et, F (**4-1**)
$E_{½}$(−1/0), V	−0.95[d]	−0.845[d]	−0.822[d]
$E_{½}$(0/+1), V	−0.146	−0.018	+0.013
$E_{½}$(+1/+2), V	1.292	1.390	1.380
a_N (S), mT	0.318	0.310	0.307
a_N, (R_1), mT	0.061	0.060	0.057
a_H (CH_2), mT	< 0.02	< 0.02	< 0.03
a_R (R_2), mT	0.228	0.030[e]	0.637
g-value	2.0082	2.0082	2.0084

[a] In CH_3CN, reference to SCE. [b] From reference 15b. [c] From reference 15a. [d] Irreversible behavior; E_{pc} value quoted. [e] ^{35}Cl isotope.

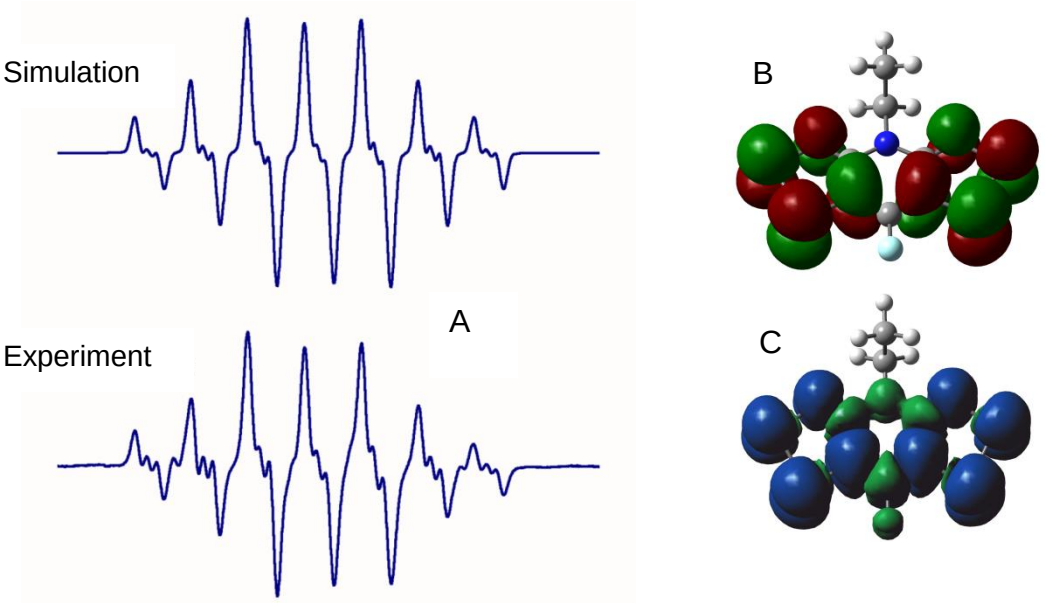

Figure 4.2 (a) Experimental and simulated EPR spectrum of **4-1** in CH_2Cl_2, SW = 3 mT, LW = 0.15 mT, L/G ratio = 0.60. (b) B3LYP/6-31G(d,p) SOMO and (c) spin density distribution for **4-1**.

4.2.2 Crystallography under Ambient Conditions

The crystal structures of both α-**4-1** and β-[**4-1**]$_2$ have been determined at ambient temperature and pressure by single crystal X-ray diffraction. Crystal metrics for the two phases are provided in Table 4.2, and ORTEP thermal ellipsoid drawings of the molecular building blocks, showing atom numbering schemes, are illustrated in Figure 4.3.

Crystals of α-**4-1** belong to the tetragonal space group $P\bar{4}2_1m$ and are isomorphous with the family of radicals discussed thoroughly in Chapter 2.[19] The crystal structure consists of undimerized radicals bisected by mirror planes and locked into pinwheel-like clusters about the $\bar{4}$ centers of the unit cell. Each of the four radicals within the pinwheel provides the basis for a slipped π-stack array running along the *z*-direction. The mean interplanar separation δ (3.478(1) Å) and the inclination angle τ (57.42(1) °) are similar to those found for related radicals under ambient conditions. Views of the crystal structure of α-**4-1** along directions parallel and perpendicular to the stacking axis are shown in

Figure 4.4. While the radicals are not dimerized, that is, there is no pairing of spins into a localized covalent bond in this polymorph, there are numerous intermolecular S···S' contacts d_1 (3.4022(13) Å), d_2 (3.5311(14) Å) and d_3 (3.5168(10) Å) within the nominal van der Waals separation for sulfur (3.6 Å).[20] As observed in related structures, these contacts generate an extensive lattice-wide network of electronic and magnetic interactions.

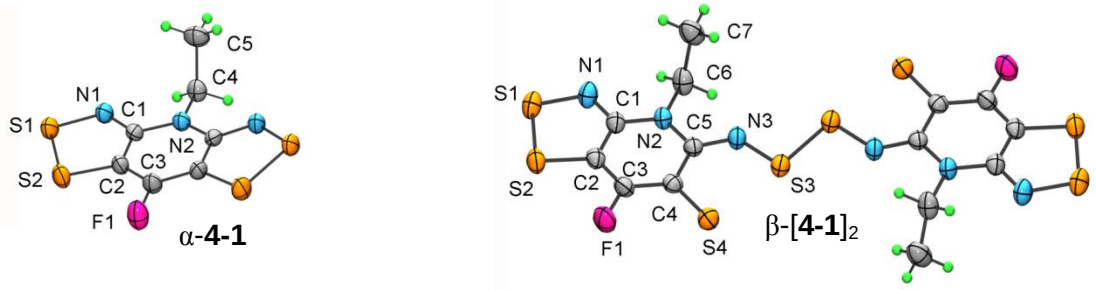

Figure 4.3 ORTEP drawings (50% probability ellipsoids) of α-**4-1** and β-[**4-1**]$_2$ at ambient pressure and temperature, showing atom numbering.

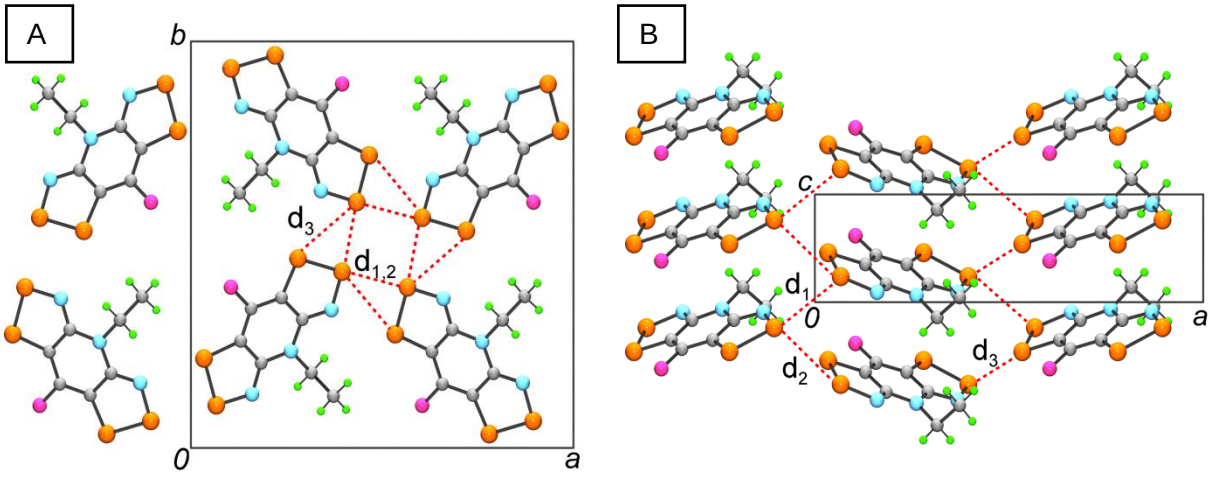

Figure 4.4 Crystal structure parallel to the (a) (stacking) *z*-axis and (b) *a*-axis for α-**4-1**.

By contrast, crystals of β-[**4-1**]$_2$ belong to the monoclinic space group $P2_1/c$,[21] and consist of interpenetrating, cross-braced slipped π-stacks of dimers, which, at ambient conditions are isomorphous to [**4-2**]$_2$, [**4-3**]$_2$ and [**4-4**]$_2$. At the molecular level these dimers comprise coplanar radicals fused in a centrosymmetric fashion by the hypervalent S4···S3−S3···S4 sequence. While the associated S3−S3' bond length is near that expected for a σ-bond, the S3−S4 distance opens to a value intermediate

between the sum of the covalent radii[22] and the expected van der Waals contact.[20] Within this supermolecule there is a series of bond length changes relative to those seen in the undisturbed radical found in the tetragonal phase above, the most notable being a shortening of the C4−N3 and C5−S4 distances, all of which are consistent with the closed shell pseudo-quinoidal valence bond formulation shown in Chart 4.1.

The packing of the dimers in β-[**4-1**]$_2$ is illustrated in Figure 4.5, which shows the ambient pressure and temperature unit cell viewed parallel to the *a* axis. Neighboring π-stacks along the *z* direction are tilted in opposite directions relative to the *a* axis so as to give the cross-braced pattern shown in Figure 4.5b. This cross-braced packing arrangement affords a series of close inter-dimer S···S' interactions d_1−d_3, the values of which are listed in Table 4.3, including the value of τ and the dimer-to-dimer separation along the π-stacks δ. Changes in these parameters, as well as in *q* and *r* (to be defined later), as a function of temperature and pressure are discussed below.

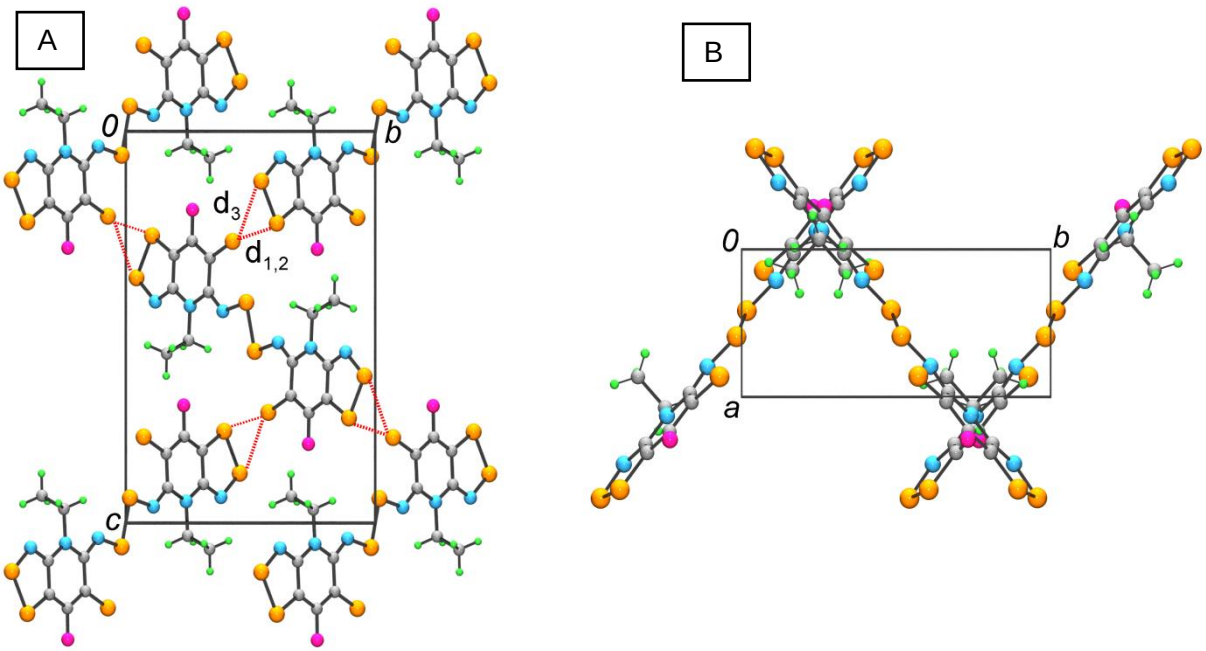

Figure 4.5 Crystal packing of β-[**4-1**]$_2$ at ambient *T* and *P*, viewed along the (a) *x* and (b) *z* directions.

Table 4.2 Crystal Data for **4-1** under Various Conditions

	α-**4-1**	β-[**4-1**]$_2$	β-[**4-1**]$_2$	β-[**4-1**]$_2$	β-[**4-1**]$_2$
Pressure	0 GPa	0 GPa	0 GPa	0.65 GPa	0.98 GPa
temp (K)	293(2)	296(2)	393(2)	293(2)	293(2)
Formula	$C_7H_5FN_3S_4$	$C_7H_5FN_3S_4$	$C_7H_5FN_3S_4$	$C_7H_5FN_3S_4$	$C_7H_5FN_3S_4$
M	278.38	278.38	278.38	278.38	278.38
a, Å	15.8542(7)	5.3256(3)	5.2038(4)	5.3225(6)	5.1026(5)
b, Å	15.8542(7)	11.3951(7)	11.6317(4)	11.0910(10)	11.0754(9)
c, Å	4.1273(3)	17.3934(10)	17.7657(9)	17.1492(15)	17.1529(16)
β, deg	90	105.105(2)	105.746(5)	105.095(8)	104.824(8)
V, Å^3	1037.42(10)	1019.06(10)	1034.99(10)	977.42(17)	937.10(15)
ρ_{calcd} (g cm^{-1})	1.782	1.814	1.786	1.891	1.973
space group	$P\bar{4}2_1m$	$P2_1/c$	$P2_1/c$	$P2_1/c$	$P2_1/c$
Z	4	4	4	4	4
μ (mm^{-1})	0.895	0.911	---	---	---
λ (Å)	0.71073	0.71073	1.54056	0.509176	0.509176
data/restr./ parameters	1095/0/76	2444/0/137	---	---	---
solution method	direct methods	direct methods	powder data[a]	powder data[b]	powder data[b]
R, R_w (on F^2)	0.0309, 0.0714	0.0364, 0.0835	0.0797, 0.1421	0.0143, 0.0284	0.0138, 0.0240

[a] Le Bail refinement. [b] Rietveld refinement.

Table 4.3 Structural Parameters for β-[**4-1**]$_2$ as a Function of Temperature and Pressure

Temp (K)	296(2)	393(2)	293(2)	293(2)
Pressure (GPa)	0	0	0.65	0.98
S3−S3' (Å)	2.1687(13)	---	2.248	---
S3−S4 (Å)	2.794	2.167	2.739	2.185
S2···S4', d_1 (Å)	3.321	3.493	3.293	3.133
S2···S4', d_2 (Å)	3.550	3.507	3.431	3.302
S1···S4', d_3 (Å)	3.375	3.835	3.311	3.351
S3···N3', d_4 (Å)	---	2.981	---	3.048
τ (deg)	42.49(1)	42.58	40.47	41.19
δ (Å)	3.584(1)	3.519	3.449	3.358
r (Å)	2.169	2.977	2.246	3.036
q (Å)	−0.046	1.526	0.093	1.946

In many ways, this structure is very similar to the related sulfur-based dimer [**4-2**]$_2$, described in detail in Chapter 3. The main difference between the two, however, is the tightness in the packing, which more than likely leads to the sharp contrast in the behavior of the materials upon perturbation. For example, the sulfur-based methyl derivative [**4-2**]$_2$ possesses strong 4-center S···N' interactions (3.092 Å) between dimers that lock the planes of dimers together. In the ethyl derivative β-[**4-1**]$_2$, these contacts are much longer and weaker (3.733 Å), leading to a "softer" structure.

4.2.3. Magnetic Measurements

Magnetic susceptibility (χ) measurements have been performed on the α- and β-phases of **4-1** over the temperature range 2−400 K using a SQUID magnetometer operating at a field (H) of 1000 Oe. Figure 4.6 shows the results of data collected over the range T = 2−300 K for α-**4-1**, presented in the form of plots of χ (corrected for diamagnetic contributions) and χT against T. The tetragonal phase α-**4-1** behaves as a Curie-Weiss paramagnet, and a fit to the 20−300 K data affords values of C = 0.348 emu·K·mol^{-1} and θ = −0.5 K. The data from the 2−300 K range was also modeled in terms of a

Heisenberg chain of AFM coupled S = ½ radicals, using a fit function based on the molecular-field modified Bonner-Fisher method[23] and the Heisenberg Hamiltonian H_{ex} = -2$\boldsymbol{J}${$S_1 \cdot S_2$}.[24] The relatively large and positive (FM) mean field term z$\boldsymbol{J'}$ = +13.3 cm^{-1} so obtained is consistent with the combined pairwise interstack exchange energies[19c,25] $\boldsymbol{J}_1$ = 2.9 cm^{-1} (with z = 4) and $\boldsymbol{J}_2$ = 0.6 cm^{-1} (with z = 4) defined in Figure 4.6 and estimated using Broken Symmetry DFT methods.[26,27] Likewise the AFM exchange energy $\boldsymbol{J}$ = −9.6 cm^{-1} extracted from the 1D-chain model is in accord with that calculated for the intrastack[25] exchange interaction $\boldsymbol{J}_\pi$ = −14.1 cm^{-1}.

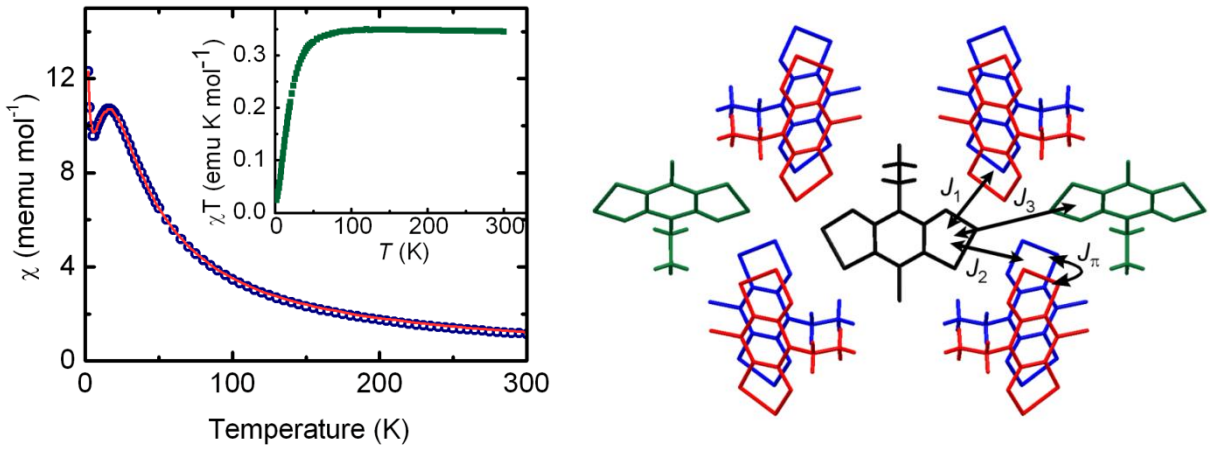

Figure 4.6 (Left) Plots of χ and χT (insert) *versus* T for α-**4-1** from T = 2−300 K. The red line shows the fit of χ *versus* T for α-**4-1** to a 1D chain of AFM coupled S = ½ radicals. (Right) Definition of magnetic interactions $\boldsymbol{J}_1$, $\boldsymbol{J}_2$, $\boldsymbol{J}_3$ and $\boldsymbol{J}_\pi$ for α-**4-1**. See ref 14 for more details.

As expected from the presence of a covalent bond between the two radicals in the dimeric unit in β-[**4-1**]$_2$, the near base-line plot (Figure 4.7) of χ *versus* T in the 2−300 K range indicates that the material is essentially diamagnetic, similarly to that found for dimer [**4-2**]$_2$. The related plot of χT against temperature indicates a very slow increase in χT to a value of 0.019 emu K mol^{-1} at 300 K, which corresponds to a defect concentration of about 5 %. This result is in keeping with the behavior of related dimers.[5] However, the fact that β-[**4-1**]$_2$ can be vaporized under relatively mild conditions (at 120 °C/10^{-4} Torr) led us to consider whether the dimer might actually dissociate in the solid state prior

to vaporization. To explore this possibility, we extended the temperature range for the measurement of the magnetic susceptibility to T = 400 K. The results reveal a sharp rise in χT at $T\uparrow$ = 380 K to a plateau near 0.33 emu K mol^{-1}, a value close to that expected (0.375 emu K mol^{-1}) for a fully dissociated radical with S = ½ and a nominal g-value of 2. Moreover, upon cooling the sample the χT value reverts to its original near-diamagnetic value, but the changeover occurs at a slightly lower temperature ($T\downarrow$ = 375 K) than that found during the heating process. Collectively these changes represent the signature of a hysteretic dimer-to-radical phase change, with a region of bistability of about 5 degrees Kelvin.

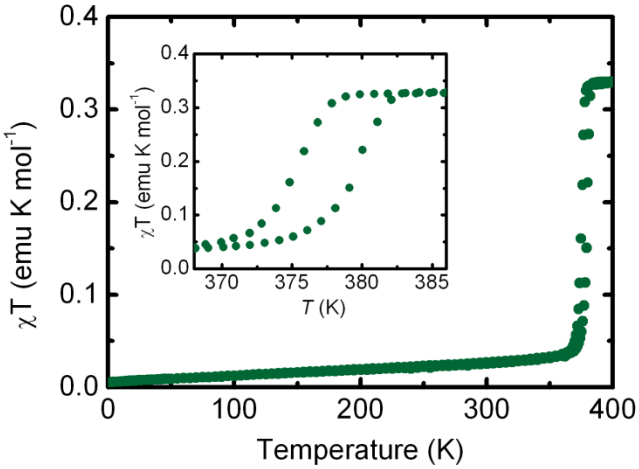

Figure 4.7 Plot of χT *versus* T for β-**4-1** from T = 2−400 K. Insert shows the hysteretic phase transition.

4.2.4 High Temperature Crystallography

In order to investigate the structural changes associated with the phase transition observed in the magnetic measurements, we performed a high temperature (T = 393 K) structural analysis of β-[**4-1**]$_2$ using powder X-ray diffraction methods. The powder pattern so obtained (Figure 4.8) was indexed and solved with DASH using a model geometry for the molecule taken from a UB3LYP/6-311G(d,p) calculation. During the initial refinement in DASH a rigid-body constraint was maintained, but the sulfur positions were later released to optimize within the plane of the molecule. Given the high thermal motion and consequent low resolution of the diffraction pattern, the final structural refinement was

successfully performed using Le Bail methods. Crystal data and relevant metrics are compiled in Tables 4.2 and 4.3, and a drawing of the crystal structure is shown in Figure 4.9.

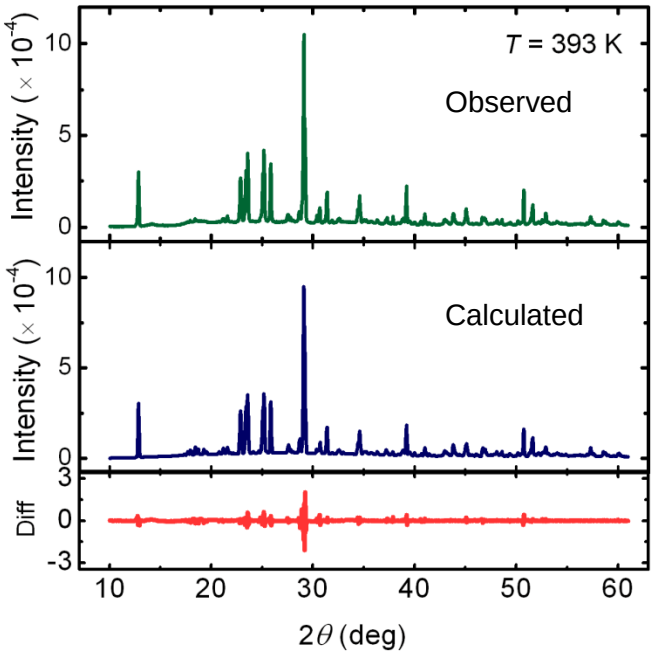

Figure 4.8 Observed and calculated powder X-ray diffraction pattern for β-[**4-1**]$_2$ at 393 K (λ = 1.54056 Å).

In accord with the magnetic measurements, the high temperature form of β-[**4-1**]$_2$ consists of undimerized radicals. The intermolecular S3−S3' bond present at ambient temperature is replaced by weak 4-center S3···N3' interactions (d_4), a common feature of the packing of thiazyl heterocycles, and the transannular hypervalent S3−S4 contact closes to a value comparable to that of S1−S2, that is, a normal covalent S−S distance. In addition there are long range intermolecular S2···S4' contacts (Table 4.3) that lace together molecules up and down the stacking direction.

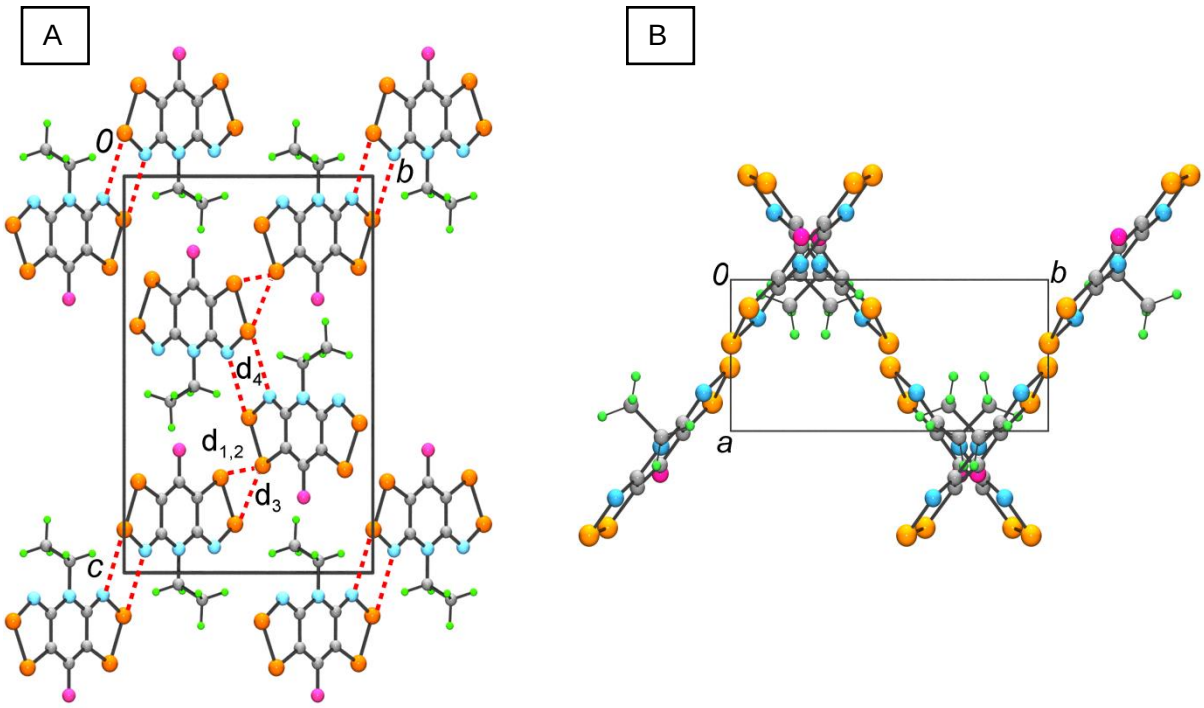

Figure 4.9 Crystal packing of β-[**4-1**]$_2$ at ambient T = 393 K, viewed along the (a) x and (b) z directions.

4.2.5 Photomagnetic Measurements

Recently, the possibility that this RDI could be effected not only thermally, but optically as well, has been raised. Indeed, when a crystalline sample of β-[**4-1**]$_2$ is carefully irradiated (at 10 K) with a laser tuned to λ = 650 nm the transformation of the diamagnetic dimer to a pair of S = ½ radicals **4-1** is observed with an increase in the magnetic susceptibility of the sample. The magnetic susceptibility, presented in the form of a $\Delta\chi T$ *versus* T plot in Figure 4.10, was measured in warming mode after turning off the laser. The resulting plot demonstrates the steady increase in χT to 230 K, after which temperature the susceptibility begins to retreat, first gradually, and then abruptly starting at 240 K suggesting a thermally activated relaxation of the photoinduced metastable radicals **4-1** to the thermodynamically favored dimer β-[**4-1**]$_2$. Above 260 K, the observed χT value matches that measured for the sample of β-[**4-1**]$_2$ prior to irradiation. Further heating results in an abrupt increase in χT around 380 K, which is consistent with the thermally induced RDI shown in Figure 4.7. X-ray diffraction data

was collected on an irradiated single crystal of β-[**4-1**]$_2$ at 100 K, demonstrating the full conversion to a pair of unassociated radicals.[28] Satisfyingly, photoinduced radical **4-1** is isostructural with the product of the thermally induced RDI, which was structurally characterized by powder crystallography (section 4.2.4).

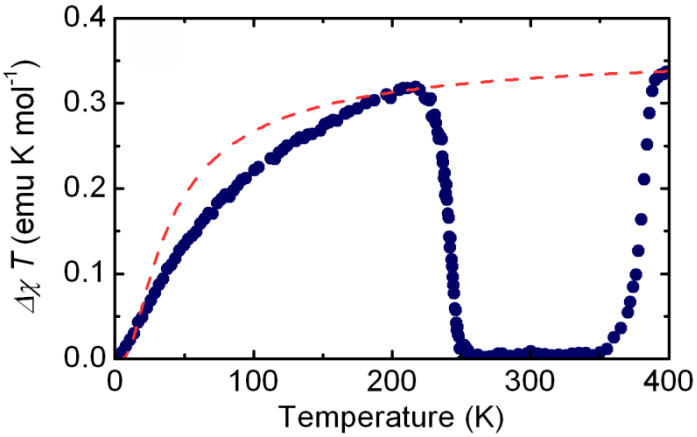

Figure 4.10 Plot of the change in χT *versus* T of the photoinduced (λ = 650 nm at 10 K) transition of β-[**4-1**]$_2$ → 2 **4-1**. The dashed red line tracks the theoretical value of χT for **4-1** estimated from exact diagonalization simulations based on exchange energies obtained from broken symmetry DFT calculations.

To understand the magnetic response of **4-1** in the low temperature (< 230 K) region, a series of broken symmetry DFT calculations at the UB3LYP/6-311G(d,p) level were carried out to estimate the magnitude of the pairwise magnetic exchange coupling constants (***J***) within the photoinduced crystal structure. As expected, the dominant exchange interactions are AFM, corresponding to coupling along the π-stacks (–18.4 cm^{-1}) and between the formerly dimerized radical pairs (–13.9 cm^{-1}). The entire set of calculated ***J***-values was then used to generate a 16-site exact diagonalization[29] simulation of the bulk magnetic susceptibility of **4-1** as a function of temperature. The resulting theoretically predicted $\chi T(T)$ function, shown in Figure 4.11 as a dashed red line, is in good qualitative agreement with the experimentally observed data over the same range. Extrapolation of the function to higher temperatures suggests that the residual effects of AFM exchange interactions may slightly suppress the χT value even of the thermally generated radical (above 380 K).

4.3 High Pressure Measurements

4.3.1 Conductivity of α-4-1 and β-[4-1]$_2$

Pressure dependent conductivity measurements over the temperature range T = 300 – 400 K have been performed on both phases of **4-1** (α-**4-1** and β-[**4-1**]$_2$) using a cubic anvil press. The initial purpose of this exercise was to extract thermal activation energies for the conductivity of the two structures as a function of pressure, but it soon became apparent that the behavior of the two phases under pressure was quite different. Figure 4.11 shows the raw data of the conductivity as a function of temperature and pressure for both α-**4-1** and β-[**4-1**]$_2$. Although the plot for α-**4-1** shows typical behavior for a Mott insulator undergoing a decrease in activation energy with pressure, the data for the dimer β-[**4-1**]$_2$ displays peculiar behavior in the low pressure (0.57 GPa – 1.41 GPa) region. There is a clear inversion of the conductivity with decreasing temperature.

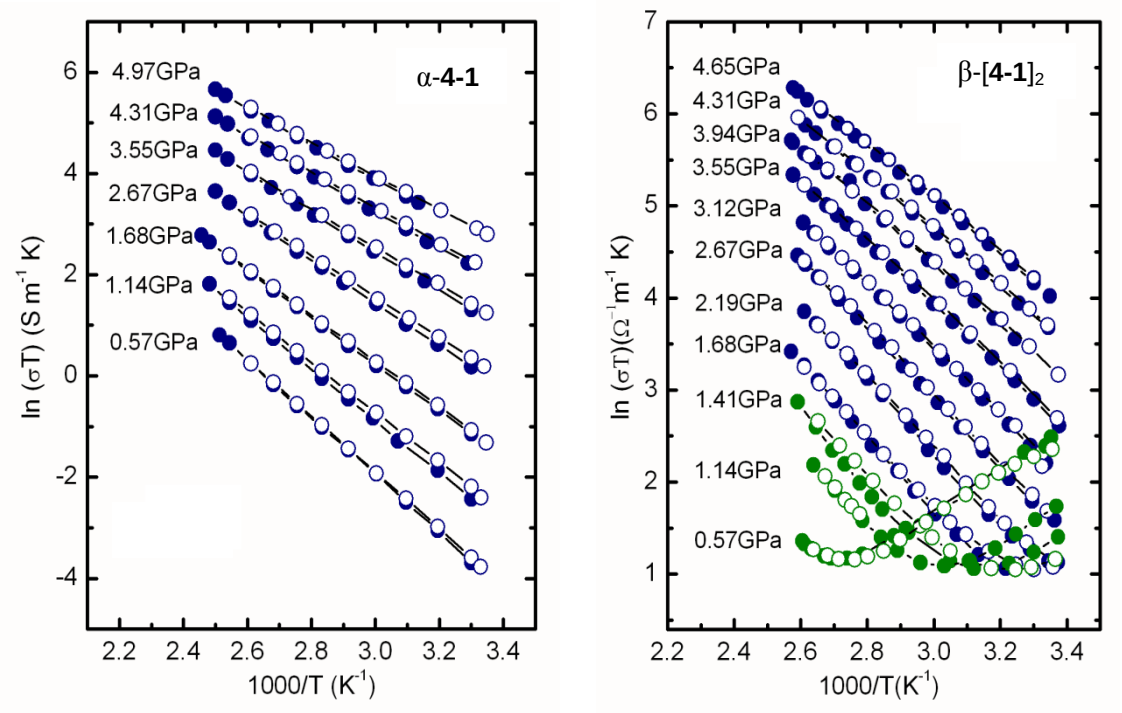

Figure 4.11 Raw data displaying ln(σT) *versus* 1000/*T* as a function of pressure for α-**4-1** (left) and β-[**4-1**]$_2$ (right) with decreasing (closed circles) and increasing (open circles) *T*.

To demonstrate this further, in Figure 4.12 plots of the pressure dependence of the conductivity of both phases are shown at ambient temperature (T = 298 K) and also at T = 383 K, that is, just above the transition temperature for the thermally induced RDI of the monoclinic β-phase. For both phases the data collected at 383 K reveal a smooth and steady increase in conductivity of about 2 orders of magnitude over the pressure range 0.5 to 5 GPa, as would be expected given that at this temperature both structures consist of slipped π-stacks of radicals. The α-phase is less conductive than the β-phase, a feature which provides a simple and elegant illustration of how changes in packing patterns based on exactly the same molecular building block can result in significant differences in solid state electronic structure and hence charge transport properties.

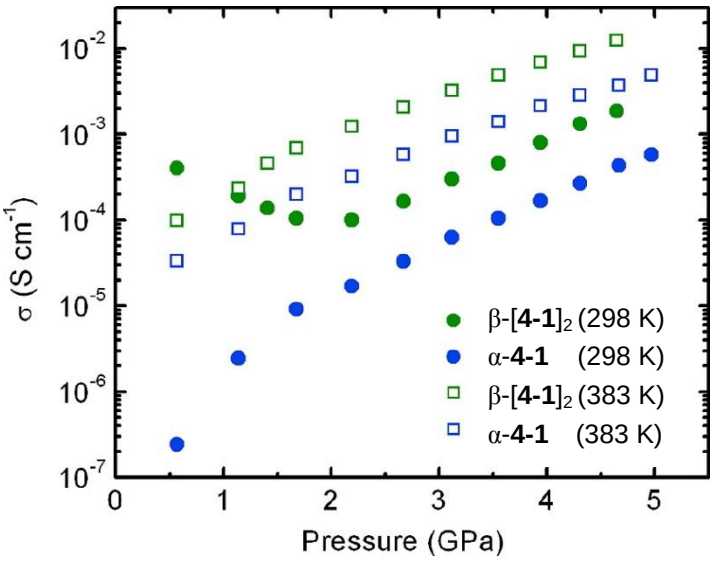

Figure 4.12 Conductivity of α-**4-1** and β-[**4-1**]$_2$ as a function of pressure at 298 K and 383 K.

At ambient temperature (298 K) the σ *versus P* plot for α-**4-1** shows the same trend as that observed at T = 383 K, although the increase in conductivity is somewhat larger, now spanning over 3 orders of magnitude. In addition, and as expected for a thermally activated process, the conductivity at 298 K at a given pressure is lower than that observed at 383 K. Values of the thermal activation energy E_{act} extracted from a series of σ(P,T) measurements over the range T = 298 to 383 K and P = 0.5−4.5 GPa are plotted in Figure 4.13. The results show a pressure driven decrease in E_{act} from near 0.50 eV at 0.5 GPa to near 0.30 eV at 5.0 GPa for α-**4-1**, a variation which parallels the trends seen for other slipped π-

stack radicals based on the bisdithiazolyl framework.[25a] Values of the thermal activation energy E_{act} above 2 GPa for β-[**4-1**]$_2$ are lower than those found for α-**4-1**, but the rate of decrease in E_{act} with pressure of the two phases is qualitatively similar.

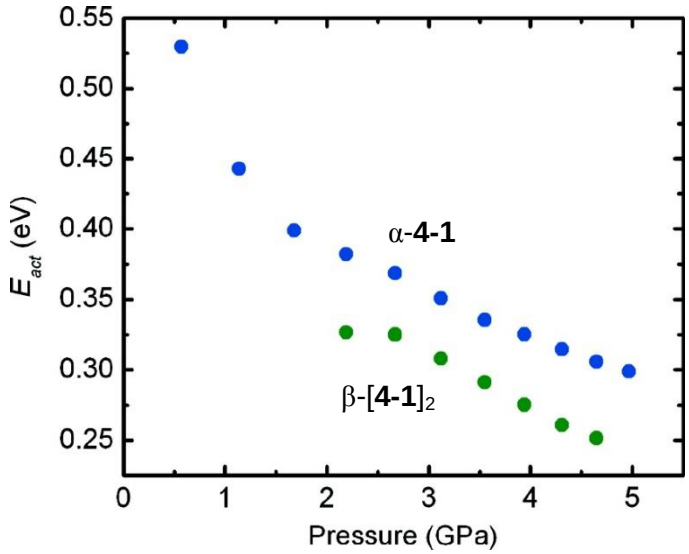

Figure 4.13 Activation energy for conductivity E_{act} (extracted over the range T = 298–383 K) of α-**4-1** and β-[**4-1**]$_2$ as function of pressure.

The pressure dependence of σ(P) for β-[**4-1**]$_2$ at 298 K is more complex than that observed for α-**4-1** at the same temperature, and indeed that displayed by β-[**4-1**]$_2$ itself at 383 K. Instead of a steady rise in conductivity with increasing pressure, the value of σ(298 K) actually decreases from 4×10^{-4} S cm^{-1} at 0.5 GPa to 1×10^{-4} S cm^{-1} at 1.5 GPa. At pressures beyond 2.0 GPa the trend reverses, and the value of σ(298 K) increases steadily along a path which parallels that observed for α-**4-1**. These changes, along with the fact that σ(298 K) for β-[**4-1**]$_2$ at 0.5 GPa is over an order of magnitude greater than σ(383 K) at the same pressure, can be interpreted in terms of the fact that in its dimeric form β-[**4-1**]$_2$ behaves as a small band gap semiconductor. With increasing temperature or pressure the dimer eventually dissociates to afford a Mott insulating radical structure, the conductivity of which is lower (by an order of magnitude) than that of the diamagnetic dimer. The rather sluggish RDI with pressure, indicated by the slow change in conductivity over the pressure range 0.5 to 2.0 GPa, probably reflects a less than perfectly isotropic pressurization of the sample in the cubic anvil press.

4.3.2 High Pressure Crystallography

In order to investigate the structural nature of the phase change observed in the high pressure conductivity measurements on β-[**4-1**]$_2$, a series of powder diffraction data sets on β-[**4-1**]$_2$ were collected at room temperature as a function of increasing pressure, using synchrotron radiation (λ = 0.509176 Å) and DAC techniques. Inspection of changes in the powder patterns and the consequent variations in the unit cell volume obtained from DASH over the pressure range 0−1.2 GPa, suggested the occurrence of a first order phase transition[30] between 0.6 and 0.8 GPa (Figure 4.14).[31]

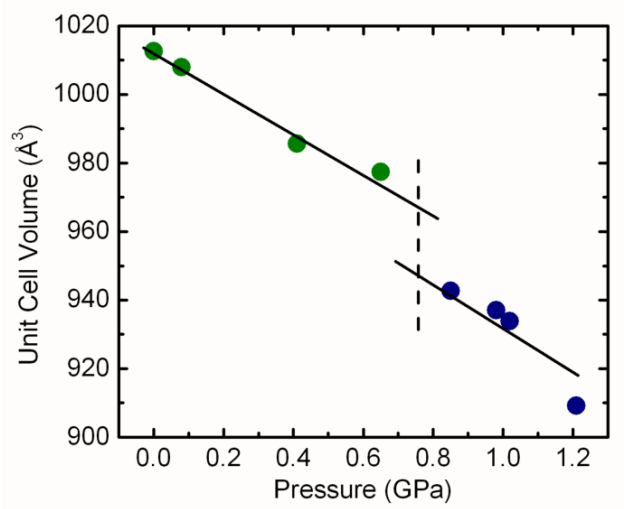

Figure 4.14 Change in unit cell volume of β-[**4-1**]$_2$ as a function of pressure.

Accordingly, two data sets collected at 0.65 GPa and 0.98 GPa, that is, just below and above and the phase transition, were solved starting from a model radical **4-1** derived from a fully optimized UB3LYP/6-311G(d,p) calculation. During the initial Rietveld refinement, performed using DASH, a rigid-body constraint was maintained, but the sulfur positions were later released to optimize within the plane of the molecule. The final Rietveld refinement, with fixed atomic positions and isotropic thermal parameters, was performed using GSAS. The experimental and final calculated powder patterns for the two data sets are shown in Figure 4.15. Final unit cell and refinement parameters are listed in Table 4.2.

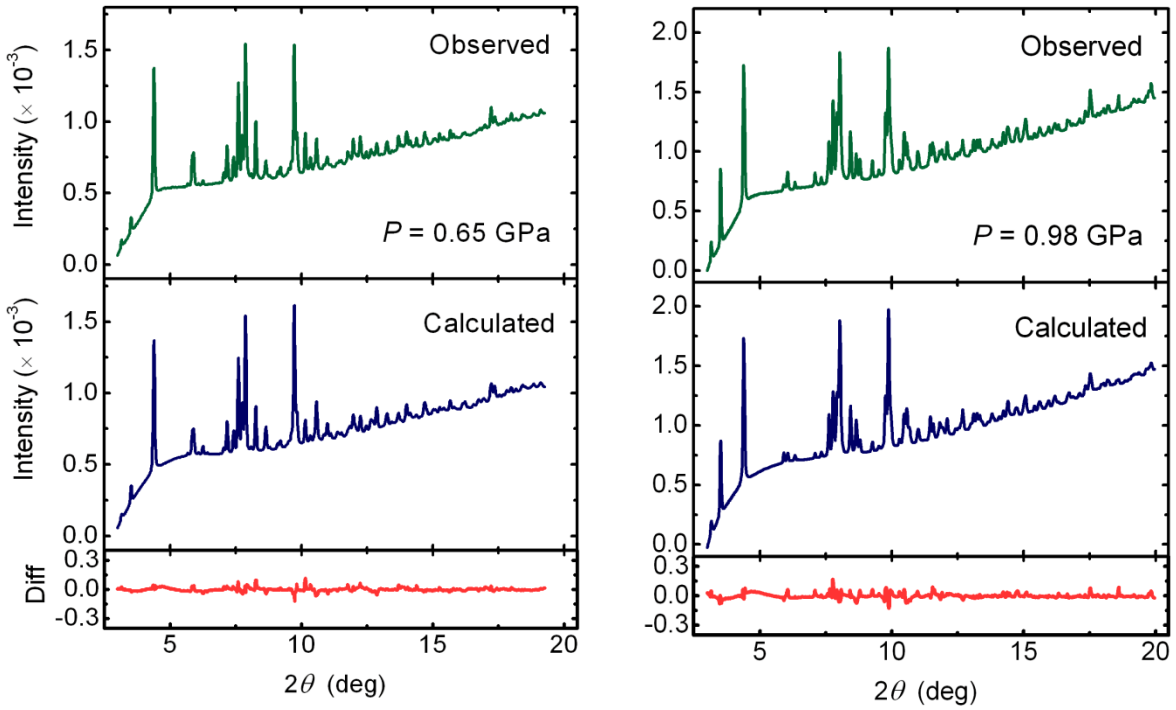

Figure 4.15 Observed and calculated powder X-ray diffraction pattern for β-[**4-1**]$_2$ at both 0.65 GPa (left) and 0.98 GPa (right) (λ = 0.509176 Å).

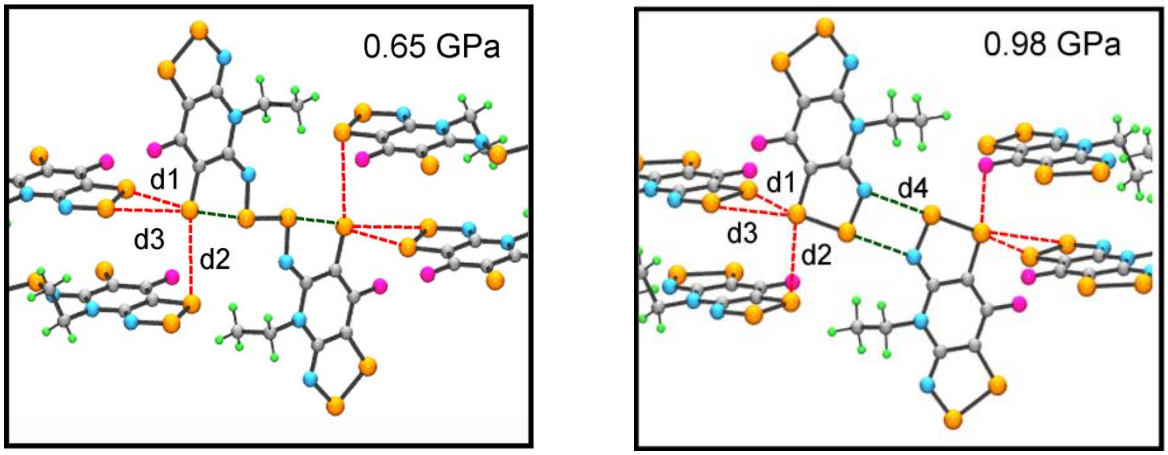

Figure 4.16 Transformation of β-[**4-1**]$_2$ from a 4c−6e σ-dimer at 0.65 GPa to a π-radical pair at 0.98 GPa.

The crystallographic results confirm a phase transition between 0.65 GPa and 0.98 GPa and establish that, at the molecular level, the structural changes are the same as those induced by heating, *i.e.*, a spin crossover from a 4c−6e hypervalent σ-dimer to a π-radical pair linked by weak intermolecular S···N'

contacts. These changes are illustrated in Figure 4.16 by means of comparative diagrams of the disulfide core at 0.65 GPa and the π-radical pair at 0.95 GPa. Concomitant with these changes, there is a general compression in the intermolecular S···S' contacts, values of which are summarized in Table 4.3.

4.4 Discussion

From a structural perspective the bisdithiazolyl radical **4-1** is interesting for several reasons. First, it is dimorphic, crystallizing in two distinct morphologies, the α-phase consisting of π-stacked radicals and the β-phase comprising π-stacked hypervalent 4c−6e σ-dimers. While the tetragonal packing motif of the α-phase has been observed before, indeed as the structure type displayed by the ferromagnetic radicals from Chapter 2,[19] the hypervalent σ-dimer motif is uncommon in the absence of selenium.[4,32] The second feature of note is the response of the β-phase to increases in temperature and pressure, and irradiation with light, all of which cause the σ-dimer to open into a pair of π-radicals. This phase transition has been identified crystallographically, but is also manifest through changes in the magnetic and conductive properties of the material. In the magnetic channel the thermal spin crossover from the σ-dimer ($S = 0$) to the π-radical ($S = ½$) is sharp and slightly hysteretic, displaying a range of bistability of about 5 K. At the same time the conversion of the closed shell σ-dimer, a small band-gap semiconductor, to an open shell π-radical, an $f = ½$ Mott insulator, gives rise to a decrease in conductivity under pressure. The transition also occurs photochemically and the metastable $S = ½$ radical phase persists almost to room temperature.

The ability to alter both the structure and transport properties of β-[**4-1**]$_2$ thermally, optically and with pressure makes this type of system of potential value in the development of new electronic and magnetoelectronic materials.[11,33] There are several questions, however, that need to be addressed before such an endeavor might be pursued. Can we understand, for example, the origin of the magnetic hysteresis associated with the dimer-to-radical interchange? Likewise, is it possible to rationalize the

structural response to pressure of β-[**4**-**1**]$_2$ with that of the hypervalent σ-dimer based on the related Se-centered radical dimer [**4**-**4**]$_2$ (R_1 = Me; R_2 = H)? While the latter crystallizes in the same space group and with the same packing pattern as β-[**4**-**1**]$_2$, and for that matter [**4**-**2**]$_2$ and [**4**-**3**]$_2$ (Chapter 3), it does not dissociate under pressure to form a Mott insulator, but instead undergoes a semiconductor-to-metal phase transition near 5 GPa.[34] Crystallographic analysis revealed not a dimer-to-radical switch-over, as observed here, but a distortion in which the *planar* σ-dimer buckles to form a strained π-dimer, as illustrated in Scheme 4.1.[2]

This deformation allows for an overall compression of the molecular framework, and also gives rise to a sharp decrease in the HOMO-LUMO gap, a process which, when coupled with the expected effects of compression on band broadening, leads to a closure of the valence-to-conduction band gap and the formation of a weakly metallic state. In the analysis of the buckling process of [**4**-**4**]$_2$ an energy barrier of about 20 kcal mol^{-1} for the conversion of the σ-dimer to a distorted π-dimer was estimated. Using the same model and theoretical method, we find an almost identical barrier for E = S, and from this result we conclude that the dissociation of β-[**4**-**1**]$_2$ to produce a pair of π-radicals must be energetically a much more facile process. If, however, that is the case, why do dimers based on [**4**-**4**]$_2$ not also slide apart under pressure to afford radicals?

To explore these issues, the total energy changes associated with the transformation of S···S−S···S and S···Se−Se···S σ-dimers into pairs of π-radicals has been examined at the (U)B3LYP/6-31G(d,p) level using models of the sulfur-based (**4**-**8**) and sulfur/selenium-based radicals (**4**-**9)** with R_1 = R_2 = H, each optimized within the constraints of C_{2h} symmetry.[35]

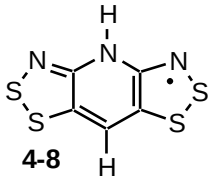

4-8

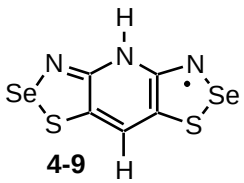

4-9

The reaction path for this idealized process, illustrated in Figure 4.17, can be conveniently expressed in terms of (i) the separation (*r*) between the E−N bonds of the two radicals and (ii) the relative slippage coordinate (*q*) of the two radicals, defined such that $q = 0$ when the hypervalent S···E−E···S sequence is colinear. Observed values for these parameters in the crystal structure of β-[**4-1**]$_2$ are provided in Table 4.3.

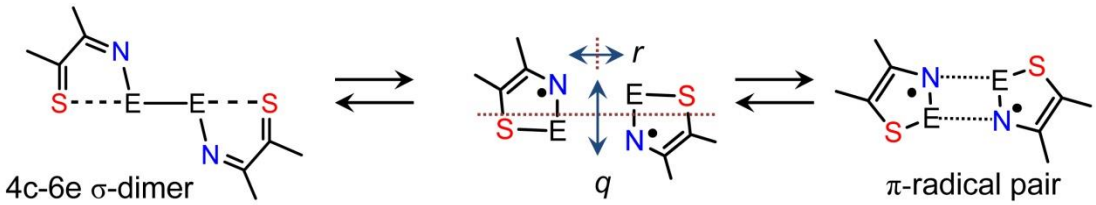

Figure 4.17 Evolution of 4c−6e model σ-dimers **4-8** and **4-9** ($R_1 = R_2 = H$; E = S, Se) into a pair of π-radicals.

Inspection of the idealized molecular orbital manifolds (Figure 4.18) of these two systems, each in C_{2h} symmetry, reveals that interconversion of the two structures requires a configurational crossover. There are three occupied σ-type orbitals (two a_g and one b_u) associated with the hypervalent 4c−6e S···E−E···S unit, whereas in the radicals there are only two occupied σ-type orbitals (a_g and b_u), essentially one for each E−S bond. The remaining two σ-electrons from the dimer are transferred to the π-SOMOs (b_g and a_u) of the radicals, high spin occupation of which gives rise to a ^3B_u state. The computational challenge lies in estimating the relative energies of the two states - the closed shell σ-dimer and the ^3B_u radical pair - as a function of *r* and *q* parameters defined in Figure 4.17.

In the case of the σ-dimer this is a relatively straightforward task. For small *q*-values, that is, relatively minor distortions of the hypervalent S···E−E···S sequence away from colinearity, the resulting state is bound, as a result of which the value of *r* could be included in the geometry optimization. By contrast, the ^3B_u radical pair state is unbound, and optimized total energy calculations as a function of *q* require that the value of *r* be fixed. In the case of **4-8** ($R_1 = R_2 = H$), we set $r = 3.0$ Å, this value being close to that observed in the high pressure and high temperature structures of β-[**4-1**]$_2$ itself (Table 4.3). For **4-9** ($R_1 = R_2 = H$), a slightly smaller value ($r = 2.8$ Å) was used, as in most

structures possessing 4-center $(Se\cdots N')_2$ interactions,[36] the intermolecular "secondary bonds" are stronger, and hence shorter, than the corresponding $(S\cdots N')_2$ interactions in the sulfur compounds.[37]

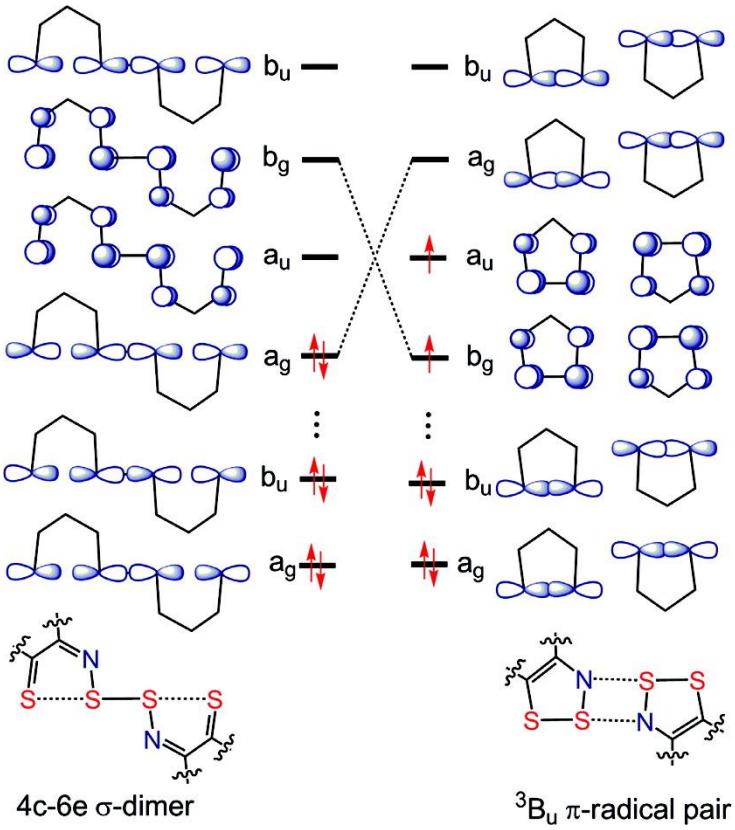

Figure 4.18 Frontier molecular orbitals of 4c−6e σ-dimer and triplet (^3B_u) π-radical pair.

The numerical results are summarized in Figure 4.19, in the form of plots of the total energy of the σ-dimer states for **4**-**8** and **4**-**9**, fully optimized at values of the slippage coordinate *q* from 0 to 1 Å, and the ^3B_u states for the corresponding radical pairs, each constrained to the preset separation parameter *r* noted above, but otherwise fully optimized. While correlation differences between the triplet and singlet states preclude a quantitative analysis, the results allow assessment of the *relative* ease of conversion of a 4c−6e σ-dimer into a pair of radicals as a function of the slippage parameter *q*. In this regard we note two features. The first is that the potential surface for distortion of the σ-dimers is much steeper for E = S than for E = Se. This may reflect a weaker long range overlap between adjacent sulfur 3*p*-orbitals in comparison to selenium 4*p*-orbitals, so that the Se-based dimer is more flexible.

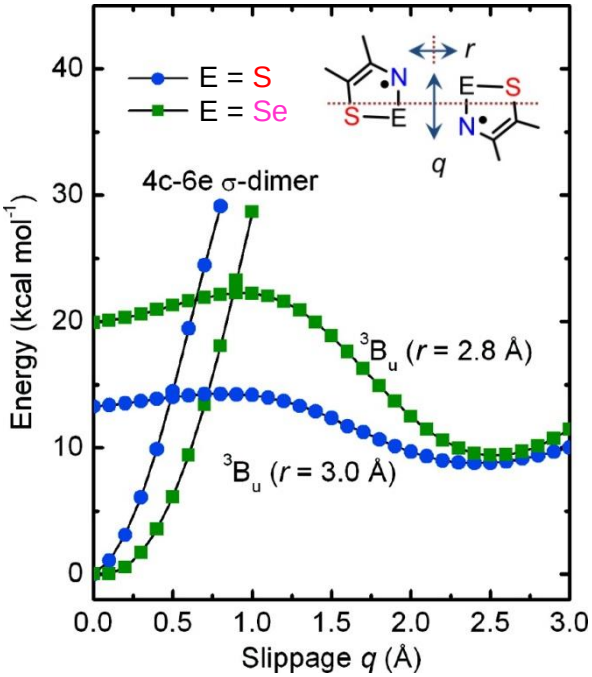

Figure 4.19 (U)B3LYP/6-31G(d,p) total electronic energy of model 4c−6e σ-dimers and triplet (^3B_u) model π-radical pairs of **4**-**8** and **4**-**9**.

The second factor that must be taken into account is the energy surface of the ^3B_u state, onto which the singlet σ-dimer surface must cross. At small values of *q*, this surface is much higher lying for E = Se than for E = S, while at larger values of *q*, the energy minimum for E = Se becomes more pronounced than for E = S, indicative of the stronger secondary bonding interactions expected at this geometry. Taken together, these two effects give rise to a situation in which the crossover from the energy surface of the σ-dimer singlet for **4**-**9** (E = Se) to the corresponding ^3B_u radical pair requires a much greater motion along the distortion coordinate *q* in comparison to **4**-**8** (E = S). As a result the barrier for the dimer-to-radical conversion for **4**-**9** (22 kcal mol^{-1}) is significantly greater than that of **4**-**8** (14 kcal mol^{-1}). Likewise the reverse process, the radical-to-dimer switch, is also associated with a higher barrier for **4**-**9** (13 kcal mol^{-1}) than for **4**-**8** (5 kcal mol^{-1}).

While the relatively low estimated barriers for the interconversion of the σ-dimer and radical pair of **4**-**8** (E = S) are broadly consistent with the ease of thermal and pressure- and photochemically-induced dissociation of β-[**4**-**1**]$_2$, the higher values calculated for the corresponding Se-based system do not, by

themselves, provide a definitive reason as to why solid state dissociation of dimers based on **4-9** (E = Se) does not occur thermally or with pressure.[38] The barrier for dissociation (22 kcal mol^{-1}) is, in fact, comparable to that estimated (20 kcal mol^{-1}) for the buckling process shown in Scheme 4.1, and yet there is no evidence for any competition between the two modes of deformation. To address this issue we need to go beyond the idealized gas phase models used so far, and to examine the supramolecular architecture of β-[**4-1**]$_2$ and [**4-4**]$_2$ (R_1 = Me; R_2 = H).

To this end the ribbon-like arrays of σ-dimers in β-[**4-1**]$_2$ and [**4-4**]$_2$, within which adjacent dimers are bridged by 4-center secondary bonding (E···N')$_2$ contacts (E = S, Se) are illustrated in Figures 4.20 and 4.21. For convenience and consistency with the previous analysis, the geometrical extent of these interactions are defined in terms of the parameters *r*' and *q*'. The large value of *r*' found for the (S···N')$_2$ contacts in β-[**4-1**]$_2$ suggests a very weak intermolecular interaction, with neighboring dimers essentially disconnected and free to move independently. As a result, the conversion of the dimers into radicals, a process which leads to compression of the overall length (S1···S1') of the supermolecule from 16.060 Å to 15.385 Å, is not compromised by the secondary bonding interactions. Consistently the interdimer contact *r*' lengthens slightly (from 3.603 Å to 3.705 Å), and *q*' decreases substantially (from 2.624 Å to 2.160 Å), as neighboring dimers slide apart. In essence, the energetics of the process can be reasonably described, to a first approximation, in terms of the gas phase molecular model described above.

By contrast, in the Se-based dimer [**4-4**]$_2$, the interdimer secondary bonding interactions are much stronger (*r* = 2.839 Å) at ambient pressure, and have the effect of locking together adjacent dimers along the ribbon. As a result, lateral motion required to convert a dimer into a pair of radicals, is energetically unfavorable. Even though the gas phase estimates suggest that opening of the Se-based σ-dimer is energetically comparable to buckling, it is the latter motion, which preserves the strong interdimer (Se···N')$_2$ supramolecular synthons,[39] which is actually observed. Indeed under a pressure of 5 GPa the value of *r*' contracts to 2.591 Å, in accord with this interpretation.

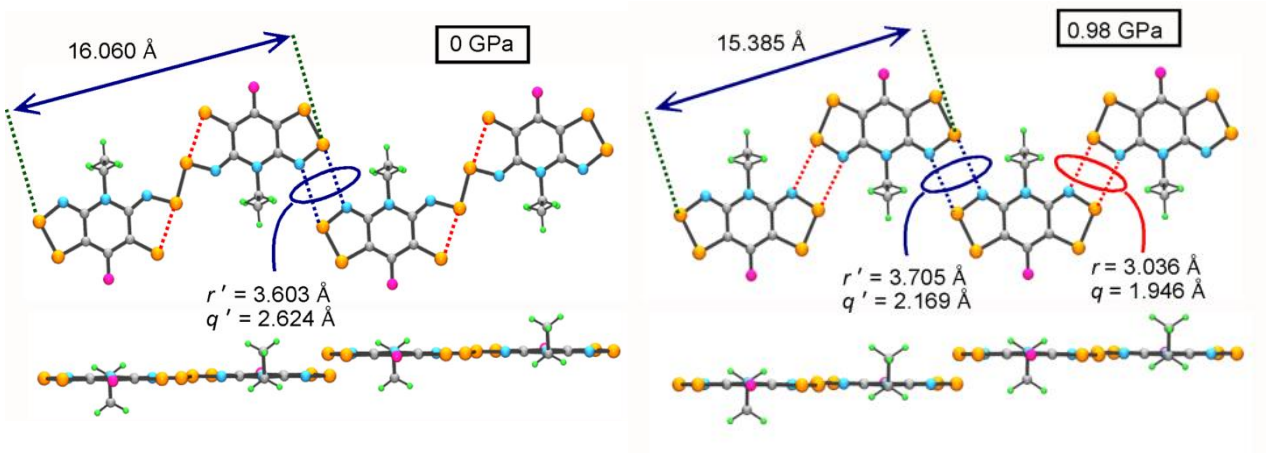

Figure 4.20 Supramolecular contacts *r*' and *q*' distances along molecular ribbons of β-[**4-1**]$_2$ at 0 and 0.98 GPa.

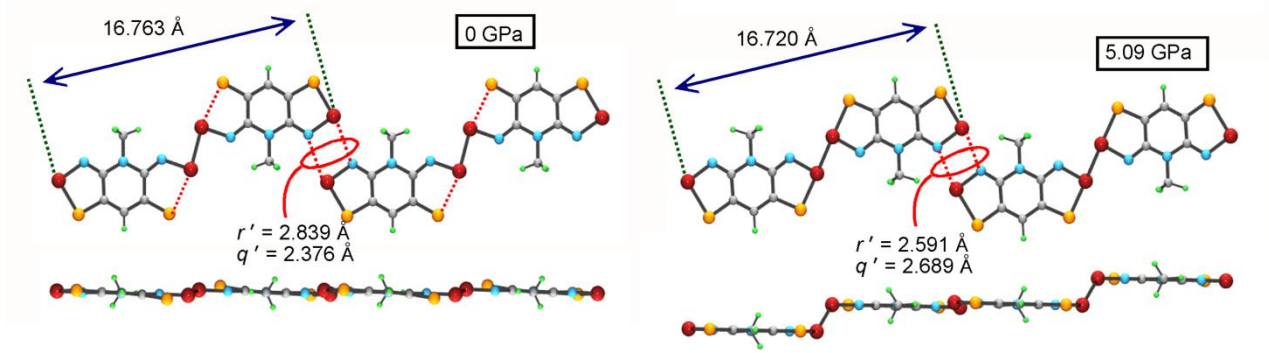

Figure 4.21 Supramolecular contacts *r*' and *q*' distances along molecular ribbons of [**4-4**]$_2$ (R_1 = Me, R_2 = H) at 0 and 5.02 GPa.

A corollary to this finding is the behavior of the related sulfur-based dimer [**4-2**]$_2$ (R_1 = Me; R_2 = F), which is isomorphous with β-[**4-1**]$_2$, yet structurally and physically more reminiscent of [**4-4**]$_2$ and, of course, [**4-3**]$_2$ (R_1 = Me; R_2 = F) (Chapter 3). The smaller size of the R_1 substituent in [**4-2**]$_2$ allows for a closer approach of the 4-center S···N' synthons, giving rise to an overall tighter structure than β-[**4-1**]$_2$, *i.e.*, *r*' is smaller (3.092 Å). As a result, despite the similarities at the molecular level, [**4-2**]$_2$ does not undergo RDI thermally or under pressure, just as the selenium variants [**4-3**]$_2$ and [**4-4**]$_2$ do not. However, recent results suggest that all of these systems undergo photoinduced RDI, although their excited state structures are as of yet unknown.[38]

4.5 Summary

In the solid state, most bisdithiazolyls studied to date crystallize as discrete radicals rather than dimers, and adopt a single crystalline phase. Compound **4-1**, the focus of this chapter, breaks with precedent in several ways. It is dimorphic, the α-phase crystallizing as π-stacked radicals in the tetragonal space group $P\bar{4}2_1m$, while the β-phase consists of π-stacked dimers in which two radicals are bound by a hypervalent 4c−6e S···S−S···S linkage. Such dimeric structures have been previously observed for selenium based radicals, including [**4-3**]$_2$ and [**4-4**]$_2$, but the response of the molecular and bulk properties of the S···E−E···S linked materials to pressure and temperature are quite different. In contrast to the behavior of related Se−Se based σ-dimers, which retain their dimeric structure under pressure, the S···S−S···S based dimer β-[**4-1**]$_2$ readily dissociates thermally, photochemically and under pressure, and this phase transition can be observed through changes in both the conductivity and magnetic susceptibility.

The difference in the behavior of the two systems, β-[**4-1**]$_2$ and [**4-4**]$_2$, compared extensively in this chapter, to increases in temperature and pressure arises from a combination of molecular and lattice-based effects. The Se-based radicals [**4-4**]$_2$ are bound more strongly, not only in terms of the hypervalent linkage but also in terms of the supramolecular 4-center (Se···N')$_2$ secondary bonding interactions which lock the dimers into rigid chains. Thermal energy (< 400 K) is insufficient to induce dissociation, while applied pressure leads to buckling of the dimers with retention of the secondary bonding linkages. By contrast, the supramolecular (S···N')$_2$ interactions in the S-based dimer β-[**4-1**]$_2$ are weak, and changes in the packing of the molecules and the lattice parameters in the course of the phase transition are minimal. As a result cooperative structural effects are likely to be small, and the hysteresis observed from the spin crossover may stem largely from the fact that dissociation of the dimers, and re-association of the radicals, is symmetry forbidden, a feature not observed for the conventional modes of dimerization open to thiazyl radicals as they are simply the result of the coupling of two magnetic orbitals, *i.e.* with a preservation of symmetry.

A summary of the frontier MO evolution diagram for the two known processes (RDI, right, and buckling, left) available to hypervalent σ-dimers of this type is shown in Figure 4.22. The orbital filling of the σ-dimer leads to a HOMO (σ_3) that evolves to a state much higher energy in both transformations. In the case of the buckling process, one of the unoccupied π-orbitals (π_-) lowers in energy to become the HOMO of the π-dimer. By contrast, the RDI gives rise to a pair of π-orbitals with opposite symmetry (π_+ and π_-) for the radical pair, each half-filled. In both cases, the interconversion from σ- to π-symmetry requires a configurational reorganization.

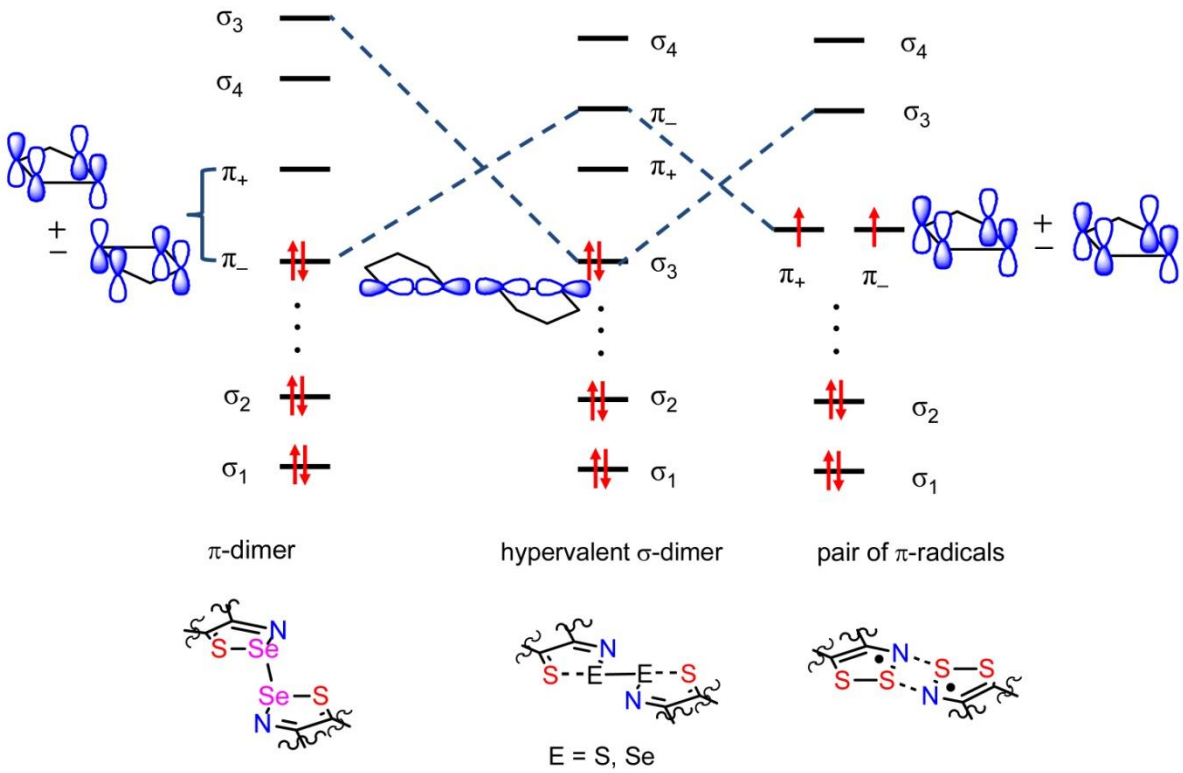

Figure 4.22 Summary of the orbital evolution diagrams for two structural processes occurring in hypervalent σ-dimers with E = S, Se.

In the photoinduced RDI, this barrier gives rise to an unprecedented stability of the photogenerated radical almost to room temperature. This is in contrast to transition-metal based spin crossover (SCO) materials, which rarely survive above 150 K.[40] Metal-based SCO is also symmetry forbidden, guaranteeing an inherent activation barrier to dissociation at the molecular level. However, where RDI and SCO processes differ is in the magnitude of the structural changes involved, that is, > 0.6 Å for the

back-reaction β-[**4-1**]$_2$ → 2 **4-1** compared to 0.2 Å for metal-ligand distances of an SCO metal ion. Under these circumstances a higher thermal stability for the photoinduced paramagnetic radical state **4-1** is to be expected.

Although it has been established that the thermal magnetic bistability observed for β-[**4-1**]$_2$ is not a general phenomenon for these hypervalent S···E−E···S radical σ-dimers, preliminary results show that the photoinduced RDI *is*. At this time, our understanding of the excited states leading to this transition is still limited. A deeper theoretical exploration into these transitions, much like that done for SCO materials, is needed. It remains to be seen whether these radical dimers will find device applications comparable to those of transition-metal-based spin-crossover compounds.

4.6 Experimental Section

General methods and procedures are described in Appendix A.

Preparation of *N*-Ethyl-2,4,6-trifluoropyridinium Triflate, 4-6. A mixture of ethyl triflate (2.74 mL, 24.0 mmol) and 2,4,6-trifluoropyridine **4-5** (2.66, 20.0 mmol) was stirred for 16 h at 60 ºC to afford a heavy white precipitate. DCE (10 mL) and diethyl ether (35 mL) was added and the product **4-6** was filtered off, washed with diethyl ether, and dried in vacuo. Yield, 5.73 g (18.4 mmol, 92%); mp 122-124 ºC. IR: 3063 (s), 1673 (vs), 1600 (vs), 1538 (m), 1508 (s), 1424 (w), 1271 (vs), 1228 (s), 1208 (m), 1168 (vs), 1095 (w), 1033 (vs), 881 (m), 759 (w), 639 (vs), 575 (w), 518 (s), 410 (w) cm^{-1}. ^{1}H NMR (δ, CD_3CN): 7.65 (dd, 2H, J = 6.89, 2.59 Hz), 4.57 (qt, 2H, J = 7.35, 2.72 Hz), 1.51 (t, 3H, J = 7.35 Hz). ^{19}F NMR (*d*, CD_3CN): 69.7 (t, 1F, J = 30 ppm), 77.7 (d, 2F, J = 30 ppm). Anal. Calcd for $C_8H_7F_6NO_3S$: C, 30.88; H, 2.27; N, 4.50. Found: C, 30.83; H, 2.36; N, 4.36.

Preparation of *N*-Ethyl-2,6-diamino-4-fluoropyridinium Triflate, 4-7. Anhydrous ammonia gas was passed over a solution of **4-6** (4.70 g, 0.0151 mol) in 50 mL MeCN at 0 ºC for 5-10 min. The yellow mixture was stirred at room temperature for 30 min, and the resulting white precipitate of NH_4F was filtered off. Evaporation of the solvent from the filtrate afforded a white solid that was recrystallized from a 1:5 mixture of MeCN/DCE as off-white flakes of **4-7**. Yield, 3.34 g (0.0109 mmol, 72 %); mp

132-134 ºC. IR: 3419 (s), 3361 (s), 3248 (s), 3116 (w), 1672 (s), 1649 (s), 1604 (s), 1548 (w), 1517 (s), 1448 (m), 1339 (m), 1280 (s), 1257 (s), 1226 (s), 1180 (s), 1166 (s), 1091 (m), 1069 (w), 1032 (s), 1015 (m), 811 (s), 793 (w), 761 (w), 642 (s), 598 (w), 580 (w), 573 (w), 515 (m) cm^{-1}. ^1H NMR (δ, CD_3CN): 6.38 (s, 4H), 5.96 (d, 2H, J = 9.63 Hz), 3.91 (q, 2H, J = 7.36 Hz), 1.31 (t, 3H, J = 7.36 Hz). Anal. Calcd for $C_8H_{11}F_4N_3O_3S$: C, 31.48; H, 3.63; N, 13.77. Found: C, 31.83; H, 3.40; N, 13.58.

Preparation of 8-Fluoro-4-ethyl-4*H*-bis[1,2,3]dithiazolo[4,5-*b*:5',4'-*e*]pyridin-2-ium Trifluoromethanesulfonate, [4-1][OTf]. A solution of sulfur monochloride (9.20 g, 0.0681 mol) in 20 mL MeCN was added to a solution of **4-7** (5.22 g, 0.0171 mol) in 90 mL MeCN. The solution was heated at a gentle reflux for 90 mins and the resulting deep blue solution was cooled to room temperature and then at –20 ºC for 2 h. The red, microcrystalline precipitate of crude [**4-1**][OTf] was filtered off, washed with 4 × 40 mL hot DCE, 20 mL CS_2 and 20 mL DCM, after which the product was dried *in vacuo*, yield 5.52 g (0.0129 mol, 75 %). Red blocks were isolated by recrystallization from MeCN, mp 291-293 °C IR: 1512 (s), 1461 (s), 1279 (s), 1239 (s), 1224 (w), 1197 (w), 1121 (w), 1025 (s), 856 (w), 790 (m), 786 (m), 716 (w), 678 (w), 671 (w), 650 (w), 635 (m), 516 (w), 479 (m), 472 (m). Anal. Calcd for $C_8H_5F_4N_3O_3S_5$: C, 22.48; H, 1.18; N, 9.83. Found: C, 22.60; H, 1.23; N, 9.66.

Preparation of 8-Fluoro-4-ethyl-4*H*-bis[1,2,3]dithiazolo[4,5-*b*:5',4'-*e*]pyridin-3-yl, **4-1.** Before use, all glassware was soaked overnight in dilute HNO_3, washed with deionized water followed by distilled water, and finally dried at 100 ºC overnight. Magnetic stir bars were glass-covered. A sample of [**4-1**][OTf] (300 mg, 0.702 mmol) and DMFc (218 mg, 0.668 mmol) were combined in 10 mL degassed (4 freeze-pump-thaw cycles) MeCN at 0 ºC. After stirring for 2 h at RT, the black-green microcrystalline product (α-**4-1**) was filtered off and washed with 5 × 10 mL MeCN, yield 155 mg (0.557 mmol, 83 %). IR: 1528 (w), 1505 (w), 1438 (s), 1456 (s), 1444 (s), 1351 (w), 1320 (m), 1233 (s), 1190 (w), 1102 (m), 1076 (m), 989 (w), 872 (w), 816 (s), 768 (s), 686 (s), 658 (m), 640 (s), 536 (w), 470 (s), 455 (w). *Radical Phase α-**4-1**:* Crystals suitable for crystallographic work were obtained by recrystallization of **4-1** (250 mg, 0.898 mmol) from 10 mL of degassed (4 freeze-pump-thaw cycles) DCE as metallic green needles of α-**4-1**. *Dimer Phase β-[**4-1**]$_2$:* Crystals suitable for crystallographic work, as well as transport property measurements, were obtained by vacuum sublimation of the bulk material at 10^{-4}

Torr in a three-zone furnace along a temperature gradient of 120 ºC to 60 ºC. This gave pure metallic bronze blocks of β-[**4-1**]$_2$. IR: 1528 (s), 1509 (s), 1436 (s), 1328 (s), 1271 (m), 1193 (m), 1168 (s), 1101 (s), 1087 (m), 1073 (m), 872 (w), 835 (m), 764 (s), 713 (m), 661 (s), 615 (w), 574 (w), 522 (w), 473 (s), 424 (w). Anal. Calcd for β-[**4-1**]$_2$: $C_7H_5FN_3S_4$: C, 30.20; H, 1.81; N, 15.09. Found: C, 30.35; H, 1.90; N, 15.13.

High Temperature Powder Crystallography. A powdered sample (ca. 60 mg) of β-[**4-1**]$_2$ was loaded into an alumina holder which was rotated and heated to 120 °C in a FUR 1400 furnace under a dynamic atmosphere of helium. X-ray diffraction data were collected on a powder diffractometer with a position sensitive detector (INEL) using Cu Kα_1 radiation (λ = 1.5406 Å). The total 2θ range was 2–112°, measured in steps of 0.029°. The powder diffraction patterns were indexed using DASH 3.01, from which it was evident that the $P2_1/c$ space group of the ambient temperature structure was retained at 120 °C. Starting with the molecular coordinates for β-[**4-1**]$_2$ taken from a UB3LYP/6-31G(d,p) geometry optimization, the crystal structure was solved using DASH 3.01. During the initial Rietveld refinement in DASH a rigid-body constraint was maintained, but the sulfur positions were later released to optimize within the plane of the molecule. These atomic coordinates were then taken into GSAS for a final Le Bail refinement of the unit cell dimensions. Atomic positions obtained from DASH were not further refined in GSAS, as a result of which standard deviations for atomic coordinates are not available. Final refinement indices R_p and R_{wp} are listed in Table 4.2.

High Pressure Powder Crystallography. High pressure diffraction experiments on β-[**4-1**]$_2$ were performed on the HXMA (High energy X-ray Materials Analysis) beamline of the Canadian Light Source, using synchrotron radiation (λ = 0.509176 Å) and a powdered sample mounted in a DAC with low viscosity (1 cst) polydimethylsiloxane as the pressure transmitting medium. The diffraction data were collected at room temperature and as a function of *increasing* pressure. A series of data sets from 0 - 1.21 GPa was indexed in DASH, and two of these, collected at 0.65 GPa and 0.98 GPa were solved, starting from a model radical **4-1** derived from a fully optimized UB3LYP/6-311G(d,p) calculation. During the initial Rietveld refinement in DASH a rigid-body constraint was maintained, but the sulfur positions were later released to optimize within the plane of the molecule. These atomic coordinates

were then taken into GSAS for a final Rietveld refinement. Data were refined with fixed atomic positions and isotropic thermal parameters with an assigned value of 0.025. Atomic positions obtained from DASH were not further refined in GSAS, as a result of which standard deviations for atomic coordinates are not available. Final Rietveld indices R_p and R_{wp} are listed in Table 4.2. Data was collected by Drs. J. S. Tse and S. Desgreniers.

Molecular Electronic Structure Calculations. All DFT calculations were performed with the Gaussian 09W suite of programs, using the (U)B3LYP hybrid functional and polarized, split-valence basis sets with double zeta (6-31G(d,p)) and triple-zeta (6-311G(d,p)) functions. Full geometry optimization was invoked for the assembly of the model of **4-1** used as the starting point in the powder diffraction work. For the calculation of the electronic energies of singlet σ-dimer and ^3B_u radical pairs for **4-8** and **4-9** ($R_1 = R_2 = H$), full geometry optimization within the confines of C_{2h} symmetry was invoked, with only the values of *q* and *r* defined in Figure 4.18 being constrained.

Chapter 5

Bisdithiazolyl Radical Spin Ladders

5.1 Introduction

With the rich diversity of properties in the family of hypervalent σ-dimers presented in the previous two chapters, we pursued related systems in the hopes of observing bistability once again. The original strategy included incremental increases in the alkyl substituent length. Although we successfully generated the target radicals, we were unable to make more dimers in this family. However, this careful substituent modification and preservation of the basal fluorine atom has led to a novel packing motif for bisdithiazolyls radicals **5-1**, which crystallize in a unique arrangement giving rise to strong spin ladder-type magnetic exchange (Chart 5.1).

One of the main advantages of materials research based on the use of molecular building blocks is the ability to fine tune physical properties at the chemical level.[1] In this regard the solid state crystal structures of radicals **5-1** – **5-4** are highly sensitive to the nature of ligands R_1 and R_2 with dramatic, and often upredictable, changes in space group and architecture arising from seemingly minor modifications.[2] In recent work on derivatives of **5-5** the Oakley group has shown that the incorporation of structure-making intermolecular contacts (supramolecular synthons)[3] can afford a degree of structural control.[4] In particular we have observed that a fluorine atom in the basal R position of the oxobenzene-bridged radicals **5-5** plays a major role by means of strong intermolecular F···S' interactions.[5]

Chart 5.1

	E_1	E_2
5-1	S	S
5-2	S	Se
5-3	Se	S
5-4	Se	Se

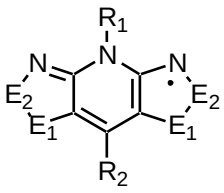

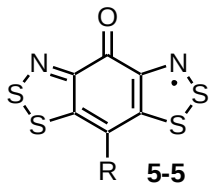

5-5

In the present chapter the exploration of the packing patterns and physical behavior of **5-1** as a function of R_1/R_2 is extended. The strategy has led us to fix R_2 = F, which generates new packing motifs by means of intermolecular F···S' contacts. Given the anticipated "pinning effect" of such interactions, we hoped to monitor the variation of structure and property with a steady increase in the size of the R_1 group. To this end four new bisdithiazolyl radicals **5-1a** – **5-1d** (Figure 5.1a; R_1 = Pr, Bu, Pn, Hx) have been synthesized, three of which have alkyl chains longer than any bisdithiazolyl reported to date. While the propyl derivative **5-1a** crystallizes in the familiar tetragonal space group $P\bar{4}2_1m$, like the corresponding compound where R_1 = Et (Chapter 4),[6] the remaining three have a common but hitherto unobserved packing pattern. This finding is particularly interesting from the perspective of crystal engineering, as the structures of **5-1b** – **5-1d** are all based on pairs of radicals "pinned" together by strong S···F' interactions (Figure 5.1b). This feature, coupled with the long alkyl chains on either end leads, almost inexorably, to π-stacking of pairs of radicals in a ladder-like topology displaying classic spin ladder magnetic behavior (Figure 5.1c).

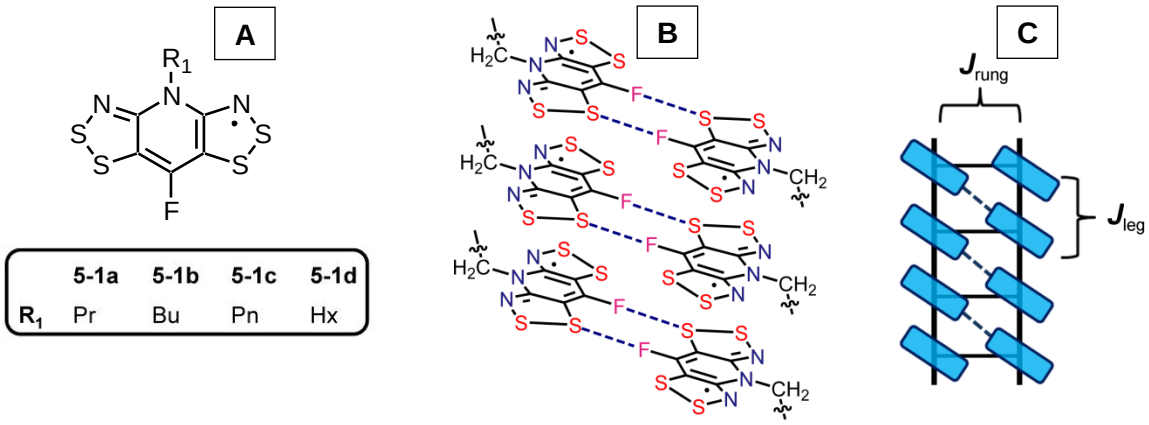

Figure 5.1 (a) Molecular labels for structures in the present chapter. (b) Intermolecular S···F' contacts (synthons) that lock radicals laterally into centrosymmetric pairs, and (c) ladder-like arrays produced by π-stacking of these pairs.

The observation of spin coupling along 1D arrays of magnetically active centers, to afford FM or AFM coupled chains, is common. Lateral coupling of two magnetic chains can lead to a spin-ladder

(Figure 5.1c), where interactions between (J_{rung}) and within (J_{leg}) the magnetic chains may be FM or AFM; the ideal spin-ladder being such that $J_{rung} = J_{leg}$.[7] To date the most thoroughly studied ladders are built from transition metal complexes of copper,[8,9] but molecular radical[10] and radical ion ladders,[11] which are easier to study due to the presence of weaker interactions, have also been reported. In all cases the interest in these systems lies in the existence of an energy gap in the spin excitation spectrum,[12] which has possible relationships to high-temperature superconductivity for lightly doped even-legged ladders.[13] The presence of ladder-like π-stacking in **5-1b** – **5-1d** has prompted a thorough analysis of their magnetic properties as a function of temperature. The results have been interpreted in the light of broken symmetry Density Functional Theory (DFT) calculations and magnetic simulations based on various spin ladder models. A full paper on this work has recently been published.[14]

5.2 Results

5.2.1 Synthesis and EPR Spectra

The preparation of **5-1a** – **5-1d** begins similarly to the previously presented fluoro-substituted materials in the earlier chapters, starting with the alkylation of 2,4,6-trifluoropyridine **5-6** with the appropriate alkyl trifluoromethanesulfonate (triflate) to generate the alkylated pyridinium triflates **5-7** as ionic liquids at room temperature (Scheme 5.1).[15] Ammonia gas is then gently bubbled into a solution of **5-7** in MeCN to afford the *N*-alkyl-2,6-diamino-4-fluoropyridinium triflate salt **5-8**, which crystallizes as white needles from water. The latter compound undergoes a double Herz cyclization reaction with S_2Cl_2 in refluxing MeCN to give bright red shard-like crystals of the bisdithiazolylium triflate salt [**5-1**][OTf]. Reduction of this salt with DMFc in degassed MeCN generates the desired radicals **5-1a** – **5-1d** in good yield. Single crystals suitable for X-ray analysis of **5-1a** and **5-1b** are grown *via* vacuum sublimation, while long needles of **5-1c** and **5-1d** are generated by recrystallization from carefully degassed (four freeze-pump-thaw cycles) heptane.[16]

Although radicals **5-1** (R_1 = Me, Et, Pr; R_2 = Cl) were fully characterized many years ago,[17] no attempts were made at the time to extend the length of the alkyl chain R_1 beyond a propyl derivative. To compare the transport properties of **5-1b** – **5-1d** to the related compounds **5-1** (R_1 = Bu, Pn; R_2 = Cl), with long alkyl chain R_1 groups but with a chlorine (rather than a fluorine) atom in the R_2-position, the appropriate bisdithiazolylium triflate salts [**5-1**][OTf] were also synthesized. However, while the chloro-substituted radicals could be successfully generated *via* reduction with DMFc, attempts to recrystallize them using similar methods to those used for the fluoro-substituted radicals led to poorly formed microcrystalline material. These results emphasize the apparent importance of the fluorine substituent as a structure-maker, an issue that will be explored more fully below. The long-chain alkyl chloro-substituted materials were not pursued further.

Scheme 5.1

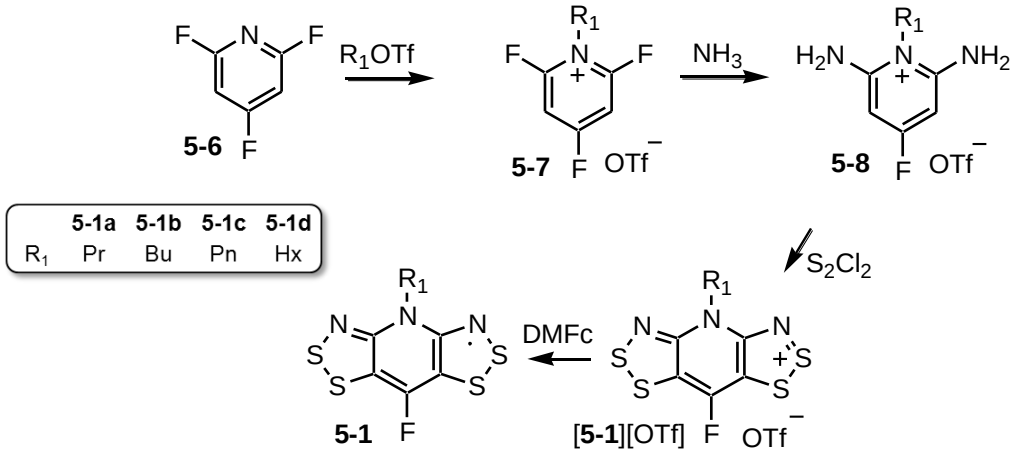

Electron paramagnetic resonance (EPR) studies on **5-1a** – **5-1d** provided confirmation of a highly delocalized spin distribution as observed in related compounds and as shown in Chapter 4. The X-band EPR spectrum (recorded at ambient temperature in dichloromethane) displays the characteristic[17] five-line hyperfine pattern from spin coupling to two equivalent ^{14}N (I = 1) nuclei on the dithiazolyl rings superimposed on the two-line pattern arising from the large coupling to the basal ^{19}F (I = ½) nucleus. As expected, the hyperfine coupling constants are very similar across the series of radicals. There is

additional fine structure present from weaker coupling to the central nitrogen atom, with no variation across the series **5-1a** – **5-1d**. Details from the simulation are provided in Table 5.1.

Table 5.1 EPR[a] Parameters for Radicals **5-1a** – **5-1d**

	5-1a	**5-1b**	**5-1c**	**5-1d**
a_N (S), mT	0.317	0.318	0.311	0.318
a_N (R_1), mT	0.056	0.056	0.056	0.056
a_H (CH_2), mT	0.020	0.020	0.016	0.021
a_F, mT	0.623	0.622	0.637	0.621
L/G	0.25	0.15	0.15	0.15
LW (mT)	0.030	0.030	0.040	0.030
g-value	2.00879	2.00871	2.00875	2.00880

[a] Derived hyperfine coupling constants and *g*-values extracted by simulation with Simfonia.[18]

5.2.2 Crystallography

The crystal structures of **5-1a** – **5-1d** have been determined at ambient temperature by single-crystal X-ray diffraction. Crystal metrics for the four structures are provided in Table 5.2, and ORTEP drawings (50% probability ellipsoids) of the molecular units, showing atom numbering schemes, are illustrated in Figure 5.2. Pertinent intermolecular distances are provided in Table 5.3.

The tetragonal unit cell motif found for **5-1a** is not new, and has been observed before in many bisdithiazolyls and their selenium variants. In particular, the structure of **5-1a** is reminiscent of the kinetically favored α-phase of **5-1** (R_1 = Et, R_2 = F)[6] presented in Chapter 4 (previously called α-**4-1a**) and also that reported for the chloro series **5-1** (R_1 = Et, Pr; R_2 = Cl).[17] Although the related compounds **5-1** (R_1 = Me, Et; R_2 = F) each crystallize in two distinct phases, one of which is the 4c-6e σ-dimer, the propyl radicals **5-1a** crystallize in a single phase. The packing motif down and along the stacking axis is shown in Figure 5.3, along with the pertinent S···S' intermolecular distances.

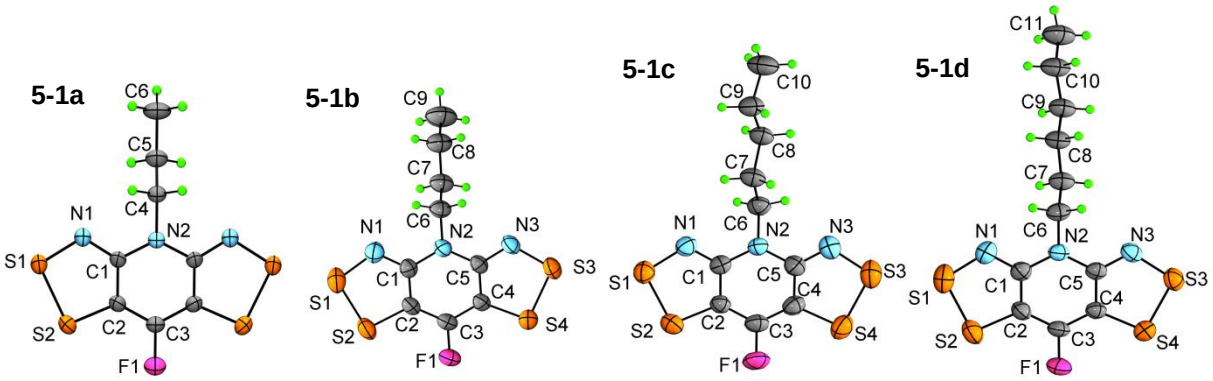

Figure 5.2 ORTEP drawings (50 % probability ellipsoids) of the four molecules **5-1a** – **5-1d** showing the atom numbering scheme.

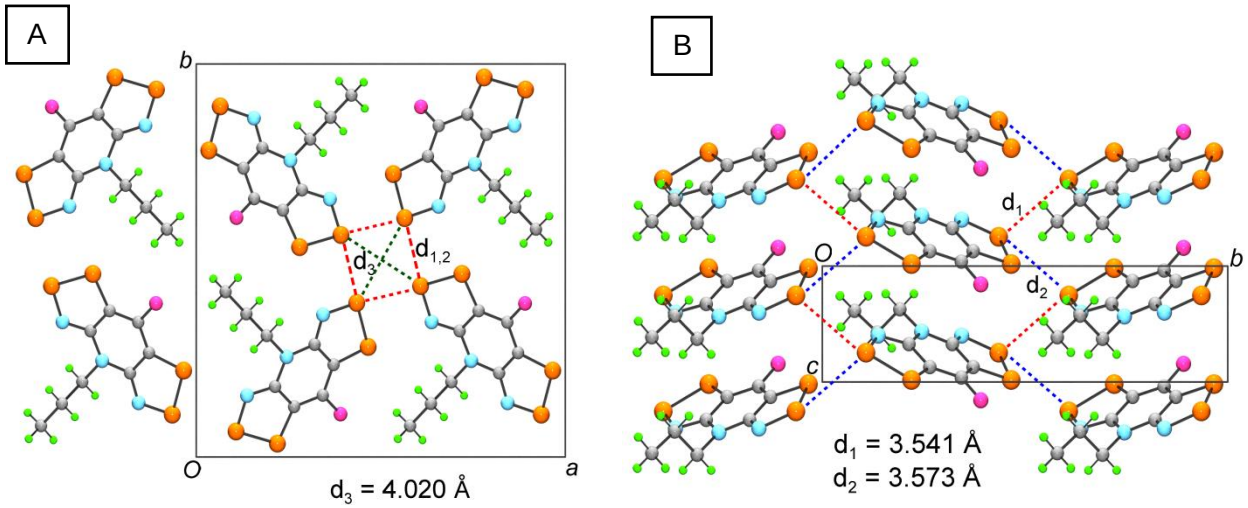

Figure 5.3 Crystal structure of **5-1a** parallel to the *z*-axis (stacking) (A) and *a*-axis (B).

All of the longer chain alkyl-substituted radicals **5-1b** – **5-1d** crystallize as an isomorphous set within the monoclinic space group $P2_1/c$ (Figure 5.4). It is apparent, then, that the variations in crystal packing attributed to modifications in R_1 cease once the length of the alkyl chain is sufficiently large. Beyond this point the packing is controlled by the combined effects of (i) the non-polar organic groups, which tend to keep the radicals apart, and (ii) strong intermolecular F···S' interactions, which cause the radicals to link laterally in a pairwise fashion (Figure 5.1). The net result is that radicals form slipped, cross-braced π-stack arrays running along the *y*-direction, as may be seen in Figure 5.5, which shows a projection of the crystal packing along the *z*-direction.

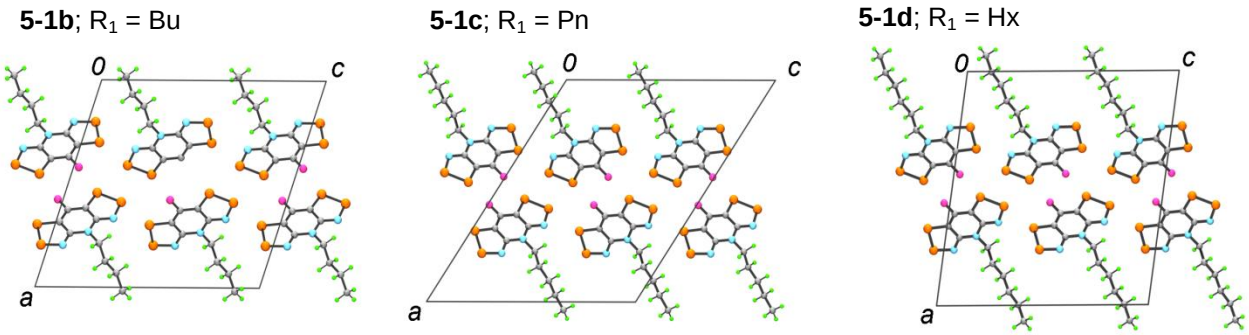

Figure 5.4 Crystal structures of **5-1b** – **5-1d** parallel to the stacking axes.

Table 5.2 Crystal Data.

	5-1a	**5-1b**	**5-1c**	**5-1d**
Formula	$C_8H_7FN_3S_4$	$C_9H_9FN_3S_4$	$C_{10}H_{11}FN_3S_4$	$C_{11}H_{13}FN_3S_4$
M	292.42	306.43	320.50	334.52
a, Å	15.9560(7)	15.6371(12)	17.8728(10)	18.0351(17)
b, Å	15.9560(7)	4.8733(4)	4.6091(3)	4.6620(4)
c, Å	4.2769(2)	17.0938(13)	17.0345(9)	17.1669(16)
β, deg	90	108.6200(10)	108.466(2)	98.334(2)
V, Å	1088.87(8)	1234.44(17)	1331.01(13)	1428.1(2)
ρ_{calcd} (g cm^{-1})	1.784	1.649	1.599	1.556
space group	$P\bar{4}2_1m$	$P2_1/c$	$P2_1/c$	$P2_1/c$
Z	4	4	4	4
temp (K)	296(2)	296(2)	295(2)	296(2)
μ (mm^{-1})	0.858	0.761	6.552	0.665
λ (Å)	0.71073	0.71073	1.54178	0.71073
data/restr./parameters	1649/0/83	2983/0/155	2324/0/163	2647/0/172
solution method	direct methods	direct methods	direct methods	direct methods
R, R_w (on F^2)	0.0214, 0.0564	0.0394, 0.0675	0.0456, 0.1134	0.0413, 0.0828

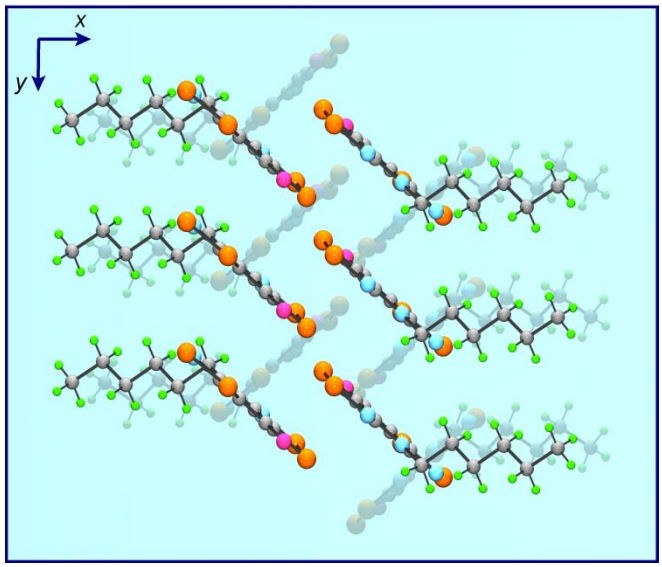

Figure 5.5 π-Stacking in **5-1d**, viewed down the *z*-axis, illustrating cross-braced nature of adjacent spin ladders.

Table 5.3 Intermolecular Structural Parameters (in Å)

		5-1b	**5-1c**	**5-1d**
d_1	S4···S2'	3.689	3.797	3.742
d_2	F1···S2'	3.210	3.198	3.232
d_3	S1···S2'	3.593	3.946	3.763
d_4	S1···S2'	3.453	3.447	3.411
d_5	S1···S1'	3.618	3.586	3.580
d_6	S2···N3'	3.089	3.288	3.187
δ		3.42	3.56	3.54
dx		1.86	2.32	2.08
dy		2.93	1.78	2.21

The spin ladders in **5-1b** – **5-1d** are based on building blocks of pairs of radicals pinned together by two F···S' (d_2) bridges, and locked into slipped π-stacks by S···S' (d_1) with π-π interactions that form the ladder "rungs" and "legs", respectively (Figure 5.6). The F···S' distances (Table 5.3) are well within the sum of the van der Waals separation for F and S (3.27 Å)[19] and the shortness and hence strength of these contacts may well contribute significantly to the stability of the crystal structures, a hypothesis supported by the difficulties encountered in growing crystals of the corresponding chloro-substituted radicals **5-1** (R_1 = Bu, Pn; R_2 = Cl). Planar supramolecular assemblies stemming from the F···S' synthons have been observed before in thiazyl radical structures.[5]

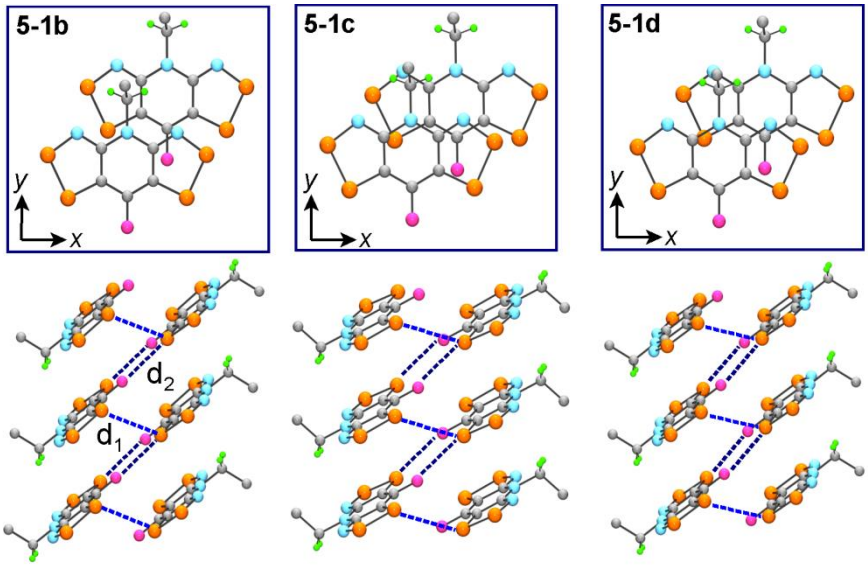

Figure 5.6 The views along the top illustrate the slippage of adjacent radicals in **5-1b** – **5-1d** along the π-stacks in local coordinates *x* and *y*. The views along the bottom demonstrate the ladder-like packing and contacts d_1 (S4···S2') and d_2 (F1···S2'). For clarity, the alkyl chains have been truncated after C2.

Adjacent ladders along the *z*-direction are connected by a series of weak S···S' and S···N' contacts (d_3-d_6), as shown in Figure 5.7. Interactions of similar magnitude have been observed in other bisdithiazolyl structures, and their magnetic implications are discussed below. The bulkiness of the alkyl chains drives the radical plates to tilt and slip severely in both the lateral (local *y* coordinate) and longitudinal (local *x* coordinate) directions. As may be seen in Figure 5.6 and Table 5.3, the extent and

direction of stack slippage varies across the series. Slippage along *x* (*dx*) is greatest for **5-1c** while movement along *y* (*dy*) is the smallest (Table 5.3). As a result, the intermolecular S···S' distances d_3 (3.946 Å) and d_6 (3.288 Å) found for **5-1c** are significantly larger than the respective lengths for **5-1b** and **5-1d**, where d_3 and d_6 range 3.593 - 3.763 and 3.089 - 3.187 Å, respectively. Lateral extension of ladders along the *z*-direction, linked by these weak contacts generates a pseudo 2D trellis in the *yz*-plane, with long chain alkyl groups protruding from either side. Packing of the layers then affords a wafer-like assembly (Figure 5.8), with interdigitized alkyl groups creating a hydrocarbon buffer, separating neighboring layers from one another.

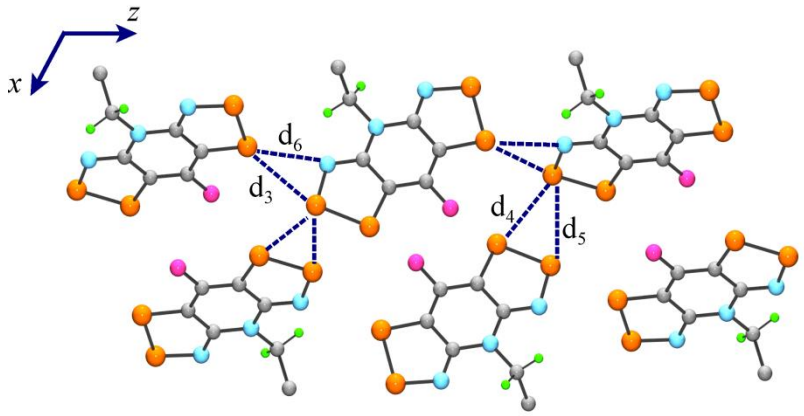

Figure 5.7 View down the π-stacking axis (*y*-direction) for **5-1b** – **5-1d** showing interladder contacts d_3–d_6. For clarity, the alkyl chains have been truncated after C2.

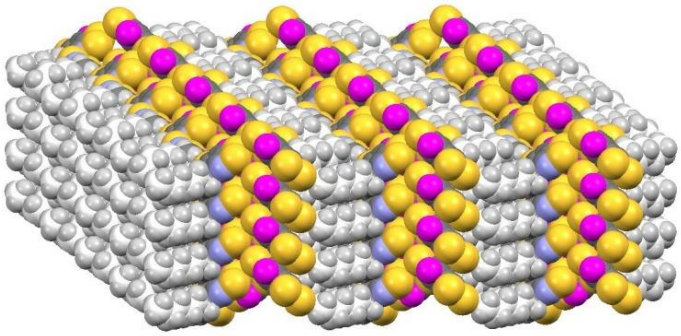

Figure 5.8 Space-filling diagram displaying wafer-like packing of **5-1d**. The long alkyl chains along the *yz*-plane separate the spin centers.

5.2.3 Magnetic Measurements and Theoretical Calculations

Variable temperature magnetic susceptibility (χ) measurements have been performed on **5-1a** – **5-1d** over the temperature range 2–300 K using a SQUID magnetometer operating at a field (H) of 1000 Oe. Figure 5.9 shows the results for **5-1a** presented in the form of plots of χ (corrected for diamagnetic contributions) *versus* T and χT against T (insert).

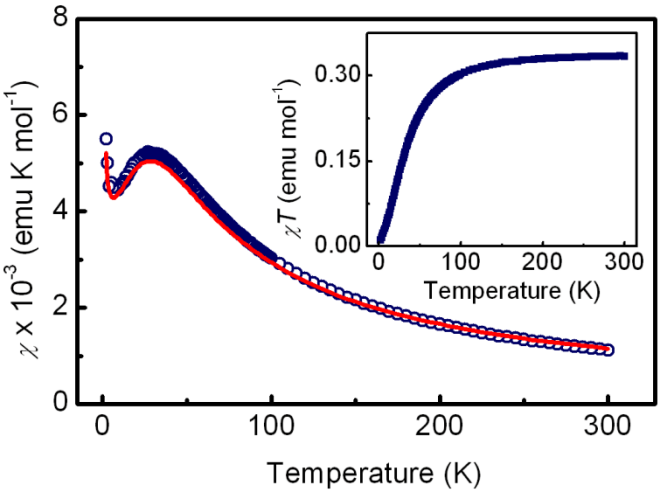

Figure 5.9 Field-cooled χ and χT (insert) *versus* T plots for **5-1a** at H = 1000 Oe. Solid red line indicates calculated χ from Bonner-Fischer AFM S = ½ chain magnetic model.[20]

The tetragonal phase **5-1a** behaves as a Curie-Weiss paramagnet, and a fit to the 20–300 K data affords values of C = 0.355 emu·K·mol^{-1} and θ = -16.5 K. The data were also modeled in terms of a Heisenberg chain of AFM coupled S = ½ radicals, using a fit function based on the molecular-field modified Bonner-Fisher method[20] and the Heisenberg Hamiltonian $H_{ex} = -2\boldsymbol{J}\{S_1 \cdot S_2\}$.[21] The intrachain AFM exchange energy of $\boldsymbol{J}$ = –15.5 cm^{-1} extracted from the 1D chain model is comparable to the value of $\boldsymbol{J}$ = –9.6 cm^{-1} obtained for the related compound **5-1** (R_1 = Et; R_2 = F, α-phase, Chapter 4). The somewhat stronger AFM coupling found for **5-1a** may be attributed to an increase in the π-stack slippage (along only the *y*-direction) associated with a longer alkyl substituent on the tetragonal bisdithiazolyl ring system.[1,22]

By contrast, χ *versus* T (Figure 5.10) plots for radicals **5-1b** – **5-1d** demonstrate significantly stronger AFM coupling than that found for **5-1a**. Attempts to fit the data to a Curie-Weiss paramagnet model were unsuccessful, providing unreasonably large θ values. Other models which we explored were the Bonner-Fischer 1D AFM chain, as well as the Bleaney-Bowers dimer,[23] neither of which provided a satisfactory fit. However, an understanding of the crystal structures led us to the spin ladder model outlined by Gu, Yu and Shen[24] and popularized by Landee,[25] with which we did have marginal success for an incomplete data range (50–300 K). The unsatisfactory fit shown in Figure 5.10 as red lines was attributed to the limitations of this model, which assumes that interactions within the ladder "rungs" ($\boldsymbol{J}_{\text{rung}}$) are much stronger than those along the "legs" ($\boldsymbol{J}_{\text{leg}}$). This condition is not satisfied in the present systems. Nonetheless, the fitting parameters from these experiments are summarized in Table 5.4.

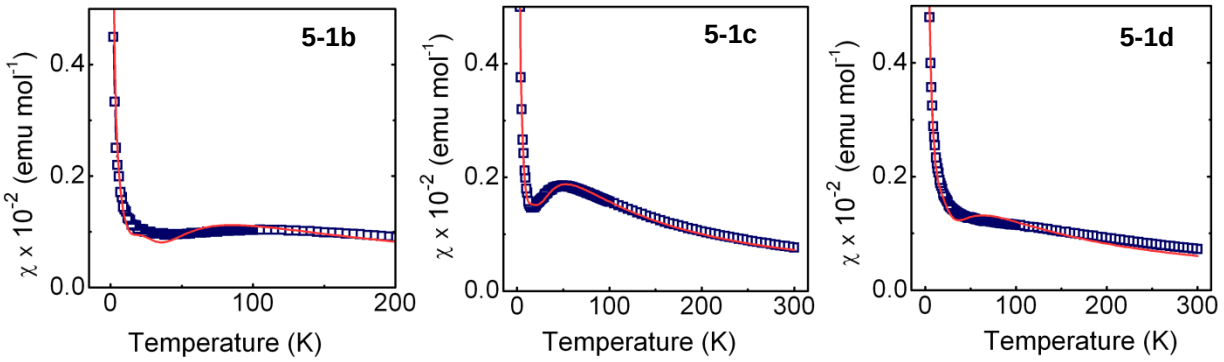

Figure 5.10 Field-cooled χ *versus* T plots for **5-1b** – **5-1d** at H = 1000 Oe. Solid red lines indicate calculated χ from *strong-rung* spin ladder model by Landee.[25]

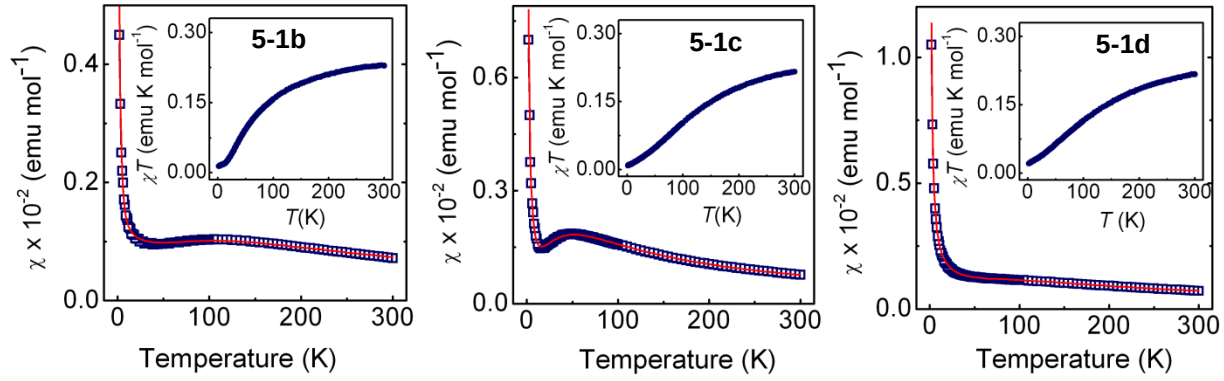

Figure 5.11 Field-cooled χ and χT (inserts) *versus* T plots for **5-1b** – **5-1d** at H = 1000 Oe. Solid red lines indicate calculated χ from *strong-leg* spin ladder model by Johnston *et al*.[26]

On the other hand, the ladder models developed by Johnston *et al*. from fits to quantum Monte Carlo (QMC) simulations of $\boldsymbol{J}_{leg} \approx \boldsymbol{J}_{rung}$ ladders provided a much more satisfying fit over the entire temperature range.[26] The results, which are tabulated in Table 5.5 and displayed graphically in Figure 5.11 (red line), indicate that all three compounds **5-1b** – **5-1d** behave as two-legged spin ladders. The radicals with even-numbered alkyl chains **5-1b** and **5-1d** have comparable $\boldsymbol{J}$ values; both demonstrate strong leg interactions and much weaker rung interactions. By contrast, the pentyl substituted radical **5-1c** is an ideal spin ladder by virtue of its strong, yet approximately equal $\boldsymbol{J}_{leg}$ and $\boldsymbol{J}_{rung}$ interactions (–26 cm^{-1}). Correspondingly, the spin gap (Δ) for **5-1c** is greater than that for the remaining three radicals due to the fact that it is the least chain-like.

Table 5.4 Magnetic Modeling Results from *Strong-Rung* (Landee) Ladder

	5-1b	**5-1c**	**5-1d**
$\boldsymbol{J}_{leg}$ (cm^{-1})	-32	-19	-28
$\boldsymbol{J}_{rung}$ (cm^{-1})	-40	-28	-35
PM impurity (%)	3.3	4.2	6.6

Table 5.5 Magnetic Modeling Results from *Strong-Leg* (Johnston) Ladder

	5-1b	**5-1c**	**5-1d**
$\boldsymbol{J}_{leg}$ (cm^{-1})	-66	-26	-57
$\boldsymbol{J}_{rung}$ (cm^{-1})	-17	-26	-13
PM impurity (%)	2.8	4.2	6.1
Δ (cm^{-1})	8.0	13.1	5.3

Although it is possible to include terms for interladder magnetic interactions, the buffering effect of the long alkyl chains in **5-1b** – **5-1d** isolates the ladders in at least the *x*-direction. There are, however, numerous close contacts (d_3–d_6) between neighboring ladders along the *z*-direction that may give rise to significant magnetic exchange. In an attempt (i) to explore the validity of the isolated ladder model for **5-1b** – **5-1d** and (ii) to understand more clearly the magnetic exchange pathway within these ladders,

we performed a series of pairwise broken-symmetry DFT calculations.[27,28] In addition to the exchange energy associated with neighboring radicals within the π-stack J_π, there are four symmetry independent pathways corresponding to J_1–J_4, all illustrated in Figure 5.12.

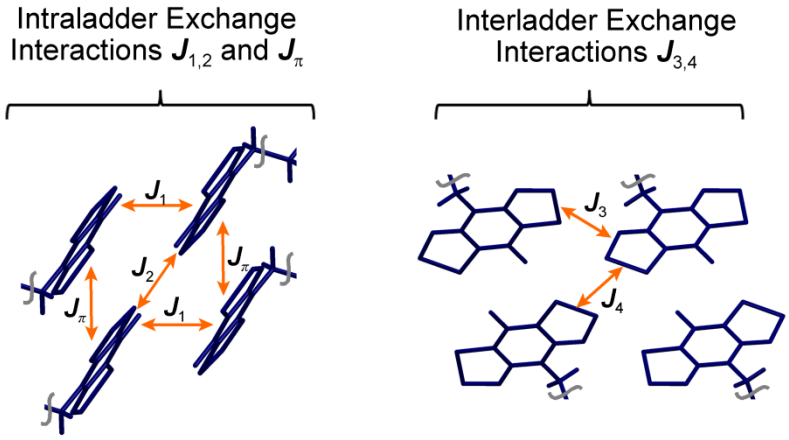

Figure 5.12 Pairwise exchange interactions J_1, J_2, J_3, J_4 and J_π.

The numerical results from these single-point calculations (Table 5.6) prompt several observations. First, J_π and J_1 (associated with the "legs" and "rungs" of the ladder, respectively) are strongly AFM, supporting the notion that the assembled radicals form a completely AFM coupled spin ladder. Second, the J_π for **5-1c** is significantly smaller in magnitude than the other two (**5-1b** and **5-1d**), which is consistent with the results obtained from the Johnston strong-leg ladder fit. The drastically different slippage of this radical, as shown in Figure 5.6 (top), with an odd-chain length hydrocarbon (*n*-pentyl) substituent likely gives rise to dramatically different overlap of the SOMOs along the π-stacks. As a result, the magnetic exchange in this direction, and the apparently anomalous magnetic response of **5-1c**, is not unexpected.

Finally, the small values associated with magnetic exchange parameters J_2-J_4 auger well for the independence of the individual ladders. Although topologically there are interactions between ladders running along the *z*-direction due to the close proximity of the radical plates, these contacts do not lead to strong magnetic exchange. However, in all cases across the series, the value for the magnetic

exchange parameter J_1 (rung) is greater than J_π (leg), which is opposite of the result of the satisfactory strong-rung magnetic ladder modeling.

Table 5.6 UB3LYP/6-31G(d,p) Exchange Energies[a]

	5-1b	**5-1c**	**5-1d**
J_π	-33.73	-9.10	-31.35
J_1	-50.37	-46.46	-65.89
J_2	0.44	0.08	0.19
J_3	3.09	0.83	1.41
J_4	3.01	-1.45	2.06

[a] In cm^{-1}, from single-point calculations.

To explore the magnetic properties suggested by the calculated exchange parameters, we simulated the magnetic susceptibility by using both exact diagonalization (ED) methods on small clusters of up to twelve radicals, and QMC simulations on extended ladders.[29,30] In each case the DFT computed exchange energies provided in Table 5.6 were employed. As might be expected, the ED calculations suggest that the interactions *between* ladders ($J_{2\text{-}4}$) are small, and their inclusion does not lead to significant difference in the simulated susceptibility. As a result the systems were treated as approximately *isolated* spin ladders, that is, the QMC simulations were carried out including only J_π (leg) and J_1 (rung) interactions. The model systems were chosen to be large enough that finite size effects were negligible.

The QMC results are shown graphically in Figure 5.13, compared with the observed response once the paramagnetic impurity suggested by fitting is subtracted. In all cases, the simulated susceptibility converges to zero at low temperatures more rapidly than was observed. This can be rationalized by considering the large and small J_{leg}/J_{rung} limits: when $J_{leg} >> J_{rung}$, the system should behave as isolated S = ½ AFM chains with no spin gap, whereas when $J_{leg} << J_{rung}$, the system should behave as isolated

AFM coupled dimers, with an exponentially decaying susceptibility at low temperatures due to a sizeable spin gap.

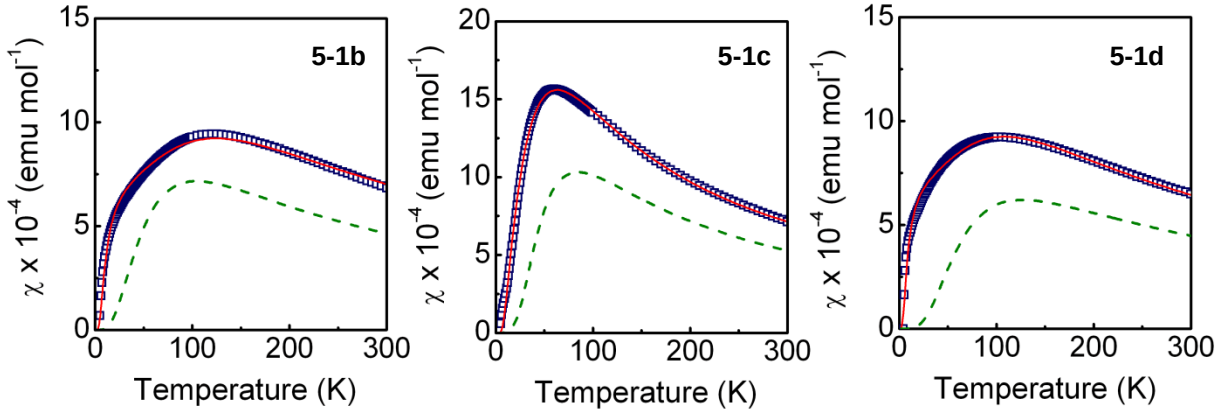

Figure 5.13 Quantum Monte Carlo (QMC) simulations on extended ladders of **5-1b** – **5-1d** (green dashed line), along with the experimental SQUID data (blue squares) and Johnston strong-leg ladder[26] fit (red line) with the subtraction of the paramagnetic impurity.

The discrepancy between the observed and simulated data can therefore be traced to the difference in computed and fit exchange parameters; fitting suggests stronger leg interactions, while the DFT calculations suggest stronger rung interactions. We therefore conclude that the so-called *bottom-up* methodology[28a] provides the correct qualitative picture of isolated spin-ladders, but the quantitative details, such as the ratio $\boldsymbol{J}_{leg}/\boldsymbol{J}_{rung}$, do not match the fitting results or experiment.

5.3 Summary

With elongation of the alkyl R_1 substituent beyond three carbons, the crystal packing of π-stacked bisdithiazolyl radicals **5-1** bearing basal fluorine substituents (R_2 = F) changes abruptly. Thus, when R_1 = Et, Pr, the radical π-stacks are locked into pinwheel clusters, but with R_1 = Bu, Pn, Hx, adjacent columns of π-stacked radicals are bridged by short intermolecular F···S' contacts to produce S = ½ spin ladder arrays. While the discovery of the role of F···S' interactions in influencing crystal packing in the present family of radicals is somewhat opportune, the notion that fluorine can, by virtue of its high electronegativity, play an important role for supramolecular structures is by no means new. For

example, intermolecular $H_3C\cdots F'$ interactions that can facilitate the interlocking of neighboring radical π-stacks were presented in Chapter 3, prohibiting these structures from undergoing a phase change with high pressure.[31] It is also well-established in nitroxyl radical structures that covalently bound fluorine atoms have the potential to enter into weak "hydrogen bridge" interactions.[32] It is thus not surprising that the electronegative fluorine atom in structures **5-1b** – **5-1d** is strongly attracted to the neighboring electropositive sulfur. The resulting centrosymmetric linking of radicals places the long alkyl chains in opposite directions, in prime position for interdigitization and the assembly of a molecular ladder.

As expected from their structures, the magnetic properties of **5-1b** – **5-1d** are consistent with spin ladder behavior. DFT broken symmetry calculations suggest that slippage of the π-stacks affords strong AFM exchange along the legs of the ladder, while the lateral $S\cdots S'$ overlap gives rise to strong AFM exchange across its rungs. Consistently, the experimental magnetic data for all three radicals can be fit to a strong leg spin ladder model. This procedure also reveals that in **5-1b** and **5-1d** AFM exchange interactions along the ladder legs are significantly stronger than those along the rungs. By contrast, **5-1c** displays ideal spin ladder behavior, with interactions along the legs and rungs being approximately equal. In a broader context, the present results provide a further demonstration of the diversity in structure and property that can be achieved by judicious modification of the R_1/R_2 substituents of bisdithiazolyls.

5.4 Experimental Section

General methods and procedures are described in Appendix A.

Preparation of *N*-propyl-2,4,6-trifluoro-pyridinium Trifluoromethanesulfonate 5-7 (R_1 = Pr). In a Schlenk tube under N_2, *n*-propyl triflate (3.0 g, 15.6 mmol) was added to 2,4,6-trifluoropyridine **5-6** (1.73 g, 13.0 mmol) and the mixture was stirred and heated at 60 °C overnight. The colorless oil was analyzed by ^1H NMR in CD_3CN and compared to other known compounds. [33] After removing volatiles *in vacuo*, the material was carried forward without further purification.

Preparation of *N*-propyl-2,6-diamino-4-fluoropyridinium Trifluoromethanesulfonate 5-8 (R_1 = Pr). The product **5-7** (R_1 = Pr, ~ 4.2 g, ~ 13 mmol) was dissolved in 50 mL of MeCN and cooled in an ice bath, over which ammonia gas was passed for 15 minutes, generating NH_4F as a white precipitate. The NH_4F was filtered off and the solvent flash evaporated to leave a white crystalline powder, which was recrystallized from 18 mL of H_2O to afford colorless crystals of **5-8** (R_1 = Pr), yield: 2.20 g (6.90 mmol, 53% over two steps); mp 179-181 °C. IR: 3426 (s), 3362 (s), 3247 (s), 3108 (m), 1671 (s), 1651 (s), 1634 (s), 1612 (s), 1513 (s), 1489 (m), 1340 (m), 1259 (s), 1227 (s), 1173 (s), 1082 (m), 1082 (w), 1032 (s), 1016 (m), 808 (m), 638 (s), 598 (w), 582 (w), 572 (w), 524 (m), 515 (m) cm^{-1}. Anal. Calcd for $C_9H_{13}F_4N_3O_3S$: C, 33.86; H, 4.10; N, 13.16. Found: C, 34.04; H, 4.30; N, 12.96.

Preparation of 8-fluoro-4-propyl-4H-bis([1,2,3]dithiazolo)[4,5-b:5',4'-e]pyridin-2-ium Trifluoromethanesulfonate [5-1a][OTf]. The *N*-propyl pyridinium triflate salt **5-8** (4.02 g, 12.6 mmol) was dissolved in 24 mL of a 3:1 v/v mixture of DCE and MeCN under nitrogen. S_2Cl_2 (4.04 mL, 50.4 mmol) was added *via* syringe and the solution was refluxed for 2.5 hours. After the allotted reaction time, the dark green solution was cooled to ambient temperature and then to 0 °C, and the subsequent red crystals were isolated by filtration, then washed with 3 × 10 mL DCE to give a crude yield of 4.93 g. The product [**5-1a**][OTf] was dissolved in 100 mL of hot HOAc, the solution hot filtered and concentrated to 60 mL, then cooled to room temperature. The red lustrous crystals were filtered off and washed with DCE, yield 3.50 g (7.94 mmol, 63 %); mp 259-260 °C. IR: 1507 (s), 1369 (s), 1353 (m), 1268 (s), 1243 (s), 1226 (m), 1181 (w), 1171 (w), 1117 (w), 1102 (w), 1087 (w), 1027 (s), 789 (s), 714 (w), 680 (m), 670 (w), 650 (w), 638 (s), 473 (s) cm^{-1}. Anal. Calcd for $C_9H_7F_4N_3O_3S_5$: C, 24.48; H, 1.60; N, 9.52. Found: C, 24.74; H, 1.90; N, 8.85.

Preparation of 8-fluoro-4-propyl-4H-bis([1,2,3]dithiazolo)[4,5-b:5',4'-e]pyridin-2-yl 5-1a. Decamethylferrocene (0.466 g, 1.43 mmol) was added to a solution of [**5-1a**] [OTf] (0.600 g, 1.36 mmol) in 14 mL bubble degassed MeCN. The slurry was stirred at room temperature for 2 hours. After the allotted reaction time, the brown, matte solid was filtered off, washed with freshly distilled MeCN to give a green microcrystalline solid **5-1a** (0.365 g, 92 %). Crystals suitable for crystallographic work, as well as transport property measurements, were obtained by vacuum sublimation of the bulk material

at 10^{-4} Torr in a three-zone furnace along a temperature gradient of 140 to 60 °C; dec (in air) > 110 °C. IR: 1503 (m), 1432 (m), 1365 (m), 1315 (m), 1281 (m), 1226 (s), 1132 (w), 1097 (s), 1084 (m), 932 (w), 900 (w), 824 (s), 769 (s), 751 (s), 722 (w), 685 (s), 659 (s), 652 (s), 535 (m), 469 (s), 452 (m) cm^{-1}. Anal. Calcd for $C_8H_7FN_3S_4$: C, 32.86; H, 2.41; N, 14.37. Found: C, 33.02; H, 2.60; N, 14.06.

Preparation of *N*-butyl-2,4,6-trifluoro-pyridinium trifluoromethanesulfonate 5-7 (R_1 = Bu). In a Schlenk tube under N_2, *n*-butyl triflate (3.0 g, 14.6 mmol) was added to 2,4,6-trifluoropyridine **5-6** (1.73 g, 13.0 mmol) and the mixture was stirred and heated at 60 °C overnight. The colorless oil was analyzed by ^1H NMR in CD_3CN and compared to other known compounds.[33] After removal of volatiles *in vacuo*, the material was carried forward without further purification.

Preparation of *N*-butyl-2,6-diamino-4-fluoropyridinium trifluoromethanesulfonate 5-8 (R_1 = Bu). The product **5-7** (R_1 = Bu, ~ 4.4 g, ~ 13 mmol) was dissolved in 30 mL of MeCN and cooled in an ice bath, over which ammonia gas was passed for 15 minutes, generating NH_4F as a white precipitate. The NH_4F was filtered off and the solvent flash evaporated to leave a white crystalline powder, which was recrystallized from 25 mL of DCE and MeCN (10:1) to afford colorless crystals of **5-8** (R_1 = Bu), yield: 2.76 g (8.28 mmol, 64 % over two steps); mp 167-169 °C. IR: 3432 (s), 3362 (s), 3245 (s), 3107 (m), 2853 (s), 1668 (s), 1614 (s), 1548 (w), 1512 (s), 1489 (m), 1355 (m), 1336 (m), 1260 (s), 1226 (s), 1173 (s), 1119 (w), 1081 (m), 1032 (s), 1014 (s), 815 (s), 762 (m), 638 (s), 601 (w), 581 (w), 571 (w), 514 (m) cm^{-1}. Anal. Calcd for $C_{10}H_{15}F_4N_3O_3S$: C, 36.04; H, 4.54; N, 12.61. Found: C, 36.24; H, 4.40; N, 12.76.

Preparation of 8-fluoro-4-butyl-4H-bis([1,2,3]dithiazolo)[4,5-b:5',4'-e]pyridin-2-ium trifluoromethanesulfonate [5-1b][OTf]. The *N*-butyl pyridinium triflate salt **5-8** (3.0 g, 9.00 mmol) was dissolved in 18 mL of a 3:1 v/v mixture of DCE and MeCN under nitrogen. S_2Cl_2 (2.89 mL, 36.0 mmol) was added *via* syringe into the reaction flask and the solution was refluxed for 2.5 hours. After the allotted reaction time, the dark green solution was cooled to rt and then to 0 °C, and the subsequent red crystals were isolated by filtration, then washed with 3 × 50 mL DCE to give a crude yield of 2.91 g (6.39 mmol, 71 %). The product [**5-1b**][OTf] was dissolved in 100 mL of hot MeCN, the solution hot filtered and concentrated to 50 mL, then cooled to room temperature. The red lustrous crystals were

filtered off and washed with DCE, recovery 1.73 g; mp 251-252 °C. IR: 1506 (s), 1268 (s), 1242 (s), 1226 (s), 1172 (m), 1124 (m), 1027 (s), 789 (s), 714 (m), 679 (s), 651 (w), 638 (s), 516 (w), 472 (m) cm^{-1}. Anal. Calcd for $C_{10}H_9F_4N_3O_3S_5$: C, 26.37; H, 1.99; N, 9.22. Found: C, 26.47; H, 2.10; N, 9.14.

Preparation of 8-fluoro-4-butyl-4H-bis([1,2,3]dithiazolo)[4,5-b:5',4'-e]pyridin-2-yl 5-1b. Decamethylferrocene (0.552 g, 1.69 mmol) was added to a solution of [**5-1b**] [OTf] (0.700 g, 1.54 mmol) in 13 mL bubble degassed MeCN. The slurry was stirred on ice for 4 hours. After the allotted reaction time, the brown, matte solid was filtered off, washed with freshly distilled MeCN to give a green microcrystalline solid **5-1b** (0.389 g, 83 %). Crystals suitable for crystallographic work were obtained by vacuum sublimation of the bulk material at 10^{-4} Torr in a three-zone furnace along a temperature gradient of 140 to 60 °C. High quality material for transport property measurements was obtained by recrystallization of 100 mg of crude radical in 10 mL of hot heptane; dec > 110 °C. IR: 1502 (w), 1481 (s), 1312 (m), 1249 (m), 1223 (m), 1114 (w), 1100 (s), 821 (m), 769 (m), 734 (w), 685 (m), 652 (m), 478 (w), 462 (w) cm^{-1}. Anal. Calcd for $C_9H_9FN_3S_4$: C, 35.27; H, 2.96; N, 13.71. Found: C, 35.38; H, 3.20; N, 13.73.

Preparation of *N*-pentyl-2,4,6-trifluoro-pyridinium trifluoromethanesulfonate 5-7 (R_1 = Pn). A mixture of *n*-pentyl triflate (3.82 g, 17.35 mmol) and 2,4,6-trifluoropyridine **5-6** (2.77 g, 20.82 mmol) was stirred and heated in an oil bath at 60 °C for 16 h. After the allotted reaction time, the product was dried *in vacuo*, after which the experimental ^{1}H NMR chemical shifts in CD_3CN compared well with literature values of related compounds.[33] This material was used in subsequent steps without further purification.

Preparation of *N*-pentyl-2,6-diamino-4-fluoropyridinium trifluoromethanesulfonate 5-8 (R_1 = Pn). The product **5-7** (R_1 = Pn, 7.27 g, ~ 20.0 mmol) was dissolved in 50 mL of MeCN and cooled in an ice bath, over which ammonia gas was passed for 15 minutes, generating NH_4F as a white precipitate. The NH_4F was filtered off and the solvent flash evaporated to leave a white crystalline powder, which was recrystallized with DCE/MeCN (10:1) to afford colorless crystals of **5-8** (R_1 = Pn), yield: 4.05 g (12 mmol, 57%); mp 149-152 °C. IR: 3425 (w), 3352 (m), 3238 (s), 3115 (w), 1682 (m), 1644 (s), 1601 (s), 1455 (m), 1278 (s), 1245 (s), 1172 (s), 1024 (s), 807 (w), 637 (w) cm^{-1}. ^{1}H NMR (δ,

CD_3CN): 6.27 (s, 4H, N*H*$_2$), 5.96 (d, 2H, *J* = 9.0 Hz), 3.77 (t, 2H, *J* = 8.4 Hz), 1.38 (m, 4H), 0.91 (m, 3H). Anal. Calcd for $C_{11}H_{17}F_4N_3O_3S$: C, 38.04; H, 4.93; N, 12.10. Found: C, 38.18; H, 4.98; N, 12.23.

Preparation of 8-fluoro-4-pentyl-4H-bis([1,2,3]dithiazolo)[4,5-b:5',4'-e]pyridin-2-ium trifluoromethanesulfonate [5-1c][OTf]. The *N*-pentyl pyridinium triflate salt **5-8** (1.5 g, 4.31 mmol) was dissolved in 10 mL of a 3:1 v/v mixture of DCE and MeCN under nitrogen. S_2Cl_2 (1.38 mL, 17.19 mmol) was added *via* syringe into the reaction flask and the solution was refluxed for 2.5 hours. After the allotted reaction time, the dark green solution was cooled to 0 °C, and the subsequent red crystals were isolated by filtration, then washed with 5 × 30 mL DCE. The product [**5-1c**][OTf] was re-dissolved in 100 mL of refluxing MeCN, the solution hot filtered and concentrated to 30 mL, then cooled to room temperature for 1 h and to 0 °C for 4 hours. The red lustrous crystals were filtered off and washed with DCE, yield 0.938 g (2.00 mmol, 46%); mp 261-262 °C. IR: 1506 (s), 1270 (m), 1246 (s), 1226 (m), 1167 (w), 1030 (m), 789 (m), 714 (w), 678 (w), 637 (m), 471 (m) cm^{-1}. Anal. Calcd for $C_{11}H_{11}F_4N_3O_3S_5$: C, 28.14; H, 2.36; N, 8.95. Found: C, 28.05; H, 2.40; N, 8.91.

Preparation of 8-fluoro-4-pentyl-4H-bis([1,2,3]dithiazolo)[4,5-b:5',4'-e]pyridin-2-yl 5-1c. Decamethylferrocene (0.255 g, 0.781 mmol) was added to a solution of [**5-1c**] [OTf] (0.745 g, 1.14 mmol) in 9 mL bubble degassed MeCN. The slurry was stirred on an ice bath for 2 hours. After the allotted reaction time, the brown, matte solid was filtered off, washed with 5 × 10 mL freshly distilled MeCN, yield 188 mg, 79 %. Recrystallization of 150 mg of crude **5-1c** from 10 mL of hot, degassed (*via* four freeze-pump-thaw cycles) heptane afforded black/green needles suitable for single crystal X-ray diffraction; dec > 120 °C. IR: 1498 (m), 1481 (s), 1365 (m), 1315 (m), 1286 (w), 1236 (s), 1219 (s), 1100 (vs), 821 (m), 772 (m), 756 (m), 733 (w), 684 (m), 651 (m), 460 (m) cm^{-1}. Anal. Calcd for $C_{10}H_{11}FN_3S_4$: C, 37.48; H, 3.46; N, 13.11. Found: C, 37.27; H, 3.69; N, 12.85.

Preparation of *N*-hexyl-2,4,6-trifluoro-pyridinium Trifluoromethanesulfonate 5-7 (R_1 = Hx). A mixture of hexyl triflate (4.37 g, 18.7 mmol) and 2,4,6-trifluoropyridine **5-6** (1.65 g, 12.4 mmol) was stirred and heated in an oil bath at 70 °C for 16 h. After the allotted reaction time, the product obtained was dried *in vacuo*, after which the experimental ^{1}H NMR chemical shifts in CD_3CN compared well

with literature values of related compounds. [33] The product was used in subsequent steps without further purification.

Preparation of *N*-hexyl-2,6-diamino-4-fluoropyridinium Trifluoromethanesulfonate 5-8 (R_1 = Hx). The product **5-7** (R_1 = Hx, ~ 4.6 g, ~ 12.4 mmol) was dissolved in 50 mL of MeCN and cooled in an ice bath, over which ammonia gas was passed for 15 minutes, generating NH_4F as a white precipitate. The NH_4F was filtered off and the solvent flash evaporated to leave a white crystalline powder, which was recrystallized with 20 mL DCE/MeCN (10:1) to afford colorless crystals of **5-8** (R_1 = Hx), yield: 2.07 g (5.97 mmol, 48 % over two steps); mp 130-131 °C. IR: 3424 (m), 3355 (m), 3239 (s), 3116 (w), 1684 (m), 1645 (s), 1601 (s), 1515 (m), 1345 (w), 1276 (vs), 1245 (vs), 1220 (s), 1171 (s), 1079 (w), 1024 (vs), 807 (m), 762 (w), 639 (s), 597 (m), 574 (w), 532 (w), 515 (m) cm^{-1}. ^1H NMR (δ, CD_3CN): 6.23 (s, 2H), 5.94 (d, 1H, J = 9.3 Hz), 3.76 (m, 2H), 1.65 (m, 2H), 1.41 (m, 2H), 1.33 (m, 2H), 0.89 (t, 3H, J = 6.3 Hz). Anal. Calcd for $C_{12}H_{19}F_4N_3O_3S$: C, 39.89; H, 5.30; N, 11.63. Found: C, 39.77; H, 5.48; N, 11.86.

Preparation of 8-fluoro-4-hexyl-4H-bis([1,2,3]dithiazolo)[4,5-b:5',4'-e]pyridin-2-ium trifluoromethanesulfonate [5-1d][OTf]. The *N*-hexyl pyridinium triflate salt **5-8** (1.02 g, 2.82 mmol) was dissolved in 7 mL of a 5:2 mixture of DCE and MeCN under nitrogen. S_2Cl_2 (0.90 mL, 11.3 mmol) was added *via* syringe into the reaction flask and the solution was refluxed for 2 hours. After the allotted reaction time, the dark green solution was cooled to room temperature and then to 0 °C, and the subsequent red crystals were isolated by filtration, then washed with 3 × 10 mL DCE. The product [**5-1d**][OTf] was redissolved in 100 mL of hot MeCN, the solution hot filtered and concentrated to 25 mL, then cooled to room temperature for 1 h and then at 0 °C for 1 h. The red lustrous crystals were filtered off and washed with DCE, yield 0.49 g (2.00 mmol, 36%); mp 270-272 °C. IR: 1506 (s), 1270 (s), 1246 (s), 1226 (s), 1167 (s), 1119 (m), 1030 (s), 910 (w), 868 (w), 789 (s), 769 (w), 758 (w), 714 (m), 678 (m), 679 (m), 650 (m), 638 (s), 573 (w), 516 (m), 473 (s) cm^{-1}. Anal. Calcd for $C_{12}H_{13}F_4N_3O_3S_5$: C, 29.80; H, 2.71; N, 8.69. Found: C, 30.07; H, 2.50; N, 8.44.

Preparation of 8-fluoro-4-hexyl-4H-bis([1,2,3]dithiazolo)[4,5-b:5',4'-e]pyridin-2-yl 5-1d. Decamethylferrocene (0.454 g, 1.39 mmol) was added to a solution of [**5-1d**] [OTf] (0.641 g, 1.32

mmol) in 15 mL bubble degassed MeCN. The slurry was stirred at 0 °C for 3 hours. After the allotted reaction time, the brown, matte solid was filtered off, washed with 5 × 10 mL freshly distilled MeCN, yield 388 mg (88 %). Recrystallization of 100 mg of crude **5-1d** from 10 mL of hot, degassed (*via* four freeze-pump-thaw cycles) heptane afforded black/green needles suitable for single crystal X-ray diffraction; dec > 150 °C IR: 1500 (m), 1481 (s), 1374 (m), 1314 (m), 1300 (w), 1267 (w), 1234 (s), 1212 (m), 1099 (s), 822 (m), 769 (m), 727 (w), 685 (m), 652 (m), 477 (w), 461 (m), 422 (w) cm^{-1}. Anal. Calcd for $C_{12}H_{19}F_4N_3O_3S$: C, 39.50; H, 3.92; N, 12.56. Found: C, 39.36; H, 3.93; N, 12.36.

Preparation of 8-chloro-4-pentyl-4H-bis([1,2,3]dithiazolo)[4,5-b:5',4'-e]pyridin-2-ium trifluoromethanesulfonate [5-1][OTf] (R_1 = Pn; R_2 = Cl). Zwitterionic ClBP[17] (0.544 g, 1.55 mmol) and PnOTf (0.444 g, 2.02 mmol) were dissolved in 10 mL of freshly distilled DCE and stirred at room temperature for 24 hours. After the allotted reaction time, the crystals were filtered off, washed twice with DCM. The product was re-dissolved in 50 mL of refluxing MeCN, the solution hot filtered, and concentrated to 10 mL, then cooled to room temperature and then to 0 °C, yield 0.555 g (1.14 mmol, 74 %). IR: 1515 (w), 1488 (s), 1450 (s), 1362 (s), 1267 (s), 1248 (s), 1223 (m), 1165 (m), 1028 (s), 767 (m), 673 (w), 637 (m), 482 (m) cm^{-1}. Anal Calc'd for $C_{10}H_9ClF_3N_3O_3S_5$: C, 25.45; H, 1.92; N, 8.90. Found: C, 25.44; H, 1.93; N, 8.77.

Preparation of 8-chloro-4-butyl-4H-bis([1,2,3]dithiazolo)[4,5-b:5',4'-e]pyridin-2-ium trifluoromethanesulfonate [5-1][OTf] (R_1 = Bu; R_2 = Cl). Zwitterionic ClBP[17] (0.545 g, 1.55 mmol) and BuOTf (0.416 g, 2.02 mmol) were dissolved in 30 mL of freshly distilled DCE and stirred at room temperature for 48 hours. After the allotted reaction time, the crystals were filtered off, washed twice with DCM. The product was re-dissolved in 75 mL of refluxing MeCN, the solution hot filtered, and concentrated to 20 mL, then cooled to room temperature and then to 0 °C, yield 0.408 g (0.733 mmol, 47 %). Anal Calc'd for $C_{11}H_{11}ClF_3N_3O_3S_5$: C, 27.18; H, 2.28; N, 8.65. Found: C, 27.06; H, 2.32; N, 8.59.

Crystallography on 5-1c and 5-1d. See the Appendix for general crystallographic methods, used for 5-1a and 5-1b. X-ray data for **5-1c** were collected using omega and phi scans with a Bruker SMART 6000 CCD detector on a 3-circle goniometer and Cu Kα (λ = 1.5418 Å) radiation. The data were

scanned using Bruker's SMART program, integrated using Bruker's SAINT[34] software, and corrected for absorption using SADABS,[35] all as part of the Apex II software suite (Bruker 2010).[36] X-ray data for **5-1d** were collected using omega and phi scans with a Bruker APEX II CCD detector on a 3-circle goniometer and Mo Kα (λ = 0.71073 Å) radiation. The data were scanned using Bruker's SMART program, integrated using Bruker's SAINT software and corrected for absorption *via* face-indexing and redundant data (SADABS) all as part of the Apex II software suite (Bruker 2010). All of the structures were solved by direct methods using SHELXS-97[37] and refined by least-squares methods on F^2 using SHELXL-97[38] incorporated in the SHELXTL[39] suite of programs.

Quantum Monte Carlo (QMC) Spin Simulations. Quantum Monte Carlo (QMC) spin simulations employed the *looper* code implemented in the the ALPS (Algorithms and Libraries for Physics Simulations) distribution version 2.1.[29] Default values were used for number of sweeps and thermalization steps.[40] The values of the exchange parameters used were those obtained from DFT calculations above. Only interactions $\boldsymbol{J}_{\text{leg}}$ and $\boldsymbol{J}_{\text{rung}}$ were retained in the simulation. The calculated susceptibility was scaled so that the asymptotic $T \rightarrow \infty$ limit of χT matched the theoretical Curie constant for an S = ½ system, that is 0.375 emu·K·mol^{-1}. In order to ensure that other interactions between ladders had negligible effect on the magnetic response, a series of exact diagonalization calculations were also carried out on various small clusters of 12 radicals. The inclusion of such small interladder interactions had little effect on the predicted susceptibility, validating the isolated ladder model employed in the QMC simulations. These interactions were not included in the QMC simulations because there is a sign problem due to a small degree of frustration.

Chapter 6

Reflections and Projections

The family of radicals based on the bisdithiazolyl framework **6-1** – **6-4** has been thoroughly studied in the last decade. Numerous radicals have been synthesized with variations in R_1/R_2 substituents[1] and selenium content.[2,3] Although, at first, the choice of substituents was opportune instead of tactical, the synthetic methodology evolved to a point where thoughtful selection of alkyl and aryl groups, basal chalcogens and selenium incorporation was a possibility. Over the years, a number of different space groups in which the radicals crystallize were observed. In some cases, isostructural families could be generated,[4] and in other cases, deceptively simple chemical modifications led to a packing arrangement that was not the anticipated one.[2,5] Early endeavors to incorporate selenium led to the development of selenium σ-dimers when E_1 = S and E_2 = Se, which crystallize in the centrosymmetric $P2_1/c$ space group.[5] At first, this suggested a future filled exclusively with dimers based on this framework, which were considered at the time to be undesirable synthetic targets. Hopefully, the thorough discussion of hypervalent σ-dimers in this thesis has instead helped shed light on the rich properties these unique structures provide.[6]

Chart 6.1

	E_1	E_2
6-1	S	S
6-2	S	Se
6-3	Se	S
6-4	Se	Se

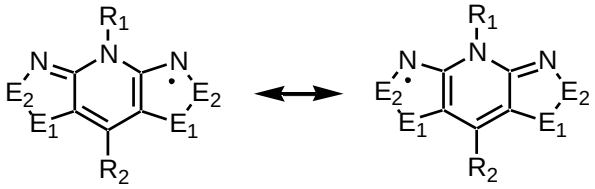

When incorporation of selenium into the framework included S/Se replacement in the E_1 position, the σ-dimer fate was avoided and isostructural families of radicals, most notably the tetragonal $P\bar{4}2_1m$ family, began to emerge.[4] These materials were unassociated in the solid state with no pairing of spins into localized bonds. However, the presence of beltline ligands R_1 and R_2 gave rise to, in most cases, the herringbone arrangement of slipped π-stacks in the solid state. This architecture led to localized

spins and, hence, Mott insulating ground states were always observed. Improvement in bandwidth could be effected by increasing selenium content, which gave rise to higher conductivity and lower activation energy.[2,3,4] Bandwidth could be improved with applied pressure, which we have explored in recent years.[2,6,7] Pressurization of the Mott insulators has led to physical changes ranging from stronger magnetic exchange to an insulator-to-metal transition (Chapter 2). Under pressure, the σ-dimers undergo an array of structural and physical changes depending on the beltline substituents (Chapters 3 and 4).

One key advantage to the Mott insulating state in these systems is that strong electron correlation leads to localized spins available to participate in magnetic exchange. As a result, we have observed a variety of magnetic properties in these systems ranging from simple AFM[1c,2,3,6b] or FM coupling[1a] of paramagnets, canted AFM ordering,[8] metamagnetism[9] and even bulk ferromagnetic ordering.[4] Table 6.1 lists the type of magnetic exchange or ordering as a function of substituents R_1 and R_2, as well as selenium content for a selection of radicals **6-1** – **6-4**. Acquired skills in crystal growth techniques coupled with determination has led to the structural characterization of all of these radicals.[10] In some cases, single crystal X-ray diffraction (XRD) was possible. When the quality of crystals was unsatisfactory, we resorted to powder XRD methods to solve and refine the structures. We have also been able to acquire powder data under pressure from synchrotron radiation, making it possible in all cases to correlate experimental properties with the known crystal structures of the radicals and radical dimers even under pressure.

Over the years, collaboration with physicists has led to the observation of remarkable results, particularly under pressure. The observation of metal-to-insulator (MIT) transitions[11] in a few of our radicals under relatively mild pressure (< 9 GPa)[7] has sparked the interest of condensed matter physicists studying highly correlated materials. An understanding of the theoretical aspects of this transition in our materials is what lies ahead. It would also be constructive to generate, with the right

tools and collaborators, phase diagrams for some of these radicals, like those that have been developed for charge transfer salts undergoing MIT.[12]

Table 6.1 Magnetic Properties* of a Selection of *N*-alkyl Pyridine-Bridged Radicals.

R_1	R_2	**5-1** (E_1, E_2 = S)	**5-2** (E_1 = S, E_2 = Se)	**5-3** (E_1 = Se, E_2 = S)	**5-4** (E_1, E_2 = Se)
Me	F	**weak AFM (α) σ-dimers (β)**	**σ-dimers**	---	---
Et	F	**AFM chains (α) σ-dimers (β)**	**σ-dimers**	---	---
Pr	F	**AFM chains**	---	---	---
Bu, Pn, Hx	F	**AFM spin ladders**	---	---	---
Me	H	metamagnet (T_N = 5 K)	σ-dimers	strong AFM	strong AFM
Et	H	weak AFM	σ-dimers	canted AFM (T_N = 18 K)	canted AFM (T_N = 28 K)
Me	Cl	weak AFM	strong AFM	strong AFM	strong AFM
Et	Cl, Br	weak FM	FM (T_c = 12–14 K)	canted AFM (T_N = 14 K)	**FM (T_c = 17–18 K)**
Pr	Cl	weak AFM	weak AFM	---	---

* In the absence of a noted ordering temperature, radicals are paramagnetic with FM/AFM coupling. Those in bold have been presented in detail in this thesis.

Although the pyridine-bridged radicals **6-1** – **6-4**, which crystallize in slipped π-stacks, have provided a diversity of physical properties, it is imperative to break out of the herringbone mold in order to improve things further. The ferromagnetic family of radicals (including **6-2** and **6-4**) with R_1 = Et and R_2 = Cl, Br all pack in the herringbone motif as slipped π-stacks, as discussed in Chapter 2. With pressurization, the π-stacks become less slipped and the herringbones "flatten" out, giving rise to better SOMO-SOMO overlap and enhanced electronic and magnetic communication. However, the great elongation of the alkyl R_1 substituent to butyl, pentyl and hexyl groups has led to a dramatic change in the crystal packing of these pyridine-bridged radicals giving rise to topological ladders (Chapter 5). This was also facilitated by the "pinning effect" of the F···S' interactions effectively negating the possibility of herringbones.

Although pressurization of herringbone structure leads to enhancement of the charge transport properties in these radicals, it is clear that a major change in the structure is necessary to generate a new motif. Certain molecular frameworks that may facilitate this breakout that could be explored are shown in Chart 6.2. For example, radicals **6-5** and **6-6**, which have been dubbed the 4-ring- and 5-ring circus, respectively, possess low *U* by virtue of the expanded resonance delocalization, as well as a high *W* due to the presence of sulfur in the ring systems. Low *U* radicals that have been synthesized and fully characterized in the Oakley group include the bis-thiadiazinyls **6-7**[13] and the hybrid dithiazolo-thiadiazinyls **6-8**.[14] Although these radicals met the low *U* criterion, limited solid state orbital overlap did not produce a large enough *W* for the known derivatives to be useful as conductive materials. Furthermore, a recent strategy for the development of extremely low *U* radicals based on graphene[15] fragments, of which phenalenyl **6-9** is a prime example, has been proposed by Morita *et al.*,[16] and includes triangulene **6-10**[17] and its derivative **6-11**.[18] While promising, the lack of heteroatoms in these structures is bound to severely hinder the possibility of high bandwidth, just as it has for phenalenyl derivatives in the past.[19] It has become increasingly clear over the years that *both* of these conditions must be met, that is, low *U* and high *W*, for the development of conductive neutral radicals.

Chart 6.2

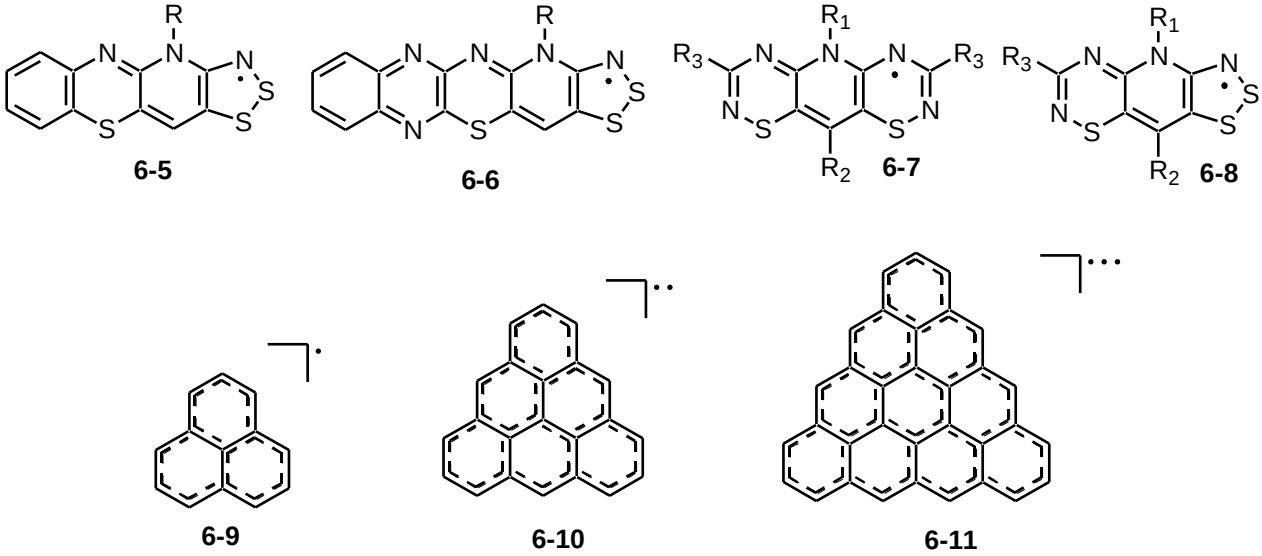

One promising new framework that has recently emerged out of the Oakley group seems to satisfy both of these conditions. The incorporation of supramolecular synthons, such as F···S' and O···S' interactions, into the oxobenzene-bridged bisdithiazolyl radicals **6-12** has produced an entirely different solid state architecture and novel properties.[20] As discussed in Chapter 1, these sulfur-based radicals pack in planar ribbon-like arrays (Figure 6.1), which, again, push the solid state packing away from the herringbone mold.[21] The resulting tightness of the crystal structures leads to improved bandwidth even in the absence of selenium.[22] The presence of the oxygen atom on the ring system also changes the electronic structure of the molecule itself, giving rise to a much lower *U* value for these materials as well.[23] Taken together, these improvements give rise to conductivities and activation energies that rival even the best selenium variants of the pyridine-bridged materials **6-4**. All of these radicals are also Mott insulators, with strong magnetic exchange that gives rise to canted AFM ordering in most cases.[24]

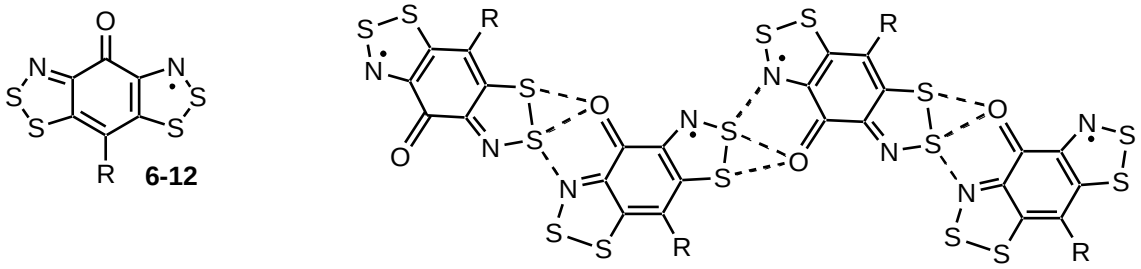

6-12

Figure 6.1 A single ribbon generated by O···S' and N···S' (top) interactions in the oxobenzene-bridged materials **6-12**.

The various ways in which derivatives of these radicals can pack include those shown in Figure 6.2, all generated by layering of the individual planar ribbons. When the substituent R is a bulky phenyl group, the ribbons assemble in ABAB layered π-stacks, an arrangement that gives rise to metamagnetism. The R = Me derivative forms ABAB layers, although the presence of two separate molecules in the asymmetric unit gives rise to columnar stacks of radicals within the cavities created by the alignment of out-of-register ribbons. With the replacement of the alkyl R substituent with a halogen atom (Cl, F), the structures become more 2D with interlayer interactions in addition to those along the π-stacks. When R = Cl, the radicals crystallize in slipped ribbon π-stacks, giving rise to very high

bandwidth and conductivity (3.0×10^{-3} cm^{-1}) with respect to the sulfur-based pyridine-bridged radicals **6-1** ($\sigma_{RT} \sim 10^{-6}$ cm^{-1}).

One notable derivative of **6-12** (R = F), coined FBBO in the group, crystallizes in such a way that layers of planar ribbons are pinned together by F···S' interactions.[24] The resulting π-stacks form a brick wall structure that leads to good orbital overlap in many directions and, hence, high bandwidth. Under ambient conditions, strong magnetic exchange along these pathways leads to an AFM ordering temperature of $T_N \sim 13$ K, $\sigma_{RT} \sim 2 \times 10^{-2}$ $S \cdot cm^{-1}$ and $E_{act} \sim 0.10$ eV. Although the selenium-based radicals of the pyridine-bridged materials **6-4** (R_1 = Et, R_2 = Cl, Br) require 7–9 GPa to metallize,[7a] FBBO undergoes an MIT at only 3 GPa. High pressure structural data has been examined, showing the compression of the structure in the absence of a phase change or CDW.

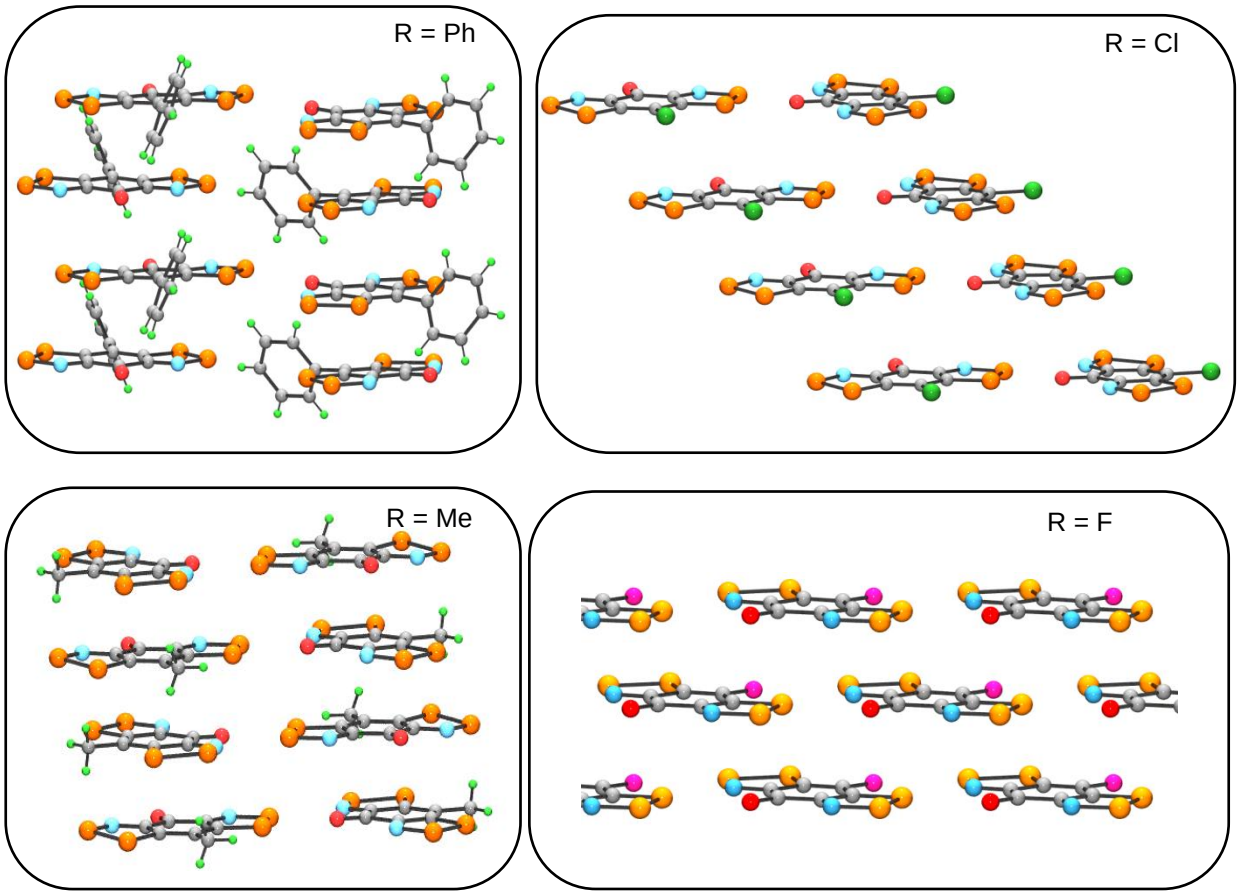

Figure 6.2 Crystal packing in the oxobenzene-bridged materials **6-12** as a function of R group.

With the remarkable properties displayed by the oxobenzene-bridge materials **6-12** in only the last few years, it is clear that this new framework is the future of neutral radical conductor science. Although variations in the substituent R are somewhat limited, the incorporation of selenium into one or both of the possible sites (E_1 and E_2) should give rise to further improvement in the properties. High pressure studies, including low temperature conductivity and magnetic measurements, are vital to the development of an understanding of the electronic transitions. This may also lead to the observation of superconductivity in some of these neutral radicals.

The vicinity of these strongly electron correlated materials, like FBBO and even **6-4** (R_1 = Et; R_2 = Cl, Br) to the metal-to-insulator transition gives rise to opportunities for rich physics. In a broader context, physicists have been investigating materials with novel properties in the area near the MIT for many years. Although changes in chemical and physical pressure have proven useful in my own work on Mott insulators and semiconducting dimers, it is the further exploration of physical pressure on highly correlated neutral radicals that will lead to the emergence of exciting, new physics.

References for Chapter 1

1. By contrast, as late as 1971, G. Herzberg's definition of a radical was "any transient species (atom, molecule, or ion)… - that is, any species that has a short lifetime in the gaseous phase under ordinary lab conditions. This definition excludes O_2, NO..." See Herzberg, G. *The Spectra and Structure of Simple Free Radicals*; Cornell University Press: Ithaca and London, **1971**.

2. (a) Tanko, J. M. *Annu. Rep. Prog. Chem. Sect. B.,* **2006**, *102*, 247. (b) Fleming, I. *Frontier Orbitals and Organic Chemical Reactions*, John Wiley & Sons, Ltd., Great Britain, **1976**, 182.

3. Hicks, R. G. *Org. Biomol. Chem.,* **2007**, *5*, 1321.

4. (a) Power, P. P. *Chem. Rev*. **2003**, *103*, 789. (b) Hicks, R. G., Ed. *Stable Radicals: Fundamentals and Applied Aspects of Odd-Electron Compounds*; J. Wiley and Sons, **2010**.

5. (a) Griller, D.; Ingold, K. U. *Acc. Chem. Res.* **1976**, *9*, 13.

6. Berliner, L. J. *Spin Labelling: Theory and Applications*, Academic Press, New York, **1979**.

7. (a) Perkins, M. J. *Adv. Phys. Org. Chem.* **1980**, *17*, 1. (b) Rehorek, D. *Chem. Soc. Rev.* **1991**, *20*, 341. (c) Beckwith, A. L. J.; Bowry, V. W.; Ingold, K. U. *J. Am. Chem. Soc.* **1992**, *114*, 4983. (d) Bowry, V. W.; Ingold, K. U. *J. Am. Chem. Soc.* **1992**, *114*, 4992.

8. (a) Yordanov, A. T.; Yamada, K.; Krishna, M. C.; Mitchell, J. B.; Woller, E.; Cloninger, M.; Brechbiel, M.W. *Angew. Chem. Int. Ed.* **2001**, *40*, 2690. (b) Reddy, T. J.; Iwama, T.; Halpern, H. J.; Rawal, V. H. *J. Org. Chem.* **2002**, *67*, 4635.

9. (a) Hawker, C. J.; Bosman, A. W.; Harth, E. *Chem. Rev*. **2001**, *101*, 3661. (b) Georges, M. K.; Veregin, R. P. N.; Kazmaier, P. M.; Hamer, G. K. *Macromolecules* **1993**, *26*, 2987.

10. Stubbe, J.; van der Donk, W. A. *Chem. Rev.* **1998**, *98*, 705.

11. Gomberg, M. *J. Am. Chem. Soc.* **1900**, *22*, 757.

12. Zhou, M.; Zhang, L.; Qin, Q. *J. Am. Chem. Soc.* **2000**, *122*, 4483.

13. Neuman, W. P.; Uzick, W.; Zarkadis, A. K. *J. Am. Chem. Soc.* **1986**, *108*, 3762.

14. Lankamp, H.; Nauta, Th.; MacLean, C. *Tetrahedron Lett.* **1968**, *9*, 249.

15. (a) Sabacky, M. J.; Johnson, C. S.; Smith, R. G.; Gutowsky, H. S.; Martin, J. C. *J. Am. Chem. Soc.* **1967**, *89*, 2054. (b) Reid, D. H. *Tetrahedron* **1958**, *3*, 339. (c) Sogo, B. P.; Nakazaki, M.; Calvin, M. *J. Chem. Phys.* **1957**, *26*, 1343.

16. Neugebauer, F. A.; Umminger, I. *Chem. Ber.*, **1980**, *113*, 1205.

17. Jang, S.-H.; Gopalan, P., Jackson, J. E.; Kahr, B. *Angew. Chem. Int. Ed.* **1994**, *33*, 775.

18. (a) Ballester, M.; Castaner, J.; Riera, J.; Ibanez, A.; Pujadas, J. *J. Org. Chem.* **1982**, *47*, 259. (b) Domingo, V. M.; Castaner, J.; Riera, J.; Labarta, A. *J. Org. Chem.* **1994**, *59*, 2604.

19. (a) Maspoch, D.; Ruiz-Molina, D.; Wurst, K.; Rovira, C.; Veciana, J. *Chem. Commun.* **2002**, 2958. (b) Maspoch, D.; Gomez-Segura, J.; Domingo, N.; Ruiz-Molina, D.; Wurst, K.; Rovira, C.; Tejada, J.; Veciana, J. *Inorg. Chem.* **2005**, *44*, 6936.

20. Veciana, J.; Ratera, I. In *Stable Radicals: Fundamentals and Applied Aspects of Odd-Electron Compounds*; Hicks, R. G., Ed.; John Wiley & Sons, Ltd.: Wiltshire, U.K., **2010**; pp 33 – 80.

21. Maspoch, D.; Ruiz-Molina, D.; Veciana, J. *Chem. Soc. Rev.* **2007**, *36*, 770.

22. Zaitsev, V.; Rosokha, S. V.; Head-Gordon, M.; Kochi, J. K. J. Org. Chem. **2006**, *71*, 520.

23. Reid, D. H. *Quart. Rev.* **1965**, *19*, 274.

24. O'Connor, G. D.; Troy, T. P.; Roberts, D. A.; Chalyavi, N.; Fückel, B.; Crossley, M. J.; Nauta, K.; Stanton, J. F.; Schmidt, T. W. *J. Am. Chem. Soc.* **2011**, *133*, 14554.

25. (a) Broser, W.; Kurreck, H.; Oestreichjanzen, S.; Schlomp, G.; Fey, H. J.; Kirste, B. *Tetrahedron* **1979**, *35*, 1159. (b) Zaitsev, V.; Rosokha, S. V.; Head-Gordon, M.; Kochi, J. K. *J. Org. Chem.* **2006**, *71*, 520.

26. (a) Goto, K.; Kubo, T.; Yamamoto, K.; Nakasuji, K. Sato, K.; Shiomi, D.; Takui, T.; Kubota, M.; Kobayashi, T.; Yakusi, K.; Ouyang, J. Y. *J. Am. Chem. Soc.* **1999**, *121*, 1619. (b) Lu, J. M.; Rosokha, S. V.; Kochi, J. K. *J. Am. Chem. Soc.* **2003**, *125*, 12161. (c) Small, D.; Zaitsev, V.; Jung, Y. S.; Rosokha, S. V.; Head-Gordon, M.; Kochi, J. K. *J. Am. Chem. Soc.* **2004**, *126*, 13850. (d) Small, D.; Rosokha, S. V.; Kochi, J. K.; Head-Gordon, M. *J. Phys. Chem. A* **2005**,

109, 11261.

27. (a) Koutentis, P. A.; Haddon, R. C.; Oakley, R. T.; Cordes, A. W.; Brock, C. P. *Acta Crystallogr*. **2001**, *B57*, 680. (b) Koutentis, P. A.; Chen, Y.; Cao, Y.; Best, T. P.; Itkis, M. E.; Beer, L.; Oakley, R. T.; Cordes, A. W.; Brock, C. P.; Haddon, R. C. *J. Am. Chem. Soc.* **2001**, *123*, 3864.

28. (a) Haddon, R. C.; Wudl, F.; Kaplan, M. L.; Marshall, J. H.; Cais, R. E.; Bramwell, F. B. *J. Am. Chem. Soc.* **1978**, *100*, 7629. (b) Haddon, R. C.; Wudl, F.; Kaplan, M. L.; Marshall, J. H.; Bramwell, F. B. *J. Chem. Soc., Chem. Commun*. **1978**, 429.

29. Beer, L.; Mandal, S. K.; Reed, R. W.; Oakley, R. T.; Tham, F. S.; Donnadieu, B.; Haddon, R. C. *Cryst. Growth & Des.* **2007**, *7*, 802.

30. Clarke, C. S.; Jornet-Somoza, J.; Mota, F.; Novoa, J. J.; Deumal, M. *J. Am. Chem. Soc.* **2010**, *132*, 17817.

31. (a) Tian, Y. –H.; Kertesz, M. *J. Am. Chem. Soc.* **2010**, *132*, 10648. (b) Tian, Y. –H.; Kertesz, M. *J. Phys. Chem. A*, **2011**, *115*, 13942.

32. Bohle, D. S. In *Stable Radicals: Fundamentals and Applied Aspects of Odd-Electron Compounds*; Hicks, R. G., Ed.; John Wiley & Sons, Ltd.: Wiltshire, U.K., **2010**; pp 149 – 171.

33. Coulson, C. A. *Valence, 2nd Ed.*; Oxford University Press: London, **1961**.

34. March, J. *Advanced Organic Chemistry: Reactions, Mechanisms, and Structure*; McGraw-Hill, Inc.: New York, **1977**.

35. Coppinger, G. M. *J. Am. Chem. Soc.* **1957**, *79*, 501.

36. Dietz, F.; Tyutyulkov, N.; Baumgarten, M. *J. Phys. Chem. B*, **1998**, *102*, 3912.

37. (a) Forrester, A. R.; Hay, J. M.; Thomson, R. H. *Organic Chemistry of Stable Free Radicals*: Academic Press, London, **1968**. (b) Rozanstev, E. G.; *Free Nitroxyl Radicals*: Plenum, New York, **1970**. (c) Rozanstev, E. G.; Sholle, V. D. *Synthesis*, **1971**, 401. (d) Rozanstev, E. G. Sholle, V. D. *Synthesis*, **1971**, 190.

38. Griffith, O. H.; Waggoner, A. S. *Acc. Chem. Res.* **1969**, *2*, 17.

39. Janzen, E. G. *Acc. Chem. Res.* **1971**, *4*, 31.

40. Khramtsov, V. V.; Grigor'ev, I. A.; Foster, M. A.; Lurie, D. J. *Antioxid. Redox Signal*, **2004**, *6*, 667.

41. Bardelang, D.; Zaman, M. B.; Moudrakovski, I. L. Pawsey, S.; Margeson, J. C.; Wang, D.; Wu, X.; Ripmeester, J. A.; Ratcliffe, C. I.; Yu, K. *Adv. Mater*. **2008**, *20*, 4517.

42. Grimaldi, S.; Finet, J. P.; Zeghdaoui, A.; Tordo, P.; Benoit, D.; Gnanou, Y.; Fontanille, M.; Nicol, P.; Pierson, J. F. *ACS Polym. Prepr*. **1997**, *38*, 651.

43. (a) Hall, D. A.; Maus, D. C.; Gerfen, G. J. Inati, S. J.; Becerra, L. R.; Dahlquist, F. W.; Griffin, R. G. *Science* **1997**, *276*, 930. (b) Joo, C. G.; Casey, A.; Turner, C. J.; Griffin, R. G. *J. Am. Chem. Soc.* **2009**, *131*, 12.

44. Recupero, F.; Punta, C. *Chem. Rev.* **2007**, *107*, 3800.

45. Kuhn, R.; Trischmann, H. *Angew. Chem., Int. Ed. Engl*. **1963**, *3*, 155.

46. Neugebauer, F. A.; Fischer, H.; Siegel, R. *Chem. Ber*. **1988**, *121*, 815.

47. Pare, E. C.; Brook, D. J. R.; Brieger, A.; Badik, M.; Schinke, M. *Org. Biomol. Chem.* **2005**, *3*, 4258.

48. Hicks, R. G. In *Stable Radicals: Fundamentals and Applied Aspects of Odd-Electron Compounds*; Hicks, R. G., Ed.; John Wiley & Sons, Ltd.: Wiltshire, U.K., **2010**; pp 317 – 380.

49. (a) Denk, M. K. *Eur. J. Inorg. Chem.* **2009**, 1358. (b) Danenand, W. C.; Newkirk, D. D. *J. Am. Chem. Soc.* **1976**, *98*, 516. (c) Maillard, B.; Ingold, K. U. *J. Am. Chem. Soc.* **1976**, *98*, 520.

50. Compare that with the dissociation enthalpy $\Delta H_{diss} \sim -34$ kcal mol^{-1} for a generic peroxide. See *J. Am. Chem. Soc.* **1996**, *118*, 12758.

51. Oakley, R. T. *Progr. Inorg. Chem.* **1988**, *98*, 516.

52. Chivers, T. *Chem. Rev.* **1985**, *85*, 341.

53. (a) Green, R. L.; Street, G. B.; Suter, L. J. *Phys. Rev. Lett.* **1975**, *34*, 577. (b) Labes, M. M.; Love, P.; Nichols, L. F. *Chem. Rev.* **1979**, *79*, 1. (c) Banister, A. J.; Gorrell, I. B. *Adv. Mater.*

1998, 1415.

54. Stejny, J.; Dlugosz, J.; Keller, A. *J. Mater. Sci.* **1979**, *14*, 1291.

55. T. Chivers, A.W. Cordes, R.T. Oakley and P.N. Swepston. *Inorg. Chem.* **1981**, *20*, 2376.

56. Kennett, F. A.; MacLean, G. K.; Passmore, J.; Rao M. N. S. *J. Chem. Soc. Dalton Trans.* **1982**, *851*.

57. Boudeulle, M. *Cryst. Struct. Commun.* **1975**, *4*, 9**.**

58. (a) Cohen, M. J.; Garito, A. F.; Heeger, A. J.; MacDiarmid, A. G.; Mikulski, C. M.; Saran, M. S.; Kleppinger, J. *J. Am. Chem. Soc.* **1976**, *98*, 3844. (b) Heger, G.; Klein, S.; Pintschovius, L.; Kahlert, H. *J. Sol. St. Chem.* **1978**, *23*, 341.

59. Berlinsky, A. J. *J. Phys. C*, **1976**, *9***,** L283.

60. Rawson, J. M.; Banister, A. J.; Lavender, I., in *Advances in Heterocyclic Chemistry*, **1995**, *62*, 137.

61. Rawson, J. M.; Alberola, A.; Whalley, A. *J. Mater. Chem.* **2006**, *16*, 2560.

62. (a) Vegas, A.; Perezsalazar, A.; Banister, A. J.; Hey, R. G. *J. Chem. Soc., Dalton Trans.*, **1980**, 1812. (b) Cordes, A. W.; Bryan, C. D.; Davis, W. M.; Delaat, R. H.; Glarum, S. H.; Goddard, J. D.; Haddon, R. C.; Hicks, R. G.; Kennepohl, D. K.; Oakley, R. T.; Scott S. R.; Westwood, N. P. C. *J. Am. Chem. Soc.* **1993**, *115*, 7232. (c) Cordes, A. W.; Haddon, R. C.; Hicks, R. G.; Kennepohl, D. K.; Oakley, R. T.; Palstra, T. T. M.; Schneemeyer, L. F.; Scott, S. R.; Waszczak, J. V. *Chem. Mater.* **1993**, *5*, 820. (d) Cordes, A. W.; Haddon, R. C.; Hicks, R. G.; Kennepohl, D. K.; Oakley, R. T.; Schneemeyer, L. F.; Waszczak, J. V. *Inorg. Chem.* **1993**, *32*, 1554. (d) Bryan, C. D.; Cordes, A. W.; Haddon, R. C.; Hicks, R. G.; Oakley, R. T.; Palstra, T. T. M.; Perel, A. J. *J. Chem. Soc., Chem. Commun.* **1994**, 1447. (e) Clarke, C. S.; Haynes, D. A.; Rawson, J. M.; Bond, A. D. *Chem. Commun.* **2003**, 2774.

63. Cordes, A. W.; Haddon, R. C.; Hicks, R. G.; Oakley, R. T.; Palstra, T. T. M. *Inorg. Chem.* **1992**, 31, 1802.

64. (a) Hofs, H. U.; Bats, J. W.; Gleiter, R.; Hartmann, G.; Mews, R.; Eckertmaksic, M.; Oberhammer, H.; Sheldrick, G. M. *Chem. Ber.* **1985**, *118*, 3781. (b) Banister, A. J.; Hansford,

M. I.; Hauptman, Z. V.; Wait, S. T.; Clegg, W. *J. Chem. Soc., Dalton Trans.* **1989**, 1705. (c) Cordes, A. W.; Goddard, J. D.; Oakley, R. T.; Westwood, N. P. C. *J. Am. Chem. Soc.* **1989**, *111*, 6147.

65. Barclay, T. M.; Cordes, A. W.; George, N. A.; Haddon, R. C.; Itkis, M. E.; Oakley, R. T. *Chem. Commun.* **1999**, 2269.

66. (a) Belluz, P. D.; Cordes, A. W.; Kristof, E. M.; Kristof, P. V.; Liblong, S. W.; Oakley, R. T. *J. Am. Chem. Soc.* **1989**, *111*, 9276. (b) Cordes, A. W.; Glarum, S. H.; Haddon, R. C.; Hallford, R.; Hicks, R. G.; Kennepohl, D. K.; Oakley, R. T.; Palstra, T. T. M.; Scott, S. R. *J. Chem. Soc., Chem. Commun.* **1992**, 1265. (c) Cordes, A. W.; Haddon, R. C.; Hicks, R. G.; Oakley, R. T.; Palstra, T. T. M.; Schneemeyer, L. F.; Waszczak, J. V. *J. Am. Chem. Soc.* **1992**, *114*, 1729. (d) Davis, W. M.; Hicks, R. G.; Oakley, R. T.; Zhao, B. Y.; Taylor, N. J. *Can. J. Chem.* **1993**, *71*, 180.

67. Feeder, N.; Less, R. J.; Rawson, J. M.; Oliete, P.; Palacio, F. *Chem. Commun.* **2000**, 2449.

68. Awere, E. G.; Burford, N.; Mailer, C.; Passmore, J.; Schriver, M. J.; White, P. S.; Banister, A. J.; Oberhammer, M.; Sutcliffe, L. H. *J. Chem. Soc., Chem. Commun.* **1987**, 66.

69. (a) Alberola, A.; Burley, J.; Collis, R. J.; Less, R. J.; Rawson, J. M. *J. Organometal. Chem.* **2007**, *695*, 2750. (b) Brusso, J. L.; Clements, O. P.; Haddon, R. C.; Itkis, M. E.; Leitch, A. A.; Oakley, R. T.; Reed, R. W.; Richardson, J. F. *J. Am. Chem. Soc.* **2004**, *126*, 8256. (c) McManus, G. D.; Rawson, J. M.; Feeder, N.; Palacio, F.; Oliete, P. *J. Mater. Chem.* **2000**, *10*, 2001.

70. (a) Brownridge, S.; Shirley, H. D.; Fairhurst, A.; Haddon, R. C.; Oberhammer, H.; Parsons, S.; Passmore, J.; Schriver, M. J.; Sutcliffe, L. H.; Westwood, N. P. C. *J. Chem. Soc., Dalton Trans.* **2000**, 3365. (b) Alberola, A.; Clements, O. P.; Collis, R. J.; Cubbitt, L.; Grant, C. M.; Less, R. J.; Oakley, R. T.; Rawson, J. M.; Reed, R. W.; Robertson, C. M. *Cryst. Growth Des.* **2008**, *8*, 155. (c) Awere, E. G.; Burford, N.; Haddon, R. C.; Parsons, S.; Passmore, J.; Waszczak, J. V.; White, P. S. *Inorg. Chem.* **1990**, *29*, 4821.

71. Barclay, T. M.; Cordes, A. W.; deLaat, R. H.; Goddard, J. D.; Haddon, R. C.; Jeter, D. Y.; Mawhinney, R. C.; Oakley, R. T.; Palstra, T. T. M.; Patenaude, G. W.; Reed, R. W; Westwood, N. P. C. *J. Am. Chem. Soc.* **1997**, *119*, 2633.

72. Barclay, T. M.; Cordes, A. W.; George, N. A.; Haddon, R. C.; Oakley, R. T.; Patenaude, G. W.; Reed, R. W.; Zhang, H. *J. Chem. Soc., Chem Commun.* **1997**, 873.

73. Barclay, T. M.; Cordes, A. W.; George, N. A.; Haddon, R. C.; Itkis, M. E.; Mashuta, M. S.; Oakley, R. T.; Patenaude, G. W.; Reed, R. W.; Richardson, J. F.; Zhang, H. *J. Am. Chem. Soc.* **1998**, *120*, 352.

74. Brusso, J. L.; Clements, O. P.; Haddon, R. C.; Itkis, M. E.; Leitch, A. A.; Oakley, R. T.; Reed, R. W.; Richardson, J. F. *J. Am. Chem. Soc.* **2004**, *126*, 14692.

75. (a) Fujita, W.; Awaga, K. *Science* **1999**, *286*, 281. (b) McManus, G. D.; Rawson, J. M.; Feeder, N.; McInnes, E. J. L.; Novoa, J. J.; Burriel, R.; Palacio, F.; Oliete, P. *J. Mater. Chem.* **2001**, *11*, 1992. (c) Fujita, W.; Awaga, K. *Synth. Met.* **2000**, *137*, 1263.

76. Andrews, M. P.; Cordes, A. W.; Douglass, D. C.; Fleming, R. M.; Glarum, S. H.; Haddon, R. C.; Marsh, P.; Oakley, R. T.; Palstra, T. T. M.; Schneemeyer, L. F.; Trucks, G. W.; Tycko, R. R.; Waszczak, J. V.; Warren, W. W.; Young, K. M.; Zimmerman, N. M. *J. Am. Chem. Soc.* **1991**, *113*, 3559.

77. Gütlich, P.; Rovira, C.; Goodwin, H. *Chem. Soc. Rev.* **2000**, *29*, 419.

78. Gütlich, P., Goodwin, H. A., Eds., *Spin Crossover in Transition Metal Compounds I-III*; Springer, **2004**. (b) Halcrow, M. A., Ed., *Spin Crossover Materials: Properties and Applications*; J. Wiley & Sons, **2013**.

79. (a) Varret, F.; Boukheddaden, K.; Chastanet, G.; Paradis, N.; Létard, J-F. Eur. J. *Inorg. Chem.* **2013**, 763. (b) Li, D.; Clérac, R.; Rou-beau, O.; Harté, E.; Mathonière, C.; Le Bris, R.; Holmes, S. M. *J. Am. Chem. Soc.* **2008**, *130*, 252.

80. Rawson, J. M.; Hayward, J. J. In *Spin-Crossover Materials: Properties and Applications*: Ed. Halcrow, M. A.: J. Wiley & Sons, **2013**, Chap 8.

81. Lekin, K.; Winter, S. M.; Downie, L. E.; Bao, X.; Tse, J. S.; Desgreniers, S.; Secco, R. A.; Dube, P. A.; Oakley, R. T. *J. Am. Chem. Soc.* **2010**, 132, 16212.

82. (a) Mayer, R., Domschke, G., Bleisch, S., and Bartl, A. *Tetrahedron Lett.* **1978**, 4003. (b) Mayer, R., Domschke, G., Bleisch, S., Bartl, A., and Stãsko, A. *Z. Chem.* **1981**, *21*, 146; *Z. Chem.* **1981**, *21*, 264. (c) Mayer, R., Domschke, G., Bleisch, S., Fabian, J., Bartl, A., and

Stãsko, A. *Collect. Czech. Chem. Commun.* **1984**, *49*, 684. (d) Mayer, R., Bleisch, S., Domschke, G., Tkáè, A., Stãsko, A., and Bartl, A. *Org. Magn. Reson.* **1979**, *12*, 532. (e) Tsveniashvili, V. Sh. *Collect. Czech. Chem. Commun.* **1982**, *47*, 203. (f) Harrison, S. R., Pilkington, R. S., and Sutcliffe, L. H. *J. Chem. Soc., Faraday Trans. 1* **1984**, *80*, 669. (g) Preston, K. F. and Sutcliffe, L. H. *Magn. Reson. Chem.* **1990**, *28*, 189. (h) Bagryansky, V. A., Vlasyuk, I. V., Gatilov, Y. V., Makarov, A. Y., Molin, Y. N., Shcherbukhin, V. V., and Zibarev, A. V. *Mendeleev Commun.* **2000**, *10*, 5.

83. Sullivan, D. J.; Clerac, R.; Jennings, M.; Lough, A. J.; Preuss, K. E. *Chem. Commun*. **2012**, *48*, 10963.

84. Appel, R.; Janssen, H.; Siray, M.; Knoch, F. *Chem. Ber*. **1985**, *118*, 1632.

85. Barclay, T. M.; Cordes, A. W.; Oakley, R. T.; Preuss, K. E.; Reed, R. W. *Chem. Commun.* **1998**, 1039.

86. Risto, M.; Assoud, A.; Winter, S. M.; Oilunkaniemi, R.; Laitinen, R. S.; Oakley, R. T. *Inorg. Chem*. **2008**, 47, 10100.

87. Oakley, R. T.; Reed, R. W.; Robertson, C. M.; Richardson, J. F. *Inorg. Chem.* **2005**, *44*, 1837.

88. Barclay, T. M.; Cordes, A. W.; Haddon, R. C.; Itkis, M. E.; Oakley, R. T.; Reed, R. W.; Zhang, H. *J. Am. Chem. Soc.* **1999**, *121*, 969.

89. Barclay, T. M.; Beer, L.; Cordes, A. W.; Oakley, R. T.; Preuss, K. E.; Taylor, N. J.; Reed, R. W. *Chem. Commun.* **1999**, 531.

90. Beer, L.; Cordes, A. W.; Haddon, R. C.; Itkis, M. E.; Oakley, R. T.; Reed, R. W.; Robertson, C. M. *Chem. Commun.* **2002**, 1872.

91. Beer, L.; Brusso, J. L.; Cordes, A. W.; Haddon, R. C.; Itkis, M. E.; Kirschbaum, K.; MacGregor, D. S.; Oakley, R. T.; Pinkerton, A. A.; Reed, R. W. *J. Am. Chem. Soc.* **2002**, *124*, 9498.

92. (a) Carlin, R. L. *Magnetochemistry*, Springer-Verlag, New York, 1986. (b) Ito, A.; Suenaga, M.; Ono, K. *J. Chem. Phys.* **1968**, *48*, 3597. (c) Day, P., Gregson, K.; Leech, D. H. *Phys. Rev. Lett.* **1973**, *30*, 19. (d) Day, P. *Acc. Chem. Res.* **1979**, *14*, 236.

93. (a) Manriques, J. M.; Yee, G. T.; McLean, R. S.; Epstein, A. J.; Miller, J. S. *Science* **1991**, *252*, 1415. (b) Rittenberg, D. K.; Sugiura, K.-I.; Sakata, Y.; Mikami, S.; Epstein, A. J.; Miller, J. S. *Adv. Mater*. **2000**, *12*, 126.

94. Miller, J. S. *Adv. Mater*. **2002**, *14*, 1105.

95. In some accounts, the exchange integral is called α, or K, and the Coulomb integral Q or K.

96. This is when the Heisenberg Hamiltonian $\hat{H} = -2J \cdot \hat{S}_a \hat{S}_b$ is employed. There are other forms of this Hamiltonian from which J may take on a slightly different meaning.

97. Deumal, M.; Robb, M. A.; Novoa, J. J. *Prog. Theo. Chem. Phys.* **2007**, *16*, 271.

98. (a) Noodleman, L.; Norman, J. G. *J. Chem. Phys*. **1979**, *70*, 4903. (b) Noodleman, L. *J. Chem. Phys.* **1981**, *74*, 5737.

99. Heisenberg, W. Z. *Z. Phys.* **1926**, *38*, 411.

100. (a) Novoa, J. J.; Deumal, M. *Struct. Bonding* **2001**, *100*, 33. (b) Jornet, J.; Deumal, M.; Ribas-Ariño, J.; Bearpark, M. J.; Robb, M. A.; Hicks, R. G.; Novoa, J. J. *Chem. Eur. J.* **2006**, *12*, 3995.

101. (a) Rawson, J. M.; Luzon, J.; Palacio, F. *Coord. Chem. Rev.* **2005**, *249*, 2631. (b) Luzon, J.; Campo, J.; Palacio, F.; McIntyre, G. J.; Rawon, J. M. *Polyhedron* **2005**, *24*, 2579. (c) Deumal, M.; LeRoux, S.; Rawson, J. M.; Robb, M. A.; Novoa, J. J. *Polyhedron* **2007**, *26* 1949. (d) Decken, A.; Mattar, S. M.; Passmore, J.; Shuvaev, D. V.; Thompson, L. K. *Inorg. Chem.* **2006**, *45*, 3878. (e) Leitch, A. A.; Oakley, R. T.; Reed, R. W.; Thompson, L. K. *Inorg. Chem.* **2007**, *46*, 6261.

102. Roberston, C. M.; Leitch, A. A.; Cvrkalj, K.; Myles, D. J. T.; Reed, R. W.; Dube, P. A.; Oakley, R. T. *J. Am. Chem. Soc.* **2008**, *130*, 14791. (b) Leitch, A. A.; Yu, X.; Winter, S. M.; Secco, R. A.; Dube, P. A.; Oakley, R. T. *J. Am. Chem. Soc.* **2009**, *131*, 7112.

103. Takano, Y.; Taniguchi, T.; Isobe, H.; Kubo, T.; Morita, Y.; Yamamoto, K.; Nakasuji, K.; Takui, T.; Yamaguchi, K. *J. Am. Chem. Soc.* **2002**, *124*, 11122.

104. Jiles, D. *Introduction to Magnetism and Magnetic Materials*; Chapman and Hall: London, 1991.

105. (a) Murugesu, M.; Wernsdorfer, W.; Christou, G.; Brechin, E. K. *Polyhedron* **2007**, *26*, 1845. (b) Nihei, M.; Yoshida, A.; Koizumi, S.; Oshio, H. *Polyhedron* **2007**, *26*, 1997. (c) Stamatotos, T. C.; Abboud, K. A.; Wrnsdorfer, W.; Christou, G. *Polyhedron* **2007**, *26*, 2042.

106. (a) Rahman, B.; Kanbara, K.; Akutsu, H.; Yamada, J.; Nakatsuji, S. *Polyhedron* **2007**, *26*, 2287. (b) Koizumi, K.; Shoji, M.; Kitagawa, Y.; Takeda, R.; Yamanaka, S.; Kawakami, T.; Okumura, M.; Yamaguchi, K. *Polyhedron* **2007**, *26*, 2135. (c). Harvey, M. D.; Pace, J. T.; Yee, G. T. *Polyhedron* **2007**, *26*, 2037.

107. (a) Lin, P.-H.; Burchell, T. J.; Clérac, R.; Murugesu, M. *Angew. Chem., Int. Ed.,* **2008**, 47, 8848. (b) Cardona-Serra, S.; Clemente-Juan, J. M.; Coronado, E.; Gaita-Ariño, A.; Camón, A.; Evangelisti, M.; Luis, F.; Martínez-Pérez, M. J.; Sesé, J. *J. Am. Chem. Soc*. **2012**, *134*, 14982.

108. Caneschi, A.; Gatteschi, D.; Renard, J. P.; Rey, P.; Sessoli, R. *Inorg. Chem.* **1989**, *28*, 1976.

109. (a) Sessoli, R.; Tsai, H. –L.; Schake, A. R.; Wang, S.; Vincent, J. B.; Folting, K.; Gatteschi, D.; Christou, G.; Hendrickson, D. N. *J. Am. Chem. Soc.* **1993**, *115*, 1804. (b) Sessoli, R.; Gatteschi, D.; Caneschi, A.; Novak, M. A. *Nature* **1993** , *365*, 141. (c) Lis, T. *Acta. Cryst.* **1980**, *B36*, 2042.

110. Chaboussant, G.; Sieber, A.; Ochsenbein, S.; Güdel, H.-U.; Murrie, M.; Honecker, A.; Fukushima, N.; Normand. B. *Phys. Rev. B*, **2004**, *70*, 104422.

111. Zhang, P.; Guo, Y. –N.; Tang, J. *Coord. Chem. Rev.* **2013**, *257*, 1728.

112. Habib, F.; Murugesu, M. *Chem. Soc. Rev.* **2013**, *42*, 3278.

113. Miller, J. S.; Calabrese, J. C.; Epstein, A. J.; Bigelow, R. W.; Zhang, J. H.; Reiff, W. M. *J. Chem. Soc., Chem. Commun.* **1986**, 1026.

114. Fujita, W.; Awaga, K. *Chem. Phys. Lett.* **2002**, *357*, 385.

115. Allemand, P.; Khemani, K. C.; Koch, A.; Wudl, F.; Holczer, K.; Donovan, S.; Grunner, G.; Thompson, J. D. *Science* **1991**, *253*, 301.

116. Narymbetov, B.; Kobayashi, H.; Tokumoto, M.; Omerzu, A.; Mihailovic, D. *Chem. Commun.* **1999**, 1511.

117. (a) Takahashi, M.; Turek, P.; Nakazawa, Y.; Tamura, M.; Nozawa, K.; Shiomi, D.; Ishikawa, M.; Kinoshita, M. *Phys. Rev. Lett.* **1991**, *67*, 746. (b) Tamura, M.; Nakazawa, Y.; Shiomi, D.; Nozawa, K.; Hosokoshi, Y.; Ishikawa, M.; Takahashi, M.; Kinoshita, M. *Chem. Phys. Lett.* **1991**, *186*, 401.

118. Chiarelli, R.; Novak, M. A.; Rassat, A.; Tholence, J. L. *Nature* **1993**, *363*, 147.

119. Alberola, A.; Less, R. J.; Pask, C. M.; Rawson, J. M.; Palacio, F.; Oliete, P.; Paulsen, C.; Yamaguchi, A.; Murphy, D. M.; Farley, R. D. *Angew. Chem., Int. Ed.*, **2003**, *42*, 4782.

120. (a) Palacio, F.; Antorrena, G.; Castro, M.; Burriel, R.; Rawson, J. M.; Smith, J. N. B.; Bricklebank, N.; Novoa J.; Ritters, C. *Phys. Rev. Lett.* **1997**, *79*, 2336. (b) Banister, A. J.; Bricklebank, N.; Lavender, I.; Rawson, J. M.; Gregory, C. I.; Tanner, B. K.; Clegg, W.; Elsegood, M. R. J.; Palacio, F. *Angew. Chem. Int. Ed. Engl.* **1996**, *35*, *No. 21*, 2533.

121. (a) Mito, M.; Kawae, T.; Takeda, K.; Takagi, S.; Matsushita, Y.; Deguchi, H.; Rawson, J. M.; Palacio, F. *Polyhedron* **2001**, *20*, 1509. (b) Thomson, R. I.; Pask, C. M.; Lloyd, G. O.; Mito, M.; Rawson, J. M. *Chem. Eur. J.* **2012**, *18*, 8629.

122. Leitch, A. A.; Brusso, J. L.; Cvrkalj, K.; Reed, R. W.; Robertson, C. M.; Dube, P. A.; Oakley, R. T. *Chem. Commun*. **2007**, 3368.

123. (a) Robertson, C. M.; Myles, D. J. T.; Leitch, A. A.; Reed, R. W.; Dooley, D. M.; Frank, N. L.; Dube, P. A.; Thompson, L. K.; Oakley, R. T. *J. Am. Chem. Soc*. **2007**, *129*, 12688. (b) Robertson, C. M.; Leitch, A. A.; Cvrkalj, K.; Reed, R. W.; Myles, D. J. T.; Dube, P. A.; Oakley, R. T. *J. Am. Chem. Soc*. **2008**, *130*, 8414.

124. Lekin, K.; Wong, J. W. L.; Winter, S. M.; Mailman, A.; Dube, P. A.; Oakley, R. T. *Inorg. Chem.* **52**, 2188-2198 (2013).

125. (a) Winter, S. M; Datta, S.; Hill, S.; Oakley, R. T. *J. Am. Chem. Soc.* **2011**, *133*, 8126. (b) Winter, S. M.; Oakley, R. T.; Kovalev, A. E.; Hill, S. *Phys. Rev. B.* **2012**, *85*, 094430.

126. Day, P. *Nature* **1993**, *363*, 113.

127. (a) McCoy, H. N.; Moore, W. C. *J. Am. Chem. Soc.* **1911**, *33*, 273. (b) Krauss, H. J. *J. Am. Chem. Soc*. **1913**, *34*, 1732.

128. Little, W. A. *Phys. Rev. A.* **1964**, *134*, A1416.

129. (a) Okamoto, Y.; Brenner, W. *Organic Semiconductors*, Rheinhold (1964). (b) Akamatu, H.; Inokuchi, H.; Matsunaga, Y. *Nature* **1954**, *173*, 4395.

130. Ferraris, J. S. *J. Am. Chem. Soc.* **1973**, *95*, 948.

131. Shirakawa, H.; Louis, E. J.; MacDiarmid, A. G.; Chiang, C. K.; Heeger, A. J. *Journal of the Chemical Society, Chemical Communications* **1977**, *16*, 578.

132. Bechgaard, K.; Carneiro, K.; Rasmussen, F. B.; Rindorf, O. G.; Jacobsen, C. S.; Pedersen, H. J.; Scott, J. C. *J. Am. Chem. Soc.* **1981**, *103*, 2440.

133. Kobayashi, A.; Fujiwara, E.; Kobayashi. H. *Chem. Rev.* **2004**, *104*, 5243.

134. Cordes, A. W.; Haddon, R. C.; Oakley, R. T. *Phosphorous, Sulfur, and Silicon.* **2004**, *197*, 673.

135. (a) Ferraris, J.; Cowan, D. O.; Walatka, V. V., Jr.; Perlstein, J. H. *J. Am. Chem. Soc.* **1973**, *95*, 948. (b) Coleman, L. B.; Cohen, M. J.; Sandman, D. J.; Yamagishi, F. G.; Garito, A. F. and Heeger, A. J. *Solid State Commun.* **1973**, *12*, 1125.

136. (a) Bendikov, M.; Wudl, F.; Perepichka, D. F. *Chem. Rev.* **2004**, *104*, 4891. (b) Jérome, D. *Chem. Rev.* **2004**, *104*, 4891. (c) Geiser, U.; Schleuter, J. A. *Chem. Rev.* **2004**, *104*, 5203. (d) Yamada, J.; Akutsu, H.; Nishikawa, H.; Kikuchi, K. *Chem. Rev.* **2004**, *104*, 5057.

137. Garito, A. F.; Heeger, A. J. *Acc. Chem. Res.*, **1974**, *7(7)*, 232.

138. (a) Engler, E. M.; Patel, V. V. *J. Am. Chem. Soc.* **1974**, *96*, 7376. (b) Bechgaard, K.; Cowan, D. O.; Bloch, A. N. *J. Chem. Soc., Chem.Commun.* **1974**, 937.

139. Bechgaard, K.; Jacobsen, C. S.; Mortensen, K.; Pedersen, H. J.; Thorup, N. *Solid State Commun.* **1980**, *33*, 5347.

140. (a) Williams, J. M.; Emge, T. J.; Wang, H. H.; Beno, M. A.; Copps, P. T.; Hall, L. N.; Carlson, K. D.; Crabtree, G. W. *Inorg. Chem.* **1984**, *23*, 2558. (b) Shibaeva, R. P.; Yagubskii, E. B. *Chem. Rev.* **2004**, *104*, 5347.

141. Jérome, D.; Mazaud, A.; Ribault, M.; Bechgaard, K. *J. Phys. Lett.* **1980**, *41*, L95.

142. Tanaka, H.; Okano, Y.; Kobayashi, H.; Suzuki, W.; Kobayashi, A. *Science*, **2001**, *291*, 285.

143. Torrance, J. B. *Acc. Chem. Res.* **1979**, *12*, 79.

144. Mott, N. F. *Metal-insulator Transitions*; Taylor and Francis: London, **1990**.

145. (a) Mott, N. F. *Proc. Phys. Soc., London Sect. A*, **1949**, *62*, 416. (b) Austin, I. G.; Mott, N. F. *Science*, **1970**, *168*, 71.

146. Whangbo, M.-H. *J. Chem. Phys.* **1979**, *70*, 4963.

147. Huang, J.; Kertesz, M. *J. Phys. Chem. A.* **2007**, *111*, 6304.

148. Friedel, J.; Noguera, C. *Int. J. Quantum Chem.* **1983**, *23*, 1209.

149. Coulson, C. A.; O'Leary, B.; Mallion, R. B. *Hückel Theory for Organic Chemists*, Academic Press, **1978**.

150. Dobrosavljević, V.; Trivedi, N.; Valles, J. M. Jr. *Conductor-Insulator Quantum Phase Transitions*; Oxford University Press: Oxford, U. K., **2012**.

151. (a) Ito, H.; Ishiguro, T.; Kubota, M.; Saito, G. *J. Phys. Soc. Jpn.* **1996**, *65*, 2987. (b) McKenzie, R. H. *Science* **1997**, *278*, 820. (c) Lefebvre, S.; Wzietek, P.; Brown, S.; Bourbonnais, C.; Jérome, D.; Mèziére, C.; Fourmigué, M.; Batail, P. *Phys. Rev. Lett.* **2000**, *85*, 5420.

152. Limelette, P.; Wzietek, P.; Florens, S.; Georges, A.; Costi, T. A.; Pasquier, C.; Jérome, D.; Mèziére, C.; Batail, P. *Phys. Rev. Lett.* **2003**, *91*, 1. In regard to Figure 1.19b, readers may view, browse, and/or download material for temporary copying purposes only, provided these uses are for noncommercial personal purposes. Except as provided by law, this material may not be further reproduced, distributed, transmitted, modified, adapted, performed, displayed, published, or sold in whole or part, without prior written permission from the American Physical Society. http://prl.aps.org/abstract/PRL/v91/i1/e016401

153. The superconducting phase below 13 K has been omitted.

154. (a) Haddon, R. C. *Nature* **1975**, *256*, 394. (b) Haddon, R. C. *Aust. J. Chem.* **1975**, *28*, 2343.

155. Peierls, R. C. *Quantum Theory of Solids*; Oxford University Press: London, U. K., **1955**, pp 108.

156. Cox, P. A. *The Electronic Structure and Chemistry of Solids*; Oxford University Press: New York, **1987**.

157. Mandal, S. K.; Samanta, S.; Itkis, M. E.; Jensen, D. W.; Reed, R. W.; Oakley, R. T.; Tham, F. S.; Donnadieu, B. Haddon, R. C. *J. Am. Chem. Soc.* **2006**, *128*, 1982.

158. (a) Pal, S. K.; Itkis, M. E.; Reed, R. W.; Oakley, R. T.; Cordes, A. W.; Tham, F. S.; Siegrist, T.; Haddon, R. C. *J. Am. Chem. Soc.* **2004**, *126*, 1478. (b) Chi, X.; Itkis, M. E.; Tham, F. S.; Oakley, R. T.; Cordes, A. W.; Haddon, R. C. *Int. J. Quant. Chem.* **2003**, *95*, 853. (c) Chi, X.; Itkis, M. E.; Reed, R. W.; Oakley, R. T.; Cordes, A. W.; Haddon, R. C. *J. Phys. Chem. B* **2002**, *202*, 8278.

159. Chi, X.; Itkis, M. E.; Patrick, B. O.; Barclay, T. M.; Reed, R. W.; Oakley, R. T.; Cordes, A. W.; Haddon, R. C. *J. Am. Chem. Soc.* **1999**, *121*, 10395.

160. (a) Pal, S. K.; Itkis, M. E.; Tham, F. S.; Reed, R. W.; Oakley, R. T.; Donnadieu, B.; Haddon, R. C. *J. Am. Chem. Soc.* **2007**, *129*, 7163. (b) Pal, S. K.; Itkis, M. E.; Tham, F. S.; Reed, R. W.; Oakley, R. T.; Haddon, R. C. *Science* **2005**, *309*, 281.

161. Pal, S. K.; Itkis, M. E.; Tham, F. S.; Reed, R. W.; Oakley, R. T.; Haddon, R. C. *J. Am. Chem. Soc.* **2008**, *130*, 3942.

162. (a) Itkis, M. E.; Chi, X.; Cordes, A. W.; Haddon, R. C. *Science* **2002**, *296*, 1443. (b) Miller, J. S. *Angew. Chem. Int. Ed.* **2003**, *42*, 27.

163. Isono, T.; Kamo, H.; Ueda, A.; Takahashi, K.; Nakao, A.; Kumai, R.; Nakao, H.; Kobayashi, K.; Murakami, Y.; Mori, H. *Nature Comm.* **2013**, *4*, 1344.

164. Morita, Y.; Suzuki, S.; Sato, K.; Takui, T. *Nature Chem.* **2011**, *3*, 197.

165. (a) Novoselov, K. S.; Geim, A. K.; Morozov, S. V.; Jiang, D.; Zhang, Y.; Dubonos, S. V.; Grigorieva, I. V.; Firsov, A. A. *Science* **2004**, 306, 666. (b) Geim, A. K.; Novoselov, K. S. *Nature Mater.* **2007**, *6*, 183.

166. Morita, Y.; Nishida, S. In *Stable Radicals: Fundamental and Applied Aspects of Odd-Electron Compounds* Hicks, R. G., Ed.; John Wiley & Sons, Ltd.: Wiltshire, U.K., **2010**; pp 81 – 145.

167. (a) Inoue, J.; Fukui, K.; Kubo, T.; Nakazawa, S.; Sato, K.; Shiomi, D.; Morita, Y.; Yamamoto, K.; Takui, T.; Nakasuji, K. *J. Am. Chem. Soc.* **2001,** *123,* 12702. (b) Fukui, K.; Inoue, J.; Kubo, T.; Nakazawa, S.; Aoki, T.; Morita, Y.; Yamamoto, K.; Sato, K.; Shiomi, D.; Nakasuji, K.; Takui, T. *Synth. Metals* **2001**, *121*, 1824.

168. P-doping did give rise to metallization. See: Cordes, A. W.; Haddon, R. C.; Oakley, R. T. *Adv. Mater*. **1994**, *6*, 798.

169. (a) Beer, L.; Brusso, J. L.; Haddon, R. C.; Itkis, M. E.; Leitch, A. A.; Oakley, R. T.; Reed, R. W.; Richardson, J. F. *Chem. Commun*. **2005**, 1543. (b) Beer, L.; Brusso, J. L.; Haddon, R. C.; Itkis, M. E.; Kleinke, H.; Leitch, A. A.; Oakley, R. T.; Reed, R. W.; Richardson, J. F.; Secco, R. A.; Yu, X. *J. Am. Chem. Soc.* **2005**, *127*, 18159.

170. Winter, S. M.; Cvrkalj, K.; Robertson, C. M.; Probert, M. R.; Dube, P. A.; Howard, J. A. K.; Oakley, R. T. *Chem. Commun*. **2009**, 7306.

171. Beer, L.; Britten, J. F.; Brusso, J. L.; Cordes, A. W.; Haddon, R. C.; Itkis, M. E.; MacGregor, D. S.; Oakley, R. T.; Reed, R. W.; Robertson, C. M. *J. Am. Chem. Soc.* **2003**, *125*, 14394.

172. Tse, J. S.; Leitch, A. A.; Yu, X.; Bao, X.; Zhang, S.; Liu, Q.; Jin, C.; Secco, R. A.; Desgreniers, S.; Ohishi, Y.; Oakley, R. T. *J. Am. Chem. Soc*. **2010**, *132*, 4876.

173. Brusso, J. L.; Cvrkalj, K.; Leitch, A. A.; Oakley, R. T.; Reed, R. W.; Robertson, C. M. *J. Am. Chem. Soc.* **2006**, *128*, 15080.

174. Leitch, A. A.; Lekin, K.; Winter, S. M.; Downie, L. E.; Tsuruda, H.; Tse, J. S.; Mito, M.; Desgreniers, S.; Dube, P. A.; Zhang, S.; Liu, Q.; Jin, C.; Ohishi, Y.; Oakley, R. T. *J. Am. Chem. Soc*. **2011**, *133*, 6051.

175. (a) Beer, L.; Britten, J. F.; Clements, O. P.; Haddon, R. C.; Itkis, M. E.; Matkovich, K. M.; Oakley, R. T.; Reed, R. W. *Chem. Mat.* **2004**, *16*, 1564. (b) Beer, L.; Brusso, J. L.; Haddon, R. C.; Itkis, M. E.; Oakley, R. T.; Reed, R. W.; Richardson, J. F.; Secco, R. A.; Yu, X. *Chem. Commun.* **2005**, 5745. (c) Brusso, J. L.; Derakhshan, S.; Itkis, M. E.; Kleinke, H.; Haddon, R. C.; Oakley, R. T.; Reed, R. W.; Richardson, J. F.; Robertson, C. M.; Thompson, L. K. *Inorg. Chem.* **2006**, *45*, 10958.

176. Leitch, A. A.; Yu, X.; Robertson, C. M.; Secco, R. A.; Tse, J. S.; Oakley, R. T. *Inorg. Chem.*

2009, *48*, 9874.

177. (a) Nakanishi, W.; Hayashi, S.; Toyota, S. *Chem. Commun.* **1996**, 371. (b) Nakanishi, W.; Hayashi, S.; Arai, T. *Chem. Commun*. **2002**, 2416. (c) Nakanishi, W.; Hayashi, S.; Morinaka, S.; Sasamori, T.; Tokitoh, N. *New J. Chem*. **2008**, *32*, 1881. (d) Sharma, S.; Selvakumar, K.; Singh, V. P.; Zade, S. S.; Singh, H. B. *Phosphorus, Sulfur Silicon Relat. Elem.* **2008**, *183*, 827.

178. Aust, R. B.; Bentley, W. H.; Drickamer, H. G. *J. Chem. Phys.* **1964**, *41*, 1856.

179. Leitch, A. A.; Reed, R. W.; Robertson, C. M.; Britten, J. F.; Yu, X.; Secco, R. A.; Oakley, R. T. *J. Am. Chem. Soc.* **2007**, *129*, 7903.

180. Yu, X.; Mailman, A.; Dube, P. A.; Assoud, A.; Oakley, R. T. *Chem. Commun.* **2011**, *47*, 4655.

181. Yu, X.; Mailman, A.; Lekin, K.; Assoud, A.; Robertson, C. M.; Noll, B. C.; Campana, C. F.; Howard, J. A. K.; Dube P. A.; Oakley, R. T. *J. Am. Chem. Soc.* **2012**, 134, 2264.

182. Mailman, A.; Winter, S. M.; Yu, X.; Robertson, C. M.; Yong, W.; Tse, J. S.; Secco, R. A.; Liu, Z.; Dube, P. A.; Howard, J. A. K.; Oakley, R. T. *J. Am. Chem. Soc.* **2012**, *134*, 9886.

References for Chapter 2

1. (a) Cordes, A. W.; Haddon, R. C.; Oakley, R. T. *Phosphorus, Sulfur Silicon Relat. Elem*. **2004**, *179*, 673. (b) Beer, L.; Brusso, J. L.; Cordes, A. W.; Haddon, R. C.; Itkis, M. E.; Kirschbaum, K.; MacGregor, D. S.; Oakley, R. T.; Pinkerton, A. A.; Reed, R. W. *J. Am. Chem. Soc*. **2002**, *124*, 9498.

2. (a) Brusso, J. L.; Derakhshan, S.; Itkis, M. E.; Kleinke, H.; Haddon, R. C.; Oakley, R. T.; Reed, R. W.; Richardson, J. F.; Robertson, C. M.; Thompson, L. K. *Inorg. Chem*. **2006**, *45*, 10958. (b) Brusso, J. L.; Cvrkalj, K.; Leitch, A. A.; Oakley, R. T.; Reed, R. W.; Robertson, C. M. *J. Am. Chem. Soc*. **2006**, *128*, 15080.

3. (a) Beer, L.; Brusso, J. L.; Haddon, R. C.; Itkis, M. E.; Kleinke, H.; Leitch, A. A.; Oakley, R. T.; Reed, R. W.; Richardson, J. F.; Secco, R. A.; Yu, X. *J. Am. Chem. Soc*. **2005**, *127*, 1815. (b) Leitch, A. A.; Yu, X.; Robertson, C. M.; Secco, R. A.; Tse, J. S.; Oakley, R. T. *Inorg. Chem.* **2009**, *48*, 9874. (c) Leitch, A. A.; McKenzie, C. E.; Oakley, R. T.; Reed, R. W.; Richardson, J. F.; Sawyer, L. D. *Chem. Commun*. **2006**, 1088.

4. (a) Tse, J. S.; Leitch , A. A.; Yu, X.; Bao, X.; Zhang, S.; Liu, Q.; Jin, C.; Secco, R. A.; Desgreniers, S.; Ohishi, Y.; Oakley. R. T. *J. Am. Chem. Soc*. **2010**, *132*, 4876. (b) Lekin, K.; Winter, S. M.; Downie, L. E.; Bao, X.; Tse, J. S.; Desgreniers, S.; Secco, R. A.; Dube, P. A.; Oakley, R. T. *J. Am. Chem. Soc*. **2010**, *132*, 16212. (c) Lekin, K.; Wong, J. W. L.; Winter, S. M.; Mailman, A.; Dube, P. A.; Oakley, R. T. *Inorg. Chem.* **2013**, *52*, 2188.

5. Leitch, A. A.; Brusso, J. L.; Cvrkalj, K.; Reed, R. W.; Robertson, C. M.; Dube, P. A.; Oakley, R. T. *Chem. Commun*. **2007**, 3368.

6. (a) Robertson, C. M.; Myles, D. J. T.; Leitch, A. A.; Reed, R. W.; Dooley, D. M.; Frank, N. L.; Dube, P. A.; Thompson, L. K.; Oakley, R. T. *J. Am. Chem. Soc*. **2007**, *129*, 12688. (b) Robertson, C. M.; Leitch, A. A.; Cvrkalj, K.; Reed, R. W.; Myles, D. J. T.; Dube, P. A.; Oakley, R. T. *J. Am. Chem. Soc*. **2008**, *130*, 8414.

7. (a) Lahti, P. M. In *Advances in Physical Organic Chemistry*; Richard, J. P., Ed.; volume 45; Elsevier: Amsterdam, Netherlands, **2011**; pp 93-169. (b) Lahti, P. M. In *Carbon-based magnetism: An overview of the magnetism of metal-free carbon-based compounds and materials*; Palacio, F.; Makarova T., Eds.; Elsevier, **2006**; pp 23-52. (c) Takahashi, M.; Turek,

P.; Nakazawa, Y.; Tamura, M.; Nozawa, K.; Shiomi, D.; Ishikawa, M.; Kinoshita, M. *Phys. Rev. Lett.* **1991**, *67*, 746. (d) Tamura, M.; Nakazawa, Y.; Shiomi, D.; Nozawa, K.; Hosokoshi, Y.; Ishikawa, M.; Takahashi, M.; Kinoshita, M. *Chem. Phys. Lett.* **1991**, *186*, 401. (e) Chiarelli, R.; Novak, M. A.; Rassat, A.; Tholence, J. L. *Nature* **1993**, *363*, 147. (f) Alberola, A.; Less, R. J.; Pask, C. M.; Rawson, J. M.; Palacio, F.; Oliete, P.; Paulsen, C.; Yamaguchi, A.; Murphy, D. M.; Farley, R. D. *Angew. Chem., Int. Ed.*, **2003**, *42*, 4782. (g) Rawson, J. M.; Alberola, A.; Whalley, A. *J. Mater. Chem.* **2006**, *16*, 2560.

8. Robertson, C. M.; Leitch, A. A.; Cvrkalj, K.; Myles, D. J. T.; Reed, R. W.; Dube, P. A.; Oakley, R. T. *J. Am. Chem. Soc.* **2008**, *130*, 14791.

9. (a) Takeda, K.; Mito, M. in *Carbon-Based Magnetism*, ed. T. Makarova and F. Palacio, Elsevier, Amsterdam, 2005, pps 131-158. (b) Mito, M.; Kawae, T.; Takumi, M.; Nagata, K.; Tamura, M.; Kinoshita, M.; Takeda, K. *Phys. Rev. B* **1997**, *56*, 14255. (c) Mito, M.; Kawae, T.; Hitaka, M.; Takeda, K.; Ishida, T.; Nogami T. *Chem. Phys. Lett*. **2001**, *333*, 69. (d) Mito, M.; Deguchi, H.; Tanimoto, T.; Kawae, T.; Nakatsuji, S.; Morimoto, H.; Anzai, H.; Nakao, H.; Murakami, Y.; Takeda, K. *Phys. Rev. B* **2003**, *67*, 024427. (e) Takeda, K.; Mito, M.; Kinoshita, K.; Novak, M. A.; Tholence, J. L.; Rassat, A. *Polyhedron* **2003**, 22, 2287. (f) Mito, M.; Fujino, M.; Komorida, Y.; Deguchi, H.; Takagi, S.; Fujita, W.; Awaga, K. *J. Phys. Soc. Jpn.* **2008**, *77*, 124713

10. Mito, M.; Komorida, Y.; Tsuruda, H.; Tse, J. S.; Desgreniers, S.; Ohishi, Y.; Leitch, A. A.; Cvrkalj, K.; Robertson, C. M.; Oakley, R. T. *J. Am. Chem. Soc.* **2009**, 131, 16012.

11. Leitch, A. A.; Lekin, K.; Winter, S. M.; Downie, L. E.; Tsuruda, H.; Tse, J. S.; Mito, M.; Desgreniers, S.; Dube, P. A.; Zhang, S.; Liu, Q.; Jin, C.; Ohishi Y.; Oakley, R. T. *J. Am. Chem. Soc*. **2011**, *133*, 6051.

12. (a) Beer, L., Brusso, J. L., Cordes, A. W., Haddon, R. C., Itkis, M. E., Kirschbaum, K., MacGregor, D. S., Oakley, R. T., Pinkerton, A. A., and Reed, R. W. *J. Am. Chem. Soc.* **2002**, *124*, 9498. (b) Beer, L., Britten, J. F., Brusso, J. L., Cordes, A. W., Haddon, R. C., Itkis, M. E., MacGregor, D. S., Oakley, R. T., Reed, R. W., and Robertson, C. M. *J. Am. Chem. Soc*. **2003**, *125*, 14394. (c) Leitch, A. A., Reed, R. W., Robertson, C. M., Britten, J. F., Yu, X., Secco, R. A., and Oakley, R. T. *J. Am. Chem. Soc*. **2007**, *129*, 7903.

13. Leitch, A. A. "Structure and Property Correlations in Heavy Atom Radicals." A thesis presented to the University of Waterloo, Waterloo, Ontario, **2009**.

14. David, W. I. F., Shankland, K., van de Streek, J., Pidcock, E., Motherwell, W. D. S., and Cole, J. C. *J. Appl. Crystallogr.* **2006**, *39*, 910.

15. Rietveld, H. M. *J. Appl. Cryst*. **1969**, *2*, 65.

16. Larson, A. C. and Von Dreele, R. B. Report No. LA-UR-86-748; Los Alamos National Laboratory: Los Alamos, NM, **1987**.

17. (a) Bondi, A. *J. Phys. Chem*. **1964**, *68*, 441. (b) Dance, I. *New J. Chem*. **2003**, *27*, 22.

18. Carlin, R. L. *Magnetochemistry*; Springer-Verlag: New York, **1986**.

19. As a result of the contribution of spin-orbit effects from selenium to the *g*-value of **2-4a** and **2-4b** the observation of values of M_{sat} slightly greater than 1 Nβ, where $M_{sat} = gSN\beta$, is not unexpected.

20. Although **2-2d** has a value of χT that is somewhat comparable to related ferromagnets **2-2b,c**, **2-2a** is an order of magnitude weaker due to the applied field (*H*) being different (1000 Oe *versus* typically 100 Oe).

21. The high value of *C* observed for **2-2d** is typical of a material contaminated with a paramagnetic impurity. Ideally, this experiment should be performed again to ensure that only radical **2-2d** is present. This should not affect the T_c of the material.

22. Mito, M.; Deguchi, H.; Tanimoto, T.; Kawae, T.; Nakatsuji, S.; Morimoto, H.; Anzai, H.; Nakao, H.; Murakami, Y.; Takeda, K. *Phys. Rev. B* **2003**, *67*, 024427.

23. Imada, M.; Fujimori, A.; Tokura, Y. *Rev. Mod. Phys*. **1998**, *70*, 1039.

24. (a) Murata K.; Kagoshima, S.; Yasuzuka, S.; Yoshino, H.; Kondo, R.; *J. Phys. Soc. Jpn*. **2007**, *75*, 051015. (b) Saito, G.; Yoshida, Y. *Bull. Chem. Soc. Jpn*. **2007**, *80*, 1. (c) Limelette, P.; Wzietek, P.; Florens, S.; Georges, A.; Costi, T. A.; Pasquier, C.; Jérome, D.; Mézière, C.; Batail, P. *Phys. Rev. Lett.* **2003**, *91*, 016401. (d) Isono, T.; Kamo, H.; Ueda, A.; Takahashi, K.; Nakao, A.; Kumai, R.; Nakao, H.; Kobayashi, K.; Murakami, Y.; Mori, H. *Nature Comm.* **2013**, *4*, 1344.

25. Dobrosavljević, V.; Trivedi, N.; Valles, J. M. Jr. *Conductor-Insulator Quantum Phase Transitions*; Oxford University Press: Oxford, U. K., **2012**.

26. (a) Mito, M.; Kawae, T.; Takeda, K.; Takagi, S.; Matsushita, Y.; Deguchi, H.; Rawson, J. M.; Palacio, F. *Polyhedron* **2001**, *20*, 1509. (b) Thomson, R. I.; Pask, C. M.; Lloyd, G. O.; Mito, M.; Rawson, J. M. *Chem. Eur. J.* **2012**, *18*, 8629.

27. For details of the theoretical procedure, see (a) Noodleman, L.; Norman, J. G. *J. Chem. Phys*. **1979**, *70*, 4903. (b) Noodleman, L. *J. Chem. Phys*. **1981**, *74*, 5737. (c) Deumal, M.; Robb, M. A.; Novoa, J. J. *Prog. Theor. Chem. Phys.* **2007**, *16*, 271.

28. (a) Kahn, O. *Molecular Magnetism*; VCH: New York, 1993. (b) Kahn, O.; Briat, B. *J. Chem. Soc., Faraday Trans.* **1976**, *2*, 268. (c) Kahn, O.; Galy, J.; Journaux, Y.; Jaud, J.; Morgenstern-Badarau, I. *J. Am. Chem. Soc*. **1982**, *104*, 2165.

29. Lekin, K.; Tse, J. S.; Oakley, R. T. *Unpublished results.*

30. Desgreniers, S.; Lagarec, K. *J. Appl. Cryst*. **1998**, *31*, 109.

31. Boultif, A.; Louer, D. *J. Appl. Cryst*. **2004**, *37*, 724

32. (a) Tsuruda, H.; Mito, M.; Deguchi, H.; Takagi, S.; Leitch, A. A.; Lekin, K.; Winter, S. M.; Oakley, R. T. *Polyhedron* **2011**, *30*, 2997. (b) Mito, M.; Hitaka, M.; Kawae, T.; Takeda, K.; Kitai, T.; Toyoshima, N. *Jpn. J. Appl. Phys*. **2001**, *40*, 6641.

References for Chapter 3

1. (a) Beer, L.; Brusso, J. L.; Haddon, R. C.; Itkis, M. E.; Kleinke, H.; Leitch, A. A.; Oakley, R. T.; Reed, R. W.; Richardson, J. F.; Secco, R. A.; Yu, X. *J. Am. Chem. Soc*. **2005**, *127*, 18159. (b) Beer, L.; Brusso J. L.; Haddon, R. C.; Itkis, M. E.; Leitch, A. A.; Oakley, R. T.; Reed R. W.; Richardson. J. F. *Chem. Commun*. **2005**, 1543.

2. (a) Nakanishi, W.; Hayashi, S.; Toyota, S. *Chem. Commun.* **1996**, 371. (b) Nakanishi, W.; Hayashi, S.; Arai, T. *Chem. Commun*. **2002**, 2416. (c) Nakanishi, W.; Hayashi, S.; Morinaka, S.; Sasamori, T.; Tokitoh, N. *New J. Chem*. **2008**, *32*, 1881. (d) Sharma, S.; Selvakumar, K.; Singh, V. P.; Zade, S. S.; Singh, H. B. *Phosphorus, Sulfur Silicon Relat. Elem.* **2008**, *183*, 827.

3. (a) Oakley, R. T.; Reed, R. W.; Cordes, A. W.; Craig, S. L.; Graham, S. B. *J. Am. Chem. Soc*. **1987**, *109*, 7745. (b) Del Bel Belluz, P.; Cordes, A. W.; Kristof, E. M.; Kristof, P. W.; Liblong, S. W.; Oakley, R. T. *J. Am. Chem. Soc*. **1989**, *111*, 9276. (c) Cordes, A. W.; Haddon, R. C.; Oakley, R. T.; Schneemeyer, L. F.; Waszczak, J. V.; Young, K. M.; Zimmerman, N. M. *J. Am. Chem. Soc*. **1991**, *113*, 582. (d) Parvez, M.; Boeré, R. T. *Acta Crystallogr*. *C* **1995**, *51*, 2118. (e) Wu, J.; MacDonald, D. J.; Clérac, R.; Jeon, I.; Jennings, M.; Lough, A. J.; Britten, J.; Robertson, C.; Dube, P. A.; Preuss, K. E. *Inorg. Chem*. **2012**, *51*, 3827.

4. (a) Bestari, K.; Cordes, A. W.; Oakley, R. T.; Young, K. M. *J. Am. Chem. Soc*. **1990**, *112*, 2249. (b) Feeder, N.; Less, R. J.; Rawson, J. M.; Oliete, P.; Palacio, F. *Chem. Commun*. **2000**, 2449.

5. (a) Grochala, W.; Hoffmann, R.; Feng, J.; Ashcroft, N. W. *Angew. Chem., Int. Ed.* **2007**, *46*, 3620. (b) MacMillan, P. F. *Chem. Soc. Rev.* **2006**, *35*, 855. (c) Hemley, R. J. *Annu. Rev. Phys. Chem.* **2000**, *51*, 763.

6. Leitch, A. A.; Yu, X.; Robertson, C. M.; Secco, R. A.; Tse, J. S.; Oakley, R. T. *Inorg. Chem.* **2009**, *48*, 9874.

7. Tse, J. S.; Leitch, A. A.; Yu, X.; Bao, X.; Zhang, S.; Liu, Q.; Jin, C.; Secco, R. A.; Desgreniers, S.; Ohishi, Y.; Oakley, R. T. *J. Am. Chem. Soc.* **2010**, *132*, 4876.

8. Selenium enters a metallic state near 25 GPa. (a) Riggleman, B. M.; Drickamer, H. G. *J. Chem. Phys.* **1962**, *37*, 446. (b) Bundy, F. P.; Dunn, K. J. *J. Chem. Phys.* **1979**, *71*, 155.

9. Lekin, K., Winter, S. M., Downie, L. E., Bao, X., Tse, J. S., Desgreniers, S., Secco, R. A., Dube, P. A. and Oakley, R. T. *J. Am. Chem. Soc.* **2010**, 132, 16212.

10. Leitch, A. A., McKenzie, C. E., Oakley, R. T., Reed, R. W., Richardson, J. F. and Sawyer, L. D. *Chem. Commun*. **2006**, 1088.

11. Beer, L., Reed, R. W., Robertson, C. M., Oakley, R. T., Tham, R. S., and Haddon, R. C. *Org. Lett*. **2008**, *10*, 3121.

12. Lekin, K.; Leitch, A. A.; Tse, J. S.; Bao, X.; Secco, R. A.; Desgreniers, S.; Ohishi, Y.; Oakley, R. T. *Cryst. Growth Des.* **2012**, *12*, 4676.

13. Lekin, K., Winter, S. M., Oakley, R. T. *Manuscript in progress*, **2013**.

14. Lekin, K., Wong, J. W. L., Winter, S. M., Mailman, A., Dube, P. A., Oakley, R. T. *Inorg. Chem.* **2013**, *52*, 2188.

15. Manual separation of the two phases was necessary in most trials to obtain phase pure material.

16. Akulin, Y. I., Gel'mont, M. M., Strelets, B. K. and Éfros, L. S. Khim. *Geterotsikl. Soedin.* **1978**, 912.

17. ORTEP ellipsoids were not provided for [**3**-**2a**]$_2$ because its molecular geometry was based on a model, and powder X-ray diffraction data did not allow for refinement of the thermal ellipsoids. See the Experimental section for more details.

18. (a) Cozzolino, A. F., Vargas-Baca, I., Mansour, S. and Mahmoudkhani, A. H. *J. Am. Chem. Soc.* **2005**, **127**, 3184. (b) Oakley, R. T., Reed, R. W., Robertson, C. M. and Richardson, J. F. *Inorg. Chem.* **2005**, *44*, 1837. (c) Risto, M., Assoud, A., Winter, S. M., Oilunkaniemi, R., Laitinen, R. S. and Oakley, R. T. *Inorg. Chem*. **2008**, *47*, 10100. (d) Dutton, J. L., Tindale, J. J., Jennings, M. C. and Ragogna, P. J. *Chem. Commun*. **2006**, 2474. (e) Berionni, G., Pégot, B., Marrot, J. and Goumont, R. *CrystEngComm* **2009**, 11, 986.

19. Chen, C. M.; Dojahn, J. G.; Wentworth, W. E. *J. Phys. Chem. A* **1997**, *101*, 3088.

20. (a) Bondi, A. *J. Phys. Chem*. **1964**, *68*, 441. (b) Dance, I. *New J. Chem*. **2003**, *27*, 22.

21. Similar variable temperature magnetic susceptibility measurements have been performed on [**3-2a**]$_2$, and the response was reported to be diamagnetic with ~ 2 % paramagnetic defects.

22. The structural results for [**3-2a**]$_2$ at 0 GPa reported here supercede those reported in reference 6, as the synchrotron diffraction data is of superior quality.

23. Riggleman, B. M.; Drickamer, H. G. *J. Chem. Phys.* **1963**, *38*, 2721.

24. (a) Takemura, K.; Minomura, S.; Shimomura, O.; Fujii, Y.; Axe, J. D. *Phys. Rev. B* **1982**, *26*, 998. (b) Kenichi, K.; Kyoko, S.; Hiroshi, F.; Mitsuko, O. *Nature* **2003**, *423*, 971.

25. (a) Akahama, Y.; Kobayashi, M.; Kawamura, H. *Phys. Rev. B* **1993**, *48*, 6862. (b) Luo, H.; Greene, R. G.; Ruoff, A. L. *Phys. Rev. Lett.* **1993**, *71*, 2943. (c) Akahama, Y.; Kobayashi, M.; Kawamura, H. *Phys. Rev. B* **1993**, *47*, 20.

26. Crapanzano, L.; Crichton, W. A.; Monaco, G.; Bellissent, R.; Meouar, M. *Nat. Mater.* **2005**, *4*, 550.

27. Cherin, P.; Unger, P. *Inorg. Chem.* **1967**, *6*, 1589.

28. Miyamoto, Y. *Jpn. J. Appl. Phys.* **1980**, *19*, 1813.

29. (a) Brillante, A.; Della Valle, R. G.; Farina, L.; Venutti, E.; Cavazzoni, C.; Emerson, A. P. J.; Syassen, K. *J. Am. Chem. Soc.* **2005**, *127*, 3038. (b) (a) Nakayama, A.; Aoki, K.; Carlòn, R. P. *Phys. Rev. B* **2001**, *64*, 064104. (b) Nakayama, A.; Fujihisa, H.; Takemura, K.; Aoki, K.; Carlòn, R. P. *Synth. Met.* **2001**, *120*, 767. (c) Iwasaki, E.; Shimizu, K.; Amaya, K.; Nakayama, A.; Aoki, K.; Carlòn, R. P. *Synth. Met.* **2001**, *120*, 1003. (f) Takemura, K.; Minomura, S.; Shimomura, O.; Fujii, Y. *Phys. Rev. Lett.* **1980**, *45*, 1881. (g) Tateyama, Y.; Ohno, T. *J. Phys.: Condens. Matter* **2002**, *14*, 10429.

30. Cui, H.; Brooks, J. S.; Kobayashi, A.; Kobayashi, H. *J. Am. Chem. Soc.* **2009**, *131*, 6358.

31. (a) Shirotani, I.; Kamura, Y.; Inokuchi, H.; Hirooka, T. *Chem. Phys. Lett.* **1976**, *40*, 257. (b) Onodera, A.; Shirotani, I.; Inokuchi, H.; Kawai, N. *Chem. Phys. Lett.* **1974**, *25*, 296.

32. Cui, H.; Okano, Y.; Zhou, B.; Kobayashi, A.; Kobayashi, H. *J. Am. Chem. Soc.* **2008**, *130*, 3738.

33. Tulip, P. R.; Bates, S. P. *J. Phys. Chem. C* **2009**, *113*, 19310.

34. (a) Mito, M.; Komorida, Y.; Tsuruda, H.; Tse, J. S.; Desgreniers, S.; Ohishi, Y.; Leitch, A. A.; Cvrkalj, K.; Robertson, C. M.; Oakley, R. T. *J. Am. Chem. Soc*. **2009**, *131*, 16012. (b) Seber, G.; Halder, G. J.; Schlueter, J. A.; Lahti, P. M. *Cryst. Growth Des*. **2011**, *11*, 4261. (c) Thomson, R. I.; Pask, C. M.; Lloyd, G. O.; Mito, M.; Rawson, J. M. *Chem. Euro. J.* **2012** *18*, 8629. (d) Schlueter, J. A.; Park, H.; Halder, G. J.; Armand, W. R.; Dunmars, C.; Chapman, K. W.; Manson, J. L.; Singleton, J.; McDonald, R.; Plonczak, A.; Kang, J.; Lee, C.; Whangbo, M.-H.; Lancaster, T.; Steele, A. J.; Franke, I.; Wright, J. D.; Blundell, S. J.; Pratt, F. L.; de George, J.; Turnbull, M. M.; Landee, C. P. *Inorg. Chem.* **2012**, *51*, 2121.

35. Leitch, A. A.; Lekin, K.; Winter, S. M.; Downie, L. E.; Tsuruda, H.; Tse, J. S.; Mito, M.; Desgreniers, S.; Dube, P. A.; Zhang, S.; Liu, Q.; Jin, C.; Ohishi, Y.; Oakley, R. T. *J. Am. Chem. Soc*. **2011**, *133*, 605.

36. (a) Halder, G. J.; Chapman, K. W.; Schlueter, J. A.; Manson, J. L. *Angew. Chem., Int. Ed.* **2011**, *50*, 419. (b) Prescimone, A.; Morien, C.; Allan, D.; Schlueter, J. A.; Tozer, S. W.; Manson, J. L.; Parsons, S.; Brechin, E. K.; Hill, S. *Angew. Chem., Int. Ed.* **2012**, *51*, 7490.

37. Desiraju, G. R. *Angew. Chem., Int. Ed.* **1995**, *34*, 2311.

38. (a) Desiraju, D. G. *Acc. Chem Res*. **2002**, *35*, 565. (b) Thakur, T. S.; Kirchner, M. T.; Bläser, D.; Boese, R.; Desiraju, D. R. *CrystEngComm* **2010**, *12*, 2079.

39. (a) Weiss, H.-C.; Boese, R.; Smith, H. L.; Haley, M. M. *Chem. Commun*. **1997**, 2403. (b) Thalladi, V. R.; Weiss, H. C.; Bläser, D.; Boese, R.; Nangia, A.; Desiraju, D. R. *J. Am. Chem. Soc.* **1998**, *120*, 8702. (c) Mele, A.; Vergani, B.;Viani, F.; Meille, S. V.; Farina, A.; Bravo, F. *Eur. J. Org. Chem*. **1999**, 187. (d) Haufe, G.; Rosen, T. C.; Meyer, O. G. J.; Fröhlich, R.; Rissanen, K. *J. Fluorine Chem*. **2002**, *114*, 189. (E) Hyla-Kryspin, E.; Haufe, G.; Grimme, S. *Chem. Eur. J*. **2004**, *10*, 3411.

40. The contacts shown and distances specified in Figure 3.15 are from the aryl proton to the methyl carbon, as the positions of the methyl protons (which are free to rotate) are arbitrary.

41. "One of the fundamental problems, however, remains unsolvable: the prediction of the crystal structure of organic molecules and the planned assembly of structures with predetermined properties is possible only within modest limits." Enkelmann, V. *Angew. Chem. Int. Ed.* **1991**,

30, 1121.

42. David, W. I. F.; Shankland, K.; van de Streek, J.; Pidcock, E.; Motherwell, W. D. S.; Cole, J. C. *J. Appl. Cryst*. **2006**, *39*, 910.

43. Rietveld, H. M. *J. Appl. Cryst*. **1969**, *2*, 65.

44. Larson, A. C.; Von Dreele, R. B. Report No. LA-UR-86-748; Los Alamos National Laboratory, Los Alamos, NM, 1987.

45. Secco, R. A. *Can. J. Phys*. **1995**, *73*, 287.

46. Secco, R. A.; Schloessin, H. H. *J. Appl. Phys*. **1986**, *60*, 1625.

47. Gaussian 09, Revision A.02, Frisch, M. J. *et al*., Gaussian, Inc., Wallingford CT, 2009.

48. (a) Kresse, G.; Hafner, J. *Phys. Rev*. **1993**, *47B*, 558. (b) Kresse, G.; Furthmüller, J. *Phys. Rev*. **1996**, *54B*, 11169.

49. (a) Blöchl, P. E. *Phys. Rev*. **1994**, *50B*, 17953. (b) Kresse, G.; Joubert, J. *Phys. Rev*. **1999**, *59B*, 1758.

50. Perdew, J. P.; Burke, K.; Ernzerhof, M. *Phys. Rev. Lett*. **1996**, *77*, 3865.

References for Chapter 4

1. Lekin, K.; Leitch, A. A.; Tse, J. S.; Bao, X.; Secco, R. A.; Desgreniers, S.; Ohishi, Y.; Oakley, R. T. *Cryst. Growth Des.* **2012**, *12*, 4676.

2. Tse, J. S.; Leitch, A. A.; Yu, X.; Bao, X.; Zhang, S.; Liu, Q.; Jin, C.; Secco, R. A.; Desgreniers, S.; Ohishi, Y.; Oakley, R. T. *J. Am. Chem. Soc.* **2010**, *132*, 4876.

3. (a) Nakanishi, W.; Hayashi, S.; Toyota, S. *Chem. Commun.* **1996**, 371. (b) Nakanishi, W.; Hayashi, S.; Arai, T. *Chem. Commun*. **2002**, 2416. (c) Nakanishi, W.; Hayashi, S.; Morinaka, S.; Sasamori, T.; Tokitoh, N. *New J. Chem*. **2008**, *32*, 1881. (d) Sharma, S.; Selvakumar, K.; Singh, V. P.; Zade, S. S.; Singh, H. B. *Phosphorus, Sulfur Silicon Relat. Elem.* **2008**, *183*, 827.

4. It was shown to occur for the pyrazine-bridged bisdithiazolyls: Leitch, A. A.; McKenzie, C. E.; Oakley, R. T.; Reed, R. W.; Richardson, J. F.; Sawyer, L. D. *Chem. Commun*. **2006**, 1088.

5. (a) Beer, L.; Brusso, J. L.; Haddon, R. C.; Itkis, M. E.; Kleinke, H.; Leitch, A. A.; Oakley, R. T.; Reed, R. W.; Richardson, J. F.; Secco, R. A.; Yu, X. *J. Am. Chem. Soc*. **2005**, *127*, 18159. (b) Beer, L.; Brusso J. L.; Haddon, R. C.; Itkis, M. E.; Leitch, A. A.; Oakley, R. T.; Reed R. W.; Richardson. J. F. *Chem. Commun*. **2005**, 1543.

6. (a) Oakley, R. T.; Reed, R. W.; Cordes, A. W.; Craig, S. L.; Graham, S. B. *J. Am. Chem. Soc*. **1987**, *109*, 7745. (b) Del Bel Belluz, P.; Cordes, A. W.; Kristof, E. M.; Kristof, P. W.; Liblong, S. W.; Oakley, R. T. *J. Am. Chem. Soc*. **1989**, *111*, 9276. (c) Cordes, A. W.; Haddon, R. C.; Oakley, R. T.; Schneemeyer, L. F.; Waszczak, J. V.; Young, K. M.; Zimmerman, N. M. *J. Am. Chem. Soc*. **1991**, *113*, 582. (d) Parvez, M.; Boeré, R. T. *Acta Crystallogr*. *C* **1995**, *51*, 2118. (e) Wu, J.; MacDonald, D. J.; Clérac, R.; Jeon, I.; Jennings, M.; Lough, A. J.; Britten, J.; Robertson, C.; Dube, P. A.; Preuss, K. E. *Inorg. Chem*. **2012**, *51*, 3827. (f) Bestari, K.; Cordes, A. W.; Oakley, R. T.; Young, K. M. *J. Am. Chem. Soc*. **1990**, *112*, 2249. (g) Feeder, N.; Less, R. J.; Rawson, J. M.; Oliete, P.; Palacio, F. *Chem. Commun*. **2000**, 2449.

7. Chi, X.; Itkis, M. E.; Kirschbaum, K.; Pinkerton, A. A.; Oakley, R. T.; Cordes, A. W.; Haddon, R. C. *J. Am. Chem. Soc.* **2001**, *123*, 4041.

8. (a) Fujita, W.; Awaga, K. *Science*, **1999**, *286*, 261. (b) Fujita, W.; Awaga, K.; Matsuzaki, H.; Okamoto, H.; *Phys. Rev. B* **2002**, *65*, 064434. (c) McManus, G. D.; Rawson, J. M.; Feeder, N.;

van Duijn, J.; McInnes, E. J. L.; Novoa, J. J.; Burriel, R.; Palacio, F.; Oliete, P. *J. Mater. Chem.* **2001**, *11*, 1992. (d) Fujita, W.; Awaga, K.; Nakazawa, Y.; Saito, K.; Sorai, M. *Chem. Phys. Lett*. **2002**, *352*, 348. (e) Shultz, D. A.; Fico, R.; Boyle. P. D.; Kampf, J. W. *J. Am. Chem. Soc.* **2001**, *123*, 10403.

9. (a) Barclay, T. M.; Cordes, A. W.; George, N. A.; Haddon, R. C.; Itkis, M. E.; Mashuta, M. S.; Oakley, R. T.; Patenaude, G. W.; Reed, R. W.; Richardson, J. F.; Zhang, H. *J. Am. Chem. Soc*. **1998**, *120*, 352. (b) Brusso, J. L.; Clements, O. P.; Haddon, R. C.; Itkis, M. E.; Leitch, A. A.; Oakley, R. T.; Reed, R. W.; Richardson, J. F. *J. Amer. Chem. Soc*. **2004**, *126*, 8256. (c) Brusso, J. L.; Clements, O. P.; Haddon, R. C.; Itkis, M. E.; Leitch, A. A.; Oakley, R. T.; Reed, R. W.; Richardson, J. F. *J. Amer. Chem. Soc*. **2004**, *126*, 14692.

10. Rota, J.-B.; Le Guennic, B.; Robert, V. *Inorg. Chem*. **2010**, *49*, 1230.

11. Itkis, M. E.; Chi, X., Cordes, A. W.; Haddon, R. C. *Science* **2002**, *296*, 1443.

12. (a) Alberola, A.; Clarke, C. S.; Haynes, D. A.; Pascu, S. I.; Rawson, J. M. *Chem. Commun*. **2005**, 4726. (b) Bond, A. D.; Haynes, D. A.; Pask, C. M.; Rawson, J. M. *J. Chem. Soc., Dalton Trans.* **2002**, 25. (c) Banister, A. J.; Bricklebank, N.; Clegg, W.; Elsegood, M. R. J.; Gregory, C. I.; Lavender, I.; Rawson, J. M.; Tanner, B. K. *J. Chem. Soc., Chem. Commun*. **1995**, 679. (d) Banister, A. J.; Bricklebank,N.; Lavender, I.; Rawson, J. M.; Gregory, C. I.; Tanner, B. K.; Clegg, W.; Elsegood, M. R. J.; Palacio, F. *Angew. Chem., Int. Ed. Engl*. **1996**, *35*, 2533. (e) Kinoshita, M. *Jpn. J. Appl. Phys*. **1994**, *33*, 5718. (f) Tamura, M.; Hosokoshi, Y.; Shiomi, D.; Kinoshita, M.; Nakazawa, Y.; Ishikawa, M.; Sawa, H.; Kitazawa, T.; Eguchi, A.; Nishio, Y.; Kajita, K. *J. Phys. Soc. Jpn.* **2003**, *72*, 1735. (g) Fatila, E. M.; Jennings, M. C.; Goodreid, J.; Preuss, K. E. *Acta Crystallogr*. **2010**, *C66*, o264.

13. Lekin, K., Winter, S. M., Downie, L. E., Bao, X., Tse, J. S., Desgreniers, S., Secco, R. A., Dube, P. A. and Oakley, R. T. *J. Am. Chem. Soc.* **2010**, 132, 16212.

14. These experiments were performed by collaborators at Florida State University. A manuscript has been submitted: Phan, H.; Lekin, K.; Winter, S. M.; Oakley, R. T; Shatruck, M. *J. Am. Chem. Soc.* June 4, 2013, ja-2013-055806.

15. (a) Beer, L.; Brusso, J. L.; Cordes, A. W.; Haddon, R. C.; Itkis, M. E.; Kirschbaum, K.; MacGregor, D. S.; Oakley, R. T.; Pinkerton, A. A.; Reed, R. W. *J. Am. Chem. Soc.* **2002**, *124*, 9498. (b) Beer, L.; Britten, J. F.; Brusso, J. L.; Cordes, A. W.; Haddon, R. C.; Itkis, M. E.;

MacGregor, D. S.; Oakley, R. T.; Reed, R. W.; Robertson, C. M. *J. Am. Chem. Soc.* **2003**, *125*, 14394. (c) Leitch, A. A.; Reed, R. W.; Robertson, C. M.; Britten, J. F.; Yu, X.; Secco, R. A.; Oakley, R. T. *J. Am. Chem. Soc.* **2007**, *129*, 7903.

16. Novriandi, I.; Brown, K. N.; Fleming, D. S.; Gulyas, P. T.; Lay, P. A.; Masters, A. F.; Phillips, L. *J. Phys. Chem.* **1999**, *103*, 2713.

17. Manual separation of the two phases was necessary in most trials to obtain phase pure material.

18. (a) Preston, K. F.; Sutcliffe, L. H. *Magn. Reson. Chem*. **1990**, *28*, 189. (b) Kaszynski, P. *J. Phys. Chem. A*, **2001**, *105*, 7615.

19. (a) Robertson, C. M.; Myles, D. J. T.; Leitch, A. A.; Reed, R. W.; Dooley, D. M.; Frank, N. L.; Dube, P. A.; Thompson, L. K.; Oakley, R. T. *J. Am. Chem. Soc*. **2007**, *129*, 12688. (b) Robertson, C. M.; Leitch, A. A.; Cvrkalj, K.; Reed, R. W.; Myles, D. J. T.; Dube, P. A.; Oakley, R. T. *J. Am. Chem. Soc*. **2008**, *130*, 8414. (c) Roberston, C. M.; Leitch, A. A.; Cvrkalj, K.; Myles, D. J. T.; Reed, R. W.; Dube, P. A.; Oakley, R. T. *J. Am. Chem. Soc.* **2008**, *130*, 14791.

20. (a) Bondi, A. *J. Phys. Chem*. **1964**, *68*, 441. (b) Dance, I. *New J. Chem*. **2003**, *27*, 22.

21. The $P2_1/c$ space group setting was used (rather than the alternate $P2_1/n$) for β-[**4-1**]$_2$ to allow for a direct comparison of this structure with the dimers [**4-4**]$_2$ and [**4-2**]$_2$, had been solved in $P2_1/c$ (Chapter 3).

22. Chen, C. M.; Dojahn, J. G.; Wentworth, W. E. *J. Phys. Chem. A* **1997**, *101*, 3088.

23. Bonner, J. C.; Fisher, M. E. *Phys. Rev. A* **1964**, *135*, 640.

24. Results from the Bonner-Fisher fitting provided the following: $\boldsymbol{J} = -9.56$ cm-1, z$\boldsymbol{J}$ = 13.26 cm-1, $g = 2.008$, $\theta = 0.52$ K, $\alpha = 0.0141$, TIP = 0, and $R_2(\chi)^* = 0.000105$.

25. Leitch, A. A.; Yu, X.; Winter, S. M.; Secco, R. A.; Dube, P. A.; Oakley, R. T. *J. Am. Chem. Soc*. **2009**, *131*,7112.

26. (a) Calculations were performed at the UB3LYP/6-311G(d,p) level. (b) Trans-annular interaction $\boldsymbol{J}_3$ is very small and slightly antiferromagnetic at -0.12 cm^{-1}. (c) Atomic coordinates were taken from crystallographic data.

27. (a) Noodleman, L.; Norman, J. G. *J. Chem. Phys*. **1979**, *70*, 4903. (b) Noodleman, L. *J. Chem. Phys*. **1981**, *74*, 5737. (c) Deumal, M.; Robb, M. A.; Novoa, J. J. *Prog. Theor. Chem. Phys.* **2007**, *16*, 271.

28. Crystal data for β-[**4-1**]$_2$ at 100K: monoclinic $P2_1/c$, a = 5.2962(6), b = 11.3270(13), c = 17.3316(18), β = 105.020(3)°, V = 1004.2(2) Å^3, Z = 4. Crystal data for **4-1** at 100 K: monoclinic $P2_1/c$, a = 5.1383(8), b = 11.4110(17), c = 17.384(3) Å, = 105.192(4)°, V = 983.7(3) Å^3, Z = 4. Data provided courtesy of collaborators at Florida State University for a personal communication. See reference 14.

29. Exact diagonalization simulations employed the ALPS library. See Bauer, B. et al. *J. Stat. Mech.* **2011**, P05001.

30. We note that the *PV* work calculated from the volume change (~20 Å^3) at the phase transition is on the same order of magnitude as the estimated thermal activation energy.

31. The higher pressure observed for the phase transition in the conductivity experiments reflect differences in the hydrostaticity of the two presses. At low pressures using silicone oil as the pressure-transmitting medium (assuming no penetration of oil into the sample) the diamond anvil cell is more hydrostatic than the solid medium high pressure cubic anvil press.

32. Beer, L.; Reed, R. W.; Robertson, C. M.; Oakley, R. T.; Tham, F. S.; Haddon, R. C. *Org. Lett.* **2008**, *10*, 3121.

33. (a) Wolf, S. A.; Awschalom, D. D.; Buhrman, R. A.; Daughton, J. M.; von Molnár, S.; Roukes, M. L.; Chtchelkanova, A. Y.; Trege, B. D. M. *Science* **2001**, *294*, 1488. (b) Prinz, G. A. *Science* **1998**, *282*, 1660. (c) Naber, W. J. M.; Faez, S.; van der Wiel, W. G. *J. Phys. D: Appl. Phys*. **2007**, *40*, R205.

34. High temperature magnetic susceptibility measurements on [**4-4**]$_2$ (R_1 = Me; R_2 = H) have confirmed that this material does not dissociate below 400 K.

35. For the calculation of the electronic energies of singlet σ-dimer and ^{3}Bu radical pairs for **4-8** and **4-9** (R_1 = R_2 = H), full geometry optimization within the confines of C_{2h} symmetry was invoked, with only the values of *q* and *r* defined in Figure 4.18 being constrained.

36. Dutton, J. L.; Tindale, J. J.; Jennings, M. C.; Ragogna, P. J. *Chem. Commun.* **2006**, 2474.

37. (a) Cozzolino, A. F.; Vargas-Baca, I.; Mansour, S.; Mahmoudkhani, A. H. *J. Am. Chem. Soc*. **2005**, *127*, 3184. (b) Cozzolino A. F., Vargas-Baca, I. *J. Organomet. Chem*. **2007**, *692*, 2657.

38. RDI has been shown to occur photochemically for some variants of S···Se−Se···S σ-dimers, but the data is still preliminary.

39. Desiraju, G. R. *Angew Chem., Int. Ed. Engl.* **1995**, *34*, 2311.

40. (a) Li, D.; Clérac, R.; Rou-beau, O.; Harté, E.; Mathonière, C.; Le Bris, R.; Holmes, S. M. *J. Am. Chem. Soc.* **2008**, *130*, 252. (b) Beneberu, H. Z.; Tian, Y.-H.; Kertesz, M. *Phys. Chem. Chem. Phys.* **2012**, *14*, 10713. (c) Haynes, D. A. *CrystEngComm* **2011**, *13*, 4793.

References for Chapter 5

1. Roberston, C. M.; Leitch, A. A.; Cvrkalj, K.; Myles, D. J. T.; Reed, R. W.; Dube, P. A.; Oakley, R. T. *J. Am. Chem. Soc.* **2008**, *130*, 14791.

2. (a) Beer, L.; Brusso, J. L.; Cordes, A. W.; Haddon, R. C.; Godde, E.; Itkis, M. E.; Oakley, R. T.; Reed, R. W. *Chem. Commun.* **2002**, 2562. (b) Leitch, A. A.; Yu, X.; Winter, S. M.; Secco, R. A.; Dube, P. A.; Oakley, R. T. *J. Am. Chem. Soc.* **2009**, *131*, 7112.

3. (a) Desiraju, G. R. *Angew. Chem., Int. Ed*. **1995**, *34*, 2311. (b) Desiraju, D. G. *Acc. Chem. Res*. **2002**, *35*, 565. (c) Thakur, T. S.; Kirchner, M. T.; Bläser, D.; Boese, R.; Desiraju, D. R. *CrystEngComm* **2010**, *12*, 2079.

4. Yu, X.; Mailman, A.; Lekin, K.; Assoud, A.; Robertson, C. M.; Noll, B. C.; Campana, C. F.; Howard, J. A. K.; Dube, P. A.; Oakley, R. T. *J. Am. Chem. Soc.* **2012**, *134*, 2264.

5. Mailman, A.; Winter, S. M.; Yu, X.; Robertson, C. M.; Yong, W.; Tse, J. S.; Secco, R. A.; Liu, Z.; Dube, P. A.; Howard, J. A. K.; Oakley, R. T. *J. Am. Chem. Soc.* **2012**, *134*, 9886.

6. Lekin, K.; Winter, S. M.; Downie, L. E.; Bao, X.; Tse, J. S.; Desgreniers, S.; Secco, R. A.; Dube, P. A.; Oakley, R. T. *J. Am. Chem. Soc*. **2010**, *132*, 16212.

7. Rovira, C. *Chem. Eur. J*. **2000**, *6*, 1723.

8. (a) Uehara, M.; Nagata, T.; Akimitsu, J.; Takahashi, H.; Mori, N.; Kinoshita, K. *J. Phys. Soc. Jpn.* **1996**, *65*, 2764. (b) Nakanishi, T.; Motoyama, N.; Mitamura, H.; Takeshita, N.; Takahashi, H.; Eisaki, H.; Uchida, S.; Mori, N. *Phys. Rev. B* **2005**, *72*, 054520. (c) Vuletic, T.; Korin-Hamzic, B.; Ivek, T.; Tomic, S.; Gorshunov, B.; Dressel, M.; Akimitsu, *J. Phys. Rep*. **2006**, *428*, 169. (d) Carter, S. A.; Batlogg, B.; Cava, R. J.; Krajewski, J. J.; Peck, W. F., Jr.; Rice, T. M. *Phys. Rev. Lett.* **1996**, *77*, 1378. (e) Azuma, M.; Hiroi, Z.; Takano, M.; Ishida, K.; Kitaoka, Y. *Phys. Rev. Lett.* **1994**, *73*, 3463. (f) Gozar, A.; Blumberg, G; Dennis, B. S.; Shastry, N.; Motoyama, N.; Eisaki, H.; Uchida, S. *Phys. Rev. Lett.* **2001**, *87*, 197202. (g) Moshchalkov, V. V.; Trappeniers, L.; Vanacken, J.; *Europhys. Lett.* **1999**, *46*, 75.

9. (a) White, J. L.; Lee, C.; Günaydin-Şen, Ö.; Tung, L. C.; Christen, H. M.; Wang, Y. J.; Turnbull, M. M.; Landee, C. P.; McDonald, R. D.; Crooker, S. A.; Singleton, J.; Whangbo, M.-H.; Musfeldt, J. L. *Phys. Rev. B* **2010**, *81*, 052407. (b) Matsumoto, T.; Miyazaki, Y.; Albrecht,

A. S.; Landee, C. P.; Turnbull, M. M.; Sorai, M. *J. Phys. Chem. B* **2000**, *104*, 9993. (c) Woodward, F. M.; Albrecht, A. S.; Wynn, C. M.; Landee, C. P.; Turnbull, M. M. *Phys. Rev. B* **2002**, *65*, 144412. (d) Awwadi, F.; Willett, R. D.; Twamley, B.; Schneider, R.; Landee, C. P. *Inorg. Chem.* **2008**, *47*, 9327. (e) Willett, R. D.; Galeriu, C.; Landee, C. P.; Turnbull, M. M.; Twamley, B. *Inorg. Chem*. **2004**, *43*, 3804. (f) Shapiro, A.; Landee, C. P.; Turnbull, M. M.; Jornet, J.; Deumal, M.; Novoa, J. J.; Robb, M. A.; Lewis, W. *J. Am. Chem. Soc*., **2007**, *129*, 952.

10. (a) Yoshida, Y.; Tateiwa, N.; Mito, M.; Kawae, T.; Takeda, K.; Hosokoshi, Y.; Inoue, K. *Phys. Rev. Lett.* **2005**, *94*, 037203. (b) Kikuchi, M.; Okamoto, K.; Okunishi, K.; Sakai, T. *Prog. Theol. Phys. Suppl.* **2005**, *159*, 251. (c) Sakai, T.; Okamoto, K.; Okunishi, K.; Kindo, K.; Narumi, Y.; Hosokoshi, Y.; Katoh, K.; Inoue, K.; Goto, T. *Physica B: Condens. Matter* **2004**, *346*, 34. (d) Tamura, M.; Hosokoshi, Y.; Shiomi, D.; Kinoshita, M.; Nakasawa, Y.; Ishikawa, M.; Sawa, H.; Kitazawa, T.; Eguchi, A.; Nishio, Y.; Kajita, K. *J. Phys. Soc. Jpn.* **2003**, *72*, 1735.

11. (a) Ribas, X.; Mas-Torrent, M.; Pérez-Benítez, A.; Dias, J. S.; Alves, H.; Lopes, E. B.; Henriques, R. T.; Molins, E.; Santos, I. C.; Wurst, K.; Foury-Leylekian, F.; Almeida, M.; Veciana, J.; Rovira, C. *Adv. Funct. Mater.* **2005**, *15*, 1023. (b) Rovira, C. in *Structure and Bonding*; Veciana, J., Ed.; Springer-Verlag: Berlin, Germany, 2001; pp 163-188.

12. (a) Schmidt, K. P.; Uhrig, G. S. *Mod. Phys. Lett. B* **2005**, *19*, 1179. (b) Dagotto, E.; Rice, T. M. *Science* **1996**, *271*, 618.

13. (a) Dagotto, E.; Riera, J.; Scalapino, D. J. *Phys. Rev. B* **1992**, *45*, 5744. (b) Dagotto, E. *Rep. Prog. Phys*. **1999**, *62*, 1525.

14. Lekin, K.; Wong, J. W. L.; Winter, S. M.; Mailman, A.; Dube, P. A.; Oakley, R. T. *Inorg. Chem.* **2013**, *52*, 2188.

15. Shaterian, H. R.; Doostmohammadi, R.; Ghashang, M. *Chin. J. Chem.* **2008**, *26*, 1709.

16. X-ray quality crystals of **5-5b** could be grown *via* vacuum sublimation and recrystallization from heptane, however, the X-ray data was obtained for crystals from sublimation, while the transport property measurements were performed on recrystallized material (easier to obtain in bulk quantities). Material from both procedures was deemed phase pure *via* FTIR, and the phases were identical to each other.

17. Beer, L.; Brusso, J. L.; Cordes, A. W.; Haddon, R. C.; Itkis, M. E.; Kirschbaum, K.; MacGregor, D. S.; Oakley, R. T.; Pinkerton, A. A.; Reed, R. W. *J. Am. Chem. Soc.* **124**, 9498.

18. *WinEPR Simfonia*, version 1.25; Bruker Instruments, Inc.: Billerica, MA, **1996**.

19. (a) Bondi, A. *J. Phys. Chem*. **1964**, *68*, 441. (b) Dance, I. *New J. Chem*. **2003**, *27*, 22.

20. (a) Bonner, J. C.; Fisher, M. E. *Phys. Rev*. **1964**, *135*, A640. (b) Estes, W. E.; Gavel, D. P.; Hatfield, W. E.; Hodgson, D. J. *Inorg. Chem*. **1978**, *17*, 1415.

21. Details of the Bonner−Fisher fit for the magnetic data of **5-1a** are as follows: $\boldsymbol{J} = -15.5$ cm^{-1}, z$\boldsymbol{J}$ = 1.31 cm^{-1}, g = 2.0079, θ = -0.60 K, α = 0.0134, TIP = 0, $R_2(\chi)$* = 0.0000633, *$R_2(\chi) = [\Sigma(\chi_{obs} - \chi_{calc})^2/\Sigma(\chi_{obs})^2]^{½}$.

22. Slippage coordinates for **5-1a** are (dx = 0 Å , dy = 2.49 Å) and for α-**4-1** (R_1 = Et, R_2 = F) are (dx = 0 Å , dy = 2.20 Å).

23. Bleaney, B.; Bowers, K. D. *Proc. R. Soc. London, A*, **1952**, 214.

24. Gu, Q.; Yu, D-K.; Shen, J.-L. *Phys. Rev. B* **1999**, *60*, 3009.

25. Landee, C. P.; Turnbull, M. M.; Galeriu, C.; Giantsidis, J.; Woodward, F. M. *Phys. Rev. B* **2001**, *63*, 100402.

26. Johnston, D. C.; Troyer, M.; Miyahara, S.; Lidsky, D.; Ueda, K.; Azuma, M.; Hiroi, Z.; Takano, M.; Isobe, M.; Ueda, Y.; Korotin, M. A.; Anisimov, V. I.; Mahajan, A.V.; Miller, L. L. arXiv:cond-mat/0001147.

27. (a) Noodleman, L. *J. Chem. Phys.* **1981**, *74*, 5737. (b) Noodleman, L.; Davidson, E. R. *Chem. Phys.* **1986**, *109*, 131. (c) Nagao, H.; Nishino, M.; Shigeta, Y.; Soda, T.; Kitagawa, Y.; Onishi, T.; Yoshioka, Y.; Yamaguchi, K. *Coord. Chem. Rev.* **2000**, *198*, 265. (d) Noodleman, L.; Norman, J. G. *J. Chem. Phys.* **1979**, *70*, 4903.

28. (a) Deumal, M.; Robb, M. A.; Novoa, J. J. *Prog. Theor. Chem. Phys*. **2007**, *16*, 271. (b) Li, L.; Turnbull, M. M.; Landee, C. P.; Jornet, J.; Deumal, M.; Novoa, J. J.; Wikaira, J. L. *Inorg. Chem*. **2007**, *46*, 11254.

29. (a) QMC simulations employed the *looper* code implemented in ALPS project distribution 2.0; see (a) Todo, S.; Kato, K. *Phys. Rev. Lett.* **2001**, *87*, 047203. (b) Bauer, B.; Carr, L. D.; Evertz, H. G.; Feiguin, A.; Freire, J.; Fuchs, S.; Gamper, L.; Gukelberger, J.; Gull, E.; Guertler, S.; Hehn, A.; Igarashi, R.; Isakov, S. V.; Koop, D.; Me, P. N.; Mates, P.; Matsuo, H.; Parcollet, O.; Pawłowski, G.; Picon, J. D.; Pollet, L.; Santos, E.; Scarola, V. W.; Schollwöck, U.; Silca, C.; Surer, B.; Todo, S.; Trebst, S.; Troyer, M.; Wall, M. L.; Werner, P.; Wessel, S. (ALPS Collaboration) *J. Stat. Mech.* **2011**, P05001.

30. Jornet-Somoza, J.; Codina-Castillo, N.; Deumal, M.; Mota, F.; Novoa, J. J.; Butcher, R. T.; Turnbull, M. M.; Keith, B.; Landee, C. P.; Wikaira, J. L. *Inorg. Chem.* **2012**, *51*, 6315.

31. Lekin, K.; Leitch, A. A.; Tse, J. S.; Bao, X.; Secco, R. A.; Desgreniers, S.; Ohishi, Y.; Oakley, R. T. *Cryst. Growth Des.*, **2012**, *12*, 4676.

32. (a) Desiraju, D. G. *Acc. Chem. Res.* **2002**, *35*, 565. (b) Thakur, T. S.; Kirchner, M. T.; Bläser, D.; Boese, R.; Desiraju, D. R. *CrystEngComm* **2010**, *12*, 2079. (c) Weiss, H.-C.; Boese, R.; Smith, H. L.; Haley, M. M. *Chem. Commun.* **1997**, 2403. (d) Thalladi, V. R.; Weiss, H. C.; Bläser, D.; Boese, R.; Nangia, A.; Desiraju, D. R. *J. Am. Chem. Soc.* **1998**, *120*, 8702. (e) Mele, A.; Vergani, B.; Viani, F.; Meille, S. V.; Farina, A.; Bravo, F. *Eur. J. Org. Chem.* **1999**, *187*. (f) Haufe, G.; Rosen, T. C.; Meyer, O. G. J.; Fröhlich, R.; Rissanen, K. *J. Fluorine Chem.* **2002**, *114*, 189. (g) Hyla-Kryspin, E.; Haufe, G.; Grimme, S. *Chem. Eur. J.* **2004**, *10*, 3411.

33. Leitch, A. A.; Yu, X.; Robertson, C. M.; Secco, R. A.; Tse, J. S.; Oakley, R. T. *Inorg. Chem.* **2009**, *48*, 9874.

34. *SAINT*, version 6.22; Bruker Advanced X-ray Solutions, Inc.: Madison, WI, **2001**.

35. Sheldrick, G.M., *SADABS (Version 2008/2), Siemens Area Detector Absorption Correction*; Universitat Göttingen: Göttingen, Germany, **2008**.

36. Bruker (2010) Apex (Version 2010-1) and SAINT (Version 7.68a). Bruker Advanced X-ray Solutions, Inc.: Madison, WI, **2010**.

37. Sheldrick, G. M. *SHELXS-90. Acta Crystallogr. A* **1990**, *46*, 467.

38. Sheldrick, G. M. *SHELXL-97, Program for the Refinement of Crystal Structures*; University of Göttingen: Göttingen, Germany, **1997**.

39. *SHELXTL, Program Library for Structure Solution and Molecular Graphics, version 6.12*; Bruker Advanced X-ray Solutions, Inc.: Madison, WI, **2001**.

40. See: http://todo.issp.u-tokyo.ac.jp/en/projects/alps-looper.

References for Chapter 6

1. (a) Beer, L.; Brusso, J. L.; Cordes, A. W.; Haddon, R. C.; Itkis, M. E.; Kirschbaum, K.; MacGregor, D. S.; Oakley, R. T.; Pinkerton, A. A.; Reed, R. W. *J. Am. Chem. Soc.* **2002**, *124*, 9498. (b) Beer, L.; Britten, J. F.; Clements, O. P.; Haddon, R. C.; Itkis, M. E.; Matkovich, K. M.; Oakley, R. T.; Reed, R. W. *Chem. Mat.* **2004**, *16*, 1564. (c) Beer, L.; Britten, J. F.; Brusso, J. L.; Cordes, A. W.; Haddon, R. C.; Itkis, M. E.; MacGregor, D. S.; Oakley, R. T.; Reed, R. W.; Robertson, C. M. *J. Am. Chem. Soc.* **2003**, *125*, 14394.

2. (a) Leitch, A. A.; Yu, X.; Winter, S. M.; Secco, R. A.; Dube, P. A.; Oakley, R. T. *J. Am. Chem. Soc.* **2009**, *131*, 7112.

3. (b) Brusso, J. L.; Cvrkalj, K.; Leitch, A. A.; Oakley, R. T.; Reed, R. W.; Robertson, C. M. *J. Am. Chem. Soc.* **2006**, *128*, 15080.

4. (a) Robertson, C. M.; Myles, D. J. T.; Leitch, A. A.; Reed, R. W.; Dooley, D. M.; Frank, N. L.; Dube, P. A.; Thompson, L. K.; Oakley, R. T. *J. Am. Chem. Soc*. **2007**, *129*, 12688. (b) Robertson, C. M.; Leitch, A. A.; Cvrkalj, K.; Reed, R. W.; Myles, D. J. T.; Dube, P. A.; Oakley, R. T. *J. Am. Chem. Soc*. **2008**, *130*, 8414. (c) Roberston, C. M.; Leitch, A. A.; Cvrkalj, K.; Myles, D. J. T.; Reed, R. W.; Dube, P. A.; Oakley, R. T. *J. Am. Chem. Soc.* **2008**, *130*, 14791.

5. (a) Beer, L.; Brusso, J. L.; Haddon, R. C.; Itkis, M. E.; Leitch, A. A.; Oakley, R. T.; Reed, R. W.; Richardson, J. F. *Chem. Commun*. **2005**, 1543. (b) Beer, L.; Brusso, J. L.; Haddon, R. C.; Itkis, M. E.; Kleinke, H.; Leitch, A. A.; Oakley, R. T.; Reed, R. W.; Richardson, J. F.; Secco, R. A.; Yu, X. *J. Am. Chem. Soc.* **2005**, *127*, 18159.

6. (a) Tse, J. S.; Leitch, A. A.; Yu, X.; Bao, X.; Zhang, S.; Liu, Q.; Jin, C.; Secco, R. A.; Desgreniers, S.; Ohishi, Y.; Oakley, R. T. *J. Am. Chem. Soc.* **2010**, *132*, 4876. (b) Lekin, K.; Leitch, A. A.; Tse, J. S.; Bao, X.; Secco, R. A.; Desgreniers, S.; Ohishi, Y.; Oakley, R. T. *Cryst. Growth Des.* **2012**, *12*, 4676. (c) Lekin, K.; Winter, S. M.; Downie, L. E.; Bao, X.; Tse, J. S.; Desgreniers, S.; Secco, R. A.; Dube, P. A.; Oakley, R. T. *J. Am. Chem. Soc.* **2010**, *132*, 16212.

7. (a) Leitch, A. A.; Lekin, K.; Winter, S. M.; Downie, L. E.; Tsuruda, H.; Tse, J. S.; Mito, M.; Desgreniers, S.; Dube, P. A.; Zhang, S.; Liu, Q.; Jin, C.; Ohishi, Y.; Oakley, R. T. *J. Am. Chem.*

Soc. **2011**, *133*, 6051. (b) Mito, M.; Komorida, Y.; Tsuruda, H.; Tse, J. S.; Desgreniers, S.; Ohishi, Y.; Leitch, A. A.; Cvrkalj, K.; Robertson, C. M.; Oakley, R. T. *J. Am. Chem. Soc*. **2009**, *131*, 16012.

8. Leitch, A. A.; Brusso, J. L.; Cvrkalj, K.; Reed, R. W.; Robertson, C. M.; Dube, P. A.; Oakley, R. T. *Chem. Commun*. **2007**, 3368.

9. Winter, S. M.; Cvrkalj, K.; Robertson, C. M.; Probert, M. R.; Dube, P. A.; Howard, J. A. K.; Oakley, R. T. *Chem. Commun*. **2009**, 7306.

10. See Appendix A for details.

11. Dobrosavljević, V.; Trivedi, N.; Valles, J. M. Jr. *Conductor-Insulator Quantum Phase Transitions*; Oxford University Press: Oxford, U. K., **2012**.

12. (a) Dressel, M. *J. Phys.: Condens. Matter* **2011**, *23*, 293201. (b) Powell, B. J.; McKenzie, R. H. *Rep. Prog. Phys.* **2011**, *74*, 056501. (c) Kanoda, K.; Miyawaga, K.; Kagawa, F. *Nature* **2005**, *436*, 534. (d) Dumm, M.; Faltermeier, D.; Drichko, N.; Dressel, M.; Mézière, C.; Batail, P. *Phys. Rev. B* 2009, 79, 195106. (e) Kanoda, K.; Miyawaga, K.; Kagawa, F. *Nature Physics* **2009**, *5*, 880. (f) Toyota, N.; Lang, M.; Müller, J. *Low-Dimensional Molecular Metals*; Springer: Germany, **2007**.

13. Beer, L.; Haddon, R. C.; Itkis, M. E.; Leitch, A. A.; Oakley, R. T.; Reed, R. W.; Richardson, J. F.; VanderVeer, D. G. *Chem. Commun.* **2005**, 1218.

14. Winter, S. M.; Balo, A. R.; Roberts, R. J.; Lekin, K.; Assoud, A.; Dube, P. A.; Oakley, R. T. *Chem Commun.* **2013**, *49*, 1603.

15. (a) Novoselov, K. S.; Geim, A. K.; Morozov, S. V.; Jiang, D.; Zhang, Y.; Dubonos, S. V.; Grigorieva, I. V.; Firsov, A. A. *Science* **2004**, *306*, 666. (b) Geim, A. K.; Novoselov, K. S. *Nature Mater*. **2007**, *6*, 183.

16. Morita, Y.; Suzuki, S.; Sato, K.; Takui, T. *Nature Chem.* **2011**, *3*, 197.

17. (a) Inoue, J.; Fukui, K.; Kubo, T.; Nakazawa, S.; Sato, K.; Shiomi, D.; Morita, Y.; Yamamoto, K.; Takui, T.; Nakasuji, K. *J. Am. Chem. Soc.* **2001,** *123*, 12702. (b) Fukui, K.; Inoue, J.; Kubo, T.; Nakazawa, S.; Aoki, T.; Morita, Y.; Yamamoto, K.; Sato, K.; Shiomi, D.; Nakasuji, K.; Takui, T. *Synth. Metals* **2001**, *121*, 1824.

18. Morita, Y.; Nishida, S. In *Stable Radicals: Fundamental and Applied Aspects of Odd-Electron Compounds* Hicks, R. G., Ed.; John Wiley & Sons, Ltd.: Wiltshire, U.K., **2010**; pp 81 – 145.

19. Ratera, I.; Veciana, J. *Chem. Soc. Rev.* **2012**,*41*, 303.

20. Yu, X.; Mailman, A.; Dube, P. A.; Assoud, A.; Oakley, R. T. *Chem. Commun.* **2011**, *47*, 4655

21. Yu, X.; Mailman, A.; Lekin, K.; Assoud, A.; Dube, P. A.; Oakley, R. T. *Cryst. Growth Des.* **2012**, *12*, 2485.

22. Yu, X.; Mailman, A.; Lekin, K.; Assoud, A.; Robertson, C. M.; Noll, B. C.; Campana, C. F.; Howard, J. A. K.; Dube P. A.; Oakley, R. T. *J. Am. Chem. Soc.* **2012**, 134, 2264.

23. The cell potential, which is an estimate of U, is E_{cell} ~ 0.60 – 0.69 eV for **6-12**, *versus* E_{cell} ~ 0.85 eV for **6-1**.

24. Mailman, A.; Winter, S. M.; Yu, X.; Robertson, C. M.; Yong, W.; Tse, J. S.; Secco, R. A.; Liu, Z.; Dube, P. A.; Howard, J. A. K.; Oakley, R. T. *J. Am. Chem. Soc.* **2012**, *134*, 9886.

Appendix A

General Experimental and Computational Methods

A.1 Procedures

A.1.1 General Procedures

Many of the reactions and manipulations were performed under an inert atmosphere of nitrogen. Those reactions carried out in solution were handled by standard or modified Schlenk techniques using a double-manifold glass vacuum line (nitrogen / vacuum) with an Edwards E2M series rotary vacuum pump. Air sensitive solids were handled and stored in a nitrogen-filled Braun MB-150M drybox.

A.1.2 Diffusion H-Cell Crystallizations

Diffusion H-cell experiments are especially useful for the preparation of air and/or moisture sensitive materials such as neutral radicals, as a thorough degassing of the solvent is possible. A diffusion H-cell apparatus is illustrated in Figure A.1, and a typical experiment proceeds as follows; two solutions containing each reactant are placed in each of the round bottom flasks and the cell is oriented as shown in Figure A.1a. The solutions are put through five freeze-pump-thaw cycles to ensure all the oxygen has been removed from the vessel. The apparatus may be kept under vacuum or flooded with an inert gas (argon or nitrogen). The H-cell is then inverted and tipped slightly askew as depicted in Figure A.1b, to allow the two solutions to combine slowly. One solution flows through the glass frit into the other resulting in crystal growth of the product at the interface of the two solutions.

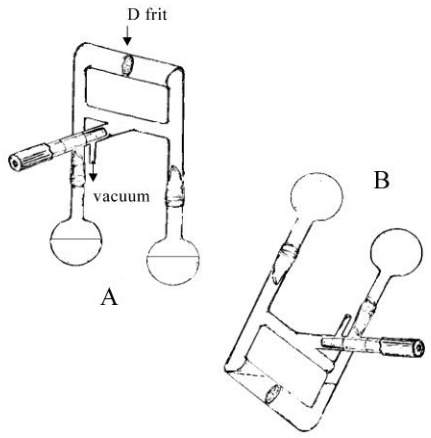

Figure A.1 Diffusion H-cell apparatus for single crystal growth.

A.1.3 Electrochemical H-Cells

The electrocrystallization method of single crystal growth requires that the product be fairly conductive, typically with a σ_{RT} value of at least 10^{-4} $S \cdot cm^{-1}$. A schematic diagram of an electrochemical H-cell apparatus is shown in Figure A.2 and the procedure used follows standard electrochemical techniques.[1] In general, the sample is dissolved in degassed acetonitrile containing 0.025 M [n-Bu_4N][PF_6] as supporting electrolyte, and placed in one side of the cell. The other side is filled with an equally degassed acetonitrile solution of 0.025 M [n-Bu_4N][PF_6], to a level equal to the adjacent compartment. Once the apparatus is assembled as in Figure A.2, current ranging from 1 to 10 μA is applied, allowing for the electrochemical reduction of the reactant and crystallization of the product on the electrode. The experiment usually runs for a period of 2 to 7 days.

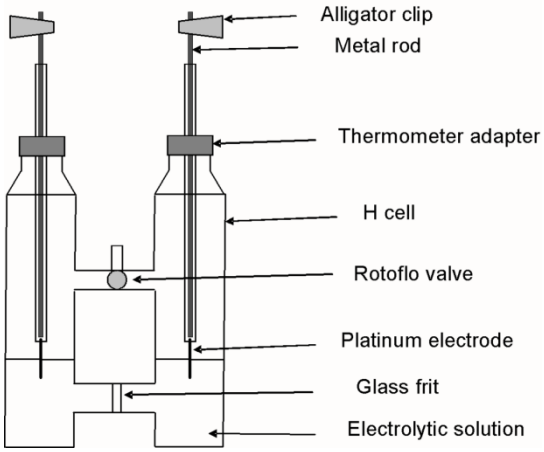

Figure A.2 Electrochemical H-cell apparatus for single crystal growth.

A.2 Techniques

A.2.1 DFT Calculations

DFT calculations were run on PC workstations using the UB3LYP method[2] available in the Gaussian 98W[3] and Gaussian 09W[4] suite of programs.

A.2.1.1 Dimer Dissociation Enthalpies

Radical association energies were estimated in terms of the total electronic energy (B3LYP/6-31G(d,p)) difference between the radicals and their dimers. Dimer geometries were optimized within a C_{2h} symmetry constraint and were confirmed to be stationary points by frequency calculations.

A.2.1.2 Exchange Energy Calculations

The exchange energy ***J*** for any pair of interacting radicals was estimated in terms of the energy difference between the triplet (E_T) and broken symmetry singlet (E_{BSS}) states derived from the phenomenological Heisenberg Hamiltonian $H_{ex} = -2J\{S_1 \cdot S_2\}$ (Figure A.3).[5] Single point energies of the triplet (E_T) and broken symmetry singlet (E_{BSS}) states were calculated using the hybrid exchange correlation functional UB3LYP and a series of polarized, split-valence basis sets with double-zeta (6-31G(d,p)) and triple-zeta (6-311G(d,p)) functions. Exchange energies were then derived from Equation (**1**), using the calculated values of E_T and E_{BSS} and the respective $<S^2>$ expectation values. Tight convergence criteria were employed, and atomic coordinates were taken from crystallographic data.

$$\psi_{BSS} = \frac{1}{\sqrt{2}}(\psi_T \pm \psi_S)$$

$$\langle S^2 \rangle_{BSS} = \frac{1}{2}\langle \psi_T + \psi_S | S^2 | \psi_T + \psi_S \rangle$$

$$= \frac{1}{2}\left[\langle \psi_T | S^2 | \psi_T \rangle + \langle \psi_S | S^2 | \psi_S \rangle\right]$$

$$= \frac{1}{2}\left[\langle S^2 \rangle_T + \langle S^2 \rangle_S\right]$$

$$= \frac{1}{2}[2+0]$$

$$= 1$$

$$H_{ex} = -2J\{S_1 \cdot S_2\}$$

where $\langle S^2 \rangle = S(S+1)$ and $S = S_1 + S_2$

$$\langle H \rangle = \langle -J(S^2 - S_1^2 - S_2^2) \rangle$$

$$E = -J(\langle S^2 \rangle - \langle S_1^2 \rangle - \langle S_2^2 \rangle)$$

$$E = -J\left[(S(S+1)) - (S_1(S_2+1)) - (S_2(S_2+1))\right]$$

$$\boxed{J = \frac{-(E_T - E_{BSS})}{\langle S^2 \rangle_T - \langle S^2 \rangle_{BSS}}} \quad (1)$$

Figure A.3 Derivation of $<S^2>_{BSS}$ value and the expansion of the Heisenberg Hamiltonian to obtain the energies of any particular spin state. Also shown is the exchange energy ***J*** equation (**1**).

The relationship between the triplet E_T, singlet E_S and broken symmetry singlet E_{BSS} energy states and the exchange energy J is presented in Figure A.4.

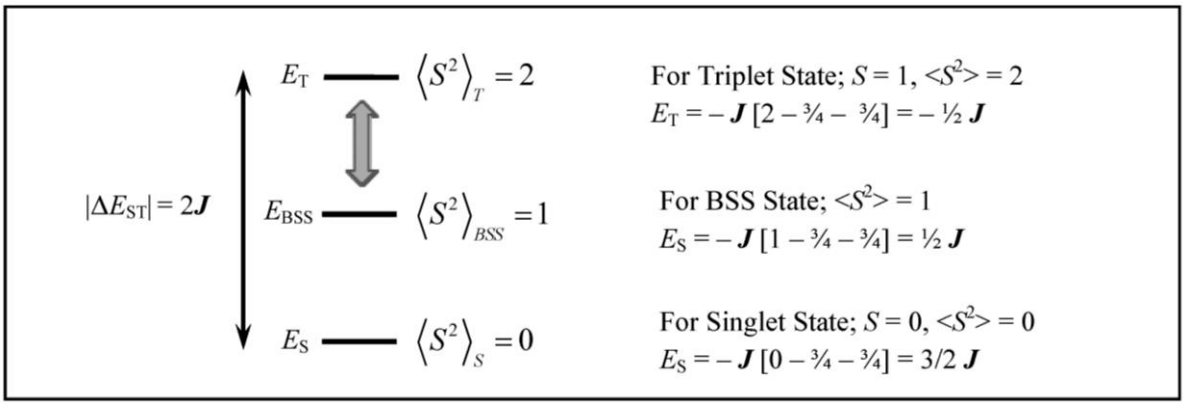

Figure A.4 Calculated energies of the triplet E_T , singlet E_S and broken symmetry singlet E_{BSS} states.

A.2.2 NMR Spectra

^{1}H NMR spectra were collected on a Bruker Avance 300 MHz NMR spectrometer.

A.2.3 Infrared Spectral Analysis

Infrared spectra were recorded (at 2 cm^{-1} resolution) as Nujol mulls or neat liquids on KBr plates, on a Nicolet Avatar 320 FT infrared spectrometer.

A.2.4 Mass Spectrometry

Low resolution mass spectra (70 eV, EI, DEI and CI, DCI) were run on either a Micromass Q-TOF Ultima Global LC/MS/MS system or a JEOL HX110 double focusing mass spectrometer at the WATSPEC Mass Spectrometry Facility.

A.2.5 Cyclic Voltammetry

Cyclic voltammetry experiments were performed using a PINE Bipotentiostat, Model AFCCIBPI, on dry acetonitrile solutions containing 0.1 M tetra-*n*-butylammonium hexafluorophosphate. Scan rates of 50 - 100 mV s^{-1} were employed. Potentials were scanned from -2.5 to 2.0 V with respect to the quasi-reference electrode in a single compartment cell fitted with Pt electrodes. The potentials were referenced to the ferrocenium/ferrocene couple at 0.38 V *vs* SCE and are cited relative to SCE in CH_3CN.[6]

A.2.6 EPR Spectra

The X-band EPR spectra were recorded on methylene chloride or toluene solutions of the radical at ambient temperature using a Bruker EMX spectrometer. Hyperfine coupling constants were obtained by spectral simulation using Simfonia[7] and WinSim.

A.2.7 Elemental Analysis

Elemental analyses were performed by MHW Laboratories, Phoenix, AZ.

A.2.8 Ambient Pressure Magnetic Susceptibility Measurements

DC magnetic susceptibility measurements were performed over the range 2−300 K in most cases, and 2−400 K for one compound (Chapter 4) on a Quantum Design MPMS SQUID magnetometer. AC susceptibility measurements were performed on an Oxford Instruments MagLab EXA. The results were corrected for diamagnetic contributions using Pascal's constants.[8]

A.2.8.1 Magnetic Modeling

For several compounds discussed in this thesis, the observed magnetic susceptibility data was fitted to a Bonner-Fisher 1D S = ½ AFM chain model[9] (Equation **2**) modified to include a molecular field parameter (zJ) to account for interchain interactions (Equation **3**).[10] Contributions from Temperature Independent Paramagnetism (TIP) and Curie-Weiss impurities (α) were also included (Equation **4**). In these equations, N is the Avogadro constant, k is the Boltzmann constant, g is the g-factor, S is the total spin angular momentum quantum number, θ is the Weiss constant and β is the Bohr magneton.

$$\chi_{BF} = \frac{Ng^2\beta^2}{k(T-\theta)}\left[\frac{0.25+0.14995X+0.30094X^2}{1.0+1.9862X+0.68885X^2+6.0626X^3}\right] \qquad where\ X = \frac{|J|}{kT} \qquad (2)$$

$$\chi_{chain} = \frac{\chi_{BF}}{1-\frac{2(zJ)\chi_{BF}}{Ng^2\beta^2}} \qquad (3)$$

$$\chi_{obsd} = \left\{\frac{\alpha\left[Ng^2\beta^2 S(S+1)\right]}{3kT} + TIP + \left[1-\alpha\right]\chi_{chain}\right\} \qquad (4)$$

In Chapter 5, the spin ladders were fit to two different models; the Johnston strong-leg ladder and the Landee strong-run ladder. The full temperature range (3-300 K) of the observed magnetic susceptibility of **5-1b – 5-1d** was fitted (Equation 5) to a S = ½ Strong-Leg Spin Ladder developed by Johnston *et. al.*[11] The same data range was also modeled to a Landée Spin Ladder Function (Equation 6),[12] modified to include contributions from Temperature Independent Paramagnetism (TIP) and Curie-Weiss impurities (α) (Equation 7).

Johnston Strong-leg ladder

***C* = Curie Constant**
***J_rung* = J_{rung} (K)**
***J_leg* = J_{leg} (K)**
***FR* = paramagnetic impurity (fraction)**
***T* = Temperature (K)**

Eqn (**5**)

```
χ = (1-FR)*(C/T)*exp(-(0.4030*(J_rung/J_leg)+0.0989*(J_rung/J_leg)^3)/(T/J_leg))*(1+(J_leg/T)*
(-0.05383784-0.67282213 *(J_rung/J_leg)+0.03896299*(J_rung/J_leg)^2+0.01103114* (J_rung/J_leg)^3)+
(J_leg/T)^2*(0.09740136+0.12334838*(J_rung/J_leg)-0.0253489* (J_rung/J_leg)^2+0.00655748*
(J_rung/J_leg)^3)+(J_leg/T)^3*(0.01446744-0.03965984*(J_rung/J_leg)-0.03120146*(J_rung/J_leg)^2+
0.02118588*(J_rung/J_leg)^3)+(J_leg/T)^4*(0.001392519+0.006657608*(J_rung/J_leg)-0.020207553*
```

(J_rung/J_leg)^2+0.008830122*(J_rung/J_leg)^3)+(J_leg/T)^5*(0.0001139343+0.0001341951*(J_rung/J_leg)+0.0016684229*(J_rung/J_leg)^2-0.0001396407*(J_rung/J_leg)^3)+(J_leg/T)^6*(0.0000422531*(J_rung/J_leg)-0.000160983*(J_rung/J_leg)^^2+0.0001335788*(J_rung/J_leg)^3))/ (1+(J_leg/T)*(0.44616216-0.82582213*(J_rung/J_leg)+0.03896299*(J_rung/J_leg)^2-0.08786886* (J_rung/J_leg)r3)+(J_leg/T)^2*(0.32048245-0.40632550*(J_rung/J_leg)+0.20252880*(J_rung/J_leg)^2-0.03801372*(J_rung/J_leg)^3)+(J_leg/T)^3*(0.13304199-0.25099527*(J_rung/J_leg)+0.11749096* (J_rung/J_leg)^2-0.07871375*(J_rung/J_leg)^3)+(J_leg/T)^4*(0.03718413-0.10249898*(J_rung/J_leg)+ 0.04316152*(J_rung/J_leg)^2+0.01936105*(J_rung/J_leg)^3)+(J_leg/T)^5*(0.002813608+0.000402749* (J_rung/J_leg)+0.001958564*(J_rung/J_leg)^2-0.003803837*(J_rung/J_leg)^3+(J_leg/T)^6*(0.0002646763-0.0010424633*(J_rung/J_leg)+0.0015813041*(J_rung/J_leg)^2-0.0002914845*(J_rung/J_leg)^3))+ (FR*(C/T))

Landee Strong-rung ladder

$$\chi_{Landee} = \frac{4C}{T}\left\{\frac{1}{3+e^{\beta}} - \frac{J_{leg}}{J_{rung}}\left[\frac{2\beta}{(3+e^{\beta})^2}\right] - \left(\frac{J_{leg}}{J_{rung}}\right)^2\left[\frac{3\beta(e^{2\beta}-1)-\beta^2(5+e^{2\beta})}{4(3+e^{\beta})^3}\right] - \left(\frac{J_{leg}}{J_{rung}}\right)^3\left[\frac{3\beta(e^{2\beta}-1)}{8(3+e^{\beta})^3} - \frac{9\beta^2e^{\beta}(1+3e^{\beta})-\beta^3(7e^{2\beta}-9e^{\beta}-12)}{12(3+e^{\beta})^4}\right]\right\} \quad \text{Eqn (6)}$$

$$where\ \beta \equiv \frac{1}{t} = \frac{-2J_{rung}}{k_BT}$$

$$\chi_{obs} = \left\{\frac{\alpha[Ng^2\beta^2S(S+1)]}{3kT} + [1-\alpha]\chi_{Landee}\right\} \quad \text{Eqn (7)}$$

These equations were incorporated into software provided by Randle Taylor (randle.taylor@gmail.com) and were built using Python version 2.5 and included the following packages: Numpy v1.2.1, Scipy v0.7.0 rc2 and wxpython v2.8.9.1 (msw-unicode). The GUI was built using wxGlade v0.6.3 and the Windows executable was created using py2exe v0.6.6.

A.2.9 Ambient Pressure Conductivity Measurements

Ambient pressure single-crystal (needle axis) conductivity measurements were made using a four-probe configuration, with in-line contacts made using silver paint. Conductivity was measured in a custom-made helium variable-temperature probe using a Lake Shore 340 temperature controller. A Keithley 236 unit was used as a voltage source and current meter, and two 6517A Keithley electrometers were used to measure the voltage drop between the potential leads in the four-probe configuration.

For pressed pellet samples, four-probe temperature dependent conductivity measurements were performed using either a Quantum Design PPMS instrument or a home-made device, to measure the voltage drop under dynamic vacuum. Silver paint was used to apply the electrical contacts.

A.2.10 Ambient Pressure Single Crystal and Powder X-ray Diffraction

Single crystal X-ray data were collected at ambient temperature (and 100 K when stated) using phi and omega scans with a (i) Bruker APEX I CCD detector on a D8 3-circle goniometer (University of Waterloo), (ii) Bruker P4/CCD diffractometer (McMaster University) and (iii) Bruker APEX II CCD detector on a D8 3-circle goniometer (McMaster University) with Mo Kα (λ = 0.71073 Å) radiation. Single crystal data were also collected on a Bruker SMART 6000 CCD on a D8 3-circle goniometer and a parallel focus Cu Kα (λ = 1.54178 Å) with a rotating anode generator. All data were scanned using Bruker's SMART program and integrated using Bruker's SAINT software[13] or by the APEX II software package. The structure was solved by direct methods using SHELXS-90[14] and refined by least-squares methods on F^2 using SHELXL-97[15] incorporated in the SHELXTL suite of programs.[16] Agreement indices were calculated as follows:

$$R = [\Sigma||F_o| - |F_c||] / [\Sigma|F_o|] \text{ for } I > 2\,\sigma(I); \; R_w = \{[\Sigma\, w(|F_o| - |F_c|)^2\,] / [\Sigma\, w|F_o|^2\,]\}^{½}.$$

Powder data were collected on an X-ray powder diffractometer with a position sensitive detector (INEL) at ambient temperature using Cu Kα radiation (λ = 1.5406 Å). The structures were obtained using DASH to index the unit cell and for simulated annealing to solve the structures, and GSAS to refine the solutions. Agreement indices were calculated as follows:

$$R_p = [\Sigma\,(I_o - I_c)] / [\Sigma(I_o)]; \; R_{wp} = \{[\Sigma\, w(I_o - I_c)^2\,] / [\Sigma\, w(I_o)^2\,]\}^{½}.$$

A.3 Source of Starting Materials

A.3.1 Purchased Chemicals that were used as Received

2,6-diaminopyridine	(Aldrich)
acetic acid, glacial	(Fisher)
ammonia gas	(Matheson)
ammonium hydroxide (aqueous)	(Fisher)
benzyltriethylammonium chloride	(Aldrich)
bromine	(Fisher)
calcium hydride	(Fisher)
chloroform-*d*	(Isotec)
decamethylferrocene	(Aldrich/Alfa Aesar)

diethyl ether	(Fisher)
dimethylsulfoxide-*d*	(Isotec)
ethanol, 95 %	(Fisher)
ethyl triflate, 99 %	(Aldrich, Synquest)
ferrocene	(Aldrich)
gallium trichloride, anhydrous, beads, -10 mesh, 99.99 %	(Aldrich)
hexane	(Fisher)
heptane	(Fisher)
hydrochloric acid, 12 M	(Fisher)
methanol	(Fisher)
methyl triflate, 99 %	(Aldrich)
nitrogen gas	(In-house supply)
octamethylferrocene	(Aldrich)
Proton Sponge (1,8-bis(dimethylamino)napthalene)	(Aldrich)
selenium dioxide	(Aldrich)
silver triflate	(Aldrich)
sodium borohydride	(Aldrich)
sodium dithionite	(Aldrich)
sulfur monochloride	(Aldrich)
tetra-*n*-butylammonium bromide	(Aldrich)
tetra-*n*–butylammonium fluoride, 1.0 M in THF	(Aldrich)
tetra-*n*-butylammonium tetrafluoroborate	(Aldrich)
tetra-*n*-butylammonium triflate	(Alfa Aesar)
tetrahydrofuran, anhydrous	(Aldrich)
thionyl chloride	(Acros)
triethylamine, 99%	(Aldrich)

triethyloxonium hexafluorophosphate (Aldrich)

triflic acid (Aldrich)

trifluoroacetic acid (Aldrich)

A.3.2 Solvents Purified Prior to Use

acetonitrile (Caledon) - distilled from P_2O_5 or CaH_2

chlorobenzene (Fisher) - distilled from P_2O_5

dichloroethane, 1,2- (Fisher) - distilled from P_2O_5

A.3.3 Chemicals Prepared "In House"

A.3.3.1 Preparation of Iodobenzene Dichloride.[17] A solution of iodobenzene (6.57 g, 0.322 mol) in 50 mL DCM was cooled to 0 °C, and chlorine gas was passed over for approximately 20 min to give a bright yellow precipitate. After stirring for another 20 min the cold bath was removed and the vessel was vented to remove excess gas. After 25 min, iodobenzene dichloride was filtered off and rinsed with cold DCM, yield 6.24 g (0.0227 mol, 71 %).

A.3.3.2 Preparation of *n*-Butyl, *n*-Pentyl and *n*-Hexyl Triflate.[18] To a solution of n-alkyl trimethylsilyl ether (13.8 g, 0.0943 mol) in 200 mL dichloromethane cooled on ice for 15 min, triflic anhydride (27 g, 0.0957 mol) was added via pipette. The mixture was stirred for 75 min on ice. Afterwards, 200 mL of H_2O was added and stirred for 1 hour. The organic phase was then extracted and washed with 2 x 100 mL H_2O. The solution was filtered and the solvent flashed off. The product was distilled at ~ 71 °C under aspirator vacuum, yield = 15.2 g (0.0487 mol, 52 %).

A.4 Conductive Behavior of Elemental and Synthetic Compounds

Table A.1 Conductive Behavior of Selected Elemental and Synthetic Compounds

Compound	**σ_{RT} ($S \cdot cm^{-1}$)**	**Type**
Cu[a]	10^{6}	Metal
Na[a]	10^{5}	Metal
(SN)x[b]	10^{3}	Metal
[TTF][TCNQ][b]	10^{2}	Metal
Ge[c]	10^{-2}	Semiconductor
GaAs[d]	10^{-4}	Semiconductor
Se[a]	10^{-6}	Semiconductor
perylene[b]	10^{-14}	Insulator
diamond[c]	10^{-16}	Insulator
S[a]	10^{-18}	Insulator

[a] Weast, R. C. *CRC Handbook of Chemistry and Physics, 64th Ed.* CRC Press, Inc.; Boca Raton, Florida, **1982**. [b] Ferraro, J. R.; Williams, J. M. *Introduction to Synthetic Electrical Conductors*. Academic Press Inc.; California, U.S., **1987**. [c] Huheey, J. E.; Keiter, E. A.; Keiter, R. L. *Inorganic Chemistry, Principles of Structure and Reactivity, 4th Ed.* HarperCollins College Publishers; New York, U. S., **1993**. [d] Patanè, A.; Allison, G.; Eaves, L.; Hopkinson, M.; Hill, G.; Ignatov, A. *J. Phys.: Condens. Matter* **2009**, *21*, 174209.

References for Appendix A

1. (a) Ferraro, J. R.; Williams, J. M. Introduction to Synthetic Electrical Conductors; Academic Press: New York, **1987**, p 25. (b) Stephens, D. A.; Rehan, A. E.; Compton, S. J.; Barkhau, R. A.; Williams, J. M. *Inorg. Synth*. **1986**, *24*, 135.

2. (a) Beck, A. D. *J. Chem. Phys.*, **1993**, *98*, 5648. (b) Lee, C.; Yang, W.; Parr, R. C. *Phys. Chem. Rev. B*, **1988**, *37*, 785.

3. Frisch, M. J.; Trucks, G. W.; Schlegel, H. B.; Scuseria, G. E.; Robb, M. A.; Cheeseman, J. R.; Zakrzewski, V. G.; Montgomery Jr., J. A.; Stratmann, R. E.; Burant, J. C.; Dapprich, S.; Millam, J. M.; Daniels, A. D.; Kudin, K. N.; Strain, M. C.; Farkas, O.; Tomasi, J.; Barons, V.; Cossi, M.; Cammi, R.; Mennucci, B.; Pomelli, C.; Adamo, C.; Clifford, S.; Ochterski, J.; Petersson, G. A.; Ayala, P. Y.; Cui, Q.; Morokuma, K.; Malick, D. K.; Rabuck, A. D.; Raghavachari, K.; Foreman, J. B.; Cioslowski, J.; Ortiz, J. V.; Stefanov, B. B.; Liu, G.; Fox, D. J.; Keith, T.; Al-Laham, M. A.; Peng, C. Y.; Nanayakkara, A.; Wong, M. W.; Andres, J. L.; Gonzalez, C.; Head-Gordon, M.; Repogle, E. S.; Pople, J. A. *Gaussian 98*, Revision A:6. Gaussian, Inc.: Pittsburg, PA, **1998**.

4. Gaussian 09, Revision A.02, Frisch, M. J.; Trucks, G. W.; Schlegel, H. B.; Scuseria, G. E.; Robb, M. A.; Cheeseman, J. R.; Scalmani, G.; Barone, V.; Mennucci, B.; Petersson, G. A.; Nakatsuji, H.; Caricato, M.; Li, X.; Hratchian, H. P.; Izmaylov, A. F.; Bloino, J.; Zheng, G.; Sonnenberg, J. L.; Hada, M.; Ehara, M.; Toyota, K.; Fukuda, R.; Hasegawa, J.; Ishida, M.; Nakajima, T.; Honda, Y.; Kitao, O.; Nakai, H.; Vreven, T.; Montgomery, Jr., J. A.; Peralta, J. E.; Ogliaro, F.; Bearpark, M.; Heyd, J. J.; Brothers, E.; Kudin, K. N.; Staroverov, V. N.; Kobayashi, R.; Normand, J.; Raghavachari, K.; Rendell, A.; Burant, J. C. Iyengar, S. S.; Tomasi, J.; Cossi, M.; Rega, N.; Millam, N. J.; Klene, M.; Knox, J. E.; Cross, J. B.; Bakken, V.; Adamo, C.; Jaramillo, J.; Gomperts, R.; Stratmann, R. E.; Yazyev, O.; Austin, A. J.; Cammi, R.; Pomelli, C.; Ochterski, J. W.; Martin, R. W.; Morokuma, K.; Zakrzewski, V. G.; Voth, G., A.; Salvador, P.; Dannenberg, J. J.; Dapprich, S.; Daniels, A. D.; Farkas, O.; Foresman, J. B.; Ortiz, J. V.; Cioslowski, J.; Fox, D. J., Gaussian, Inc., Wallingford CT, **2009**.

5. Heisenberg, W. *Z. Phys*. **1926**, *38*, 411.

6. Boeré, R. T.; Moock, K. H.; Parvez, M. Z. *Anorg. Allg. Chem.*, **1994**, *620*, 1589.

7. *WinEPR Simfonia, version 1.25*; Bruker Instruments, Inc.: Billerica, MA, **1966**.

8. Carlin, R. L. *Magnetochemistry*; Springer-Verlag: New York, **1986**.

9. Bonner, J. C.; Fisher, M. E. *Phys. Rev*. **1964**, *135*, A640.

10. Estes, W. E.; Gavel, D. P.; Hatfield, W. E.; Hodgson, D. J. *Inorg. Chem*. **1978**, *17*, 1415.

11. Johnston, D. C.; Troyer, M.; Miyahara, S.; Lidsky, D.; Ueda, K.; Azuma, M.; Hiroi, Z.; Takano, M.; Isobe, M.; Ueda, Y.; Korotin, M. A.; Anisimov, V. I.; Mahajan, A.V.; Miller, L. L. arXiv:cond-mat/0001147.

12. Landee, C. P.; Turnbull, M. M.; Galeriu, C.; Giantsidis, J.; Woodward, F. M. *Phys. Rev. B* **2001**, *63*, 100402.

13. *SAINT, version 6.22*; Bruker Advanced X-ray Solutions, Inc.: Madison, WI, **2001**.

14. Sheldrick, G. M. SHELXS-90. *Acta Crystallogr. A* **1990**, *46*, 467.

15. Sheldrick, G. M. SHELXL-97. *Program for the Refinement of Crystal Structures*; University of Göttingen, Göttingen, Germany, **1997**.

16. SHELXTL, VERSION 6.12 *Program Library for Structure Solution and Molecular Graphics*; Bruker Advanced X-ray Solutions, Inc.: Madison, WI, **2001**.

17. Brauer, G. *Handbook of Preparative Inorganic Chemistry*; Academic Press: New York, **1963**; Vol. 1, p 423.

18. Shaterian, H. R.; Doostmohammadi, R.; Ghashang, M. *Chin. J. Chem.* **2008**, *26*, 1709.